TECHNISCHE UNIVERSITÄT MÜNCHEN
Munich School of Engineering
Research group „Control of renewable energy systems“

Dissertation

Modelling, Control and Post-Fault Operation of Dual Three-phase Drives for Airborne Wind Energy

Hisham Magdy Gamal Eldeeb

TECHNISCHE UNIVERSITÄT MÜNCHEN
Munich School of Engineering
Research group „Control of renewable energy systems“

Modelling, Control and Post-Fault Operation of Dual Three-phase Drives for Airborne Wind Energy

Hisham Magdy Gamal Eldeeb

Vollständiger Abdruck der von der Munich School of Engineering der Technischen Universität München zur Erlangung des akademischen Grades eines

Doktor–Ingenieurs

genehmigten Dissertation.

Vorsitzender:
Prof. Dr. Carlo L. Bottaso

Prüfer der Dissertation:
1. Prof. Dr.-Ing. Christoph M. Hackl
2. Prof. Dr. Thomas Hamacher
3. Prof. Ayman S. Abdel-Khalik, Ph.D.

Die Dissertation wurde am 10.01.2019 bei der Technischen Universität München eingereicht und durch die Munich School of Engineering am 05.06.2019 angenommen.

Acknowledgment

This work would not have been completed without acknowledging the following factors: support, motivation, and vision. I would like to express my gratitude to my parents for their endless support, which was the necessary foundation to start such journey. I'm grateful to my wife, without her encouragement and continuous supply of motivation it would have been impossible to deliver this work. I would like to thank my supervisor Prof. Hackl for his remarkable leadership, vision and support, personally and technically, since my arrival in Germany. I'm also thankful to Prof. Ayman Abdel-Khalik's collaboration throughout this PhD. His expertise and contributions are extraordinary. Additionally, I extend my appreciation to my examiner Prof. Hamacher. Finally, I would like to also thank all the AWESCO project members as well as my fellow CRES-group colleagues Julian Kullick, Korbinian Schechner, Markus Landerer and Christian Dirscherl.

I hereby acknowledgment the support of the European Commission, Research and Innovation for their financial support of the EU-AWESCO H2020 ITN project, which hopefully would be the "*magic-bullet*" that tackles the challenges facing the commercialization of the airborne wind energy technology.

Munich, November 2018 Hisham Eldeeb

Contents

List of Figures

List of Tables

Nomenclature

Notation	
$\mathbb{R}$	Set of real numbers
$\mathbb{N}$	Set of natural numbers
$n \in \mathbb{N}$	Number of rows
$m \in \mathbb{N}$	Number of columns
$\zeta \in \mathbb{R}$	Real scalar
$\boldsymbol{\zeta} \in \mathbb{R}^n$	Real vector (bold), expressed as $\boldsymbol{\zeta} = (\zeta_1, \zeta_2, ..., \zeta_n)^\top$
$\lvert\lvert\boldsymbol{\zeta}\rvert\rvert$	Euclidean norm of $\boldsymbol{\zeta}$ as $\lvert\lvert\boldsymbol{\zeta}\rvert\rvert = \sqrt{(\zeta_1)^2 + (\zeta_1)^2 ... + (\zeta_n)^2}$
$\lvert\lvert\boldsymbol{\zeta}\rvert\rvert_\infty$	The maximum norm of $\boldsymbol{\zeta}$, i.e. $\lvert\lvert\boldsymbol{\zeta}\rvert\rvert_\infty = \max\{\lvert\zeta_1\rvert, \lvert\zeta_2\rvert, ..., \lvert\zeta_n\rvert\}$
$\boldsymbol{Z} \in \mathbb{R}^{n \times m}$	Real $n \times m$ matrix (capital bold)
Sub- and superscripts	
$\square^\top$	Transpose operator applied to either a vector or a matrix
$\square_\mathrm{s}$	Subscript 's' denotes referencing to the stator
$\square_\mathrm{s}^\lambda$	Superscript 'λ' is an arbitrary variable representing a subspace (i.e. $\lambda \in \{dq,\ XY,\ xy,\ 0,\ d_0q_0\}$)
$\square_\mathrm{s}^\Lambda$	Superscript 'Λ' is an arbitrary variable representing one of the coordinates of λ
$\bar{\square}$	Phasor description of a variable at *steady state*
$\hat{\square}$	Amplitude of a variable
General	
$\boldsymbol{I}_n \in \mathbb{R}^{n \times n}$	Identity matrix
$\boldsymbol{O}_n \in \mathbb{R}^{n \times n}$	Zero square matrix
$\det(\cdot)$,	Determinant operator
$\boldsymbol{T}_{\mathrm{C},1} \in \mathbb{R}^{3 \times 3}$	Clarke's transformation for $a_1b_1c_1$
$\boldsymbol{T}_{\mathrm{C},2} \in \mathbb{R}^{3 \times 3}$	Clarke's transformation for $a_2b_2c_2$
$\boldsymbol{T}_\mathrm{VSD} \in \mathbb{R}^{6 \times 6}$	Vector space decomposition matrix
$\boldsymbol{T}_\mathrm{p}(\phi) \in \mathbb{R}^{2 \times 2}$	Park transformation adopted for three-phase quantities
$\boldsymbol{T}_\mathrm{p}^{'}(\phi) \in \mathbb{R}^{6 \times 6}$	Generalized Park transformation
$\boldsymbol{T}_\mathrm{k}^{'} \in \mathbb{R}^{6 \times 2}$	Post-fault optimization matrix
$k_\Gamma^\alpha,\ k_\Gamma^\beta$	Scalar optimization parameters in $\boldsymbol{T}_\mathrm{k}^{'}$ of the $\Gamma \in \{X,\ Y\}$ coordinate
$\boldsymbol{J} \in \mathbb{R}^{2 \times 2}$	Rotation matrix, where $\boldsymbol{J} := \boldsymbol{T}_\mathrm{p}(\frac{\pi}{2})$
s	Laplace operator of continuous-time systems
z	Operator of discrete-time systems

$G_{\mathrm{PI}}(s)$	Continuous proportional-integral controller transfer function
$G_{\mathrm{R}}(z)$	Discrete resonant controller transfer function
u	Electrical voltage (in V)
i	Electrical current (in A)
ψ	Flux linkage (in Wb)
$\hat{i}_{\mathrm{s,rated}}$	Rated stator peak current (in A)
$\hat{u}^{ltl}_{\mathrm{s,rated}}$	Rated stator peak line-to-line voltage (in V)
$\hat{u}^{\mathrm{ph}}_{\mathrm{s,rated}}$	Rated stator peak phase voltage (in V)
$\boldsymbol{\zeta}^{a_1\rightarrow c_2}_{\mathrm{s}}$	Stator space vector expressed in the $(\mathrm{a_1b_1c_1}\text{-}\mathrm{a_2b_2c_2})$ frame, where $\boldsymbol{\zeta} \in \{\boldsymbol{u}, \boldsymbol{\psi}, \boldsymbol{i}\}$)
$\boldsymbol{\psi}^{\lambda}_{\mathrm{s,pm}}$	λ subspace flux linkage harmonic component owing to the permanent magnet contribution (in Wb)
$\boldsymbol{s}^{\mathrm{a_1\rightarrow c_2}}_{\mathrm{VSI}}$	Inverter switching vector.
$\boldsymbol{u}^{\mathrm{a_1\rightarrow c_2}}_{\mathrm{s}}$	Inverter phase voltages (in V)
$\boldsymbol{u}^{\lambda}_{\mathrm{PI}}$	Control action applied by the PI controller (in V)
$\boldsymbol{u}^{\lambda}_{\mathrm{R}}$	Control action applied by the resonant controller (in V)
$\boldsymbol{u}^{\lambda}_{\mathrm{s,dist}}$	Disturbance feed-forward voltage (in V)
u_{dc}	DC-link voltage (in V)
V_{p}	Proportional gain (in Ω)
T_{i}	Integral time constant (in s)
T_{R}	Resonant controller time constant (in s)
$m_{\mathrm{e,max}}$	Maximum torque for a given neutral point configuration (in N m)
m_{e}	Electromechanical torque (in N m)
ν	Viscous friction coefficient (in N m s)
m_{load}	Load torque (in N m)
m_{c}	Coulomb friction torque (in N m)
m_{fric}	Total friction torque (in N m)
Θ	Mechanical inertia (in $\mathrm{kg\,m^2}$)
n_{p}	Pole-pair number
ω_{e}	Electrical angular speed (in rad/s)
ω_{c}	Carrier frequency of the encoderless technique (in rad/s)
$\Omega^{\mathrm{MTPC}}_{\mathrm{e}}$	Speed trajectories per every permissible m_{e} of the MTPC criteria rad/s)
ϕ_{e}	Electrical angular position referred to the flux axis of phase a_1 (in rad)
$\Omega^{\mathrm{FW}}_{\mathrm{e}}$	Speed trajectories per every permissible m_{e} of the FW criteria (in rad/s)
$\omega^{\mathrm{FW}}_{\mathrm{e,max}}$	Maximum speed within the $\Omega^{\mathrm{FW}}_{\mathrm{e}}$ loci (in rad/s)
h	Harmonic order, where $h \in \mathbb{N}$
ψ^{h}_{pm}	Flux linkage amplitude of the PM h^{th} harmonic (in Wb)
ϕ^{h}_{o}	Initial phase angle of the PM h^{th} harmonic (in rad)
u^{h}_{emf}	Back-*emf* voltage of the PM h^{th} harmonic (in V)
t	Time (in s)

R_s	Stator electrical resistance (in Ω)
$\boldsymbol{L}_\mathrm{s}^{\lambda}$	Differential inductance matrix (in H)
L_m^{λ}	Cross-coupling inductance between the axes of the λ subspace (in H)
$\bar{\bar{L}}_\mathrm{s}^{\Lambda}$	Constant inductance of the axis Λ (in H)
L_s^{Λ}	Inductance of Λ axis (in H)
P_Cu	Stator copper losses (in W)
p_Cu	Post-fault copper losses (in p.u.)
t_{V_ρ}	Dwell time of the active voltage vectors, where $\rho \in \{1, 2, 3, 4\}$
f_sw	Sampling rate (in kHz)
T_sw	Sampling period, where $T_\mathrm{sw} = \frac{1}{f_\mathrm{sw}}$ (in s)
T_s	Half the sampling period T_sw (in s)
Abbreviations	
CWT	Conventional wind turbines
AWE	Airborne wind energy
GG-AWE	Ground-generator AWE
FG-AWE	Flying-generator wind energy
DT	Dual three-phase
DTM	Dual three-phase machines
PV	Photo-voltaic
LCOE	Levelized cost of energy
AWESCO	Airborne wind energy system, control, and optimization
PM	Permanent-magnet
IPMSM	Interior PM synchronous machine
SPMSM	Surface PM synchronous machine
IM	Induction machine
ADT	Asymmetrical dual three-phase
VSI	Voltage source inverter
VSD	Vector space decomposition
PI	Proportional-integral
R	Resonant
PR	Proportional-resonant
FFT	Fast Fourier transform
PWM	Pulse-width-modulation
SVPWM	Space-vector PWM
SPWM	Sinusoidal PWM
LOH	Low-order harmonics
THD	Total harmonic distortion
DSP	Digital signal processor
A/D	Analog-to-digital conversion
MTPC	Maximum-torque-per-current
p.u.	Per-unit value
FW	Field-weakening

ML	Minimum Joule copper losses optimization
MT	Maximum torque optimization
MLMT	Minimum losses and maximum torque optimization
MMC	Modular multi-level converter
KVL	Kirchhoff's voltage law

Kurzzusammenfassung

Flugwindkraftanlagen (FWA) verfügen theoretisch über ein großes Potenzial als effizienter und kostengünstiger Ersatz für konventionelle Windkraftanlagen (WKA). Allerdings behindern mehrere hoch korrelierte Engineering-, Design- und Betriebsaspekte die Kommerzialisierung der FWA-Technologie. Eine dieser Herausforderungen in elektrischer Hinsicht ist die Auswahl eines effizienten, fehlertoleranten elektrischen Antriebs. Der anhaltende Trend, den selben Typ Drehstromantrieb wie für WKA einzusetzen, ist nicht optimal; Statistiken haben gezeigt, dass die Ausfallraten von leistungselektronischen Umrichtern, sowie die Verbindungen zu den Maschinenklemmen und den Statorwicklungen die höchsten Ausfallraten unter den WKA-Komponenten besitzen. Wenn Sicherheitsmaßnahmen ergriffen werden, wird die fehlerbehaftete Komponente getrennt, was zum einphasigen Betrieb der Maschine führt. Dieser gefährdet die Luftmembran und schließlich das gesamte FWA-System.

Eine geeignete Alternative ist die Leistungssegmentierung der Maschine durch Umwicklung als doppelt drei-phasige Maschine, die aufgrund ihrer fehlertoleranten Eigenschaften einen zuverlässigen Dauerbetrieb gewährleistet. In dieser Arbeit wird die Verwendung einer doppelt drei-phasigen permanenterregten Synchronmaschine mit vergrabenen Magneten vorgeschlagen. Im Vergleich zum Stand der Technik sind die Hauptbeiträge der durchgeführten Arbeiten: (i) Identifizieren der Maschinen-Nichtlinearitäten; (ii) Modellieren und Simulieren der Maschinendynamik; (iii) effizienter Betrieb in Verbindung mit einem stationären Fehlerstromregler; und (iv) Entwicklung einer optimierten Betriebsstrategie im Fehlerfall ohne Überschreiten der Motorbegrenzungen (d.h. Nennstrom und -spannung). Die theoretischen Erkenntnisse werden experimentell am Maschinenprüfstand validiert.

Abstract

Airborne wind energy (AWE) systems possess *theoretically* a strong potential as an efficient cost-effective replacement for conventional wind turbines (CWTs). However, several highly correlated design, operational and engineering aspects; hinder the commercialization of such technology. One of those challenges, from an electrical perspective, is the selection of an efficient fault-tolerant electrical drive. The ongoing trend of employing three-phase drives as those for CWTs is *non-optimal*; since statistics revealed that failure rates of power electronic converters, their connections to the machine terminal and stator windings represent the highest failure rates among the CWT components. When safety measures are embraced, the faulty part is disconnected leading to a single phase operation, which jeopardizes the airborne membrane and eventually a complete failure of the AWE system.

A suitable alternative is power-segmentation of the machine by rewinding to a dual three-phase (DT) machine, ensuring reliable continuous operation owing to their inherent fault-tolerant capability. This thesis proposes the utilization of DT interior permanent magnet synchronous machines. Compared to the available body of literature, the main contributions of the carried-out work are: (i) identifying the machine non-linearities; (ii) modeling and simulating the machine dynamics; (iii) efficient operation coupled with a *zero* steady-state error current regulator; and (iv) deriving a post-fault optimization without exceeding the machine ratings (i.e. currents and voltages). Experimental results are provided for the sake of validation.

Scientific environment and outcomes

This PhD project was part of the European Union Horizon H2020 project "**A**irborne **W**ind **E**nergy **S**ystem **C**ontrol and **O**ptimization" (AWESCO). 14 multidisciplinary PhD candidates were assigned to the project distributed among eight acadmeic institutes and four industrial partners, where this PhD was carried-out at the Technical University of Munich (TUM). Throughout this 39 months PhD, the involved publications were not only concerned with multi-phase drives in terms of modelling and control, but additional aspects -driven by scientific curiosity- were also tackled in terms of efficiently controlling three-phase drives as well as grid-connected converters. The total number of publications were 13 papers divided into five Journal manuscripts and eight conference publications as listed below.

Journal publications

1. H. Eldeeb, A. S. Abdel-Khalik, J. Kullick, and C. M. Hackl, "Pre and post-fault current control of dual three-phase reluctance synchronous drives", *IEEE Transactions on Industrial Electronics*, 2019 (doi: 10.1109/TIE.2019.2921276).

2. H. Eldeeb, A. S. Abdel-Khalik, and C. M. Hackl, "Post-fault full torque speed exploitation of dual three-phase IPMSM drives", *IEEE Transactions on Industrial Electronics*, vol. 66, pp. 6746–6756, Sept. 2019.

3. H. Eldeeb, A. S. Abdel-Khalik, and C. M. Hackl, "Dynamic modelling of dual three phase IPMSMs with different neutral configurations", *IEEE Transactions on Industrial Electronics*, vol. 66, pp. 141–151, Jan. 2019.

4. H. Eldeeb, C. M. Hackl, L. Horlbeck, and J. Kullick, "A unified theory for optimal feedforward torque control of anisotropic synchronous machines", *International Journal of Control*, June 2017 (doi:10.1080/00207179.2017.1338359, open access).

5. H. Eldeeb, A. Massoud, A. S. Abdel-Khalik, and S. Ahmed, "A sensorless Kalman filter-based active damping Technique for grid-tied VSI with LCL filter", *International Journal of Electrical Power & Energy Systems*, vol. 93, pp. 146 – 155, Dec. 2017.

Conference publications

1. H. Eldeeb, M. Abdelrahem, A. S. Abdel-khalik and C. M. Hackl, "Enhanced electromechanical modeling of asymmetrical dual three-phase IPMSM drives", *in Proceedings of the IEEE International Symposium on Industrial Electronics (ISIE 2018)*, Cairns, Australia, Jun. 2018.

2. M. Abdelrahem, H. Eldeeb, C. M. Hackl and R. Kennel, "Computationally efficient predictive direct torque control for PMSGs without weighting factors", *Power Electronics, Control and Intelligent Motion (PCIM)*, Nuremburg, Germany, Jun. 2018.

3. H. Eldeeb, M. Abdelrahem, A. S. Abdel-khalik and C. M. Hackl, "A unified SVPWM realization for minimizing circulating currents of dual three-phase machines", 12th *IEEE International Conference on Power Electronics and Drive Systems (PEDS)*, Hawaii, USA, Dec. 2017.

4. H. Eldeeb, A. S. Abdel-khalik and C. M. Hackl, "Highly efficient fault-tolerant electrical drives for airborne wind energy systems", 7th *International Airborne Wind Energy Conference (AWEC'17)*, Freiburg, Germany, 2017.

5. M. Abdelrahem, Z. Zhang, R. Kennel, H. Eldeeb and C. M. Hackl, "Simple and robust direct-model predictive control technique for PMSGs in variable-speed wind turbines", 4th *IEEE Symposium on Predictive Control of Electric Drives and Power Electronics*, Pilsen, Czech Republic, Sept. 2017.

6. H. Eldeeb, C. M. Hackl, J. Kullick and L. Horlbeck, "Analytical solutions for the optimal reference currents for MTPC/MTPA, MTPV and MTPF control of anisotropic synchronous machines considering stator resistance and mutual inductance", 17th *European Conference on Power Electronics and Applications (Energy Conversion Conference and Exhibition), EPE'17 ECCE Europe*, Warsaw, Poland, Sept. 2017.

7. H. Eldeeb, C. M. Hackl, J. Kullick and L. Horlbeck, "Analytical solutions for the optimal reference currents for MTPC/MTPA, MTPV and MTPF control of anisotropic synchronous machines", *IEEE International Electric Machines and Drives Conference (IEMDC)*, Miami, FL, USA, May 2017.

8. H. Eldeeb, C. Hackl and J. Kullick, "Efficient operation of anisotropic synchronous machines for wind energy systems", *Journal of Physics, Conference series*, Vol. 753, pp. 112009, Munich, Germany, Oct. 2016.

Chapter 1

Introduction

1.1 Transforming to renewables

Driven by the urge to find a sustainable reliable energy resource, while running out of fossil fuels, the adoption of renewable energy resources experienced a rapid exponential growth within the last two decades [1, 2]. Within the second decade, environmental advocates and global warming supporters have influenced politicians and decision-makers for serious amendments of energy production and consumption [3–6]. Furthermore, the momentum of pursuing nuclear-based power plants, characterized by its highest energy densities, has declined; stimulated by harmful nuclear wastes and catastrophic accidents that took place in Chernobyl in Russia 1986 and Fukushima in Japan 2011. Accordingly, denuclearization took place with full-throttle in many countries as in Germany, where 18 out of its 25 nuclear power plants are currently out of service; with a plan of complete denuclearization by the end of 2022 [7]. Moreover, studies indicated that the excessive unregulated CO_2 has lead to severe climate changes, where drought and temperature rise have been recorded all over the world. Thus, scientists devoted considerable effort to apprehend the magnitude of necessary emissions reductions for a sustainable life on Earth. This lead to the definition of the so called *Carbon-Budget*, which is the estimated amount of CO_2 the world can emit, below which a 2 °C global temperature rise would be avoided by 2045 with the current CO_2 emissions [8]. Otherwise, sea and ocean levels would rise by nearly 1 m and heavy rain precipitation would increase, leading to floods and and in some cases drowning of some areas around the world. As a direct effect of temperature rise, coral bleaching and the intensity and frequency of wildfires will increase 1.5-2 times [9]. The Paris climate pact 2015, which will take effect in 2020, has called on 196 nations worldwide to hold the increase in average global temperature and pursue the goal of not more than 1.5 °C above the pre-industry level [8].

To achieve such ambitious goal, it is necessary to reduce greenhouse gas emissions generated by burning fossil fuel in power plants. However, rapid economic development is driving up electricity consumption. Many locations in the world are still suffering from electrical shortages [10]. Efficiently generating, storing and distributing energy are becoming not only critical challenges, but also opportunities for research and development to excel [11–13]. On the other hand, such energy reforms

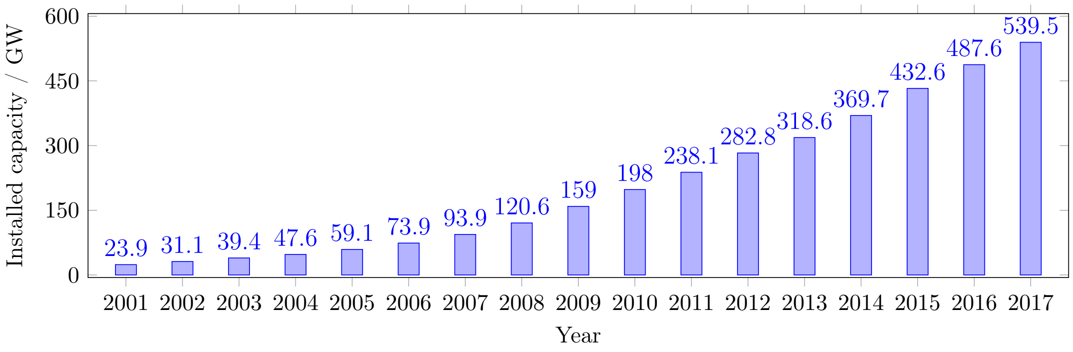

Fig. 1.1. The global accumulative installed wind capacity from 2001 to 2017 [19].

have also affected the transportation sector; owing to its significant contribution to global warming, with approximately 26% of the total US greenhouse emissions in 2016 [14] and 25.8% in Europe in 2015 [15]. In [16], the authors studied the relationship between vehicle ownership and per capital revenue; they estimated that 2.08 billion vehicles will be driving across the world's roads by 2030, while there were only 70 million cars after World War II and only 900 million today. This trend implies a huge increase in fuel demand. In fact, vehicular fuel consumption has jumped from 57 880 million gallons in 1960 (which cost about 40 800 million dollars) to 168 597 million gallons in 2011 (which cost 1 079 400 million dollars) [14]. Consequently, the transform from oil-based to hybrid or full electric vehicles is inevitable to accomplish the strategic targets for limiting the greenhouse emissions. This explicitly means that in the near future, a major portion of the transportation sector will impose a significant burden on the electrical network.

Motivated by the aforementioned challenges, a tremendous growth and spread of renewable energy plants have been recorded in the last decades. Since the energy supplied by renewables still lacks reliability and continuity of supply; owing to their high dependency on environmental conditions, diversifying the different renewable energy sources, which rely on different generation principles (i.e. wind turbines, photo-voltaic (PV), geothermal, tidal, etc.) is mandatory [17]. According to [**?**, 18], wind and solar energy are the most harvested type of renewable energy resources worldwide, where the former is of interest in this thesis. Wind generators are the most widespread type of intermittent renewable energy harvesters with their 540 GW of cumulative installed power at the end of 2017 [19], as shown in Fig. 1.1. Starting from the first deployment of the first commercial wind turbine in the 1980s, vast amount of research has been carried-out in improving efficiency, energy harvesting and operation; given that these enhancements were economically feasible and the initial capital costs would be reimbursed through out the life time of the tower (25-30 years). Since 2015, the annually installed wind capacity has been decreasing; due to saturation of appropriate on-shore windy sites, where wind plants could be installed [20]. In this context, many research programs trend in designing wind turbines with long rotor diameter (more than 250 m) along with increasing the tower height, in order to increase the power capacity per unit of land area [20], as depicted in Fig. 1.2. Meanwhile, since the beginning of this century, many industries have been financing research projects to study the feasibility and profitability of installing

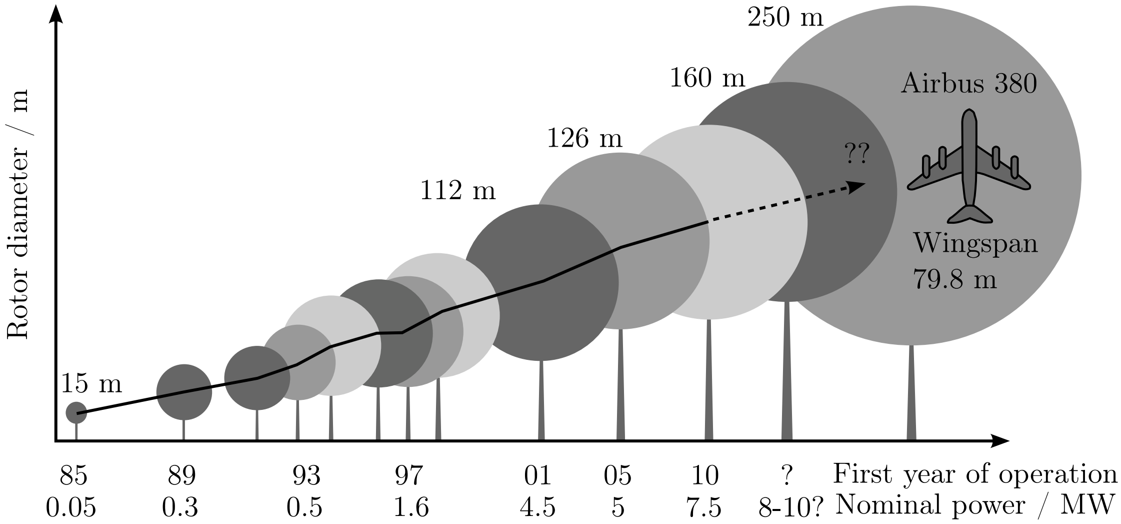

Fig. 1.2. Time line evolution of conventional wind turbines in terms of power capability, height and rotor diameter [21].

off-shore wind turbines [2]. They have the advantage of utilizing the wind sources away enough from the shore, where the winds are more regular, stronger and less disturbed by the rough terrain of the land. Moreover, off-shore wind turbines are socially accepted, since they do not disturb the landscape and do not cause noise pollution. The cumulative installed capacity due to the running projects is expected to exceed 30 GW only in Europe and the anticipated growth rate is quite promising [22].

1.2 Airborne wind energy

Along with the advantages of employing conventional wind turbines (CWTs) in supplying power to the grid, that comes at the expense of:

- Strong steady winds are available at altitudes higher than 150 m, which are available in only 2% of the land worldwide [23];
- The generated power is discontinuous and highly dependable on the weather conditions;
- High transportation costs of the plant components during construction and maintenance from and to the off-shore site;
- For off-shore wind turbines, building robust and secure wind farms over deep water is a challenging and time-consuming procedure;
- These aforementioned drawbacks increase the total investment and operational costs of the power plant in comparison with the on-shore power plants; and
- Off-shore turbines are exposed to heavy storms or hurricanes that might damage the blades or elevate the design specifications.

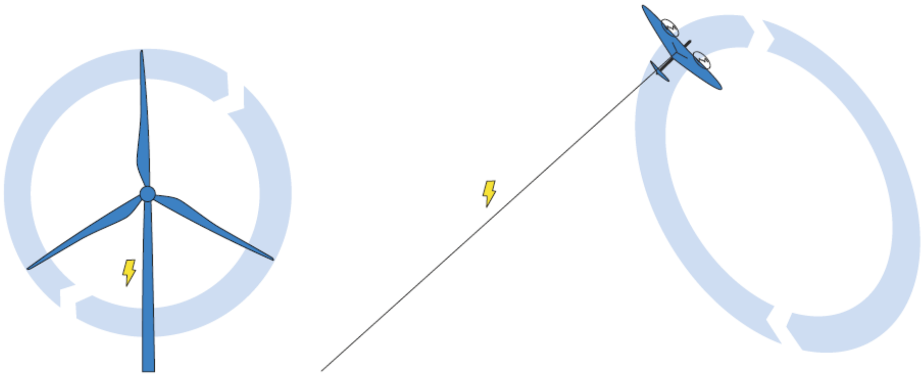

(a) (b)

Fig. 1.3. (a) Conventional wind turbine and (b) an airborne wind energy system illustrating the followed path for the generation of electrical energy and the means of transporting it, which is through the tower and tether, respectively [24].

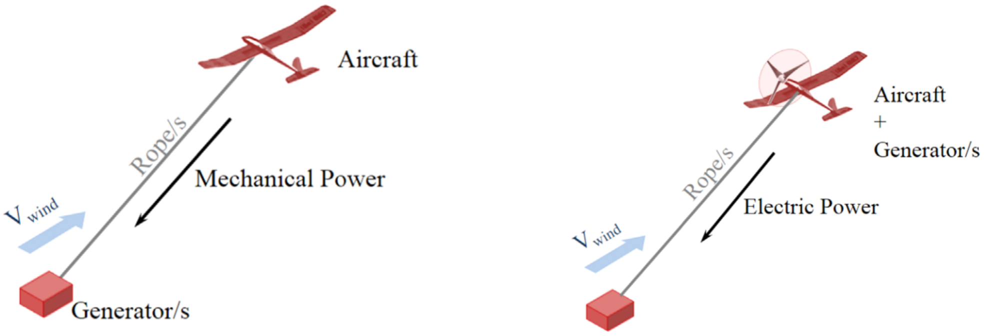

(a) (b)

Fig. 1.4. General Scheme of AWE concepts (a) Ground-Gen and (b) Fly-Gen systems [24].

As an alternative to the CWTs, a novel renewable energy technology emerged, known as airborne wind energy (AWE). AWE systems aim at harvesting wind energy at elevated altitudes compared to CWTs ($\geq 350\,\text{m}$). Instead of the rotor blades that generate energy by rotation, the blades are replaced by a specially designed kite/aircraft and the wind tower is replaced by a tether (see Fig. 1.3). This idea was introduced initially by Loyd in 1980 [25], when he theoretically analyzed the maximum possible energy that could be extracted from a flying kite connected to the ground with a tether. Since then, AWE did not attract the investors; as the means of realizing such technology at that time were not at that level of advancement when compare to modern technology. However, in the last decade, this sector has gained attention from several companies and investors, due to rapid gained experience in the research field of high-altitude wind energy [24].

1.2.1 Types of AWEs

So far, the number of prototypes have been developed, each with different philosophy aiming at maximizing as much as possible the performance, feasibility, and reliability

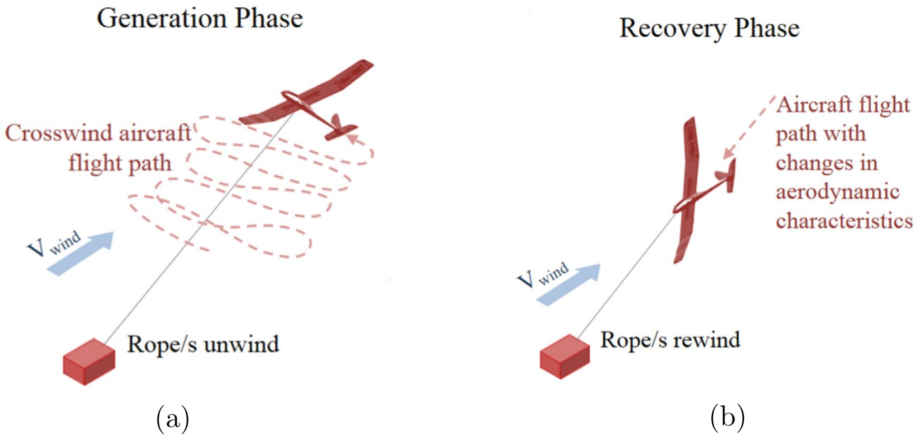

(a) (b)

Fig. 1.5. Operation phases of a pumping type GG-AWE system showing the (a) reeling-out (i.e. generator mode) and (b) reeling-in (motor mode) [24].

of the adopted AWE system; given that the aforementioned features are not always directly proportional leading to compromises. Even though hundreds of patents have been registered, the AWE systems can be divided into Ground-Gen AWE (GG-AWE) systems and Fly-Gen AWE (AWE) systems [26] (see Fig. 1.4). In GG-AWE systems, the electrical generators are placed on the ground. The wind energy at high altitudes is harvested by the aircraft, that produces mechanical work on the generator side via the traction forces. This mechanical energy is transmitted to the ground through one or more tethers, producing the desired motion for electric power generation (see Fig. 1.4(a)). Enerkite GmbH in Germany and Ampyx Power in the Netherlands are key companies for such technology architecture [23, 27].

For the FG-AWE systems, the aircraft is equipped with on-board high speed generators, where the generated electrical power is transmitted to the ground station via embedded power cables within the tether (see Fig. 1.4(b)). Usually power is transmitted at higher voltage levels in comparison with the voltage level of GG-AWE systems; to reduce the electric current in the embedded conductor and hence the electrical losses. Makani in the United States of America is one of the main contributors excelling in the field of FW-AWE systems [28]. There are also other types of FG-AWE systems as the one developed by Altaeros Energies in the United States of America [29]. However, such systems are characterized by low operating hours in comparison with those seen in Fig. 1.4. Further classifications of AWE systems in terms of materials used to built the aircraft, tether, rigid (i.e. aircraft) or soft wings (i.e. kite/parashoot) can be found in [24].

The pumping type GG-AWE system is the one considered in this thesis, which has the operating phases as indicated in Fig. 1.5. Upon taking off, the aircraft flies cross-wind in a figure of 8, as seen in Fig. 1.5(a), pulling the tether and generating power. Owing to the limited length of the tether, the aircraft is directed towards the ground station, adjusted with minimum tension in the tether. Accordingly, the aircraft is pulled at high speed and the electrical drive operates in motoring mode (see Fig. 1.5(b)). The net resultant of reeling-in/out powers represents the useful power transferred later to local loads or grid. The complete layout for a typical grid-connected GG-AWE system is shown in Fig. 1.6. The generated power on the

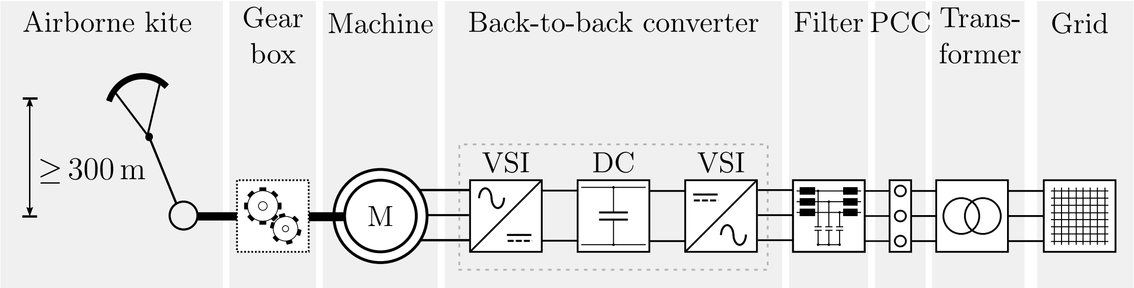

Fig. 1.6. Typical electrical layout of a grid-connected GG-AWE system with its different components. The point of common coupling (PCC) refers to the point where the grid voltage and current sensors are introduced in the circuit.

machine side is transferred to the grid via the back-to-back converter topology[1] through a passive inductive or inductive-capacitive-inductive filter; to adhere to the IEEE 519-2014 and IEEE 115-2009 grid codes [30, 31].

1.2.2 Feasibility of AWEs

The first work presented an evaluation of AWE potential was carried-out by Archer and Caldeira [32]. This work aimed at providing an analysis of a worldwide wind data at altitudes between 0.5 km and 12 km and studying the geographical distributions as well as the consistency of winds at these altitudes. It was concluded, that the power density increases monotonically at higher elevations, yet the power density reaches its maximum at altitudes between 8-10 km. The decrease of the power density at altitudes higher than 10 km could be interpreted by the significant decrease in the air density; since the power density is proportional to the air density, which decreases exponentially at higher atmospheric elevations [25, 26].
In [33], a techno-economical assessment has been conducted as well. The costs of building and setting-up two 2 MW power plants in Northern Ireland were compared. One of these power plants was a CWT and the other was a pumping type GG-AWE power plant. The preliminary cost of the pumping type GG-AWE is estimated to be approximately half of the costs of the conventional wind power plant with the same rated power; owing to the rotor replacement of CWT with a light-weight kite. Besides, no tower structure is needed in the pumping type GG-AWE power plant. In addition, transporting and mounting the wind turbine component is an expensive process in comparison with the GG-AWE, which is easy to transport and mount. However, to make this comparison impartial, the levelized cost of energy (LCOE) for both power plants was evaluated, which is obtained by dividing the total cost of the power plant by the aggregated or potential energy production throughout life time of the plant. In this example, the LCOE from the pumping type GG-AWE 0.106 £/kWh was about three times the LCOE of CWT 0.03-0.04 £/kWh. The main reason for this difference, despite the fact that the preliminary cost of the pumping type GG-AWE is half that of the CWT, is that the pumping type GG-AWE was a

---

[1] A back-to-back converter consists of two voltage-source inverters (VSIs) sharing the same DC-link, such that a VSI is connected to the machine and the other one is related to the grid. Through the back-to-back topology, the power flow can be from the machine to the grid and vice versa.

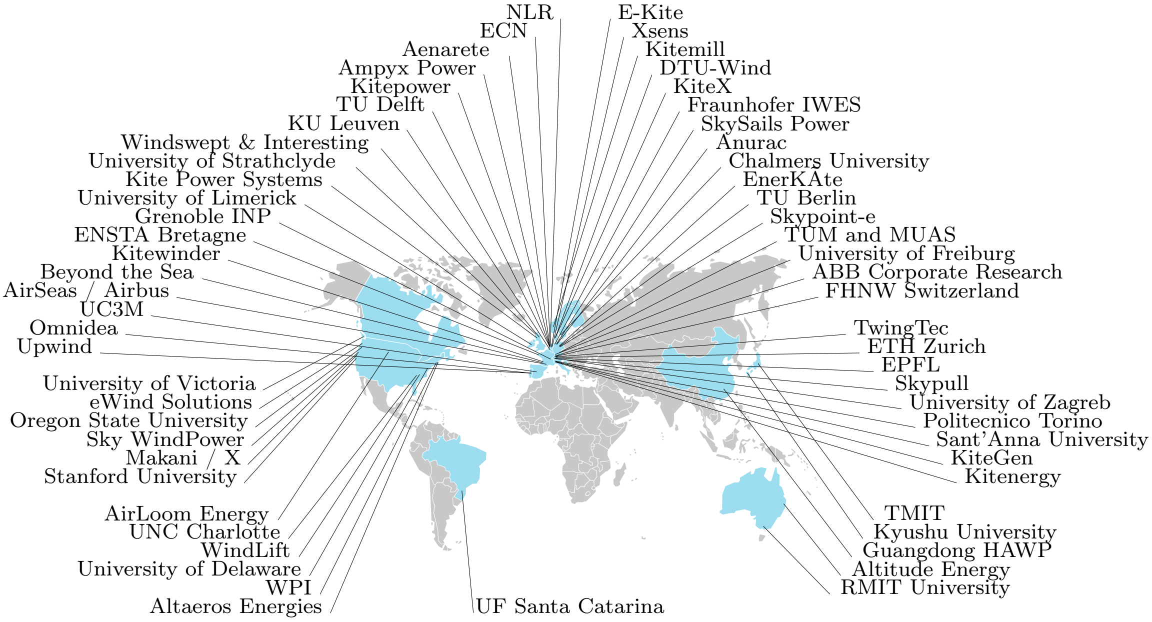

Fig. 1.7. Airborne wind energy research and development activities in 2017 [24].

study project and the total cost of the pumping type GG-AWE was divided by the total produced energy in only one year, unlike the CWT case, where the total cost is normally divided by the potential energy generated throughout the life time of the wind turbine, which is usually between 25 and 30 years. Furthermore, in this project the kite was replaced 6 times during the operation period, which was the major cost of the plant (approx. 70% of the total cost). This result only reflects the prematurity of this technology, that the material of the kite was expensive and vulnerable to degradation. Since that time, development has been carried-out in several fields related to the material, equipment and tools used to set up a pumping type GG-AWE system. In [26, Chapter 15], it is expected that by the time of high-scale commercialization such technology would take place, the LCOE curtailment could be more than 50%, where expertise would be gained and stable operation at higher altitudes would be permissible.

In general, AWE is a promising renewable source of energy and its potential is propitious. However, the available technologies nowadays are still premature and incapable of providing a concept, which tackles all challenging aspects of commissioning AWE systems. It is expected, however, that significant changes will take place in the near future, evident by the increasing number of institutes and companies involved in the development of such technology, as illustrated in Fig. 1.7. In this framework, other research fields related to AWE is rapidly expanding including machine design, electronics, control, material science.

1.3 Problem statement and motivation

AWE systems demonstrate *theoretically* strong potential as efficient cost-effective replacement for CWTs as explained in Section 1.2. However, several correlated

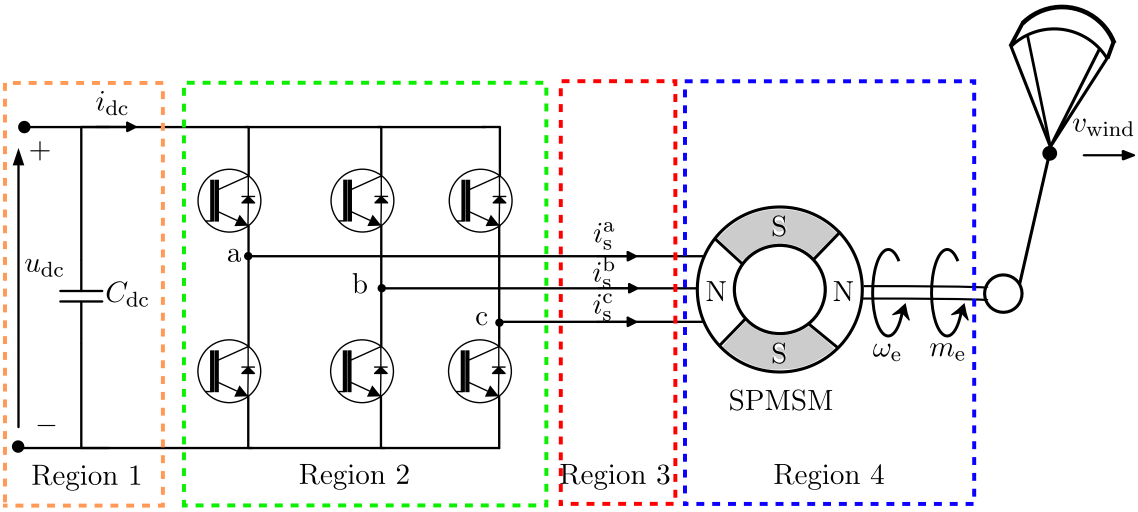

Fig. 1.8. Layout of a three-phase AWE-based electrical drive, classified into 4 distinct fault regions: Region 1 represents the DC-link section, Region 2 contains the three-phase VSI, Region 3 the wiring between the VSI and the stator terminals, and Region 4 representing the surface-mounted permanent magnet synchronous machine (SPMSM) with its mechanical couplings to the AWE-Kite.

design and engineering aspects; hinder the commercialization of such technology. The selection of a highly efficient fault-tolerant electrical drive is still challenging especially for those AWE concepts based on reel-in/out for power generation (i.e. pumping type GG-AWE). After carrying out two internships in 2016 at Ampyx Power and Enerkite, it was clear that standard off-the-shelf three-phase drives were adopted (see Fig. 1.8), which have a similar electrical topology to those employed by CWTs. By consulting literature and upon discussing the general specifications of an optimal drive train for a GG-AWE system with the industrial partners of the EU-AWESCO project [34], it was clear that the adopted standard three-phase drives, which are the adopted topologies by *almost* all AWE enthusiasts, have the following limitations:

- Some of the industrial partners of the AWESCO project selected a SPMSM. Since both partners utilize the pumping-type AWE system (i.e. high-speed-low-torque operation during reeling-in and a low-speed-high-torque is pursued during reeling-out), this type of machine is not the optimal choice when compared to other types of permanent magnet machines; since it has one of the lowest constant power-speed range curves [35]. Others employ induction machines (IMs) which are cheap but inefficient [35].

- The drive operates only when information concerning the rotor position is fed to it, which is normally done via a position sensor (i.e. encoder). An encoder failure, without any source of backup, means a complete shutdown of the drive operation. In literature, encoderless (i.e. sensorless) techniques are popular schemes, which estimate the rotor position instead [37]. For SPMSM, it is challenging, however, to implement an encoderless scheme at very low speeds and impossible at zero speed. This is due to the rotor isotropy throughout the entire air-gap resulting, from a control perspective, in an unobservable system.

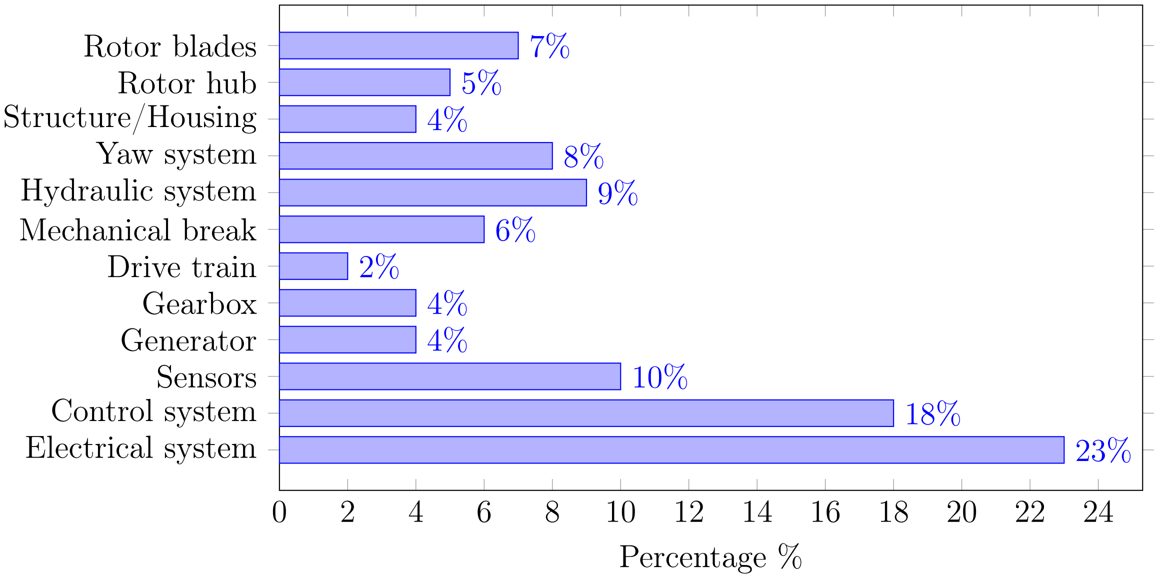

Fig. 1.9. Share of failures of the different subsystems of a CWT collected over 15 years from 1500 WTs [36].

- Fig. 1.9 shows the share of failure each component of a CWT collected over 15 years from 1500 WTs. Such information should be considered since both CWTs and GG-AWE systems have similar components from an electrical drive point of view. The electrical and control system share the highest contributions in terms of failure, where power converters have the highest probability of fault occurrence among any electrical systems in a CWT [38–44]. This corresponds to a fault within region 3 in Fig. 1.8. Irrespective of the machine type, if a fault is detected and cleared in regions 1-3 (see Fig. 1.8), the three-phase drive is converted to a single-phase drive; leading to [45]

  - 67% torque reduction to avoid thermal stresses;
  - Incapability of reversing the direction of rotation. In other words, the machine can stay only in the reeling-in or reeling-out phases which is practically unacceptable;
  - Significant vibratory behavior due to the associated huge torque ripples; and
  - Single-phase machines are not self-starting. For an AWES, if *hypothetically* the kite was brought to a safe state, the system can by no means operate once more without carrying-out the necessary maintenance.

- Non-linear modelling and optimal control of the electrical drive were not considered a priority within the ongoing design procedure at the industrial partners, even though optimized electrical generation meant maximizing life time and minimizing failures. This lead to the employment of highly over rated drives.

1.4 Proposed solution and contribution

Motivated by the aforementioned limitations and challenges, this PhD thesis proposes the adoption of a multi-phase electrical drive, in particular dual three-phase drives, which can be realized from the original machine winded in a three-phase connection[2]. The new topology as well as the proposed underlying controller fulfill to the aforementioned AWE drive requirements and challenges; where almost no additional hardware is needed to realize the proposed drive. As explained later and compared to the adopted drive by the industrial partners, the proposed AWE electrical drive and the adopted control are able to achieve the following:

- Efficiency enhancement by adopting an interior PMSM (IPMSM) instead of a SPMSM and appropriate optimal feedforward control [46, 47]. Moreover, the embedded magnets within the rotor of IPMSMs eventually extend the speed range in comparison to SPMSMs, where the magnets are vulnerable to be centrifugal forces with increased speeds [35];
- Removing one of the two single sources of failures through encoderless control (i.e. estimating the rotor position through the entire speed range and feeding it to the control system), which is applicable to IPMSMs owing to their air-gap saliency [37];
- Enhancing the fault-tolerance capability due to the proposed use of multi-phase machines and the underlying controller, where the torque reserve can reach under faulty conditions up to approximately 67% depending on the stator windings layout;
- The necessary DC-link voltage is halved [2] in comparison with that in Fig. 1.8. This lowers the costs of DC switchgear devices;
- The effective power per phase decreases in the topology for the same machine power rating in Fig. 1.10. Combined with manipulated pulse-width-modulation (PWM) schemes [48, 49], switching losses can be reduced significantly;
- The rating of the each VSI in Fig. 1.10 is half [2] that of the single VSI in Fig. 1.8. This is advantageous specially in high power ratings (i.e. ≥ 100 kW), where the combined costs of the two VSI in Fig. 1.10 would be lower than that of the single VSI [50] (see Fig. 1.11). Accordingly, less expensive cables of lower current rating in Region 3 in Fig. 1.10 can be utilized; and
- Improved operation during pre- and post-fault operations with low torque ripples (i.e. lower acoustic noise). Thus, lowering the tendency of the tether failure owing fatigue stresses as well as the resultant acoustic noise [44, 47, 51].

Compared to the available body of research in terms of dual three-phase IPMSMs, the work carried-out during this PhD aimed at not only realizing efficiently the

---

[2] The rewinding procedure and the impact of halving the machine rated current or voltage are explained in detail in the Appendix A.2.

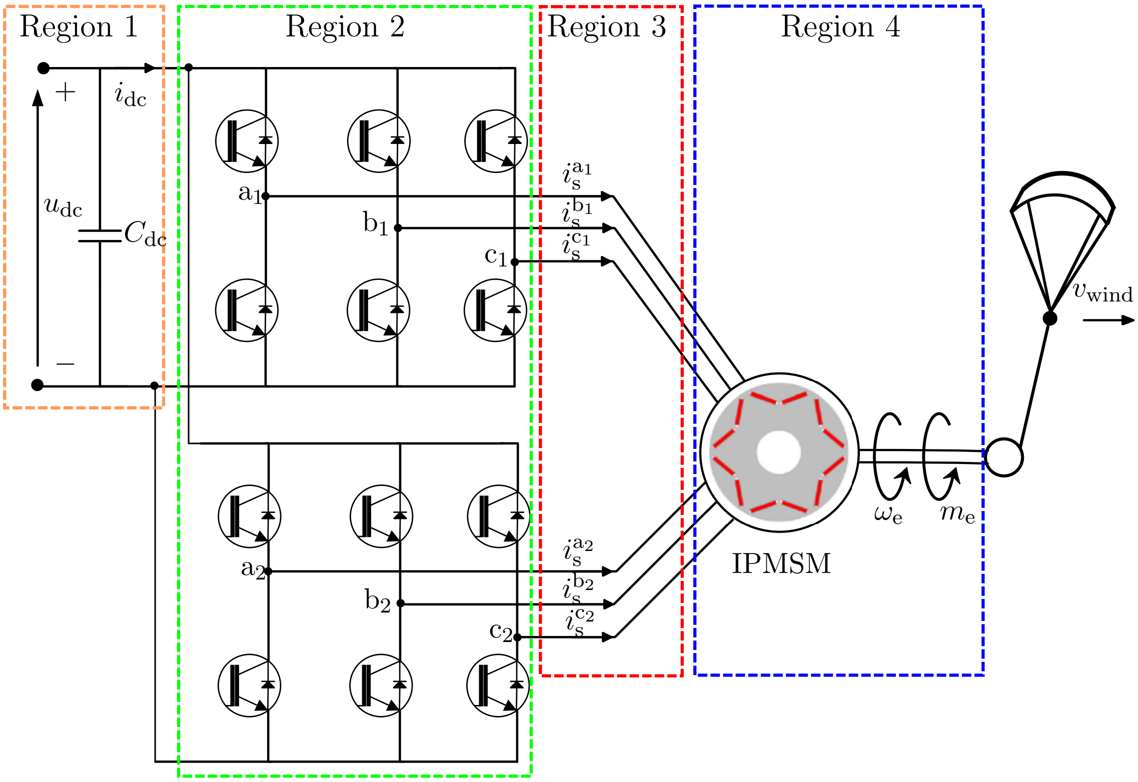

Fig. 1.10. Proposed topology for an AWE electrical drive comprising a multi-phase IPMSM machine; overcoming the challenges imposed by the topology used in Fig. 1.8.

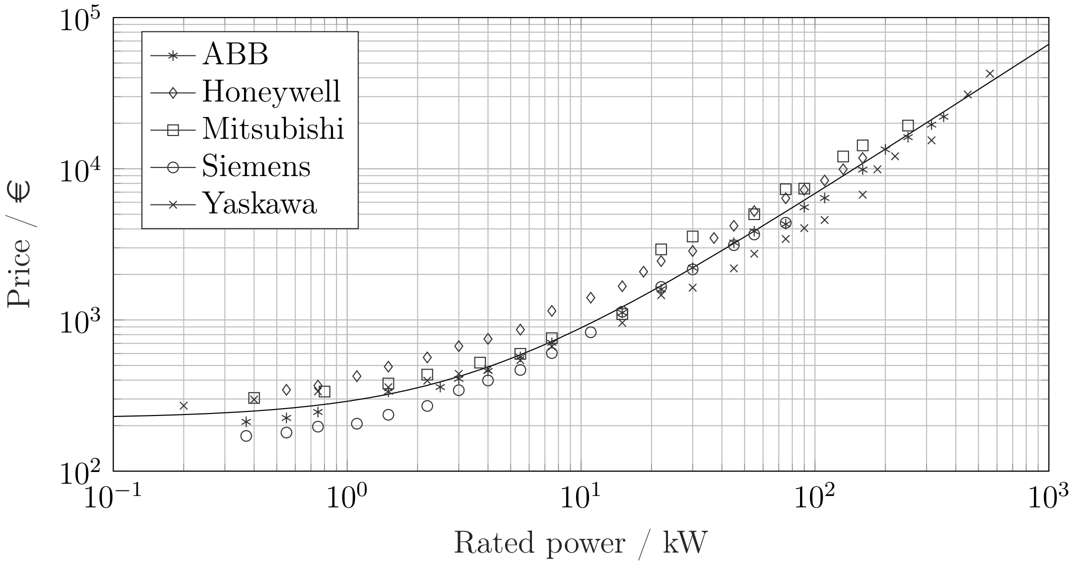

Fig. 1.11. Low voltage inverter pricing with respect to price from several suppliers, where the solid line —— represents a fitted linear regression curve [50].

aforementioned advantages upon employing such drive, but also contributing by providing precise mathematical models and improving the performance in the pre- and post-fault cases. This thesis is organized as follows:

- Chapter 1 is an introduction to the thesis, discussing the rapid adoption of renewable energy resources, AWE, motivation for the thesis, and the proposed solution;

- Chapter 2 discusses the acquisition of high fidelity non-linear models of the machine, modelling the VSI, simulating the drive using Matlab/Simulink and their comparison with the results acquired from the set-up test-bench. The obtained results are published in the *IEEE Transactions of Industrial Electronics* [51];

- Chapter 3 further utilizes the developed non-linear models in designing an efficient fast-tracking stator current controller, that ensures a high-performance operation with low torque ripples [51]. Based on identifying the machine non-linearities, enhancement in term of the electromechanical modelling was realized and published in [47]. Moreover, an improved space-vector pulse-width-modulation was proposed [48], which simplifies the digital implementation of the VSI switching scheme;

- Chapter 4 discusses the fault detection and post-fault operation of the adopted drive, where the proposed optimization strategy exploits the full torque-speed characteristics of the dual three-phase IPMSM drive, which was not covered by literature. Furthermore, the proposed post-fault optimization expands the torque and speed limits of the drive compared to the available body of literature concerning fault tolerance of such drives. This work is published in the *IEEE Transactions of Industrial Electronics* [44]; and

- Finally, Chapter 5 concludes this thesis and illustrates the propositions for future work.

Theoretical findings are simulated and compared to the experimental results corroborated on a 2.5 kW lab prototype, as explained in detail in Appendix A. Appendix B provides lengthy derivations, which were omitted from the main chapters.

Chapter 2

Non-linear modelling of dual three-phase IPMSM drives

As introduced in Chapter 1, the electrical drive is considered the medium, through which the mechanical energy generated via the kite is dispatched to the electrical grid (i.e. electromechanical energy conversion). An electrical drive is composed of three main parts: the electrical machine, the power electronic converter, and finally the underlying controller. It is necessary to ensure that the aforementioned components are functioning as efficiently as possible; in order to ensure high performance operation, maximize the profit of such technology in terms of energy production (i.e. minimize losses), and extend the lifetime of the electrical components. When rewinding a the three-phase machine to a dual three-phase one, the electrical phase shift between the new windings is a degree of freedom. In literature, there are two possible phase shifts, which are $\pi/6$ leading to the so called asymmetrical windings [51,52] $\big($see Fig. 2.1(a)$\big)$ or $\pi/3$ representing the symmetrical windings [53] $\big($see Fig. 2.1(b)$\big)$. The former arrangement (i.e. asymmetrical) is the preferred choice and also utilized in this thesis, owing to its enhanced air-gap flux distribution [54] and higher DC-link voltage utilization [55]. For either winding, connecting the neutral points (i.e. 1N in Fig. 2.1) or isolating them (i.e. 2N in Fig. 2.1) affects not only the employed controller, but also the dynamic model. Based on the non-linear model, a fast tracking controller is designed (in Section 3.3) and minimum stator copper losses are ensured (in Section 3.2.1). Section 2.1 shows the different approaches in literature with respect to modelling asymmetrical dual three-phase IPMSMs (ADT-IPMSMs), along with the proposed non-linear modelling. Section 2.2 derives the VSI model for 1N and 2N configurations. Finally, Section 2.3 validates the proposed drive model with simulation and experimental results.

2.1 Asymmetrical ADT-IPMSM drive

2.1.1 State-of-the-art review

In recent literature concerning the control of an ADT-IPMSM with double neutral (i.e 2N) connection, the different harmonic components in the three subspaces are due to inverter non-idealities, approximated sinusoidal flux distributions from both

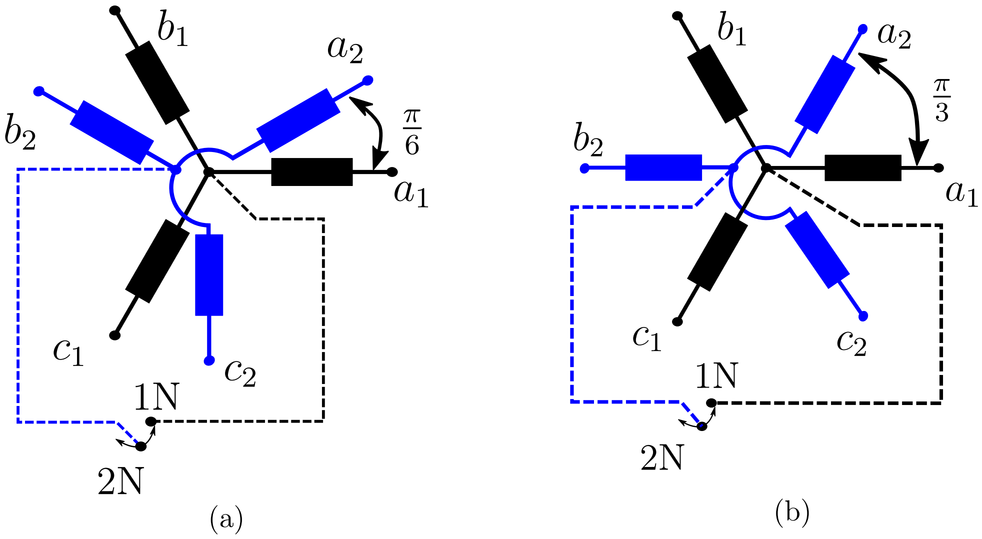

Fig. 2.1. Stator layout showing the phase shift between the DT sets, 1N and 2N neutral configurations for the (a) asymmetrical and (b) symmetrical windings.

the stator windings and the rotor permanent magnets. However, a clear mathematical model to describe and simulate the machine fundamental-harmonic dynamics is still not available. From an AWE perspective, such high fidelity non-linear models are essential to couple them with the kite simulations and thus quantify the net of electrical power to be exported to the grid. In [56, 57], the proposed decoupled model relied on the knowledge of machine internal dimensions to perform finite-element (FE) simulations, which lead to an agreement between the experimental and simulated results. However, the availability of such information (i.e. dimensions and/or FE data) is not the general case. On the other hand, the single neutral (i.e. 1N) connection has an advantage over the 2N connection in terms of enhancing the fault-tolerance capability [39] and improving the torque density if tied to the DC-link through filter circuits [52]. However, a clear mathematical model for a 1N connection was scarcely investigated.

This chapter introduces an effective mathematical model capable of capturing both the fundamental and harmonic dynamics of a practical non-linear ADT-IPMSM with the aid of the experimentally identified flux linkage maps. The method relies on simple tests to identify the different fundamental and harmonic components in the different subspaces for the isolated and connected neutral point connections (i.e. 1N and 2N connection). A novel method to identify the zero sequence parameters is illustrated. The cross-coupling between the different subspace flux-linkage elements is identified and taken into account. The computed parameters are inserted into a computer simulation on Matlab/Simulink, where the simulated electrical quantities (i.e. stator current, subspace currents) are compared, at the same conditions, to those obtained from an experimental setup comprising a 2.5 kW ADT-IPMSM.

2.1.2 Modelling techniques of ADT-IPMSMs

Fig. 2.2 depicts the windings arrangement of an ADT-IPMSM, where the electrical dynamics are governed by

$$\boldsymbol{u}_{\mathrm{s}}^{\mathrm{a}_1\to\mathrm{c}_2} = R_{\mathrm{s}}\boldsymbol{i}_{\mathrm{s}}^{a_1\to\mathrm{c}_2} + \tfrac{\mathrm{d}}{\mathrm{d}t}\boldsymbol{\psi}_{\mathrm{s}}^{\mathrm{a}_1\to\mathrm{c}_2}, \tag{2.1}$$

where R_{s} is the stator electrical resistance (in Ω), $\boldsymbol{f}_{\mathrm{s}}^{\mathrm{a}_1\to\mathrm{c}_2} = (f_{\mathrm{s}}^{\mathrm{a}_1}, f_{\mathrm{s}}^{\mathrm{b}_1}, f_{\mathrm{s}}^{\mathrm{c}_1}, f_{\mathrm{s}}^{\mathrm{a}_2}, f_{\mathrm{s}}^{\mathrm{b}_2}, f_{\mathrm{s}}^{\mathrm{c}_2})^\top \in \mathbb{R}^6$ is a vector representing either the voltage u (in V), current i (in A) or flux linkage ψ (in Wb) of the DT sets $a_1b_1c_1$ and $a_2b_2c_2$ (i.e. $f \in \{u, i, \psi\}$). The key to exact or approximate modelling relies on the laid down assumptions in (2.1), in particular how sophisticated the flux linkage vector $\boldsymbol{\psi}_{\mathrm{s}}^{\mathrm{a}_1\to\mathrm{c}_2}$ is modelled. This would result in a tradeoff in terms of complexity and precision. Thus, it is crucial to state in advance the following assumptions before proceeding:

- ***Assumption 1:*** The air-gap length is negligible compared to the stack length, which is the length of the coil turns in the stator slots that contribute to the electromechanical energy conversion;
- ***Assumption 2:*** Iron losses are neglected, as these losses are significant and must be considered only at high operational speeds ($\geq$ 10000 rpm) [58], which is not the case for AWESs;
- ***Assumption 3:*** The flux in the air-gap is radially distributed;
- ***Assumption 4:*** The winding layout is sinusoidally distributed in the slots; and
- ***Assumption 5:*** The spacing between two consecutive slots is neglected.

The dynamic modelling and control in three-phase drives are mostly based on decomposing the three-phase quantities (i.e. voltage, current, and flux linkage) by means of Clarke's transformation into orthogonal stationary subspaces: the $\alpha\beta$ subspace responsible for the electromechanical modelling and the *zero* subspace represented by the *zero* vector. The *zero* current flows only if a path exists for such component as for instance the connection between the neutral point and the DC-link [59]. Such three-phase models are considered the foundation, on which the models of multiphase drives were derived. Similar to three-phase drives, modelling and controlling the dual three-phase drive in the natural frame (i.e. $a_1b_1c_1$-$a_2b_2c_2$) as in (2.1) would be tedious. Thus, coordinate transformations are also pursued for the sake of simplifying the model and control structures. For dual three-phase drives in particular, literature has exploited the modelling and control of dual three-phase drives using two main approaches:

1. Using the superposition principle, the two sets of three phase windings $\mathrm{a}_1\mathrm{b}_1\mathrm{c}_1$ $\mathrm{a}_2\mathrm{b}_2\mathrm{c}_2$ are decomposed on the $\alpha\beta$ coordinates (see Fig. 2.2) as $\alpha_1\beta_1$ and $\alpha_2\beta_2$, respectively, such that

$$\boldsymbol{f}_{\mathrm{s}}^{\alpha\beta0} = \underbrace{\boldsymbol{T}_{\mathrm{C},1}\boldsymbol{f}_{\mathrm{s}}^{\mathrm{a}_1\to\mathrm{c}_1}}_{=:\boldsymbol{f}_{\mathrm{s}}^{\alpha_1\beta_1 0^+}} + \underbrace{\boldsymbol{T}_{\mathrm{C},2}\boldsymbol{f}_{\mathrm{s}}^{\mathrm{a}_2\to\mathrm{c}_2}}_{=:\boldsymbol{f}_{\mathrm{s}}^{\alpha_2\beta_2 0^-}} \tag{2.2}$$

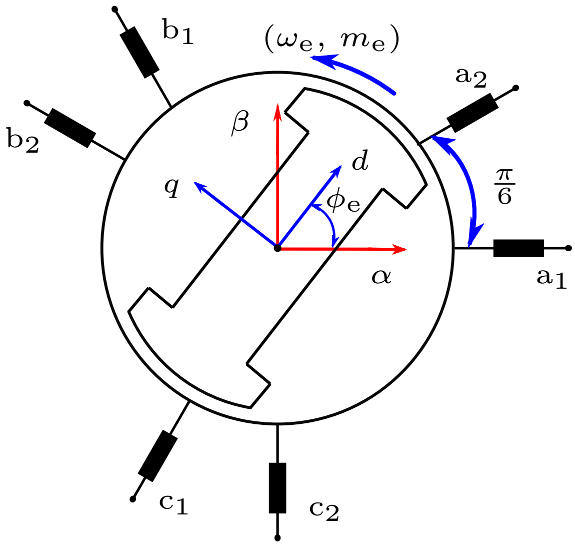

Fig. 2.2. Asymmetrical dual three-phase windings showing the $\alpha\beta$ stationary frame, aligned with the reference axis of a_1, and the dq synchronously rotating frame with the displacement angle ϕ_e.

where

$$\boldsymbol{T}_{\mathrm{C},1} = \frac{1}{3}\begin{bmatrix} \cos(0) & \cos(\frac{2\pi}{3}) & \cos(\frac{4\pi}{3}) \\ \sin(0) & \sin(\frac{2\pi}{3}) & \sin(\frac{4\pi}{3}) \\ 1 & 1 & 1 \end{bmatrix}, \boldsymbol{T}_{\mathrm{C},2} = \frac{1}{3}\begin{bmatrix} \cos(\frac{\pi}{6}) & \cos(\frac{5\pi}{6}) & \cos(\frac{3\pi}{2}) \\ \sin(\frac{\pi}{6}) & \sin(\frac{5\pi}{6}) & \sin(\frac{3\pi}{2}) \\ 1 & 1 & 1 \end{bmatrix}, \tag{2.3}$$

represents Clarke's transformations of the two three-phase sets. The *zero* sequence components 0^+ and 0^- are the zero variables which are significant to study only during the post-fault operation (i.e. after isolating the faulty phase(s)), while connecting the neutral points of the two sets depending on the operating conditions (see Chapter 4). Note that the scaling factor $1/3$ in (2.3) is half than that in [60]; owing to the rewinding technique, where the number of turns per phase of the ADT-IPMSM is half that of the original three-phase machine (see Appendix A). Applying Park's transformation

$$\boldsymbol{T}_{\mathrm{p}}(\phi_e)^{-1} = \begin{bmatrix} \cos(\phi_e) & -\sin(\phi_e) \\ \sin(\phi_e) & \cos(\phi_e) \end{bmatrix}, \tag{2.4}$$

rotates the stator quantities of the ADT-IPMSM with the same frequency as the rotor, simplifying the electromechanical model as well as the carried-out control strategy [61]. Taking into account the phase shift of $\pi/6$ between the two sets, would result into two synchronously rotating frames d_1q_1 and d_2q_2 as

$$\boldsymbol{f}_{\mathrm{s}}^{d_1q_1} = \boldsymbol{T}_{\mathrm{p}}(\phi_e)^{-1}\,\boldsymbol{f}_{\mathrm{s}}^{\alpha_1\beta_1}, \quad \boldsymbol{f}_{\mathrm{s}}^{d_2q_2} = \boldsymbol{T}_{\mathrm{p}}(\phi_e + \frac{\pi}{6})^{-1}\,\boldsymbol{f}_{\mathrm{s}}^{\alpha_2\beta_2}. \tag{2.5}$$

Finally the resultant torque would be

$$m_{\mathrm{e}} = \frac{3}{2} n_{\mathrm{p}} (\boldsymbol{i}_{\mathrm{s}}^{d_1q_1} \boldsymbol{J} \boldsymbol{\psi}_{\mathrm{s}}^{d_1q_1} + \boldsymbol{i}_{\mathrm{s}}^{d_2q_2} \boldsymbol{J} \boldsymbol{\psi}_{\mathrm{s}}^{d_2q_2}) = m_{\mathrm{e},1} + m_{\mathrm{e},2}, \tag{2.6}$$

where $m_{\mathrm{e},1}$ and $m_{\mathrm{e},2}$ are the contributions of each three-phase set in the torque production. The design of the corresponding current controller in such case would follow the same principle when tuning the controller of a three-phase system [62], but additionally tune the controller of the added set (i.e.tuning the controllers of d_1q_1 and d_2q_2) [40]. The main draw back of the aforementioned approach is the lack of harmonic mapping and information about the differences between the $\alpha_1\beta_1$ and $\alpha_2\beta_2$ coordinates during operation, which would be observed in the presence of non-idealities such as different impedances per every phase originating from the machine side and inverter point of view.

2. The second approach, which is the one followed in this thesis, is defining new coordinates XY

$$\boldsymbol{f}_{\mathrm{s}}^{XY} = \begin{bmatrix} 1 & 0 & -1 & 0 \\ 0 & -1 & 0 & 1 \end{bmatrix} \begin{pmatrix} \boldsymbol{f}_{\mathrm{s}}^{\alpha_1\beta_1} \\ \boldsymbol{f}_{\mathrm{s}}^{\alpha_2\beta_2} \end{pmatrix}, \tag{2.7}$$

which describe the degree of unbalance between the two three phase sets, where $f \in \{u, i, \psi\}$. During the pre-fault (i.e. healthy case), $\boldsymbol{i}_{\mathrm{s}}^{XY}$ should be regulated to zero; to nullify the difference between the DT sets and, thus, each set would contribute equally to the torque production (i.e. $m_{\mathrm{e},1} = m_{\mathrm{e},2}$ in (2.6)). In the post-fault operation, the machine electrical circuit unbalance (i.e. due to fault occurrence) is counteracted by setting $\boldsymbol{i}_{\mathrm{s}}^{XY} \neq 0$ to force the currents in the healthy phases to follow certain optimization criteria for stator copper losses minimization [43, 44]. Moreover, the control system will deal with the total $\boldsymbol{f}_{\mathrm{s}}^{\alpha\beta} = \boldsymbol{f}_{\mathrm{s}}^{\alpha_1\beta_1} + \boldsymbol{f}_{\mathrm{s}}^{\alpha_2\beta_2}$ components instead of dealing with $\boldsymbol{f}_{\mathrm{s}}^{\alpha_1\beta_1}$ and $\boldsymbol{f}_{\mathrm{s}}^{\alpha_2\beta_2}$ separately. Further explanations will be presented shortly in the upcoming section.

2.1.3 Asymmetrical ADT-IPMSM machine model

Similar to Clarke's transformation applied for three-phase drives [60, 62] and based on the explanations in Section 2.1.2 and in (2.7), a generalized Clarke's transformation for a DTM drive, also known as vector space decomposition (VSD) [63],

$$\boldsymbol{T}_{\mathrm{VSD}} = \frac{1}{3} \begin{bmatrix} \cos(0) & \cos(\frac{2\pi}{3}) & \cos(\frac{4\pi}{3}) & \cos(\frac{\pi}{6}) & \cos(\frac{5\pi}{6}) & \cos(\frac{3\pi}{2}) \\ \sin(0) & \sin(\frac{2\pi}{3}) & \sin(\frac{4\pi}{3}) & \sin(\frac{\pi}{6}) & \sin(\frac{5\pi}{6}) & \sin(\frac{3\pi}{2}) \\ \cos(0) & \cos(\frac{2\pi}{3}) & \cos(\frac{4\pi}{3}) & -\cos(\frac{\pi}{6}) & -\cos(\frac{5\pi}{6}) & -\cos(\frac{3\pi}{2}) \\ -\sin(0) & -\sin(\frac{2\pi}{3}) & -\sin(\frac{4\pi}{3}) & \sin(\frac{\pi}{6}) & \sin(\frac{5\pi}{6}) & \sin(\frac{3\pi}{2}) \\ 1 & 1 & 1 & 0 & 0 & 0 \\ 0 & 0 & 0 & 1 & 1 & 1 \end{bmatrix}, \tag{2.8}$$

Table 2-I. Parameters of the ADT-IPMSM drive.

Parameter	Value
Stator resistance	$R_\mathrm{s} = 1.1\,\Omega$
Pole-pair	$n_\mathrm{p} = 3$
Inertia*	$\Theta = 0.01\,\mathrm{kg\,m^2}$
Viscous friction coefficient*	$\nu = 0.8 \times 10^{-3}\ \mathrm{N\,m\,s}$
Coulomb friction torque*	$m_\mathrm{c} = 0.2725\ \mathrm{N\,m}$
Rated stator peak current	$\hat{i}_\mathrm{s,rated} = 4.1\sqrt{2}\ \mathrm{A}$
Rated stator peak voltage	$\hat{u}^{ltl}_\mathrm{s,rated} = 170\sqrt{2}\ \mathrm{V}$
Rated torque	$m_\mathrm{e,rated} = 10.6\ \mathrm{N\,m}$
Rated mechanical speed	2300 rpm
DC-link voltage	$u_\mathrm{dc} = 580\ \mathrm{V}$
Sampling and switching frequencies	$f_\mathrm{sw} = 8\ \mathrm{kHz}$

* Parameters obtained as in [65].

decomposes the asymmetrical six-phases quantities $\boldsymbol{f}_\mathrm{s}^{a_1\to c_2}$ to three orthogonal planes $\left(\boldsymbol{f}_\mathrm{s}^{\alpha\beta},\ \ \boldsymbol{f}_\mathrm{s}^{XY},\ \ \boldsymbol{f}_\mathrm{s}^{0}\right)^\top = \boldsymbol{T}_\mathrm{VSD}\boldsymbol{f}_\mathrm{s}^{a_1\to c_2}$, namely the equivalent $\alpha\beta$ subspace, 0^+0^- in the "0" subspace representing the *zero* sequence components from both three-phase sets, and the XY subspace, which directly controls the degree of unbalance between the DT sets [38, 39, 41]. $\boldsymbol{T}_\mathrm{VSD}$ maps different harmonics to such subspaces, where $\alpha\beta$ plane holds the $12\gamma \pm 1$ harmonics, for $\gamma = \{1,\ 2,\ 3,\ ...\}$, XY is concerned with the $6\gamma \pm 1$ harmonics, for $\gamma = \{1,\ 3,\ 5,\ ...\}$, and 0^+0^- is responsible for the triplets harmonics 3γ, where $\gamma = \{1,\ 3,\ 5,\ ...\}$ [52, 63]. Using the generalized Park transformation [64]

$$\boldsymbol{T}_\mathrm{p}^{'}(\phi_\mathrm{e})^{-1} \;=\; \begin{bmatrix} \boldsymbol{T}_\mathrm{p}(\phi_\mathrm{e})^{-1} & \boldsymbol{O}_2 & \boldsymbol{O}_2 \\ \boldsymbol{O}_2 & \boldsymbol{T}_\mathrm{p}(-\phi_\mathrm{e})^{-1} & \boldsymbol{O}_2 \\ \boldsymbol{O}_2 & \boldsymbol{O}_2 & \boldsymbol{I}_2 \end{bmatrix}, \tag{2.9}$$

the ADTM-IPMSM dynamic model is

$$\left.\begin{aligned} \boldsymbol{u}_\mathrm{s}^{dq} &= R_\mathrm{s}\,\boldsymbol{i}_\mathrm{s}^{dq} + \omega_\mathrm{e}\,\boldsymbol{J}\boldsymbol{\psi}_\mathrm{s}^{dq} + \tfrac{\mathrm{d}}{\mathrm{d}t}\boldsymbol{\psi}_\mathrm{s}^{dq}, \\ \boldsymbol{u}_\mathrm{s}^{xy} &= R_\mathrm{s}\,\boldsymbol{i}_\mathrm{s}^{xy} - \omega_\mathrm{e}\,\boldsymbol{J}\boldsymbol{\psi}_\mathrm{s}^{xy} + \tfrac{\mathrm{d}}{\mathrm{d}t}\boldsymbol{\psi}_\mathrm{s}^{xy}, \\ \boldsymbol{u}_\mathrm{s}^{0} &= R_\mathrm{s}\,\boldsymbol{i}_\mathrm{s}^{0} + \tfrac{\mathrm{d}}{\mathrm{d}t}\boldsymbol{\psi}_\mathrm{s}^{0}, \\ \tfrac{\Theta}{n_\mathrm{p}}\tfrac{\mathrm{d}\omega_\mathrm{e}}{\mathrm{d}t} &= \underbrace{3\,n_\mathrm{p}\boldsymbol{i}_\mathrm{s}^{dq^\top}\boldsymbol{J}\,\boldsymbol{\psi}_\mathrm{s}^{dq}}_{=m_\mathrm{e}} - m_\mathrm{load} - \underbrace{\nu\,\tfrac{\omega_\mathrm{e}}{n_\mathrm{p}} + m_\mathrm{c}}_{=m_\mathrm{fric}}, \end{aligned}\right\} \tag{2.10}$$

where $\boldsymbol{i}_\mathrm{s}^{dq} = \left(i_\mathrm{s}^{d},\ \ i_\mathrm{s}^{q}\right)^\top$ (in A) is the dq current vector, $\boldsymbol{i}_\mathrm{s}^{xy} = \left(i_\mathrm{s}^{x},\ \ i_\mathrm{s}^{y}\right)^\top$ (in A) is xy current vector, and $\boldsymbol{i}_\mathrm{s}^{0} = \left(i_\mathrm{s}^{0+},\ \ i_\mathrm{s}^{0-}\right)^\top$ (in A) is *zero* current vector. $\boldsymbol{\psi}_\mathrm{s}^{dq} = \left(\psi_\mathrm{s}^{d},\ \ \psi_\mathrm{s}^{q}\right)^\top$, $\boldsymbol{\psi}_\mathrm{s}^{xy} = \left(\psi_\mathrm{s}^{x},\ \ \psi_\mathrm{s}^{y}\right)^\top$, and $\boldsymbol{\psi}_\mathrm{s}^{0} = \left(\psi_\mathrm{s}^{0+},\ \ \psi_\mathrm{s}^{0-}\right)^\top$ are the flux linkage vectors (in Wb) in the three decoupled subspaces, which are modelled as shown in the next subsection. Θ and n_p are parameters representing the mechanical inertia (in $\mathrm{kg\,m^2}$) and the magnetic pole-pair, respectively, m_load is the load torque (in $\mathrm{N\,m}$)

which for AWE represents the kite-load torque, m_c is the Coulomb friction (in N m), and m_fric is the total friction torque (in N m). The ADT-IPMSM parameters are shown in Table 2-I. Since the xy plane rotates in the anti-synchronous frame, a negative sign is placed in front of the position and speed in (2.9) and (2.10), respectively [66]. The model in (2.10) assumes non-linear flux linkage variations with the corresponding currents. In the upcoming subsections, a clear harmonic model, dependent on the permanent magnet (PM) harmonic flux distribution is proposed and is capable of reproducing the results obtained from the practical ADT-IPMSM, during the evaluation of the proposed model shown later in Section 2.3.

2.1.4 Identification of non-linear flux linkages

The unique difference between different asymmetrical drives is the way the flux linkage vectors $\boldsymbol{\psi}_\mathrm{s}^{dq}$, $\boldsymbol{\psi}_\mathrm{s}^{xy}$, and $\boldsymbol{\psi}_\mathrm{s}^{0}$ in (2.10) are modelled. Compared to the models in [52, 56, 67], the current-dependency of inductance matrices as well as harmonic flux linkages per subspace are considered in the proposed model. The objective is to excite the stator windings with the desired subspace currents and identify the corresponding flux linkages, without provoking the remaining subspaces. Moreover, the presence of harmonic components during the identification process of $\boldsymbol{\psi}_\mathrm{s}^{dq}$, $\boldsymbol{\psi}_\mathrm{s}^{xy}$, and $\boldsymbol{\psi}_\mathrm{s}^{0}$ should be compensated; as inspired by the identification of $\boldsymbol{\psi}_\mathrm{s}^{dq}$ for three-phase systems as shown in [68].

2.1.4.1 dq subspace flux linkages

The dq non-linear model is initiated by defining $\frac{\mathrm{d}}{\mathrm{d}t}\boldsymbol{\psi}_\mathrm{s}^{dq}$ in (2.10) as

$$\frac{\mathrm{d}}{\mathrm{d}t}\boldsymbol{\psi}_\mathrm{s}^{dq} = \boldsymbol{L}_\mathrm{s}^{dq}(\boldsymbol{i}_\mathrm{s}^{dq})\,\frac{\mathrm{d}}{\mathrm{d}t}\boldsymbol{i}_\mathrm{s}^{dq} = \begin{bmatrix} \frac{\partial\psi_\mathrm{s}^{d}}{\partial i_\mathrm{s}^{d}} & \frac{\partial\psi_\mathrm{s}^{d}}{\partial i_\mathrm{s}^{q}} \\ \frac{\partial\psi_\mathrm{s}^{q}}{\partial i_\mathrm{s}^{d}} & \frac{\partial\psi_\mathrm{s}^{q}}{\partial i_\mathrm{s}^{q}} \end{bmatrix} \frac{\mathrm{d}}{\mathrm{d}t}\boldsymbol{i}_\mathrm{s}^{dq} = \begin{bmatrix} L_\mathrm{s}^{d}(\boldsymbol{i}_\mathrm{s}^{dq}) & L_\mathrm{m}^{dq}(\boldsymbol{i}_\mathrm{s}^{dq}) \\ L_\mathrm{m}^{qd}(\boldsymbol{i}_\mathrm{s}^{dq}) & L_\mathrm{s}^{q}(\boldsymbol{i}_\mathrm{s}^{dq}) \end{bmatrix} \frac{\mathrm{d}}{\mathrm{d}t}\boldsymbol{i}_\mathrm{s}^{dq} \tag{2.11}$$

where $\boldsymbol{L}_\mathrm{s}^{dq}(\boldsymbol{i}_\mathrm{s}^{dq})$ (in H) is the differential inductance matrix (i.e. non-linear and current-dependant[1]). This mathematical approach is similar to that shown in [68], which is also known as the flux linkage maps identification. $\boldsymbol{\psi}_\mathrm{s}^{dq}$ is estimated at a 2N connection (see Figs. 2.3 and 2.4), to eliminate the effect of $\boldsymbol{i}_\mathrm{s}^{0}$, where the current vector $\boldsymbol{i}_\mathrm{s}^{dq}$ is varied to cover the entire operating range of the adopted ADT-IPMSM at a given speed. The reference currents $\boldsymbol{i}_\mathrm{s,ref}^{xy}$, shown in Fig. 2.3, are set to $\boldsymbol{i}_\mathrm{s,ref}^{xy} = (0,\ 0)$. The control action in the dq subspace in Fig. 2.3 is given by

$$\boldsymbol{u}_\mathrm{s,ref}^{dq} = \boldsymbol{u}_\mathrm{PI}^{dq} + \boldsymbol{u}_\mathrm{R}^{dq}, \tag{2.12}$$

where $\boldsymbol{u}_\mathrm{PI}^{dq}$ (in V) regulates the fundamental component in the dq subspace, while $\boldsymbol{u}_\mathrm{R}^{dq}$ (in V) of the resonant (R) controller is tuned at a resonant angular frequency of $2\omega_\mathrm{e}$; ensuring equal current amplitudes in per every three-phase set [51,64]. Higher order harmonics in the dq subspace - namely the 11th and 13th harmonics - are neglected

---

[1] Details on nonlinear modelling and the use of differential inductances in electrical drives can be found in [60, Chap. 14].

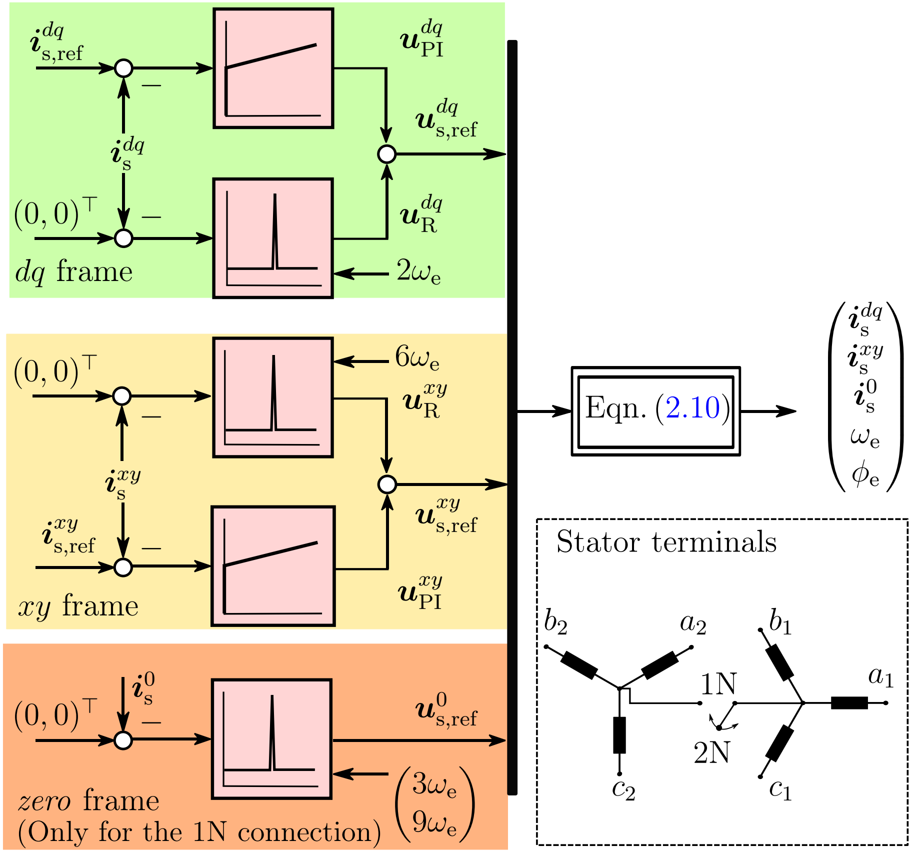

Fig. 2.3. Proportional-integral and resonant current controllers for the different subspaces with the corresponding resonant angular frequencies [52, 64].

owing to their minor amplitudes and negligible impact on the performance, similar to three-phase and other forms of multi-phase drives [69, 70]. Accordingly, at *steady-state* using the control structure in Fig. 2.3, the flux linkage vector can be computed by

$$\boldsymbol{\psi}_s^{dq} = \frac{\boldsymbol{J}^{-1}}{\omega_e}\,(\boldsymbol{u}_{PI}^{dq} - R_s\,\boldsymbol{i}_s^{dq}), \tag{2.13}$$

where it is clear that the adopted method is valid only at $\omega_e \neq 0$. Note that the ADT-IPMSM must be rotated by means of an external prime mover. In this thesis was done by means of an external machine, as presented in the description of the hardware setup in Appendix A. The acquired flux linkages $\boldsymbol{\psi}_s^{dq}$ and the corresponding differential inductances elements in $\boldsymbol{L}_s^{dq}(\boldsymbol{i}_s^{dq})$ are shown in Figs. 2.5(a)-(b) and Figs. 2.6(a)-(d), respectively, through 11 point-variations per i_s^d and i_s^q within the intervals $-\hat{i}_{s,rated} \leq i_s^d \leq \hat{i}_{s,rated}$ and $-\hat{i}_{s,rated} \leq i_s^q \leq \hat{i}_{s,rated}$. Consequently, the flux linkages and inductances are stored as 11×11 look-up tables, which is considered a compromise between accuracy, precision and memory requirements based on the available lab facilities. The PI and R controllers are initially tuned using trial and error as presented in Table 2-II.

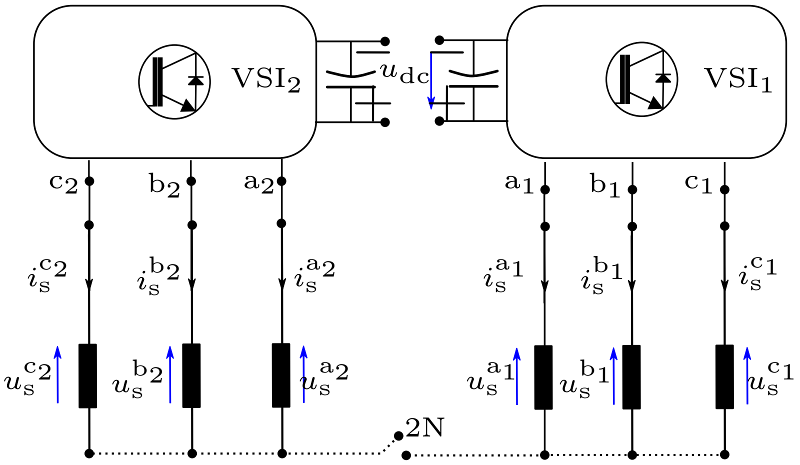

Fig. 2.4. Hardware configuration for identifying the non-linear flux linkages of the dq and xy subspaces with isolated neutrals.

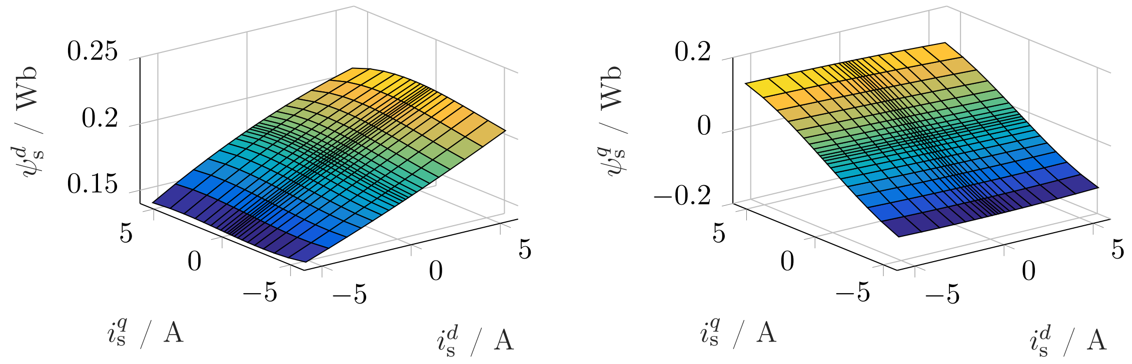

(a) (b)

Fig. 2.5. Measured flux linkage maps of (a) ψ_{s}^{d} and (b) ψ_{s}^{q} within the interval $||\boldsymbol{i}_{\mathrm{s}}^{dq}|| \leq \hat{i}_{\mathrm{s,rated}}$.

Table 2-II. Table showing the different connections, control structures and gains used to compute the parameters per subspace.

P gain* in Ω	I gain* in $\frac{\Omega}{\mathrm{s}}$	Connection	Control structure	R gain* in $\frac{\Omega}{\mathrm{s}}$
dq : 5	dq : 5555	Fig. 2.4	Fig. 2.3 at $\boldsymbol{i}_{\mathrm{s,ref}}^{xy} = (0, 0)$	dq : 1300
xy : 2.5	xy : 2778	Fig. 2.4	Fig. 2.3 at $\boldsymbol{i}_{\mathrm{s,ref}}^{dq} = (0, 0)$	xy : 1300

* Tuned using trial and error.

2.1.4.2 xy subspace flux linkages

The xy subspace comprises both the fundamental component (i.e. recall from (2.7) and (2.9) that $\boldsymbol{f}_{\mathrm{s}}^{xy} = \boldsymbol{T}_{\mathrm{p}}(-\phi_{\mathrm{e}})^{-1}(\boldsymbol{f}_{\mathrm{s}}^{\alpha_1\beta_1} - \boldsymbol{f}_{\mathrm{s}}^{\alpha_2\beta_2})$) and low-order harmonics. The 5th and 7th harmonics are considered the significant dominant harmonics in such plane, sourced by the PM rotor flux harmonics [51, 52, 64]. Thus, the total stator flux linkage $\boldsymbol{\psi}_{\mathrm{s}}^{xy}$ of the xy subspace in (2.10) is expressed by

$$\boldsymbol{\psi}_{\mathrm{s}}^{xy} = \boldsymbol{\psi}_{\mathrm{s,f}}^{xy} + \boldsymbol{\psi}_{\mathrm{s,pm}}^{xy}, \tag{2.14}$$

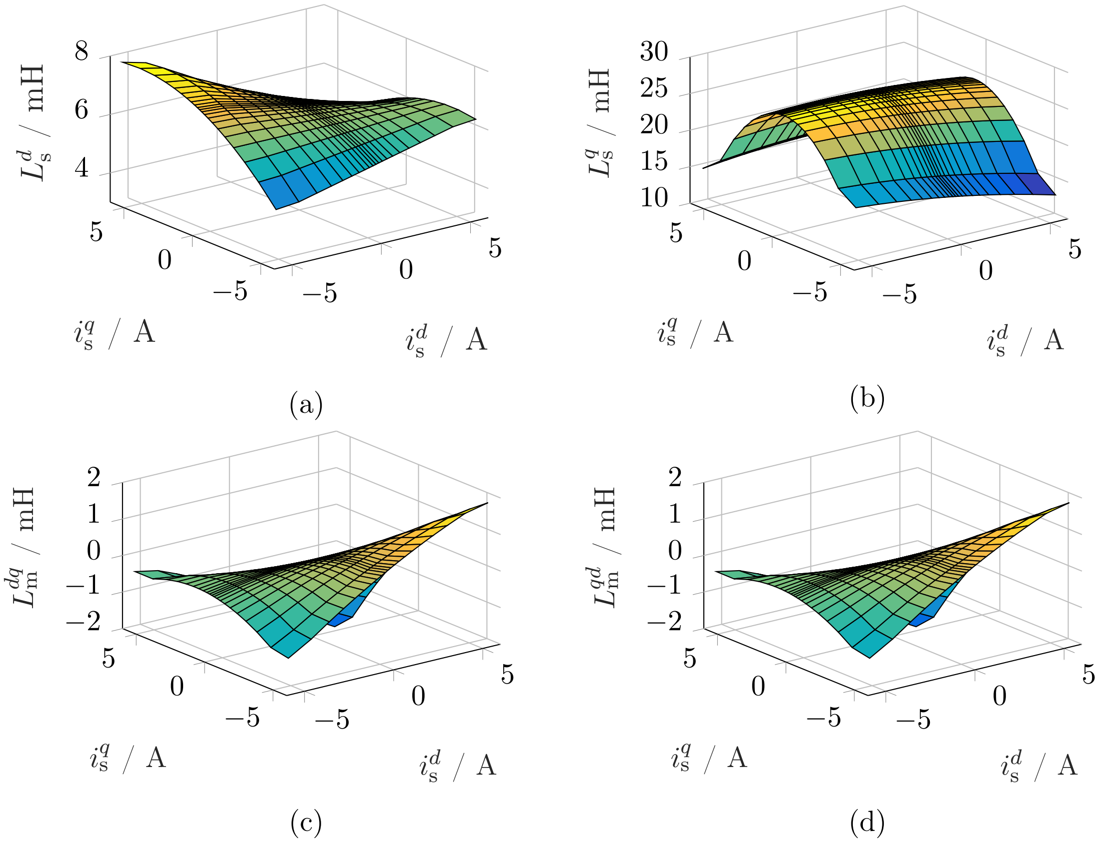

(a) (b)

(c) (d)

Fig. 2.6. Measured differential inductances of (a) L_s^d, (b) L_s^q, (c) L_m^{dq}, and (d) L_m^{qd}, within the domain $||\boldsymbol{i}_\mathrm{s}^{dq}|| \leq \hat{i}_\mathrm{s,rated}$.

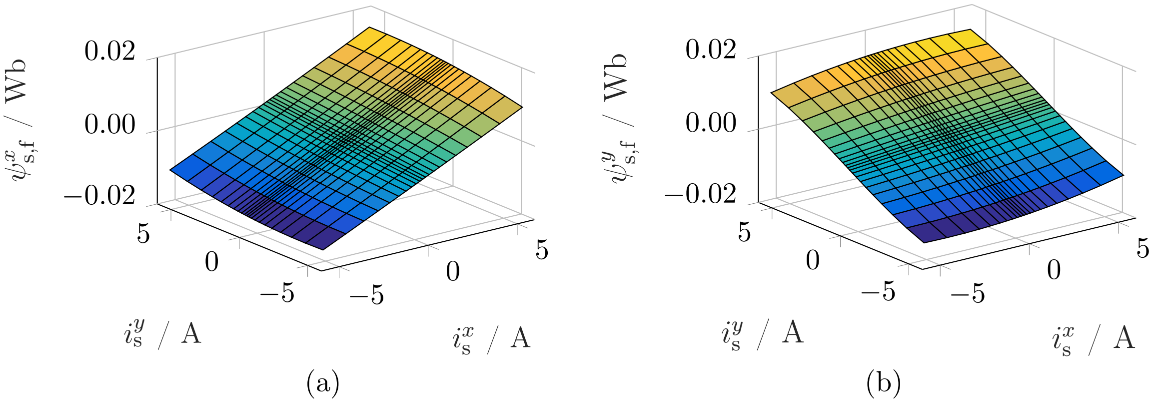

(a) (b)

Fig. 2.7. Measured flux linkage maps of (a) $\psi_\mathrm{s,f}^x$ and (b) $\psi_\mathrm{s,f}^y$ within the interval $||\boldsymbol{i}_\mathrm{s}^{xy}|| \leq \hat{i}_\mathrm{s,rated}$.

representing the sum of the fundamental $\boldsymbol{\psi}_\mathrm{s,f}^{xy}$ (in Wb) and harmonic flux linkage $\boldsymbol{\psi}_\mathrm{s,pm}^{xy}$ (in Wb) components, respectively; owing to the non-ideal drive properties. The PM harmonic flux linkage $\boldsymbol{\psi}_\mathrm{s,pm}^{xy}$ in the xy subspace, which will be presented shortly, is the main enhancement within the xy subspace model in comparison with recent literature [52, 56, 57, 67]. The flux linkage $\boldsymbol{\psi}_\mathrm{s}^{xy}$ models the unbalance between the fundamental components of the two-three phase sets [64, 66], which is identified by using the same control structure shown in Figs. 2.3 and the hardware connection in Fig. 2.4 at a 2N connection. In this case, upon sweeping the current vector $\boldsymbol{i}_\mathrm{s}^{xy}$,

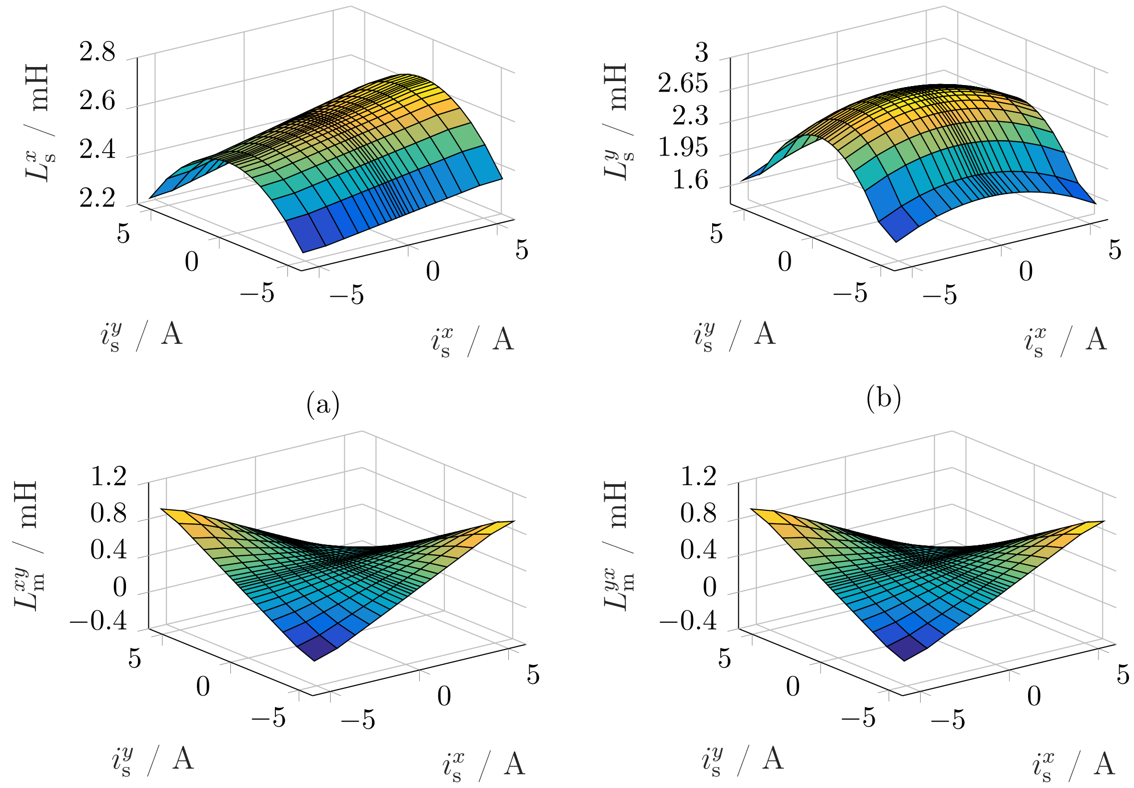

(a) (b)

(c) (d)

Fig. 2.8. Measured differential inductances of (a) L_s^x, (b) L_s^y, (c) L_m^{xy}, and (d) L_m^{yx} within the domain $||\boldsymbol{i}_\mathrm{s}^{xy}|| \leq \hat{i}_\mathrm{s,rated}$.

the flux linkages at *steady-state* and for $\boldsymbol{i}_\mathrm{s,ref}^{dq} = (0,\,0)$ can be computed by

$$\boldsymbol{\psi}_\mathrm{s,f}^{xy} = -\frac{\boldsymbol{J}^{-1}}{\omega_\mathrm{e}}\,(\boldsymbol{u}_\mathrm{PI}^{xy} - R_\mathrm{s}\,\boldsymbol{i}_\mathrm{s}^{xy}), \tag{2.15}$$

where the harmonic currents produced by $\boldsymbol{\psi}_\mathrm{s,pm}^{xy}$ are suppressed by means of R controllers tuned at $6\omega_\mathrm{e}$ [64]. Controller gains are set as presented in Table 2-II. $\boldsymbol{\psi}_\mathrm{s,f}^{xy}$ can be expressed in terms of the fundamental xy differential inductance matrix $\boldsymbol{L}_\mathrm{s}^{xy}$, similar to that in section 2.1.4.1. Hence, $\frac{\mathrm{d}}{\mathrm{d}t}\boldsymbol{\psi}_\mathrm{s,f}^{xy} = \boldsymbol{L}_\mathrm{s}^{xy}(\boldsymbol{i}_\mathrm{s}^{xy})\,\frac{\mathrm{d}}{\mathrm{d}t}\boldsymbol{i}_\mathrm{s}^{xy}$, where

$$\boldsymbol{L}_\mathrm{s}^{xy}(\boldsymbol{i}_\mathrm{s}^{xy}) = \begin{bmatrix} \frac{\partial\psi_\mathrm{s,f}^x}{\partial i_\mathrm{s}^x} & \frac{\partial\psi_\mathrm{s,f}^x}{\partial i_\mathrm{s}^y} \\ \frac{\partial\psi_\mathrm{s,f}^y}{\partial i_\mathrm{s}^x} & \frac{\partial\psi_\mathrm{s,f}^y}{\partial i_\mathrm{s}^y} \end{bmatrix} = \begin{bmatrix} L_\mathrm{s}^x & L_\mathrm{m}^{xy} \\ L_\mathrm{m}^{yx} & L_\mathrm{s}^y \end{bmatrix}, \tag{2.16}$$

is the differential inductance matrix in the xy subspace, showing variable L_s^x and L_s^y with relative coupling between the xy coordinates represented by L_m^{xy} (argument $\boldsymbol{i}_\mathrm{s}^{xy}$ is dropped). $\psi_\mathrm{s,f}^x$ and $\psi_\mathrm{s,f}^y$ are shown in Figs. 2.7(a)-(b), while the elements of $\boldsymbol{L}_\mathrm{s}^{xy}(\boldsymbol{i}_\mathrm{s}^{xy})$ are shown in Figs. 2.8(a)-(d). The maps are obtained within the domain $||\boldsymbol{i}_\mathrm{s}^{xy}|| \leq \hat{i}_\mathrm{s,rated}$ with the same number of data points as in section 2.1.4.1.

The XY subspace encompasses the rotor 5th and 7th harmonics, each rotating with an angular frequency $-5\omega_\mathrm{e}$ and $7\omega_\mathrm{e}$, respectively. Applying the anti-synchronous

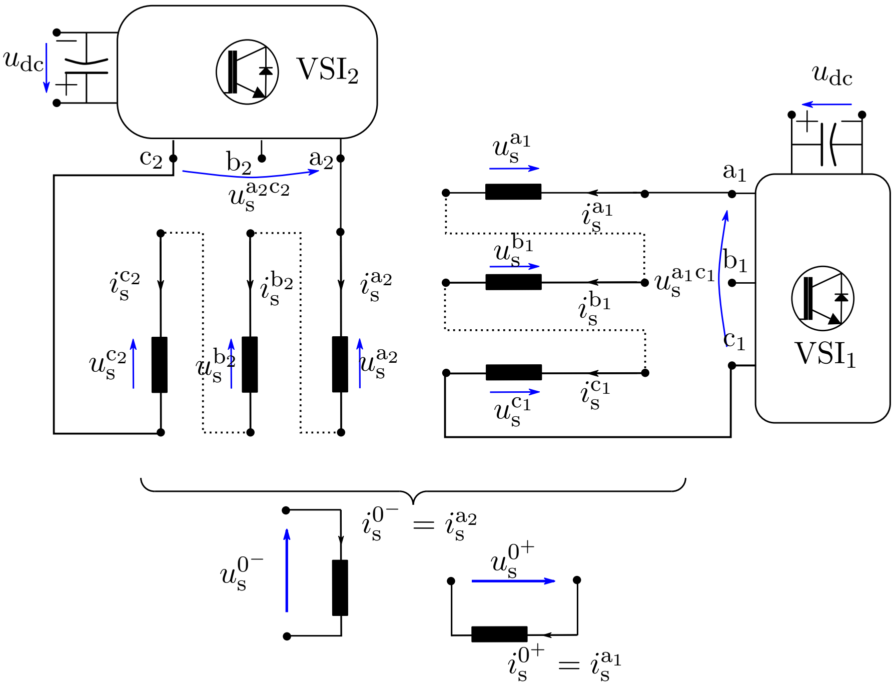

Fig. 2.9. Hardware configuration for parameters identification of the zero frame flux linkages showing the equivalent two-phase circuit.

(i.e. rotating in the direction $-\phi_{\mathrm{e}}$ with an angular speed $-\omega_{\mathrm{e}}$) $\boldsymbol{T}_{\mathrm{p}}(-\phi_{\mathrm{e}})^{-1}$ in (2.9) maps such harmonics to the xy plane rotating at $\mp 6\omega_{\mathrm{e}}$[2]. The proposed model for such harmonics is given by [51]

$$\boldsymbol{\psi}_{\mathrm{s,pm}}^{xy} = \begin{pmatrix} \psi_{\mathrm{pm}}^{7^{\mathrm{th}}} \sin(6\omega_{\mathrm{e}} t + \phi_{\mathrm{o}}^{7^{\mathrm{th}}}) - \psi_{\mathrm{pm}}^{5^{\mathrm{th}}} \sin(6\omega_{\mathrm{e}} t + \phi_{\mathrm{o}}^{5^{\mathrm{th}}}) \\ \psi_{\mathrm{pm}}^{7^{\mathrm{th}}} \cos(6\omega_{\mathrm{e}} t + \phi_{\mathrm{o}}^{7^{\mathrm{th}}}) + \psi_{\mathrm{pm}}^{5^{\mathrm{th}}} \cos(6\omega_{\mathrm{e}} t + \phi_{\mathrm{o}}^{5^{\mathrm{th}}}) \end{pmatrix}, \tag{2.17}$$

where the constants $\psi_{\mathrm{pm}}^{5^{\mathrm{th}}}$, $\psi_{\mathrm{pm}}^{7^{\mathrm{th}}}$, $\phi_{\mathrm{o}}^{5^{\mathrm{th}}}$, and $\phi_{\mathrm{o}}^{7^{\mathrm{th}}}$ are identified through the open circuit test as explained in Section 2.1.4.4.

2.1.4.3 *zero* subspace flux linkages

The *zero* sequence currents $\boldsymbol{i}_{\mathrm{s}}^{0}$ flow upon connecting the 1N connection shown in Fig.2.3. Since the *zero* sequence components (i.e. $\boldsymbol{u}_{\mathrm{s}}^{0}$, $\boldsymbol{i}_{\mathrm{s}}^{0}$, and $\boldsymbol{\psi}_{\mathrm{s}}^{0}$) are by nature stationary, the shown control structure in Fig. 2.3 makes it impossible to sweep $\boldsymbol{i}_{\mathrm{s}}^{0}$ through all the possible values, as in Sections 2.1.4.1 and 2.1.4.2; since the available degrees of freedom in such 1N connection permits only $i_{\mathrm{s}}^{0^+} = -i_{\mathrm{s}}^{0^-}$. Furthermore, the pulsating behaviour of zero sequence elements obstructs the rotation of the control frame to create the corresponding flux linkage maps. In order to sweep all the possible values for $\boldsymbol{i}_{\mathrm{s}}^{0}$, the proposed circuitry in Fig. 2.9 allows the flow of only $\boldsymbol{i}_{\mathrm{s}}^{0}$ within the stator terminals, by connecting the phases per three-phase set in series.

---

[2] From a R controller perspective, its control action u_{R} is independent from the sign of the assigned resonant angular frequency ω_{R}; since the transfer function of such controllers is function of ω_{R}^{2}. Further details on such controller are discussed in Section 3.3.2 of Chapter 3.

This is proved by equating the currents within the same three-phase set

$$i_{\mathrm{s}}^{\mathrm{a}_1} = i_{\mathrm{s}}^{\mathrm{b}_1} = i_{\mathrm{s}}^{\mathrm{c}_1} \text{ and } i_{\mathrm{s}}^{\mathrm{a}_2} = i_{\mathrm{s}}^{\mathrm{b}_2} = i_{\mathrm{s}}^{\mathrm{c}_2}, \tag{2.18}$$

then equating accordingly the $\alpha\beta$, XY and 0^+0^- components as

$$\begin{pmatrix} i_{\mathrm{s}}^{\alpha} \\ i_{\mathrm{s}}^{\beta} \\ i_{\mathrm{s}}^{X} \\ i_{\mathrm{s}}^{Y} \\ i_{\mathrm{s}}^{0^+} \\ i_{\mathrm{s}}^{0^-} \end{pmatrix} \overset{(2.18)}{=} \underbrace{\frac{1}{3}\begin{bmatrix} 1 & -\frac{1}{2} & -\frac{1}{2} & \frac{\sqrt{3}}{2} & -\frac{\sqrt{3}}{2} & 0 \\ 0 & \frac{\sqrt{3}}{2} & -\frac{\sqrt{3}}{2} & \frac{1}{2} & \frac{1}{2} & -1 \\ 1 & -\frac{1}{2} & -\frac{1}{2} & -\frac{\sqrt{3}}{2} & \frac{\sqrt{3}}{2} & 0 \\ 0 & -\frac{\sqrt{3}}{2} & \frac{\sqrt{3}}{2} & \frac{1}{2} & \frac{1}{2} & -1 \\ 1 & 1 & 1 & 0 & 0 & 0 \\ 0 & 0 & 0 & 1 & 1 & 1 \end{bmatrix}}_{\overset{(2.8)}{=} \boldsymbol{T}_{\mathrm{VSD}}} \begin{pmatrix} i_{\mathrm{s}}^{\mathrm{a}_1} \\ i_{\mathrm{s}}^{\mathrm{a}_1} \\ i_{\mathrm{s}}^{\mathrm{a}_1} \\ i_{\mathrm{s}}^{\mathrm{a}_2} \\ i_{\mathrm{s}}^{\mathrm{a}_2} \\ i_{\mathrm{s}}^{\mathrm{a}_2} \end{pmatrix} = \begin{pmatrix} 0 \\ 0 \\ 0 \\ 0 \\ i_{\mathrm{s}}^{0^+} \\ i_{\mathrm{s}}^{0^-} \end{pmatrix}. \tag{2.19}$$

Note that $\boldsymbol{i}_{\mathrm{s}}^{\alpha\beta} = \boldsymbol{i}_{\mathrm{s}}^{XY} = 0$ in (2.19) is applicable to the fundamental and harmonic components in the $\alpha\beta$ and XY subspaces.

It is worth to mention that a parallel connection of the windings (i.e. short circuiting the windings) as shown in [71] is not suitable for ADT-IPMSMs; since the back-emf will permit the flow of $\boldsymbol{i}_{\mathrm{s}}^{dq}$ within the windings along with $\boldsymbol{i}_{\mathrm{s}}^{0}$ which is undesirable to obtain $\boldsymbol{\psi}_{\mathrm{s}}^{0}$. In Fig. 2.9, the machine is transformed to an equivalent balanced two-phase machine (i.e. $i_{\mathrm{s}}^{0^+}$ and $i_{\mathrm{s}}^{0^-}$ are orthogonal) with $3n_{\mathrm{p}}$ equivalent electrical number of pole pairs, which is explained as follows. From the fundamental of electric machinery [45], the electromechanical energy conversion occurs when the stator air-gap flux *interlocks* with the rotor flux. In other words, the stator generated electromagnets in the air-gap is coupled with the rotor PM. This interlock occurs only if the stator air-gap magnet and the rotor PM have the same number of pole-pairs. The dominant component from both stator and rotor fluxes govern the electromechanical conversion, which is normally the fundamental component. As proved in (2.19), the resultant fundmental and non-triplet harmonics stator air-gap fluxes are nullified owing to the connection in Fig. 2.9, while the 3rd harmonic component is, at that particular connection, the dominant component.

The *zero* current vector $\boldsymbol{i}_{\mathrm{s}}^{0}$ is transformed to its corresponding d_0q_0 components (i.e. $\boldsymbol{i}_{\mathrm{s}}^{d_0q_0}$) by applying $\boldsymbol{T}_{\mathrm{p}}(3\phi_{\mathrm{e}})^{-1}$. Accordingly, a simplified closed loop controller is proposed to regulate $\boldsymbol{i}_{\mathrm{s}}^{d_0q_0}$, which is shown in Fig. 2.10, enabling the sweep of $\boldsymbol{i}_{\mathrm{s}}^{d_0q_0}$ and computing the corresponding $\boldsymbol{\psi}_{\mathrm{s}}^{d_0q_0}$ shown in Figs. 2.11(e)-(f), within the domain $-\hat{i}_{\mathrm{s,rated}} \leq i_{\mathrm{s}}^{d_0} \leq \hat{i}_{\mathrm{s,rated}}$ and $-\hat{i}_{\mathrm{s,rated}} \leq i_{\mathrm{s}}^{q_0} \leq \hat{i}_{\mathrm{s,rated}}$ similar to the cases in Sections 2.1.4.1 and 2.1.4.2. In Fig. 2.10, a compensation of the 9th and 15th harmonics, rotating in the d_0q_0 subspace at $-6\omega_{\mathrm{e}}$ and $12\omega_{\mathrm{e}}$, was implemented (see $\boldsymbol{u}_{\mathrm{R}}^{d_0q_0}$ in Fig. 2.10) to enhance the quality of $\boldsymbol{i}_{\mathrm{s}}^{d_0q_0}$ during the post-processing for computing $\boldsymbol{\psi}_{\mathrm{s}}^{d_0q_0}$ [51]. Applying Kirchhoff's voltage law (KVL) in Fig. 2.10 along with the corresponding tuning shown in Table 2-III, the inverter voltages can be modulated as

$$\left.\begin{aligned} \begin{pmatrix} u_{\mathrm{s}}^{\mathrm{a}_1\mathrm{c}_1} \\ u_{\mathrm{s}}^{\mathrm{a}_2\mathrm{c}_2} \end{pmatrix} &= \begin{bmatrix} 1 & 1 & 1 & 0 & 0 & 0 \\ 0 & 0 & 0 & 1 & 1 & 1 \end{bmatrix} \boldsymbol{u}_{\mathrm{s}}^{\mathrm{a}_1\to\mathrm{c}_2}, \\ &\overset{(2.8)}{=} \; 3\boldsymbol{u}_{\mathrm{s,ref}}^{0} = 3\,\boldsymbol{T}_{\mathrm{p}}(3\phi_{\mathrm{e}})\,\boldsymbol{u}_{\mathrm{s,ref}}^{d_0q_0}, \end{aligned}\right\} \tag{2.20}$$

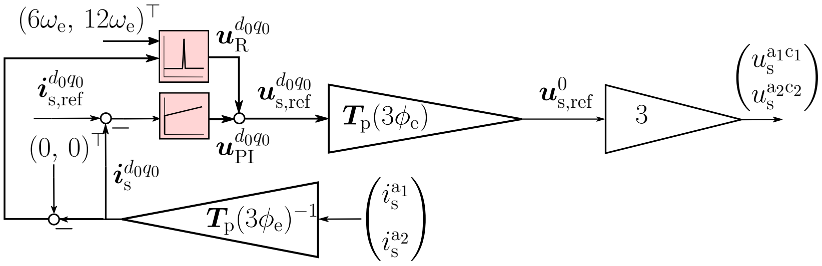

Fig. 2.10. Controller block diagram for the connection in Fig. 2.9, where the inverter voltages $u_\mathrm{s}^{\mathrm{VSI_1}}$ and $u_\mathrm{s}^{\mathrm{VSI_2}}$ are generated according to (2.20).

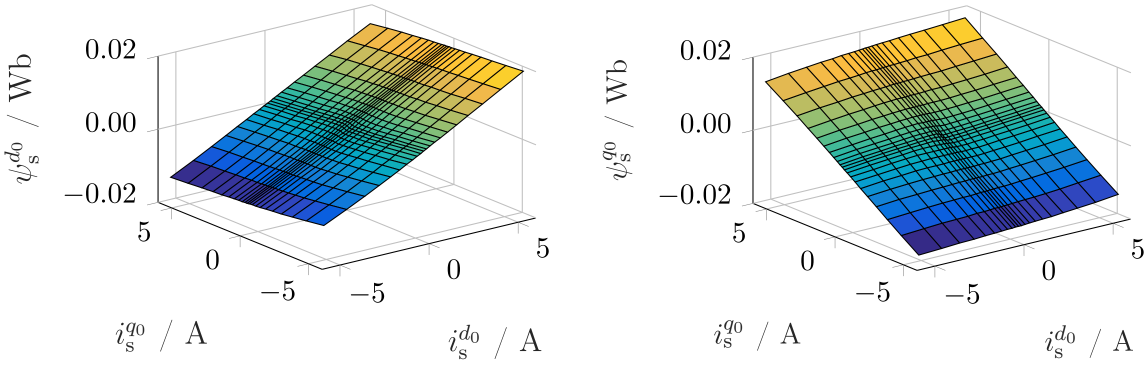

(a) (b)

Fig. 2.11. Measured flux linkage maps of (a) $\psi_\mathrm{s}^{d_0}$ and (b) $\psi_\mathrm{s}^{q_0}$ within the interval $||\boldsymbol{i}_\mathrm{s}^{d_0q_0}|| \leq \hat{i}_\mathrm{s,rated}$.

Table 2-III. Summary of the hardware configuration, control structure and gains used to estimate $\boldsymbol{\psi}_\mathrm{s}^{d_0q_0}$, while running at 2000 rpm.

P gain* in Ω	I gain* in $\frac{\Omega}{\mathrm{s}}$	Hardware connection	Control structure	R gain* in $\frac{\Omega}{\mathrm{s}}$
3	3333	Fig. 2.9	Fig. 2.10	1300

* Tuned using trial and error.

while $\boldsymbol{\psi}_\mathrm{s}^{d_0q_0}$ is computed by

$$\boldsymbol{\psi}_\mathrm{s}^{d_0q_0} = \frac{\boldsymbol{J}^{-1}}{3\omega_\mathrm{e}} (\boldsymbol{u}_\mathrm{PI}^{d_0q_0} - R_\mathrm{s}\, \boldsymbol{i}_\mathrm{s}^{d_0q_0}). \tag{2.21}$$

The elements of the differential inductance $\boldsymbol{L}_\mathrm{s}^{d_0q_0}(\boldsymbol{i}_\mathrm{s}^{d_0q_0})$ are plotted in Fig. 2.12(a)-(c), which shows that $L_\mathrm{s}^{d_0}$ and $L_\mathrm{s}^{q_0}$ variate within $\approx \pm 13\%$ from their origin points and relatively small coupling inductance $L_\mathrm{m}^{d_0q_0}$ (argument $\boldsymbol{i}_\mathrm{s}^{d_0q_0}$ is dropped). Accordingly, coming back to the 1N connection, $\boldsymbol{\psi}_\mathrm{s}^{0}$ in the presented pulsating *zero* frame in (2.10) can be approximated by

$$\boldsymbol{\psi}_\mathrm{s}^{0} \quad = \quad \boldsymbol{L}_\mathrm{s}^{0}\, \boldsymbol{i}_\mathrm{s}^{0} + \boldsymbol{\psi}_\mathrm{s,pm}^{0}, \tag{2.22}$$

where $\boldsymbol{L}_\mathrm{s}^{0}$ is approximated to a constant inductance matrix and defined as $\boldsymbol{L}_\mathrm{s}^{0} = \begin{bmatrix} \mathrm{mean}(L_\mathrm{s}^{d_0}) & 0 \\ 0 & \mathrm{mean}(L_\mathrm{s}^{q_0}) \end{bmatrix}$, while the proposed PM contribution to the zero sequence

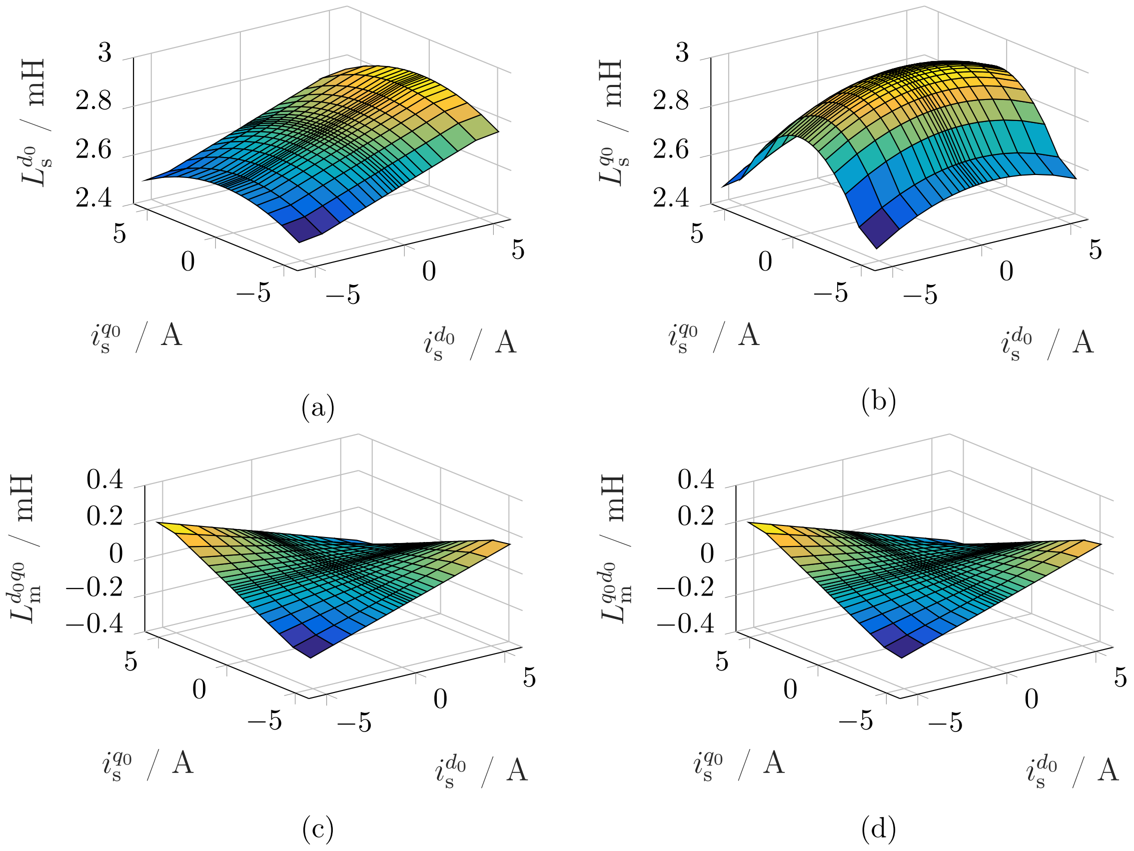

(a) (b)

(c) (d)

Fig. 2.12. Measured differential inductances of (a) $L_{\mathrm{s}}^{d_0}$, (b) $L_{\mathrm{s}}^{q_0}$, (c) $L_{\mathrm{m}}^{d_0q_0}$, and $L_{\mathrm{m}}^{q_0d_0}$ within the domain $||\boldsymbol{i}_{\mathrm{s}}^{d_0q_0}|| \leq \hat{i}_{\mathrm{s,rated}}$.

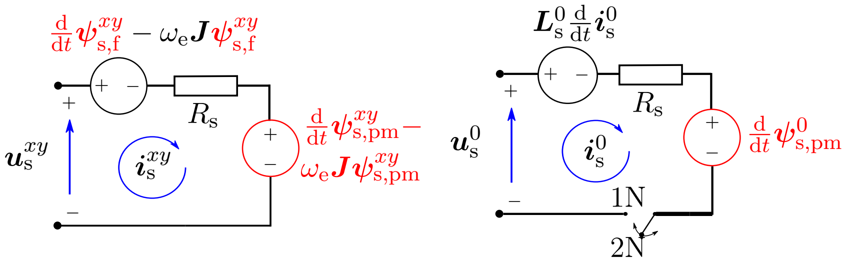

Fig. 2.13. Equivalent circuits for the fundamental xy and *zero* frames along with the enhanced model elements as explained in Sections 2.1.4.2 and 2.1.4.3, which are highlighted in red.

flux linkage is

$$\boldsymbol{\psi}_{\mathrm{s,pm}}^{0} = \begin{pmatrix} \psi_{\mathrm{pm}}^{3\mathrm{rd}} \sin(3\omega_{\mathrm{e}}t + \phi_{\mathrm{o}}^{3\mathrm{rd}}) + \psi_{\mathrm{pm}}^{9\mathrm{th}} \sin(9\omega_{\mathrm{e}}t + \phi_{\mathrm{o}}^{9\mathrm{th}}) \\ \psi_{\mathrm{pm}}^{3\mathrm{rd}} \cos(3\omega_{\mathrm{e}}t + \phi_{\mathrm{o}}^{3\mathrm{rd}}) + \psi_{\mathrm{pm}}^{9\mathrm{th}} \cos(9\omega_{\mathrm{e}}t + \phi_{\mathrm{o}}^{9\mathrm{th}}) \end{pmatrix}. \tag{2.23}$$

The constants in (2.23) are identified as explained in section 2.1.4.4. Finally, the equivalent circuits for the proposed models in the xy and *zero* subspaces are shown in Fig. 2.13, which corresponds to the following dynamics

$$\left.\begin{aligned} \boldsymbol{u}_{\mathrm{s}}^{xy} &= R_{\mathrm{s}}\,\boldsymbol{i}_{\mathrm{s}}^{xy} - \omega_{\mathrm{e}}\,\boldsymbol{J}(\boldsymbol{\psi}_{\mathrm{s,f}}^{xy} + \boldsymbol{\psi}_{\mathrm{s,pm}}^{xy}) + \tfrac{\mathrm{d}}{\mathrm{d}t}(\boldsymbol{\psi}_{\mathrm{s,f}}^{xy} + \boldsymbol{\psi}_{\mathrm{s,pm}}^{xy}), \\ \boldsymbol{u}_{\mathrm{s}}^{0} &= R_{\mathrm{s}}\,\boldsymbol{i}_{\mathrm{s}}^{0} + \boldsymbol{L}_{\mathrm{s}}^{0}\tfrac{\mathrm{d}}{\mathrm{d}t}\boldsymbol{i}_{\mathrm{s}}^{0} + \tfrac{\mathrm{d}}{\mathrm{d}t}\boldsymbol{\psi}_{\mathrm{s,pm}}^{0}, \end{aligned}\right\} \tag{2.24}$$

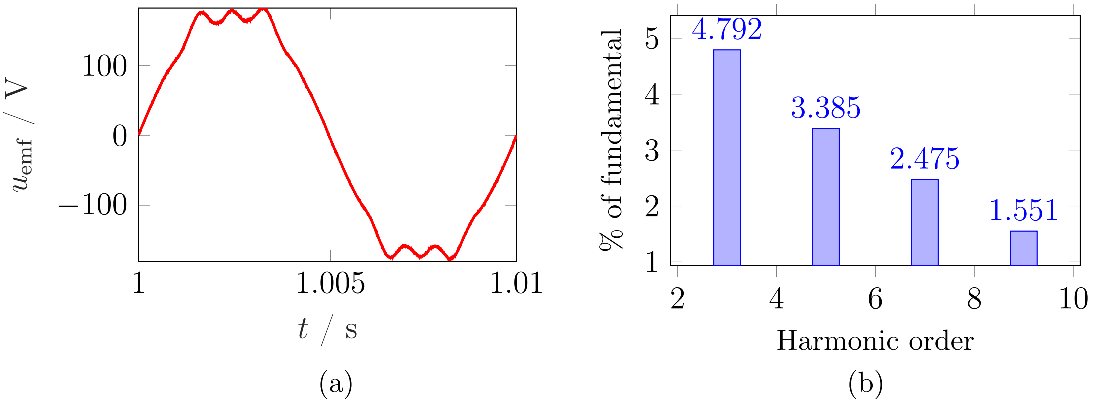

Fig. 2.14. (a) Measured back *emf* u_{emf} at 2000 rpm and (b) the corresponding FFT.

Table 2-IV. Rotor flux linkage constants at 2000 rpm.

Order	Magnitude (Wb)	Phase (rad)
1	$\psi_{\mathrm{pm}}^{1\mathrm{st}} = 180 \times 10^{-3}$	0
3	$\psi_{\mathrm{pm}}^{3\mathrm{rd}} = 6.6 \times 10^{-3}$	$\phi_{\mathrm{o}}^{3\mathrm{rd}} = 0.0297$
5	$\psi_{\mathrm{pm}}^{5\mathrm{th}} = 5 \times 10^{-3}$	$\phi_{\mathrm{o}}^{5\mathrm{th}} = 3.3755$
7	$\psi_{\mathrm{pm}}^{7\mathrm{th}} = 4.7 \times 10^{-3}$	$\phi_{\mathrm{o}}^{7\mathrm{th}} = 0.2077$
9	$\psi_{\mathrm{pm}}^{9\mathrm{th}} = 4 \times 10^{-3}$	$\phi_{\mathrm{o}}^{9\mathrm{th}} = 0.4398$

2.1.4.4 Harmonic PM constants identification

To identify the constants in (2.17) and (2.23), the ADT-IPMSM was rotated using an external prime mover (see Fig. A.1-1 in Appendix A) at a constant speed of 2000 rpm while the ADT-IPMSM was open circuited. The resulting back-*emf* voltage u_{emf} in V is shown in Fig. 2.14(a). Using Fast Fourier transform (FFT) as shown in Fig. 2.14(b), the flux-linkage of the h^{th} harmonic was derived from the back-*emf* as

$$\psi_{\mathrm{pm}}^{h} = \mathrm{Amplitude}\left(\frac{u_{emf}^{h}}{h\,\omega_{\mathrm{e}}}\right), \tag{2.25}$$

leading to the results shown in Table 2-IV. The initial phase angles ϕ_{o}^{h} in Table 2-IV were given by the Fourier analyses with respect to the fundamental component. Finally a summary of the required tests to identify the different ADT-IPMSM parameters is demonstrated in the flowchart shown in Fig. 2.15.

2.2 Dual three-phase two-level inverter model

As previously stated, one of the main advantages of multi-phase drives is its power segmentation property, making it attractive for high-power applications and/or applications demanding a high level of fault-tolerance. A dual three-phase VSI is a power electronic device, producing output voltages of variable frequency and magnitude from a constant direct-current (DC) supply (i.e. DC-link). Such variable

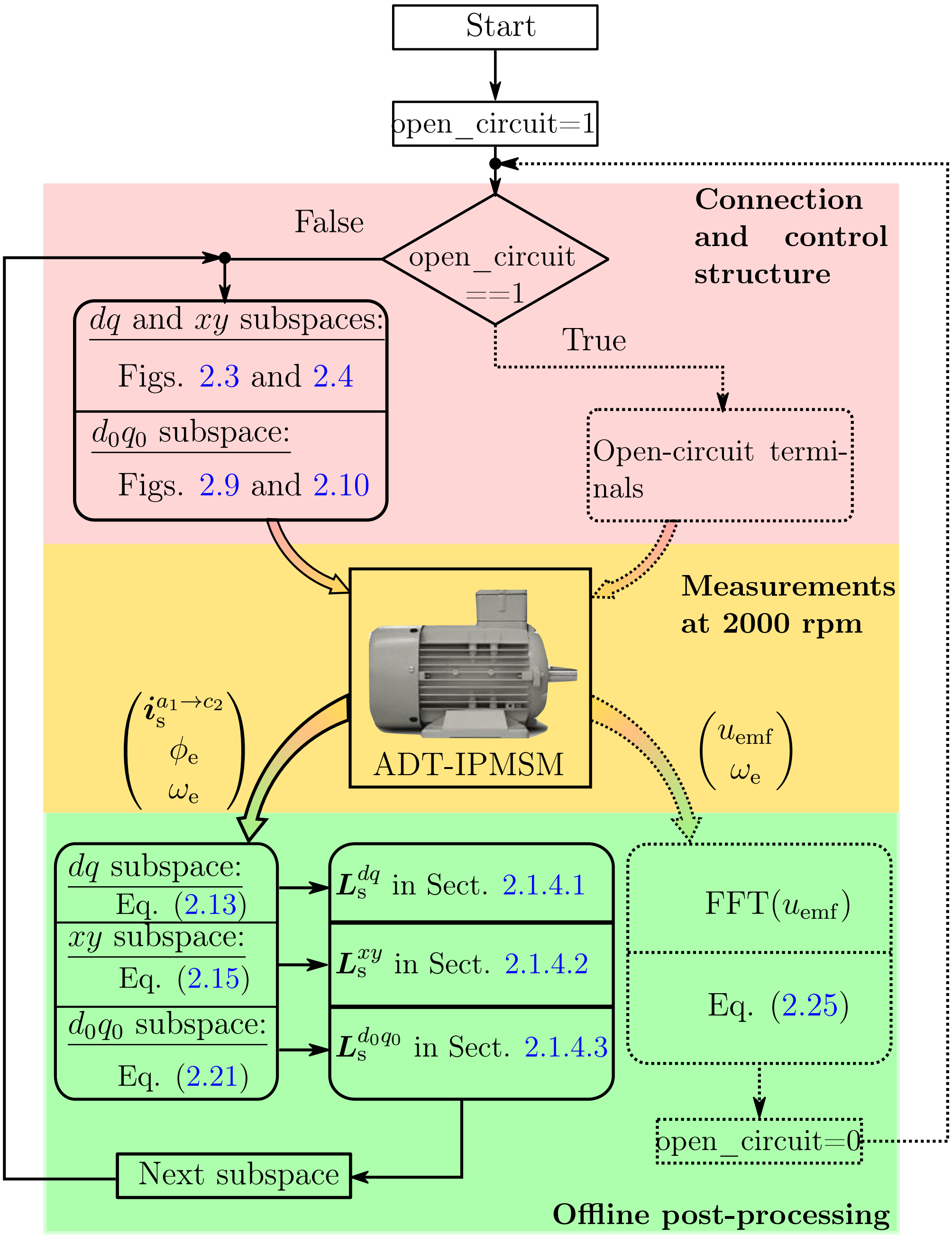

Fig. 2.15. Flowchart summarizing the identification sequence to obtain the full parameters of the different subspaces of an ADT-IPMSM in section 2.1.4.

voltage output is controlled via inverter semiconductor device per each phase. The selection of the semiconductor switches, designing the gate driver boards (i.e. hardware circuits that receive the control signal and toggle accordingly the switch state) and switching frequency are key factors that influence the operation of the inverter and correspondingly its modelling. The presented model, however, assumes ideal switching characteristics, where the switches toggle their switching state ON/OFF instantly; since the inverters employed in the test bench were off-the-shelf standard inverters. This section models the dual three-phase VSIs, based on which the volt-

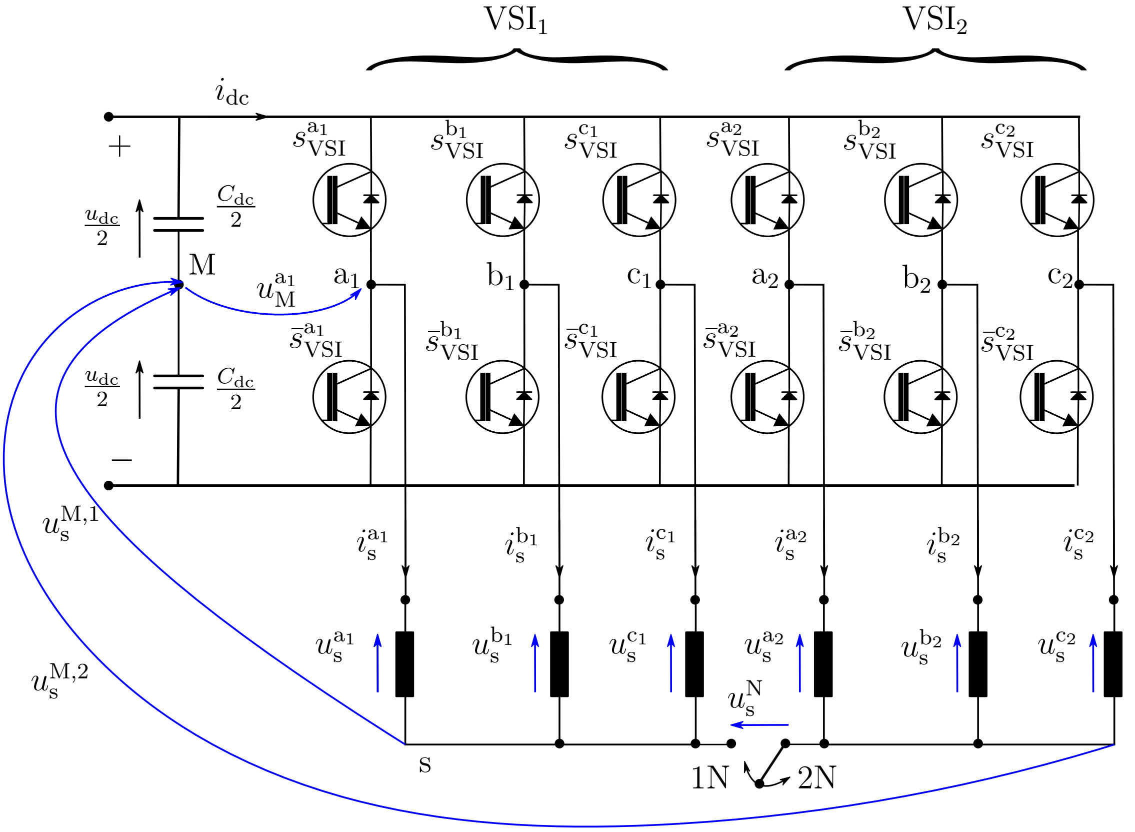

Fig. 2.16. Dual three-phase VSI composed of two three-phase two-level voltage-source inverters VSI_1 and VSI_2.

age synthesis will be derived in Section 3.1.1.3.

A virtual mid-point M is pointed out in Fig. 2.16 to facilitate the upcoming derivations, where the voltage termed *leg voltage* is represented by $\boldsymbol{u}_{\mathrm{M}}^{\mathrm{a}_1\to\mathrm{c}_2} := (u_{\mathrm{M}}^{\mathrm{a}_1}, u_{\mathrm{M}}^{\mathrm{b}_1}, u_{\mathrm{M}}^{\mathrm{c}_1}, u_{\mathrm{M}}^{\mathrm{a}_2}, u_{\mathrm{M}}^{\mathrm{b}_2}, u_{\mathrm{M}}^{\mathrm{c}_2})^\top$. From Fig. 2.16, the leg voltages are represented by

$$\boldsymbol{u}_{\mathrm{M}}^{\mathrm{a}_1\to\mathrm{c}_2} = u_{\mathrm{dc}}\,(\boldsymbol{s}_{\mathrm{VSI}}^{\mathrm{a}_1\to\mathrm{c}_2} - \frac{1}{2}\mathbf{1}_6), \tag{2.26}$$

in terms of the switching vector $\boldsymbol{s}_{\mathrm{VSI}}^{\mathrm{a}_1\to\mathrm{c}_2} := (s_{\mathrm{VSI}}^{\mathrm{a}_1}, s_{\mathrm{VSI}}^{\mathrm{b}_1}, s_{\mathrm{VSI}}^{\mathrm{c}_1}, s_{\mathrm{VSI}}^{\mathrm{a}_2}, s_{\mathrm{VSI}}^{\mathrm{b}_2}, s_{\mathrm{VSI}}^{\mathrm{c}_2})^\top$ and $\mathbf{1}_n \in \mathbb{R}^n = (1, 1, ...1)^\top$. The elements of $\boldsymbol{s}_{\mathrm{VSI}}^{\mathrm{a}_1\to\mathrm{c}_2}$ represent the switching state per phase $s_{\mathrm{VSI}}^{\kappa} \in \{0, 1\}$ and $\kappa \in \{a_1, b_1, ..., c_2,\}$, where the values 0 and 1 indicate that the upper switch is turned OFF or ON, respectively, while the opposite applies to the lower switch. Thus, the possible values for each element in $\boldsymbol{u}_{\mathrm{M}}^{\mathrm{a}_1\to\mathrm{c}_2}$ is $\pm\frac{u_{\mathrm{dc}}}{2}$. Given that the inverter output is in terms of line-to-line voltages $\boldsymbol{u}_{\mathrm{s}}^{ltl} := (u_{\mathrm{s}}^{\mathrm{a}_1\mathrm{a}_2}, u_{\mathrm{s}}^{\mathrm{a}_2\mathrm{b}_1}, u_{\mathrm{s}}^{\mathrm{b}_1\mathrm{b}_2}, u_{\mathrm{s}}^{\mathrm{b}_2\mathrm{c}_1}, u_{\mathrm{s}}^{\mathrm{c}_1\mathrm{c}_2}, u_{\mathrm{s}}^{\mathrm{c}_2\mathrm{a}_1})^\top$, the relation between the line-to-line voltages $\boldsymbol{u}_{\mathrm{s}}^{ltl}$ and the leg voltage vector $\boldsymbol{u}_{\mathrm{M}}^{\mathrm{a}_1\to\mathrm{c}_2}$ can be expressed by applying KVL as

$$\left.\begin{array}{rcl} \boldsymbol{u}_{\mathrm{s}}^{ltl} & = & \boldsymbol{T}_{\mathrm{VSI}}\,\boldsymbol{u}_{\mathrm{M}}^{\mathrm{a}_1\to\mathrm{c}_2} = u_{\mathrm{dc}}\,\boldsymbol{T}_{\mathrm{VSI}}\,\boldsymbol{s}_{\mathrm{VSI}}^{\mathrm{a}_1\to\mathrm{c}_2}, \\ i_{\mathrm{dc}} & = & \boldsymbol{s}_{\mathrm{VSI}}^{\mathrm{a}_1\to\mathrm{c}_2}\,\boldsymbol{i}_{\mathrm{s}}^{a_1\to c_2}, \end{array}\right\} \tag{2.27}$$

where

$$\boldsymbol{T}_{\mathrm{VSI}} = \begin{bmatrix} 1 & 0 & 0 & -1 & 0 & 0 \\ 0 & -1 & 0 & 1 & 0 & 0 \\ 0 & 1 & 0 & 0 & -1 & 0 \\ 0 & 0 & -1 & 0 & 1 & 0 \\ 0 & 0 & 1 & 0 & 0 & -1 \\ -1 & 0 & -1 & 0 & 0 & 1 \end{bmatrix} \text{ and } \operatorname{rank}(\boldsymbol{T}_{\mathrm{VSI}}) = 5.$$

The mathematical formula in (2.27) represents the relation between the output line-to-line $\boldsymbol{u}_{\mathrm{s}}^{ltl}$ voltages and the switching state vector $\boldsymbol{s}_{\mathrm{VSI}}^{\mathrm{a_1 \to c_2}}$, where the possible values for a line-to-line voltage are $\pm u_{\mathrm{dc}}$. Hence, the term two-level inverter corresponds to the only two possible output values. On the other hand, electric drives are modelled per phase. Therefore, the relation between the switching vector $\boldsymbol{s}_{\mathrm{VSI}}^{\mathrm{a_1 \to c_2}}$ and and the phase voltages $\boldsymbol{u}_{\mathrm{s}}^{\mathrm{a_1 \to c_2}}$ is of interest. Upon connecting the VSI terminals to the stator, the leg voltages $\boldsymbol{u}_{\mathrm{M}}^{\mathrm{a_1 \to c_2}}$ using KVL can be expressed in terms of the phase voltages $\boldsymbol{u}_{\mathrm{s}}^{\mathrm{a_1 \to c_2}} := (u_{\mathrm{s}}^{\mathrm{a_1}},\, u_{\mathrm{s}}^{\mathrm{b_1}},\, u_{\mathrm{s}}^{\mathrm{c_1}},\, u_{\mathrm{s}}^{\mathrm{a_2}},\, u_{\mathrm{s}}^{\mathrm{b_2}},\, u_{\mathrm{s}}^{\mathrm{c_2}})^\top$ as

$$\boldsymbol{u}_{\mathrm{M}}^{\mathrm{a_1 \to c_2}} = \boldsymbol{u}_{\mathrm{s}}^{\mathrm{a_1 \to c_2}} - \left(u_{\mathrm{s}}^{\mathrm{M,1}}\, \mathbf{1}_3, \quad u_{\mathrm{s}}^{\mathrm{M,2}}\, \mathbf{1}_3\right)^{\top} \overset{(2.26)}{=} u_{\mathrm{dc}}\, (\boldsymbol{s}_{\mathrm{VSI}}^{\mathrm{a_1 \to c_2}} - \tfrac{1}{2}\mathbf{1}_6). \tag{2.28}$$

Similar to the three-phase derivations in [60], the common mode voltages $u_{\mathrm{s}}^{\mathrm{M,1}}$ and $u_{\mathrm{s}}^{\mathrm{M,2}}$, as well as the voltage $u_{\mathrm{s}}^{\mathrm{N}} = u_{\mathrm{s}}^{\mathrm{M,2}} - u_{\mathrm{s}}^{\mathrm{M,1}}$ between the winding neutrals (see Fig. 2.16 and applying KVL) , can be expressed as

$$\left.\begin{aligned} u_{\mathrm{s}}^{\mathrm{M,1}} &\overset{(2.28)}{=} \begin{cases} -\sum\limits_{q \in \{a_1, b_1, c_1\}} \tfrac{1}{3} u_{\mathrm{s}}^{q} + \tfrac{u_{\mathrm{dc}}}{3} (\sum\limits_{q \in \{a_1, b_1, c_1\}} s_{\mathrm{VSI}}^{q} - \tfrac{3}{2}) & \text{for 2N,} \\ -\tfrac{1}{6}(\mathbf{1}_6^\top\, \boldsymbol{u}_{\mathrm{s}}^{\mathrm{a_1 \to c_2}}) + \tfrac{u_{\mathrm{dc}}}{6} (\mathbf{1}_6^\top\, \boldsymbol{s}_{\mathrm{VSI}}^{\mathrm{a_1 \to c_2}} - 3) & \text{for 1N,} \end{cases} \\ u_{\mathrm{s}}^{\mathrm{M,2}} &\overset{(2.28)}{=} \begin{cases} -\sum\limits_{q' \in \{a_2, b_2, c_2\}} \tfrac{1}{3} u_{\mathrm{s}}^{q'} + \tfrac{u_{\mathrm{dc}}}{3} (\sum\limits_{q' \in \{a_2, b_2, c_2\}} s_{\mathrm{VSI}}^{q'} - \tfrac{3}{2}) & \text{for 2N,} \\ u_{\mathrm{s}}^{\mathrm{M,1}} & \text{for 1N,} \end{cases} \\ u_{\mathrm{s}}^{\mathrm{N}} &= \begin{cases} \sum\limits_{q' \in \{a_2, b_2, c_2\}} \tfrac{1}{3} u_{\mathrm{s}}^{q'} - \sum\limits_{q \in \{a_1, b_1, c_1\}} \tfrac{1}{3} u_{\mathrm{s}}^{q} + \tfrac{u_{\mathrm{dc}}}{3} (\sum\limits_{q \in \{a_1, b_1, c_1\}} s_{\mathrm{VSI}}^{q} - \sum\limits_{q' \in \{a_2, b_2, c_2\}} s_{\mathrm{VSI}}^{q'}) & \text{for 2N ,} \\ 0 & \text{for 1N.} \end{cases} \end{aligned}\right\} \tag{2.29}$$

By substituting the inverter leg voltages $\boldsymbol{u}_{\mathrm{M}}^{\mathrm{a_1 \to c_2}}$ in equation (2.27) with the obtained expression (2.28), the line-to-line voltages $\boldsymbol{u}_{\mathrm{s}}^{ltl}$ can be rewritten as

$$\boldsymbol{u}_{\mathrm{s}}^{ltl} = \boldsymbol{T}_{\mathrm{VSI}} \left(u_{\mathrm{s}}^{\mathrm{a_1}}, \quad u_{\mathrm{s}}^{\mathrm{b_1}}, \quad u_{\mathrm{s}}^{\mathrm{c_1}} \quad (u_{\mathrm{s}}^{\mathrm{a_2}} - u_{\mathrm{s}}^{\mathrm{N}}), \quad (u_{\mathrm{s}}^{\mathrm{b_2}} - u_{\mathrm{s}}^{\mathrm{N}}), \quad (u_{\mathrm{s}}^{\mathrm{c_2}} - u_{\mathrm{s}}^{\mathrm{N}})\right)^{\top}. \tag{2.30}$$

2.2.1 Voltage-source inverter with a 2N neutral configuration

For a balanced supply voltage, the following balance equations hold

$$u_{\mathrm{s}}^{\mathrm{a_1}} + u_{\mathrm{s}}^{\mathrm{b_1}} + u_{\mathrm{s}}^{\mathrm{c_1}} = 0 \text{ and } u_{\mathrm{s}}^{\mathrm{a_2}} + u_{\mathrm{s}}^{\mathrm{b_2}} + u_{\mathrm{s}}^{\mathrm{c_2}} = 0. \tag{2.31}$$

By substituting $u_{\mathrm{s}}^{\mathrm{c}_1} = -u_{\mathrm{s}}^{\mathrm{a}_1} - u_{\mathrm{s}}^{\mathrm{b}_1}$ in 5th row in $\boldsymbol{T}_{\mathrm{VSI}}$ one obtains

$$\boldsymbol{u}_{\mathrm{s}}^{ltl} = \underbrace{\begin{bmatrix} 1 & 0 & 0 & -1 & 0 & 0 \\ 0 & -1 & 0 & 1 & 0 & 0 \\ 0 & 1 & 0 & 0 & -1 & 0 \\ 1 & 0 & -1 & 0 & 1 & 0 \\ -1 & -1 & 0 & 0 & 0 & -1 \\ -1 & 0 & 0 & 0 & 0 & 1 \end{bmatrix}}_{=:\boldsymbol{T}_{\mathrm{VSI,2N}} \text{ with rank } (\boldsymbol{T}_{\mathrm{VSI,2N}})=6} \begin{pmatrix} u_{\mathrm{s}}^{\mathrm{a}_1} \\ u_{\mathrm{s}}^{\mathrm{b}_1} \\ u_{\mathrm{s}}^{\mathrm{c}_1} \\ (u_{\mathrm{s}}^{\mathrm{a}_2} - u_{\mathrm{s}}^{\mathrm{N}}) \\ (u_{\mathrm{s}}^{\mathrm{b}_2} - u_{\mathrm{s}}^{\mathrm{N}}) \\ (u_{\mathrm{s}}^{\mathrm{c}_2} - u_{\mathrm{s}}^{\mathrm{N}}) \end{pmatrix}. \tag{2.32}$$

Therefore, the phase voltages can be represented in terms of the switching states $\boldsymbol{s}_{\mathrm{VSI}}^{\mathrm{a}_1 \to \mathrm{c}_2}$ with matrix inversion as

$$\begin{pmatrix} u_{\mathrm{s}}^{\mathrm{a}_1} \\ u_{\mathrm{s}}^{\mathrm{b}_1} \\ u_{\mathrm{s}}^{\mathrm{c}_1} \\ (u_{\mathrm{s}}^{\mathrm{a}_2} - u_{\mathrm{s}}^{\mathrm{N}}) \\ (u_{\mathrm{s}}^{\mathrm{b}_2} - u_{\mathrm{s}}^{\mathrm{N}}) \\ (u_{\mathrm{s}}^{\mathrm{c}_2} - u_{\mathrm{s}}^{\mathrm{N}}) \end{pmatrix} = \frac{u_{\mathrm{dc}}}{3} \begin{bmatrix} 2 & -1 & -1 & 0 & 0 & 0 \\ -1 & 2 & -1 & 0 & 0 & 0 \\ -1 & -1 & 2 & 0 & 0 & 0 \\ -1 & -1 & -1 & 3 & 0 & 0 \\ -1 & -1 & -1 & 0 & 3 & 0 \\ -1 & -1 & -1 & 0 & 0 & 3 \end{bmatrix} \boldsymbol{s}_{\mathrm{VSI}}^{\mathrm{a}_1 \to \mathrm{c}_2}. \tag{2.33}$$

Substituting

$$u_{\mathrm{s}}^{\mathrm{N}} \overset{(2.29)}{=} \frac{1}{3} \underbrace{\sum_{q' \in \{a_2, b_2, c_2\}} \tfrac{1}{3} u_{\mathrm{s}}^{q'}}_{\overset{(2.31)}{=} 0} - \frac{1}{3} \underbrace{\sum_{q \in \{a_1, b_1, c_1\}} \tfrac{1}{3} u_{\mathrm{s}}^{q}}_{\overset{(2.31)}{=} 0} + \frac{u_{\mathrm{dc}}}{3} \Big(\sum_{q \in \{a_1, b_1, c_1\}} s_{\mathrm{VSI}}^{q} - \sum_{q' \in \{a_2, b_2, c_2\}} s_{\mathrm{VSI}}^{q'} \Big), \text{ for the 2N case,} \tag{2.34}$$

in (2.33), the relation between stator phase voltages $\boldsymbol{u}_{\mathrm{s}}^{\mathrm{a}_1 \to \mathrm{c}_2}$ and switching states becomes [72]

$$\boldsymbol{u}_{\mathrm{s}}^{\mathrm{a}_1 \to \mathrm{c}_2} = \frac{u_{\mathrm{dc}}}{3} \begin{bmatrix} 2 & -1 & -1 & 0 & 0 & 0 \\ -1 & 2 & -1 & 0 & 0 & 0 \\ -1 & -1 & 2 & 0 & 0 & 0 \\ 0 & 0 & 0 & 2 & -1 & -1 \\ 0 & 0 & 0 & -1 & 2 & -1 \\ 0 & 0 & 0 & -1 & -1 & 2 \end{bmatrix} \boldsymbol{s}_{\mathrm{VSI}}^{\mathrm{a}_1 \to \mathrm{c}_2}. \tag{2.35}$$

Based on the DC-link voltage u_{dc}, it is of interest to quantify the maximum output voltage that the VSI can produce. This motivated defining the term modulation index as

$$m_{\mathrm{VSI}} = \frac{u_{\mathrm{s}}^{q''}}{(u_{\mathrm{dc}}/2)}, \text{ such that } q'' \in \{\mathrm{a}_1,\ \mathrm{b}_1\, \mathrm{c}_1\, \mathrm{a}_2\, \mathrm{b}_2\, \mathrm{c}_2\}, \tag{2.36}$$

as the ratio between the amplitude of the magnitude of the phase voltage $u_{\mathrm{s}}^{q''}$ and $\frac{u_{\mathrm{dc}}}{2}$ (i.e. magnitude of the maximum value for each element in $\boldsymbol{u}_{\mathrm{M}}^{\mathrm{a}_1 \to \mathrm{c}_2}$) [73]. Fig. 2.17 shows the voltage phasors for a 2N configuration, there exists only one value of amplitude for all the line-to-line voltages; as the voltage phasors for each three-phase are treated separately [73]. From (2.27), setting the line-to-voltages $u_{\mathrm{s}}^{\mathrm{a}_1\mathrm{b}_1}$ and

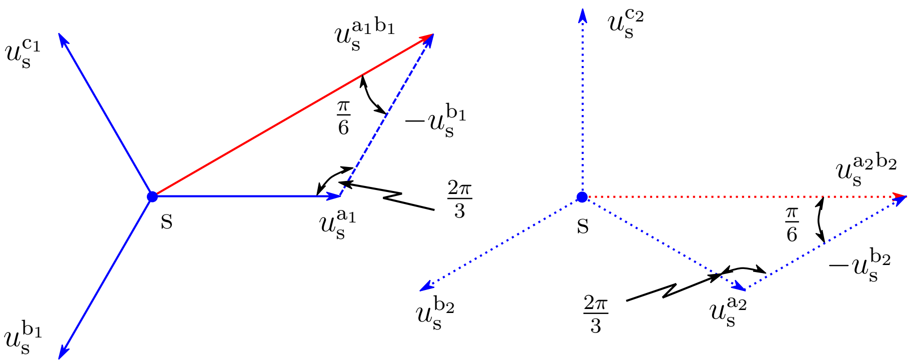

Fig. 2.17. Phasor representation of the stator phase voltages, illustrating the possible amplitudes of the line-to-line voltages applied to asymmetrical windings with 2N connection.

$u_s^{a_2b_2}$ to the maximum possible amplitude u_{dc} as

$$u_s^{a_1b_1} = u_s^{a_2b_2} = u_{dc}, \xrightarrow[\text{identities Fig. 2.17}]{\text{geometric}} u_s^{a_1} = u_s^{a_2} = u_{dc}\frac{\sin(\pi/6)}{\sin(2\pi/3)} = \underbrace{u_{dc}\frac{1}{\sqrt{3}}}_{=:\hat{u}_{\mathrm{VSI,max}}}, \tag{2.37}$$

which is identical to the modulation index obtained through the adoption of Space-vector PWM (SVPWM) for three-phase VSIs [74, Chapter 5]. The modulation index accordingly is

$$m_{\mathrm{VSI,max}}^{2\mathrm{N}} \overset{(2.36),(3.4)}{=} \frac{u_{dc}/\sqrt{3}}{u_{dc}/2} = \frac{2}{\sqrt{3}}. \tag{2.38}$$

To conclude, the output voltage per phase of a VSI $u_s^{q''}$ with a 2N configuration ranges within the interval $0 \leq u_s^{q''} \leq u_{dc}/\sqrt{3}$ and accordingly leads to $0 \leq m_{\mathrm{VSI}} \leq 2/\sqrt{3}$. The computed range for m_{VSI} corresponds to the limits of the operating region, where exceeding such limit, also known as *over-modulation*, will lead to significant generation of low order harmonics (LOHs), with added losses and deteriorated performance of the drive [73].

2.2.2 Voltage-source inverter with a 1N neutral configuration

For balanced stator voltages $u_s^{a_1} + u_s^{b_1} + u_s^{c_1} + u_s^{a_2} + u_s^{b_2} + u_s^{c_2} = 0$, by substituting that within $\boldsymbol{T}_{\mathrm{VSI}}$ and recalling $u_s^{\mathrm{N}} \overset{(2.29)}{=} 0$, then the relation between the line-to-line voltages $\boldsymbol{u}_s^{ltl}$ and $\boldsymbol{u}_s^{a_1\to c_2}$ is

$$\boldsymbol{u}_s^{ltl} = \underbrace{\begin{bmatrix} 2 & 1 & 1 & 1 & 1 & 0 \\ -1 & 0 & 0 & 1 & 0 & 0 \\ 0 & 1 & 0 & 0 & 1 & 1 \\ 0 & -1 & 0 & 0 & 1 & 0 \\ 0 & 0 & 1 & 0 & -1 & 0 \\ 0 & 0 & -1 & 0 & 0 & 1 \end{bmatrix}}_{=:\boldsymbol{T}_{\mathrm{VSI,1N}} \text{ with rank } (\boldsymbol{T}_{\mathrm{VSI,1N}})=6} \boldsymbol{u}_s^{a_1\to c_2}, \tag{2.39}$$

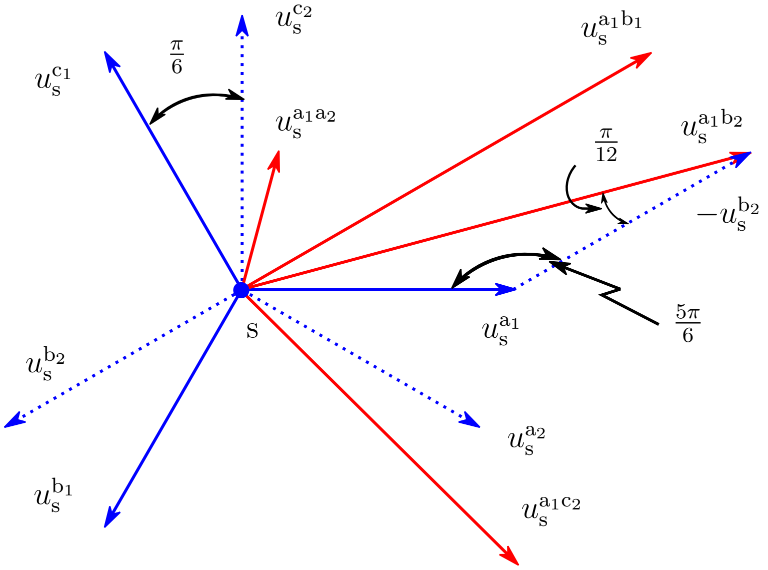

Fig. 2.18. Phasor representation of the stator phase voltages, illustrating the possible amplitudes of the line-to-line voltages applied to asymmetrical windings with 1N connection.

which leads to [63]

$$\boldsymbol{u}_{\mathrm{s}}^{\mathrm{a}_1\to\mathrm{c}_2} = \frac{u_{\mathrm{dc}}}{6}\begin{bmatrix} 5 & -1 & -1 & -1 & -1 & -1 \\ -1 & 5 & -1 & -1 & -1 & -1 \\ -1 & -1 & 5 & -1 & -1 & -1 \\ -1 & -1 & -1 & 5 & -1 & -1 \\ -1 & -1 & -1 & -1 & 5 & -1 \\ -1 & -1 & -1 & -1 & -1 & 5 \end{bmatrix} \boldsymbol{s}_{\mathrm{VSI}}^{\mathrm{a}_1\to\mathrm{c}_2}, \tag{2.40}$$

as the relation between the stator phase voltages $\boldsymbol{u}_{\mathrm{s}}^{\mathrm{a}_1\to\mathrm{c}_2}$ and the switching vector $\boldsymbol{s}_{\mathrm{VSI}}^{\mathrm{a}_1\to\mathrm{c}_2}$ for a 1N connection. To derive the maximum output voltage the inverter can output within the 1N connection, upon observing Fig. 2.18, one concludes that there are four different line-to-line voltage magnitudes highlighted in ——. From (2.27), the maximum amplitude for a line-to-line voltage cannot exceed u_{dc}. By comparing the length of the voltage vectors —— in Fig. 2.18 and setting the line-to-line voltage of maximum length $u_{\mathrm{s}}^{\mathrm{a}_1\mathrm{b}_2}$ in Fig. 2.18 to u_{dc}, the amplitude of the phase voltage $u_{\mathrm{s}}^{\mathrm{a}_1}$ using geometric identities is

$$u_{\mathrm{s}}^{\mathrm{a}_1} = u_{\mathrm{dc}}\frac{\sin(\pi/12)}{\sin(5\pi/6)} \xrightarrow{\text{yielding}} m_{\mathrm{VSI,max}}^{1\mathrm{N}} \overset{(2.36)}{=} 1.0353. \tag{2.41}$$

Comparing (2.38) and (2.41), the maximum modulation index for the 1N connection drops by 10.34% in comparison with the 2N connection, confirming the findings in [55,75]. This motivates operating the machine with a 2N connection in the healthy case; to enhance the DC-link voltage utilization. Based on this fact, the design of voltage synthesis space-vector pulse-width-modulation (SVPWM) shown in Section (3.1.1) for improved VSI performance is carried-out for the 2N connection. Nevertheless, the simulation and experimental results in Section (2.3) will show results for both 1N and 2N connections for the sake of ADT-IPMSM model validation.

2.3 Simulation results and experimental validations

This section evaluates the outcomes of the proposed ADT-IPMSM model with those implemented on the practical setup depicted in Fig. A.1-1 shown in Appendix A. With the aid of Matlab/Simulink, the proposed model in Section 2.1.3 has been simulated using the flux linkage maps in Fig. 2.11 and the corresponding differential inductances in Figs. 2.6, 2.8, and 2.12. The flux linkages were used as the states per each subspace for the carried out simulations, while the corresponding currents were obtained using the inverse interpolation algorithm that extracts the currents $\boldsymbol{i}_\mathrm{s}^{dq}$, $\boldsymbol{i}_\mathrm{s}^{xy}$ and $\boldsymbol{i}_\mathrm{s}^{0}$ from the corresponding flux linkages $\boldsymbol{\psi}_\mathrm{s}^{dq}$, $\boldsymbol{\psi}_\mathrm{s}^{xy}$, and $\boldsymbol{\psi}_\mathrm{s}^{0}$, respectively [51,68,76]. Thus, the effect of cross-coupling, saturation, and different machine non-linearities can be included to a high extent. The mathematical modelling of the VSI for the 1N and 2N cases is given by (2.40) and (2.35), respectively. Sampling and switching frequencies are set equal as seen in Table 2-I, where sampling instants are triggered in the middle of the switching period. The stator current control was carried out as shown in Fig. 2.3. Due to the discrete-time delay, the provided voltage references to the VSIs consider the position error when applying the Park transformation (i.e. $\boldsymbol{T}_\mathrm{p}'(\phi_\mathrm{e} + \omega_\mathrm{e} T_\mathrm{sw})$) [60, Chapter 14].

The proposed fundamental and harmonic models for 1N and 2N configurations are validated in terms of $\boldsymbol{i}_\mathrm{s}^{dq}$ and $\boldsymbol{i}_\mathrm{s}^{xy}$, $\boldsymbol{i}_\mathrm{s}^{0}$, and $(i_\mathrm{s}^{\mathrm{a}_1}, i_\mathrm{s}^{\mathrm{a}_2})$ at steady-state at a reference speed of 120 rad/s and $(i_\mathrm{s,ref}^{d},\, i_\mathrm{s,ref}^{q}) = (0\,\mathrm{A},\, 3\,\mathrm{A})^\top$. For the 2N case (i.e. $\boldsymbol{i}_\mathrm{s}^{0}$ is discarded), Figs. 2.19(a)-(b) and 2.20(a)-(b) represent the outcomes **without** and **with** harmonic compensation (HC) via the R controllers, respectively. If the xy harmonic model presented in Section 2.1.4.2 is neglected or unclearly defined [56, 64], the simulations are incapable of generating results identical to those in Fig. 2.19(a). In terms of total harmonic distortion (THD), simulations indicate that the uncompensated stator currents impose a THD=30.17% compared to the 41.37% obtained by experimental measurements. Also, one could observe a slight difference between $\boldsymbol{i}_\mathrm{s}^{xy}$ in Fig 2.19 in terms of amplitudes with a minor phase shift between the simulated and the experimental cases. This anomalous experimental THD is due to the unmodeled non-linearities such as the generated 5th and 7th harmonics by the VSIs; owing to the unmodeled $2\,\mu$s fixed dead-time, generated by the gate drivers of the VSIs. Other possible sources of non-linearities are mentioned in [63, 77] such as stator slots mutual coupling, core-losses, and end-turns effects. Including such non-linear effect, if possible, will converge the simulated model in the xy subspace to the practical case. For instance, by including the dead-time effect in the simulations, the 5th and 7th harmonics increased, and accordingly, the THD= 35.8%. For other inverter topologies, as the Z-source inverter, such inverter configuration allows dead-time free operation [78]. Thus, it is expected that for such inverter, simulations would produce better results that further converge to the practical results for the xy subspace. Nevertheless, by comparing the stator current $i_\mathrm{s}^{\mathrm{a}_1}$ in Figs. 2.19(a)-(b), the proposed model is still acceptable [51]. As for the compensated case, simulations

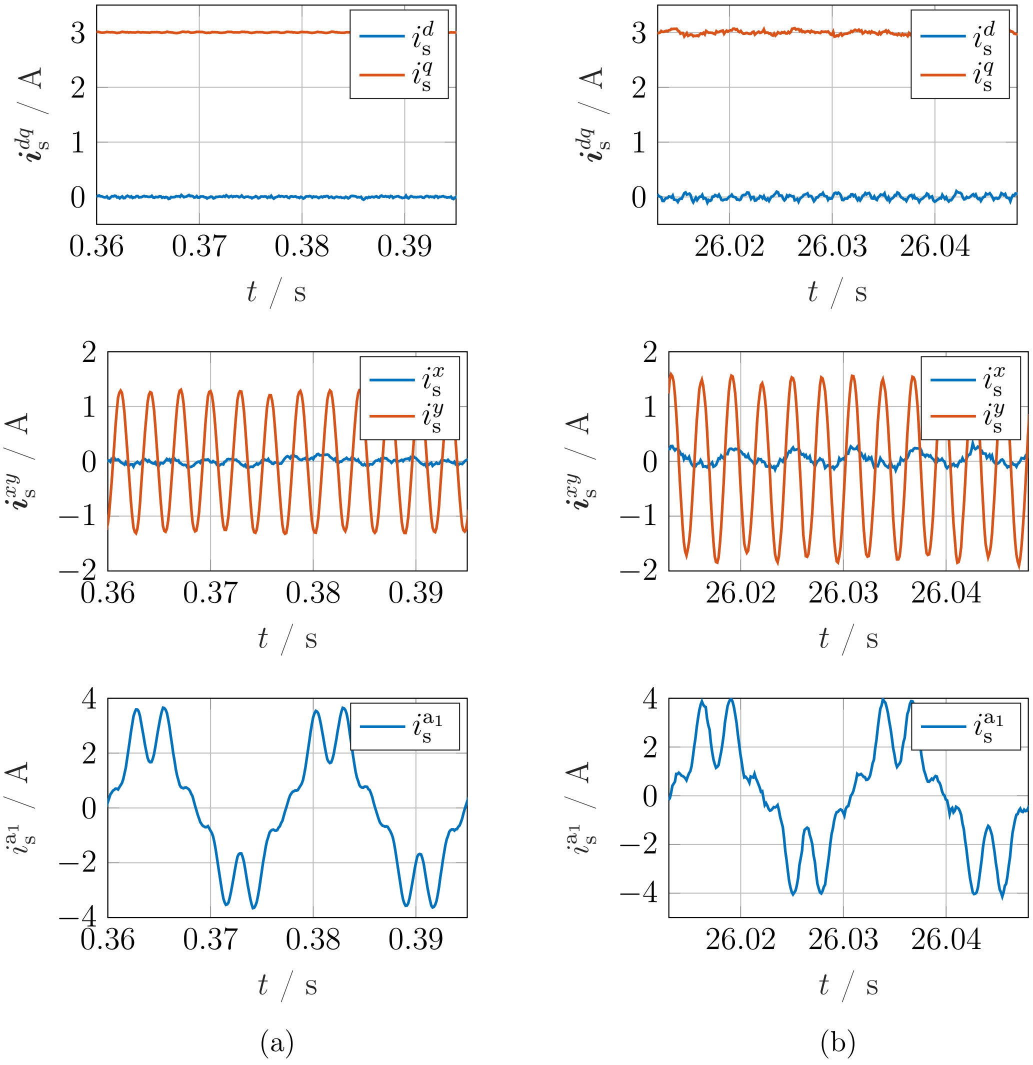

Fig. 2.19. (a) Simulation and (b) experimental results comparison for the 2N case **without** $\boldsymbol{i}_s^{xy}$ harmonic compensation at steady state for $\boldsymbol{i}_{s,\mathrm{ref}}^{dq} = (0\,\mathrm{A}, 3\,\mathrm{A})^\top$ (top to bottom): $\boldsymbol{i}_s^{dq}$, $\boldsymbol{i}_s^{xy}$ and $i_s^{a_1}$.

lead to a THD$= 3.06\%$ compared to the experimental case THD$= 3.82\%$ indicated in Fig. 2.20. Accordingly, to compare the simulations and experimental measurements for the 1N case, the $\boldsymbol{i}_s^{xy}$ currents were compensated; to overcome the discrepancy between the simulated and experimental harmonic models in the xy plane and their influence on $i_s^{a_1}$ and $i_s^{a_2}$. Figs. 2.21 and 2.22 illustrate the results **without** and **with** HC, respectively, where the simulations were able to adhere to a high extent to the experimental results. The detailed harmonic content and THD for both 1N and 2N cases are shown in Table 2-V. It is concluded that the proposed simulated harmonic models of the xy and *zero* subspaces coincide with acceptable degree to the experimental waveforms obtained, as illustrated in $\boldsymbol{i}_s^{xy}$ and $\boldsymbol{i}_s^{0}$ in Figs. 2.19-2.22.

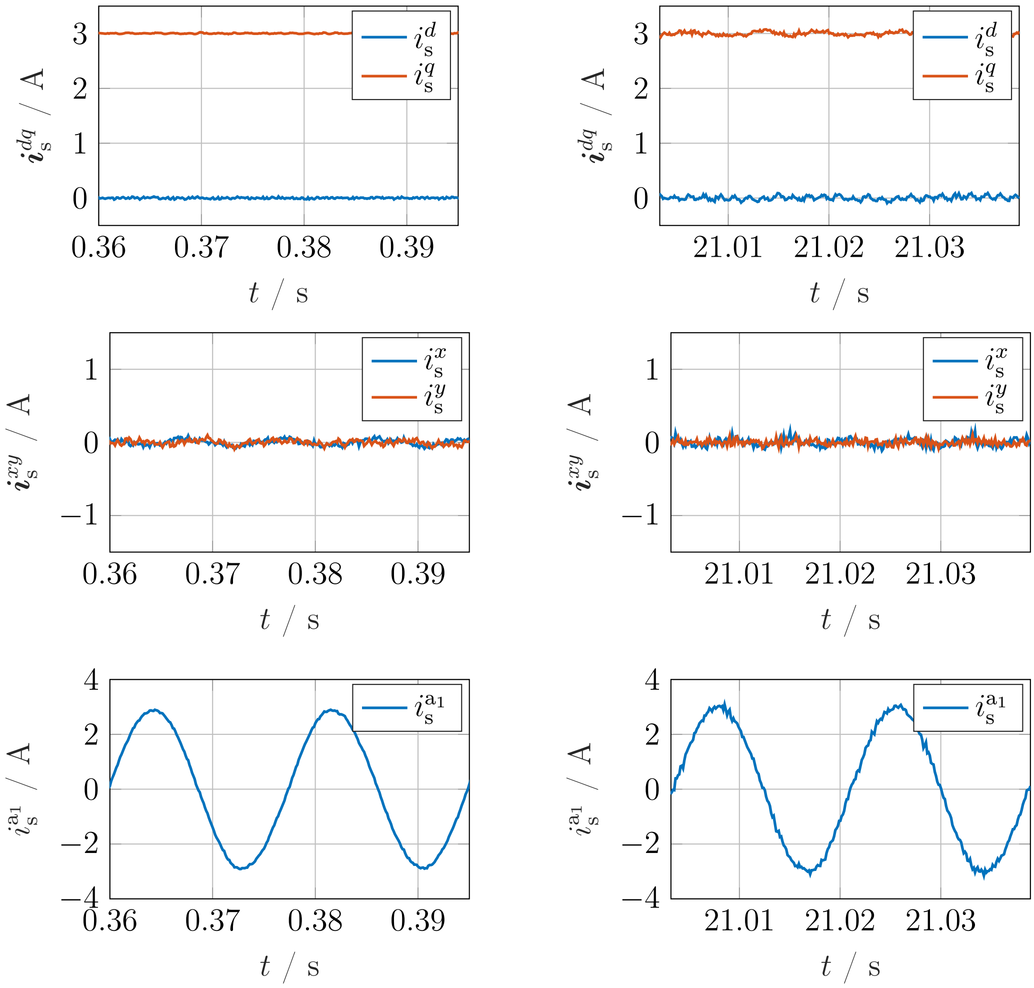

(a) (b)

Fig. 2.20. (a) Simulation and (b) experimental results comparison for the 2N case **with** $\boldsymbol{i}_\mathrm{s}^{xy}$ harmonic compensation at steady state for $\boldsymbol{i}_\mathrm{s,ref}^{dq} = (0\,\mathrm{A},\, 3\,\mathrm{A})^\top$ (top to bottom): $\boldsymbol{i}_\mathrm{s}^{dq}$, $\boldsymbol{i}_\mathrm{s}^{xy}$ and $i_\mathrm{s}^{\mathrm{a}_1}$.

Table 2-V. THD and harmonic content of $i_\mathrm{s}^{\mathrm{a}_1}$ compared to the fundamental component.

Connection	Order	Simulation		Experimental	
		without HC	with HC	without HC	with HC
2N	5	20.88%	0.79%	28.91%	0.77%
	7	19.56%	0.28%	28.97%	0.32%
	THD	30.17%	3.06%	41.37%	3.82%
1N	3	17.77%	1.56%	18.1%	0.94%
	5	-	0.77%	-	0.44%
	7	-	0.3%	-	0.58%
	9	6.39%	1.53%	7.12%	0.39%
	THD	19.17%	3.29%	20.1%	4.9%

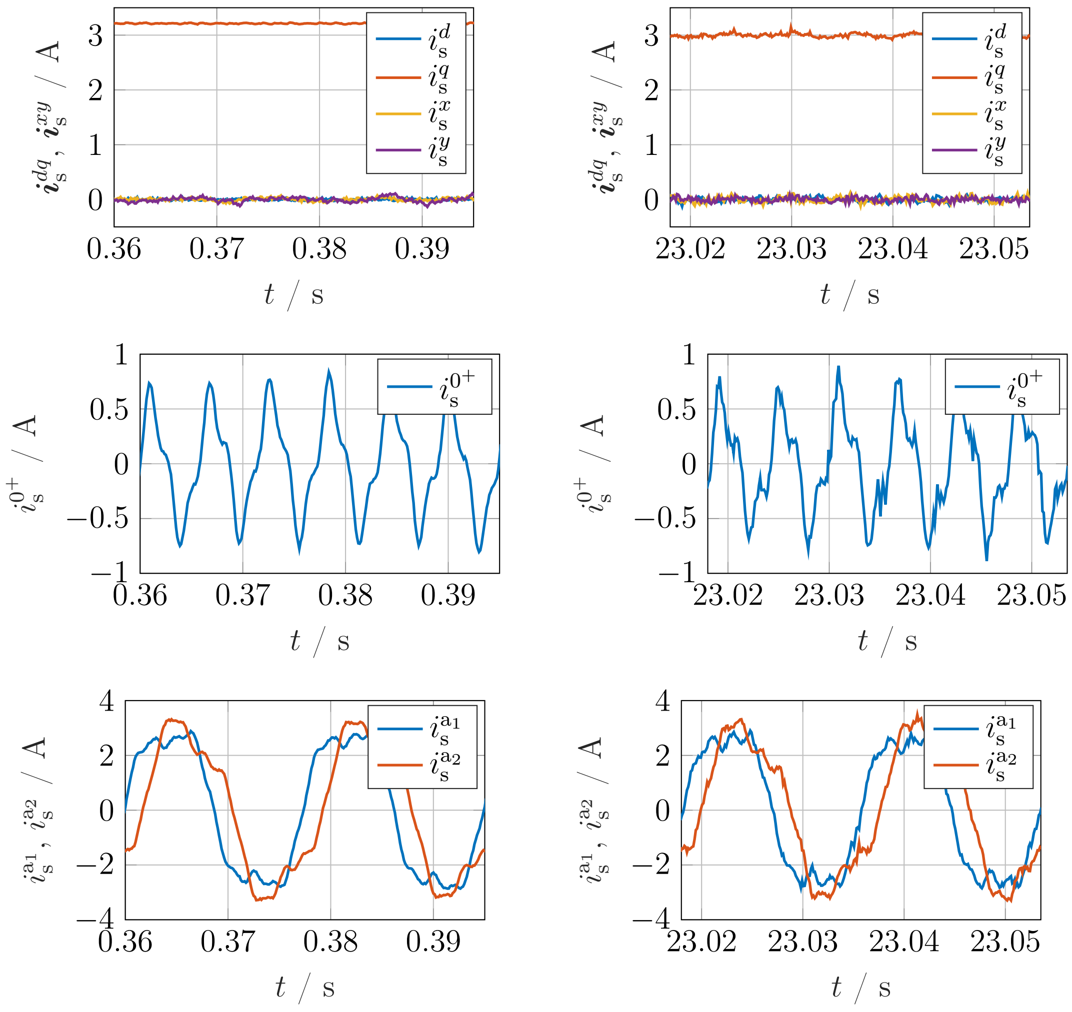

(a) (b)

Fig. 2.21. (a) Simulation and (b) experimental results comparison for the 1N case **without** $\boldsymbol{i}_s^0$ compensation at steady state for $\boldsymbol{i}_{s,\mathrm{ref}}^{dq} = (0\,\mathrm{A}, 3\,\mathrm{A})^\top$ and $\boldsymbol{i}_{s,\mathrm{ref}}^{xy} = (0\,\mathrm{A}, 0\,\mathrm{A})^\top$ (top to bottom): $(\boldsymbol{i}_s^{dq}, \boldsymbol{i}_s^{xy})$, $\boldsymbol{i}_s^0$ and $(i_s^{a_1}, i_s^{a_2})$.

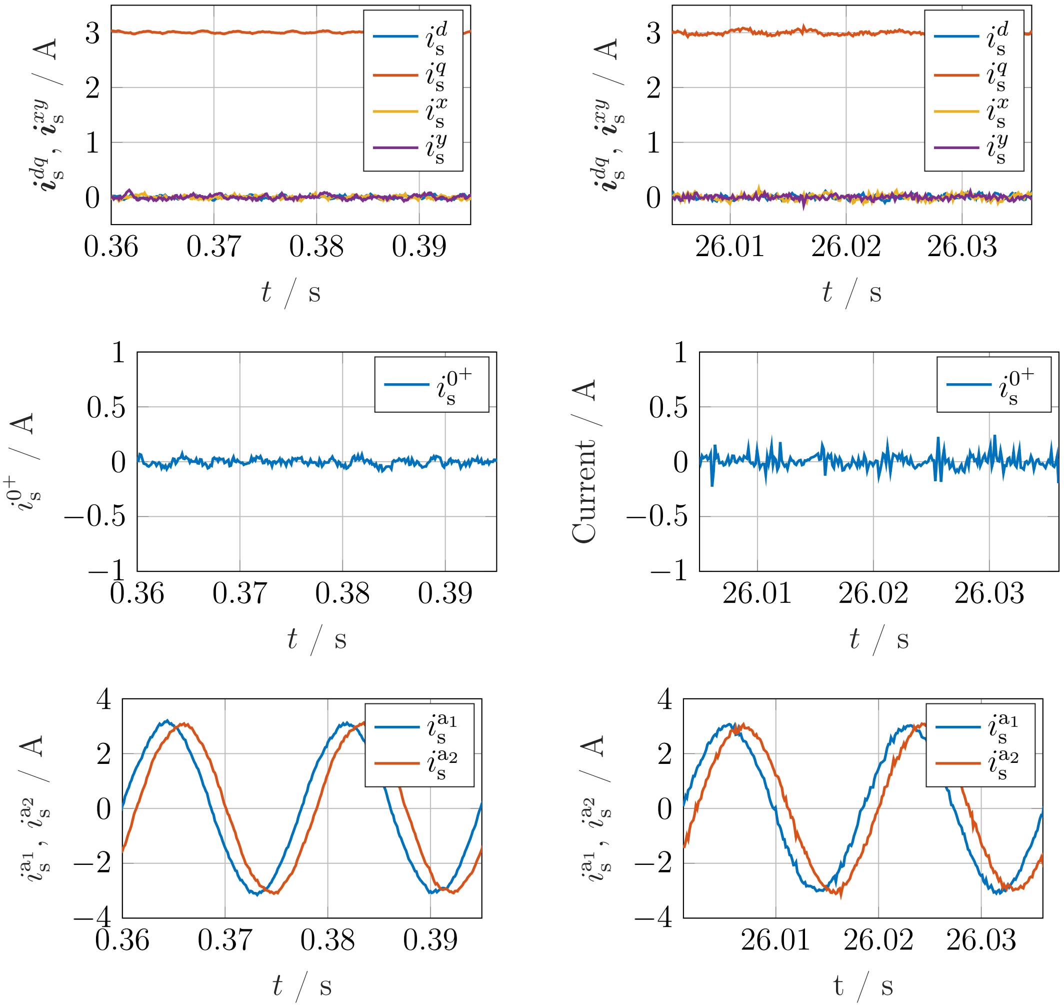

(a) (b)

Fig. 2.22. (a) Simulation and (b) experimental results comparison for the 1N case **with** $\boldsymbol{i}_\mathrm{s}^0$ compensation at steady state for $\boldsymbol{i}^{dq}_{\mathrm{s,ref}} = (0\,\mathrm{A},\,3\,\mathrm{A})^\top$ and $\boldsymbol{i}^{xy}_{\mathrm{s,ref}} = (0\,\mathrm{A},\,0\,\mathrm{A})^\top$ (top to bottom): ($\boldsymbol{i}_\mathrm{s}^{dq}$, $\boldsymbol{i}_\mathrm{s}^{xy}$), $\boldsymbol{i}_\mathrm{s}^0$ and ($i_\mathrm{s}^{\mathrm{a}_1}$, $i_\mathrm{s}^{\mathrm{a}_2}$).

Chapter 3

Control of dual three-phase IPMSM drives

Based on the proposed non-linear ADT-IPMSM model in Chapter 2, two main outcomes are realized: (i) model-based fast-tracking stator current controllers are implemented. In comparison with the available body of literature concerning the stator current controller, the proposed approach in this chapter takes into account the non-linearity effects within the entire operating range of the drive. Additionally, the desired reference currents are tracked with zero steady-state error. (ii) A feed-forward torque controller is employed, where its output is fed to the underlying stator current controllers. Such torque controller ensures not only precise torque production, but also minimizes the stator copper losses through the the generated stator current references. On the other hand, a switching scheme for of the VSI is proposed. The proposed scheme is similar to those available in literature in terms of minimizing the VSI switching losses, but can additionally eliminate undesired currents in the none torque-producing subspaces. Moreover, a simple real-time realization method is proposed making it feasible for modest real-time controllers currently available. Furthermore, the switching of the VSI in the post-fault case is presented.

This chapter is divided as follows: Section 3.1 is related to the switching schemes of the VSI. The feed-forward torque controller and minimum stator copper losses are shown in Section 3.2, while the underlying proposed stator current control is designed in Section 3.3.

3.1 Control of the voltage-source inverter

There exists in literature two pulse-width-modulation (PWM) schemes to control a VSI, which are either the space-vector PWM (SVPWM), as derived in Section 3.1.1, or carrier-based PWM, which is explained in Section 3.1.2. The employed SVPWM scheme is applicable only in the pre-fault (i.e. healthy) case, while the carrier-based PWM is utilized in the post-fault operation.

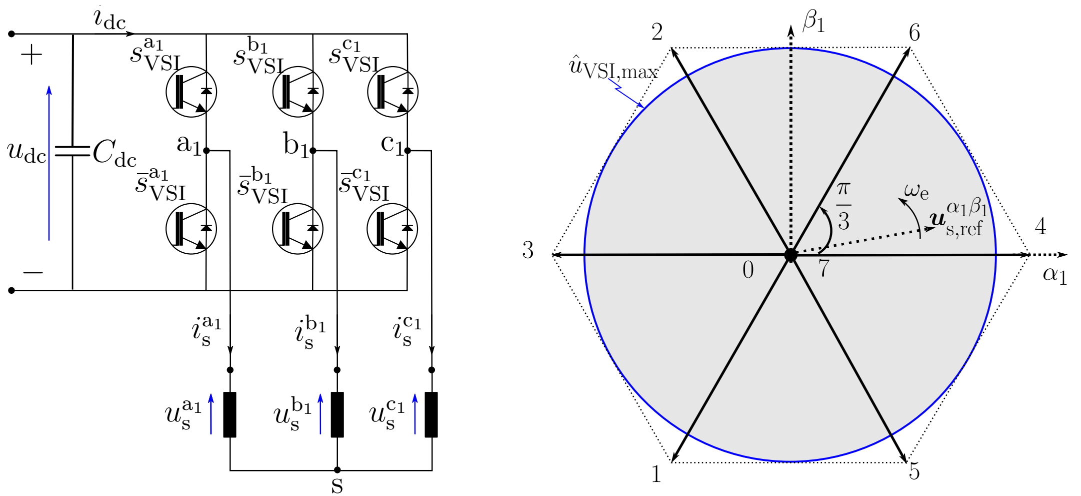

(a) (b)

Fig. 3.1. (a) Three phase two-level VSI and (b) the corresponding voltage vectors in the $\alpha_1\beta_1$ frame with respect to (3.2). The shaded area in ▨ is the feasible linear region of maximum magnitude $\hat{u}_{\mathrm{VSI,max}}$.

3.1.1 Space-vector pulse-width-modulation

The concept of SVPWM for three-phase VSIs is explained in Section 3.1.1.1, based on which the SVPWM for dual three-phase VSIs is derived in Section 3.1.1.2. The proposed modification to the recent SVPWM schemes in literature are laid out in Section 3.1.1.3, with the corresponding experimental results.

3.1.1.1 Concept of space-vector pulse-width-modulation

Space-vector pulse-width-modulation (SVPWM) is a well-established theory for the control of three-phase VSIs, where its main benefit lies in achieving high performance overall operation of the drive through the minimization of the harmonic content and better utilization of the DC-link supply [73, Chapter 6]. In order to comprehend, the SVPWM technique, it is crucial to briefly introduce first the concept of SVPWM developed for three-phase drives, based on which the SVPWM for asymmetrical dual three-phase drives were derived.

The three-phase VSI in Fig. 3.1(a) is regarded as one of the two VSIs used for dual three-phase drives, which in that case will be connected to the three-phase stator terminals $a_1b_1c_1$. Thus, the relation between the three-phase voltages $\boldsymbol{u}_{\mathrm{s}}^{\mathrm{a}_1\to\mathrm{c}_1} := (u_{\mathrm{s}}^{\mathrm{a}_1}, u_{\mathrm{s}}^{\mathrm{b}_1}, u_{\mathrm{s}}^{\mathrm{c}_1})^\top$ (in V) and the switching vector $\boldsymbol{s}_{\mathrm{VSI}}^{\mathrm{a}_1\to\mathrm{c}_1} := (s_{\mathrm{VSI}}^{\mathrm{a}_1}, s_{\mathrm{VSI}}^{\mathrm{b}_1}, s_{\mathrm{VSI}}^{\mathrm{c}_1})^\top$ can be directly excerpted from the relation between the stator phase voltages $\boldsymbol{u}_{\mathrm{s}}^{\mathrm{a}_1\to\mathrm{c}_2}$ and the switching vector $\boldsymbol{s}_{\mathrm{VSI}}^{\mathrm{a}_1\to\mathrm{c}_2}$ for the 2N connection in (2.35) by only considering the $a_1b_1c_1$ elements. This would result in

$$\boldsymbol{u}_{\mathrm{s}}^{\mathrm{a}_1\to\mathrm{c}_1} \overset{(2.35)}{=} \frac{u_{\mathrm{dc}}}{3}\begin{bmatrix} 2 & -1 & -1 \\ -1 & 2 & -1 \\ -1 & -1 & 2 \end{bmatrix} \boldsymbol{s}_{\mathrm{VSI}}^{\mathrm{a}_1\to\mathrm{c}_1}, \tag{3.1}$$

which is identical to the three-phase VSI model in [60]. Applying Clarke's transformation $\boldsymbol{T}_{\mathrm{C},1}$ in (2.3) for three-phase systems will map the three phase quantities $\boldsymbol{f}^{a_1 b_1 c_1}$, where $f \in \{\boldsymbol{u},\, \boldsymbol{i},\, \boldsymbol{\psi}\}$, to the $\alpha_1\beta_1$ and 0^+ subspaces (i.e. $\boldsymbol{f}_{\mathrm{s}}^{\alpha_1\beta_1 0^+} = \boldsymbol{T}_{\mathrm{C},1}\boldsymbol{f}_{\mathrm{s}}^{\mathrm{a}_1\to\mathrm{c}_1}$). Therefore, applying $\boldsymbol{T}_{\mathrm{C},1}$ to (3.1) leads to

$$\begin{pmatrix} u_{\mathrm{s}}^{\alpha_1} \\ u_{\mathrm{s}}^{\beta_1} \\ u_{\mathrm{s}}^{0^+} \end{pmatrix} = \boldsymbol{T}_{\mathrm{C},1}\boldsymbol{u}_{\mathrm{s}}^{\mathrm{a}_1\to\mathrm{c}_1} \overset{(3.1)}{=} \frac{u_{\mathrm{dc}}}{3}\begin{bmatrix} 2 & -1 & -1 \\ 0 & \sqrt{3} & -\sqrt{3} \\ 0 & 0 & 0 \end{bmatrix} \boldsymbol{s}_{\mathrm{VSI}}^{\mathrm{a}_1\to\mathrm{c}_1}. \tag{3.2}$$

The three-phase VSI in Fig. 3.1(a) has eight possible switching states, since $s_{\mathrm{VSI}}^{\kappa} = \{1,\, 0\}$ where $\kappa := \{a_1,\, b_1,\, c_1\}$, represents either an ON and OFF state, respectively. Accordingly, the switching vector $\boldsymbol{s}_{\mathrm{VSI}}^{\mathrm{a}_1\to\mathrm{c}_1}$ switching states, in a binary form ranging $000 \to 111$, correspond to $0 \to 8$. Substituting the binary switching states in (3.2) maps the eight possible switching vectors to the $\alpha_1\beta_1$ frame, as seen in Fig. 3.1(b). There are two vectors mapped at the origin (i.e. vectors 0 and 7), while the other *active* vectors are as designated in Fig. 3.1(b). Table 3-I summarizes the projection of each switching vector on the $\alpha_1\beta_1$ coordinates. Joining the tips of the voltage vectors in Fig. 3.1(b) results in the so called *voltage hexagon*, divided into six sectors every $\frac{\pi}{3}$. For three-phase machine rotating with an angular velocity ω_{e} and an initial position ϕ_{o}, the reference $\alpha_1\beta_1$ voltage vector can be represented by

$$\boldsymbol{u}_{\mathrm{s,ref}}^{\alpha_1\beta_1}(t) = \hat{u}\cos(\omega_{\mathrm{e}}t + \phi_o), \text{ where } 0 \leq \hat{u} \leq \frac{u_{\mathrm{dc}}}{\sqrt{3}} \text{ and } \phi_{\mathrm{e}} = \int \omega_{\mathrm{e}}\,\mathrm{d}t + \phi_{\mathrm{o}}, \tag{3.3}$$

which is translated as a *rotating* voltage space-vector in the $\alpha_1\beta_1$ frame, as indicated in Fig. 3.1, where the maximum amplitude for the $\alpha_1\beta_1$ voltage vector $\boldsymbol{u}_{\mathrm{s,ref}}^{\alpha_1\beta_1}$ (argument t is dropped for simplification) is identical to that of dual three-phase VSI, denoted as [60]

$$\hat{u}_{\mathrm{VSI,max}} \overset{(3.4)}{=} \frac{u_{\mathrm{dc}}}{\sqrt{3}}. \tag{3.4}$$

The principle of SVPWM is projecting the rotating voltage vector $\boldsymbol{u}_{\mathrm{s,ref}}^{\alpha_1\beta_1}$ in the Fig. 3.1(b) during every sampling period T_{sw} (in s) on the two adjacent switching vectors and a zero vector (i.e. vectors 0 or 7). Moreover, the zero vector and each of the two active are enabled for an interval of time known as the *dwell* times, which are termed t_{V_1} (in s), t_{V_2} (in s) and T_0 (in s). Each dwell time is determined such that the total Volt-second of the reference vector $\boldsymbol{u}_{\mathrm{s,ref}}^{\alpha_1\beta_1}T_{\mathrm{sw}}$ is identical to that of the active and zero space vectors, i.e. [73, Chapter 6]

$$\left.\begin{array}{lcl} \boldsymbol{u}_{\mathrm{s,ref}}^{\alpha_1\beta_1}T_{\mathrm{sw}} & = & \boldsymbol{u}_{\mathrm{V}_1}^{\alpha_1\beta_1}t_{\mathrm{V}_1} + \boldsymbol{u}_{\mathrm{V}_2}^{\alpha_1\beta_1}t_{\mathrm{V}_2} + \boldsymbol{u}_{\mathrm{V}_0}^{\alpha_1\beta_1}t_{\mathrm{V}_0}, \\ T_{\mathrm{sw}} & = & t_{\mathrm{V}_1} + t_{\mathrm{V}_2} + t_{\mathrm{V}_0}, \end{array}\right\} \tag{3.5}$$

where $\boldsymbol{u}_{\mathrm{V}_1}^{\alpha_1\beta_1} := (u_{\mathrm{V}_1}^{\alpha_1},\, u_{\mathrm{V}_1}^{\beta_1})^{\top}$ (in V) and $\boldsymbol{u}_{\mathrm{V}_2}^{\alpha_1\beta_1} := (u_{\mathrm{V}_2}^{\alpha_1},\, u_{\mathrm{V}_2}^{\beta_1})^{\top}$ (in V) are two active voltage vectors within an arbitrary sector in Fig. 3.1(b). The elements $u_{\mathrm{V}_1}^{\alpha_1}$, $u_{\mathrm{V}_1}^{\beta_1}$, $u_{\mathrm{V}_2}^{\alpha_1}$, and $u_{\mathrm{V}_2}^{\beta_1}$ are the projections of the vectors $\boldsymbol{u}_{\mathrm{V}_1}^{\alpha_1\beta_1}$ and $\boldsymbol{u}_{\mathrm{V}_2}^{\alpha_1\beta_1}$ on the $\alpha_1\beta_1$ coordinates in Fig. 3.1(b), as seen per every switching vector in Table 3-I. The vector $\boldsymbol{u}_{\mathrm{V}_0}^{\alpha_1\beta_1}$ (in V) is the zero voltage vector (vectors 0 and 7 in Table 3-I) and is projected at the origin $\big($i.e. $\boldsymbol{u}_{\mathrm{V}_0}^{\alpha_1\beta_1} = (0\,\mathrm{V}, 0\,\mathrm{V})\big)$. It is worth to mention that the number of active voltage

Table 3-I. Switching table for three-phase VSI, showing the projection of each voltage vector in Fig. 3.1 on the $\alpha_1\beta_1$ coordinates according to (3.2).

Vector number	Switching vector $\boldsymbol{s}_{\mathrm{VSI}}^{\mathrm{a_1 \to c_1}}$	$u_{\mathrm{s}}^{\alpha_1}/u_{\mathrm{dc}}$	$u_{\mathrm{s}}^{\beta_1}/u_{\mathrm{dc}}$
0	$(0,\, 0,\, 0)^{\top}$	$0\,\mathrm{V}$	$0\,\mathrm{V}$
1	$(0,\, 0,\, 1)^{\top}$	$-1/3\mathrm{V}$	$-1/\sqrt{3}\mathrm{V}$
2	$(0,\, 1,\, 0)^{\top}$	$-1/3\mathrm{V}$	$1/\sqrt{3}\mathrm{V}$
3	$(0,\, 1,\, 1)^{\top}$	$-2/3\mathrm{V}$	$0\,\mathrm{V}$
4	$(1,\, 0,\, 0)^{\top}$	$2/3\mathrm{V}$	$0\,\mathrm{V}$
5	$(1,\, 0,\, 1)^{\top}$	$1/3\mathrm{V}$	$-1/\sqrt{3}\mathrm{V}$
6	$(1,\, 1,\, 0)^{\top}$	$1/3\mathrm{V}$	$1/\sqrt{3}\mathrm{V}$
7	$(1,\, 1,\, 1)^{\top}$	$0\,\mathrm{V}$	$0\,\mathrm{V}$

vectors is *equal* to the number of independent control variables, which is also *two* from Fig. 3.1(a) (i.e. $i_{\mathrm{s}}^{\mathrm{a_1}}$ and $i_{\mathrm{s}}^{\mathrm{b_1}}$ are independent variables, while $i_{\mathrm{s}}^{\mathrm{c_1}} = -i_{\mathrm{s}}^{\mathrm{a_1}} - i_{\mathrm{s}}^{\mathrm{b_1}}$). The dwell times $t_{\mathrm{V_1}}$, $t_{\mathrm{V_2}}$ and $t_{\mathrm{V_0}}$ can be computed for any reference voltage $\boldsymbol{u}_{\mathrm{s,ref}}^{\alpha_1\beta_1}$ by expanding (3.5) as

$$\begin{pmatrix} u_{\mathrm{s}}^{\alpha_1} T_{\mathrm{sw}} \\ u_{\mathrm{s}}^{\beta_1} T_{\mathrm{sw}} \\ T_{\mathrm{sw}} \end{pmatrix} = \underbrace{\begin{bmatrix} u_{\mathrm{V_1}}^{\alpha_1} & u_{\mathrm{V_2}}^{\alpha_1} & 0 \\ u_{\mathrm{V_1}}^{\beta_1} & u_{\mathrm{V_2}}^{\beta_1} & 0 \\ 1 & 1 & 1 \end{bmatrix}}_{=:\boldsymbol{T}_{\mathrm{t_V}}} \begin{pmatrix} t_{\mathrm{V_1}} \\ t_{\mathrm{V_2}} \\ t_{\mathrm{V_0}} \end{pmatrix}. \tag{3.6}$$

The determinant of $\boldsymbol{T}_{\mathrm{t_V}}$ is none-zero (i.e. $\det(\boldsymbol{T}_{\mathrm{t_V}}) = u_{\mathrm{V_1}}^{\alpha_1} u_{\mathrm{V_2}}^{\beta_1} - u_{\mathrm{V_2}}^{\alpha_1} u_{\mathrm{V_1}}^{\beta_1} \overset{!}{\neq} 0$) as the space vectors $\boldsymbol{u}_{\mathrm{V_1}}^{\alpha_1\beta_1}$ and $\boldsymbol{u}_{\mathrm{V_1}}^{\alpha_1\beta_1}$ are always selected as the active switching vectors (i.e. $\boldsymbol{u}_{\mathrm{V_1}}^{\alpha_1\beta_1} \neq (0\,\mathrm{V},\, 0\,\mathrm{V})$ and $\boldsymbol{u}_{\mathrm{V_2}}^{\alpha_1\beta_1} \neq (0\,\mathrm{V},\, 0\,\mathrm{V})$). Moreover, the determinant $\det(\boldsymbol{T}_{\mathrm{t_V}})$ always exist when substituting with the vectors in Table 3-I belonging to the same sector. Accordingly, the dwell times can be computed by

$$\left.\begin{aligned} \begin{pmatrix} t_{\mathrm{V_1}} \\ t_{\mathrm{V_2}} \\ t_{\mathrm{V_0}} \end{pmatrix} &= \boldsymbol{T}_{\mathrm{t_V}}{}^{-1} \begin{pmatrix} u_{\mathrm{s,ref}}^{\alpha_1} T_{\mathrm{sw}} \\ u_{\mathrm{s,ref}}^{\beta_1} T_{\mathrm{sw}} \\ T_{\mathrm{sw}} \end{pmatrix}, \\ &= \frac{T_{\mathrm{sw}}}{\det(\boldsymbol{T}_{\mathrm{t_V}})} \begin{bmatrix} u_{\mathrm{V_2}}^{\beta_1} & -u_{\mathrm{V_2}}^{\alpha_1} & 0 \\ -u_{\mathrm{V_1}}^{\beta_1} & u_{\mathrm{V_1}}^{\alpha_1} & 0 \\ u_{\mathrm{V_1}}^{\beta_1} - u_{\mathrm{V_2}}^{\beta_1} & u_{\mathrm{V_2}}^{\alpha_1} - u_{\mathrm{V_1}}^{\alpha_1} & u_{\mathrm{V_1}}^{\alpha_1} u_{\mathrm{V_2}}^{\beta_1} - u_{\mathrm{V_2}}^{\alpha_1} u_{\mathrm{V_1}}^{\beta_1} \end{bmatrix} \begin{pmatrix} u_{\mathrm{s,ref}}^{\alpha_1} \\ u_{\mathrm{s,ref}}^{\beta_1} \\ 1 \end{pmatrix}. \end{aligned}\right\} \tag{3.7}$$

3.1.1.2 State-of-the-art SVPWM for dual three-phase VSI

A dual three-phase VSI (DT-VSI) comprises two three-phase VSIs as seen in Fig. 3.2(a). The stator neutral points are isolated (i.e. 2N configuration), since the 2N connection has a higher utilization of the DC-link voltage in comparison with 1N connection (see in (2.41) and (2.38) in Section 2.2). Since the phase shift between the two three-phase sets is $\pi/6$, it is possible to project the voltage hexagon of the

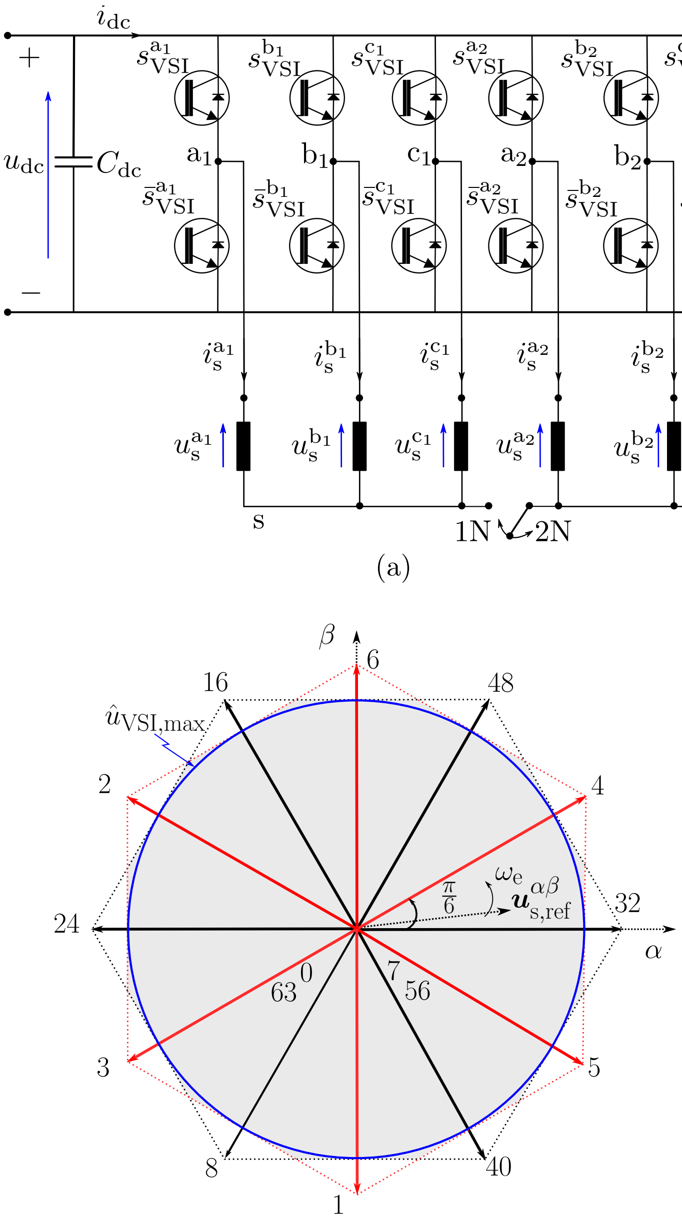

Fig. 3.2. (a) Dual three-phase two-level VSI and (b) the corresponding voltage vectors in the $\alpha\beta$ frame. The shaded area in ▨ is the feasible linear region of maximum magnitude $\hat{u}_{\mathrm{VSI,max}}$.

added three-phase set $a_2b_2c_2$ to that of the $a_1b_1c_1$ in Fig. 3.1(b), which results in Fig. 3.2(b) in the $\alpha\beta$ subspace. Based on the discussion in Section 3.1.1.1, one can deduce:

- The corresponding SVPWM for DT-VSI comprises four dwell times t_{V_1}, t_{V_2}, t_{V_3}, and t_{V_4}; since the 2N connection in Fig. 3.2(a) has four independent control variables (i.e. $i^{\mathrm{a}_1}_{\mathrm{s}}$, $i^{\mathrm{b}_1}_{\mathrm{s}}$, $i^{\mathrm{a}_2}_{\mathrm{s}}$, and $i^{\mathrm{b}_2}_{\mathrm{s}}$ are independent variables, while $i^{\mathrm{c}_1}_{\mathrm{s}} = -i^{\mathrm{a}_1}_{\mathrm{s}} - i^{\mathrm{b}_1}_{\mathrm{s}}$ and $i^{\mathrm{c}_2}_{\mathrm{s}} = -i^{\mathrm{a}_2}_{\mathrm{s}} - i^{\mathrm{b}_2}_{\mathrm{s}}$);
- Each VSI has *independently* 6 switching states. Recall the defined switching vector for DT-VSI as $\boldsymbol{s}^{\mathrm{a}_1\to\mathrm{c}_2}_{\mathrm{VSI}} \overset{(2.26)}{=} (s^{\mathrm{a}_1}_{\mathrm{VSI}}, s^{\mathrm{b}_1}_{\mathrm{VSI}}, s^{\mathrm{c}_1}_{\mathrm{VSI}}, s^{\mathrm{a}_2}_{\mathrm{VSI}}, s^{\mathrm{b}_2}_{\mathrm{VSI}}, s^{\mathrm{c}_2}_{\mathrm{VSI}})^\top$. Based on

Table 3-II. Switching table for the active switching vectors depicted in Fig. 3.2(b)

Vector number	VSI $a_1b_1c_1$	Vector number	VSI $a_2b_2c_2$
8	$(0,\ 0,\ 1,\ 0,\ 0,\ 0)^\top$	1	$(0,\ 0,\ 0,\ 0,\ 0,\ 1)^\top$
16	$(0,\ 1,\ 0,\ 0,\ 0,\ 0)^\top$	2	$(0,\ 0,\ 0,\ 0,\ 1,\ 0)^\top$
24	$(0,\ 1,\ 1,\ 0,\ 0,\ 0)^\top$	3	$(0,\ 0,\ 0,\ 0,\ 1,\ 1)^\top$
32	$(1,\ 0,\ 0,\ 0,\ 0,\ 0)^\top$	4	$(0,\ 0,\ 0,\ 1,\ 0,\ 0)^\top$
40	$(1,\ 0,\ 1,\ 0,\ 0,\ 0)^\top$	5	$(0,\ 0,\ 0,\ 1,\ 0,\ 1)^\top$
48	$(1,\ 1,\ 0,\ 0,\ 0,\ 0)^\top$	6	$(0,\ 0,\ 0,\ 1,\ 1,\ 0)^\top$

the numbering and location of the voltage vectors in Fig. 3.1(b), it is possible to determine the location of the voltage vectors in Fig. 3.2(b) such that the vectors drawn in black line —— represent those of the VSI connected to $a_1b_1c_1$, while the vectors in red line —— represent the vectors of the $a_2b_2c_2$ VSI. The corresponding numbering of the vectors is indicated in Table 3-II. Such vectors are termed the *characteristic* vectors;

- It is possible to formulate a SVPWM scheme for DT-VSI based on 12 sectors compared to only 6 sectors for three-phase VSI;
- There exists four zero voltage vectors, which correspond to the switching vectors 0, 7, 56, and 63 (i.e. in binary form $(0,\ 0,\ 0,\ 0,\ 0)$, $(0,\ 0,\ 1,\ 1,\ 1)$, $(1,\ 1,\ 1,\ 0,\ 0)$, and $(1,\ 1,\ 1,\ 1,\ 1)\big)$.

The complexity of the SVPWM for DT-VSI arises when one realizes the combination of switching states between the two VSIs. A DT-VSI has a total number of $2^6 = 64$ switching vectors. Excluding the four zero vectors means that there exist 60 active voltage vectors for a DT-VSI. Furthermore, the adopted machine with a 2N configuration consists of two active subspaces, namely the torque-producing $\alpha\beta$ subspace and the none torque producing XY subspace. The next step is to identify all voltage vectors and their mapping to the different subspaces.
Following a similar procedure as in (3.1) and (3.2), it is possible to map the different voltage vectors to the $\alpha\beta$ and XY subspaces. Thus, one can write

$$
\left.
\begin{aligned}
\begin{pmatrix} u_{\mathrm{s}}^{\alpha} \\ u_{\mathrm{s}}^{\beta} \\ u_{\mathrm{s}}^{X} \\ u_{\mathrm{s}}^{Y} \\ u_{\mathrm{s}}^{0+} \\ u_{\mathrm{s}}^{0-} \end{pmatrix}
&\overset{(2.8),(2.35)}{=} \boldsymbol{T}_{\mathrm{VSD}} \frac{u_{\mathrm{dc}}}{3}
\begin{bmatrix}
2 & -1 & -1 & 0 & 0 & 0 \\
-1 & 2 & -1 & 0 & 0 & 0 \\
-1 & -1 & 2 & 0 & 0 & 0 \\
0 & 0 & 0 & 2 & -1 & -1 \\
0 & 0 & 0 & -1 & 2 & -1 \\
0 & 0 & 0 & -1 & -1 & 2
\end{bmatrix}
\boldsymbol{s}_{\mathrm{VSI}}^{\mathrm{a}_1\to\mathrm{c}_2}, \\
&= \frac{u_{\mathrm{dc}}}{3}
\begin{bmatrix}
1 & -\frac{1}{2} & -\frac{1}{2} & \frac{\sqrt{3}}{2} & -\frac{\sqrt{3}}{2} & 0 \\
0 & \frac{\sqrt{3}}{2} & -\frac{\sqrt{3}}{2} & \frac{1}{2} & \frac{1}{2} & -1 \\
1 & -\frac{1}{2} & -\frac{1}{2} & -\frac{\sqrt{3}}{2} & \frac{\sqrt{3}}{2} & 0 \\
0 & -\frac{\sqrt{3}}{2} & \frac{\sqrt{3}}{2} & \frac{1}{2} & \frac{1}{2} & -1 \\
0 & 0 & 0 & 0 & 0 & 0 \\
0 & 0 & 0 & 0 & 0 & 0
\end{bmatrix}
\boldsymbol{s}_{\mathrm{VSI}}^{\mathrm{a}_1\to\mathrm{c}_2},
\end{aligned}
\right\}
\tag{3.8}
$$

such that the voltage vectors in the $\alpha\beta$ and XY subspaces with respect to all possible voltage vectors $0 \rightarrow 63$ are shown in Figs. 3.3(a)-(b), where the following is deduced:

- Every voltage vector in the $\alpha\beta$ subspace has a corresponding vector in the XY subspace. Voltage vectors that share the same magnitude are given a particular color in Fig. 3.3(a) and the same color highlights such vectors in Fig. 3.3(b). The larger the magnitude of a voltage vector in the $\alpha\beta$ subspace, the lower the magnitude of the corresponding vector in the XY subspace;

- In the $\alpha\beta$ subspace, the voltage vectors of maximum magnitude (drawn in red line —) do not correspond to any of the characteristic vectors per each VSI in Table 3-II, but to the combinations of switching states between the VSIs. Identifying the vectors of maximum magnitudes in the $\alpha\beta$ subspace is crucial; as such vectors will induce higher currents in the torque-producing $\alpha\beta$ subspace, thus, will accelerate the electromechanical dynamics in comparison with the other voltage vectors of lower magnitude;

- The lowest magnitude switching vectors drawn in blue line — in Fig. 3.3(a) in the $\alpha\beta$ subspace correspond to the vectors of maximum magnitude in the XY subspace. Thus, such vectors discarded from the SVPWM scheme;

- In literature, the definition of a sector for DT-VSI has two possibilities. For a given voltage reference $\boldsymbol{u}_{\mathrm{s,ref}}^{\alpha\beta}$ in the $\alpha\beta$ subspace (see Fig. 3.3(a)), if the sector is defined between two consecutive — vectors (i.e. vectors of maximum magnitudes), then the $\alpha\beta$ subspace would be divided into 12 sectors resulting in the so called 12-sector SVPWM scheme [49]. If the sector is defined between the vectors depicted in red — and green — lines (i.e. vectors of maximum magnitude and the characteristic vectors in Table 3-II), then the 24-sector SVPWM scheme is applied; as the $\alpha\beta$ subspace would be divided into 24 sectors [48, 72, 79]. In Fig. 3.3(a), the first sector for the 12-sector SVPWM (I-12) and the 24-sector SVPWM (I-24) are indicated as previously described. The difference between the 12- and 24-sector SVPWMs is that the latter is simpler to realize from a real-time implementation perspective along with lower VSI switching losses and improved harmonic content of the stator currents [72, 79]. Thus, only the 24-sector SVPWM is discussed further.

As the reference voltage vector $\boldsymbol{u}_{\mathrm{s,ref}}^{\alpha\beta}$ in Fig. 3.3(a) rotates with an angular frequency ω_{e}[1], four active voltage vectors should be selected and four dwell times are computed correspondingly. Moreover, the reference voltage vector $\boldsymbol{u}_{\mathrm{s,ref}}^{XY}$ in the XY subspace contributes to the dwell times; to avoid undesired flow of currents in the XY subspace. In the context of DT drives, all currents which do not contribute to the electromechanical torque production are often termed as *circulating* currents [48, 72, 79].

Similar to (3.6), it is possible to define the voltage-second relation for a DT-VSI as

$$\begin{pmatrix} \boldsymbol{u}_{\mathrm{s,ref}}^{\alpha\beta} \\ \boldsymbol{u}_{\mathrm{s,ref}}^{XY} \\ 1 \end{pmatrix} T_{\mathrm{sw}} = \begin{pmatrix} \boldsymbol{u}_{\mathrm{V}_1}^{\alpha\beta} \\ \boldsymbol{u}_{\mathrm{V}_1}^{XY} \\ 1 \end{pmatrix} t_{\mathrm{V}_1} + \begin{pmatrix} \boldsymbol{u}_{\mathrm{V}_2}^{\alpha\beta} \\ \boldsymbol{u}_{\mathrm{V}_2}^{XY} \\ 1 \end{pmatrix} t_{\mathrm{V}_2} + \begin{pmatrix} \boldsymbol{u}_{\mathrm{V}_3}^{\alpha\beta} \\ \boldsymbol{u}_{\mathrm{V}_3}^{XY} \\ 1 \end{pmatrix} t_{\mathrm{V}_3} + \begin{pmatrix} \boldsymbol{u}_{\mathrm{V}_4}^{\alpha\beta} \\ \boldsymbol{u}_{\mathrm{V}_4}^{XY} \\ 1 \end{pmatrix} t_{\mathrm{V}_4} \begin{pmatrix} \boldsymbol{u}_{\mathrm{V}_0}^{\alpha\beta} \\ \boldsymbol{u}_{\mathrm{V}_0}^{XY} \\ 1 \end{pmatrix} t_{\mathrm{V}_0}, \quad (3.9)$$

---

[1] Direction of rotation is anti-clockwise and is omitted from Fig. 3.3(a) for simplification.

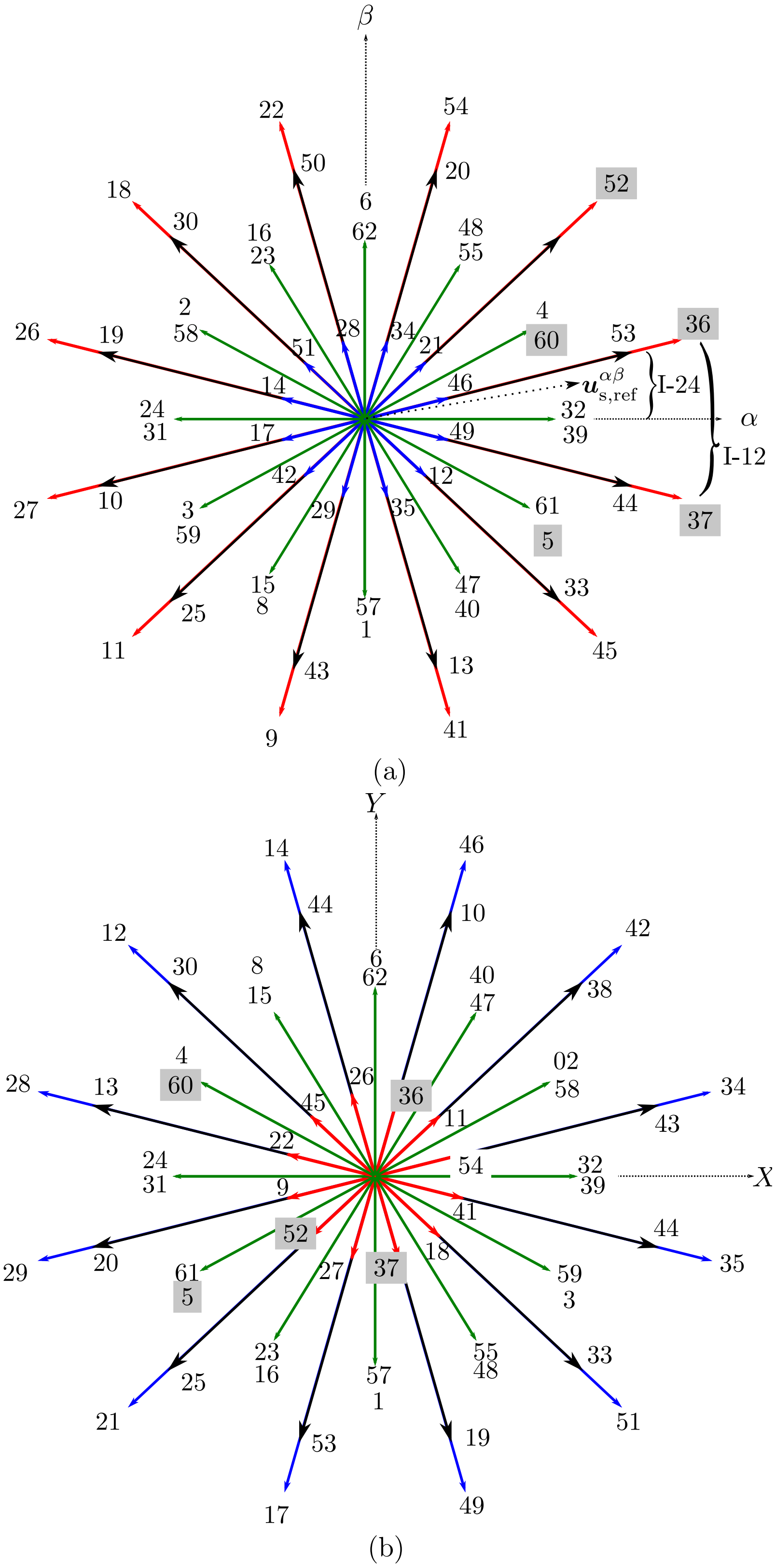

Fig. 3.3. Voltage space vectors in (a) the $\alpha\beta$ plane showing the reference vector $\boldsymbol{u}^{\alpha\beta}_{\mathrm{s,ref}}$ and (b) XY plane. The voltage vectors 0, 7, 56, and 63 are mapped at the origin of the $\alpha\beta$ and XY subspaces. The highlighted vectors (in ▨) are related to the voltage vectors discussed with respect to Fig. 3.5.

which can be expanded similar to (3.6) into

$$\left.\begin{aligned}
\begin{pmatrix} u^{\alpha}_{\mathrm{s,ref}} \\ u^{\beta}_{\mathrm{s,ref}} \\ u^{X}_{\mathrm{s,ref}} \\ u^{Y}_{\mathrm{s,ref}} \\ 1 \end{pmatrix} T_{\mathrm{sw}} &\overset{(3.9)}{=} \underbrace{\begin{bmatrix} u^{\alpha}_{\mathrm{V}_1} & u^{\alpha}_{\mathrm{V}_2} & u^{\alpha}_{\mathrm{V}_3} & u^{\alpha}_{\mathrm{V}_4} & 0 \\ u^{\beta}_{\mathrm{V}_1} & u^{\beta}_{\mathrm{V}_2} & u^{\beta}_{\mathrm{V}_3} & u^{\beta}_{\mathrm{V}_4} & 0 \\ u^{X}_{\mathrm{V}_1} & u^{X}_{\mathrm{V}_2} & u^{X}_{\mathrm{V}_3} & u^{X}_{\mathrm{V}_4} & 0 \\ u^{Y}_{\mathrm{V}_1} & u^{Y}_{\mathrm{V}_2} & u^{Y}_{\mathrm{V}_3} & u^{Y}_{\mathrm{V}_4} & 0 \\ 1 & 1 & 1 & 1 & 1 \end{bmatrix}}_{=:\boldsymbol{T}^{'}_{\mathrm{tV}}} \begin{pmatrix} t_{\mathrm{V}_1} \\ t_{\mathrm{V}_2} \\ t_{\mathrm{V}_3} \\ t_{\mathrm{V}_4} \\ t_{\mathrm{V}_0} \end{pmatrix} \\
\xRightarrow{\text{yielding}} \begin{pmatrix} t_{\mathrm{V}_1} \\ t_{\mathrm{V}_2} \\ t_{\mathrm{V}_3} \\ t_{\mathrm{V}_4} \\ t_{\mathrm{V}_0} \end{pmatrix} &= (\boldsymbol{T}^{'}_{\mathrm{tV}})^{-1} \begin{pmatrix} u^{\alpha}_{\mathrm{s,ref}} \\ u^{\beta}_{\mathrm{s,ref}} \\ u^{X}_{\mathrm{s,ref}} \\ u^{Y}_{\mathrm{s,ref}} \\ 1 \end{pmatrix} T_{\mathrm{sw}},
\end{aligned}\right\} \tag{3.10}$$

where $\boldsymbol{u}^{\mathrm{Z_1Z_2}}_{\mathrm{V_z}} = (u^{\mathrm{Z_1}}_{\mathrm{V_z}}, u^{\mathrm{Z_2}}_{\mathrm{V_z}})$ (in V), represents the projection of the selected voltage vector z in the $\mathrm{Z_1Z_2}$ subspace such that $\mathrm{z} \in \{1, 2, 3, 4\}$ and $\mathrm{Z_1Z_2} \in \{\alpha\beta, \mathrm{XY}\}$. Note that the inverse of the matrix $\boldsymbol{T}^{'}_{\mathrm{tV}}$ always exists similar to the $\boldsymbol{T}_{\mathrm{VSI}}$ in (3.7) [72, 79].

3.1.1.3 Proposed SVPWM

In the previous section, the computation of the dwell times for DT-VSI in (3.10) was derived based on the reference voltages $\boldsymbol{u}^{\alpha\beta}_{\mathrm{s,ref}}$ and $\boldsymbol{u}^{XY}_{\mathrm{s,ref}}$. To finalize the SVPWM scheme, the selection of voltage vectors in each of the 24-sectors in Fig. 3.3(a)-(b) along with the timing sequence (i.e. distribution of the dwell times within every switching period T_{sw}) is elucidated. This thesis employs the 24-sector scheme in [79] with its proposed timing sequence. However, the contribution of this work lies in modifying the the scheme in [79], to minimize the circulating currents (i.e. $\boldsymbol{i}^{XY}_{\mathrm{s}} \to 0\,\mathrm{A}$), and proposing simple real-time implementation strategy. This work was published in [48]

Minimizing circulating current

Recent publications related to SVPWM schemes focused on testing the developed schemes on either induction machines or PM drives with low harmonic content from the rotor side [72, 79]. The XY subspace for those machines is modelled *without* harmonic contributions from the rotor side. This is considered accurate for an induction machine; since its rotor is not equipped with PMs. The employed PMSM in [79] had an exceptionally designed rotor with low harmonic content, approximating the XY model to that of an induction machine. It is possible to further elaborate using the equivalent circuit of the XY subspace in the anti-synchronous frame (i.e. xy subspace) in Fig. 3.4. The equivalent circuit of the ADT-IPMSM is represented by Fig. 3.4(a), while Fig. 3.4(b) is that employed for the induction and PM machine in [49, 72, 79]. In comparison with the ADT-IPMSM at steady state (i.e. $\frac{\mathrm{d}}{\mathrm{d}t}\boldsymbol{i}^{xy}_{\mathrm{s}} = 0$) in Fig. 3.4(a), the current $\boldsymbol{i}^{xy}_{\mathrm{s}}$ would not flow in the equivalent xy circuit shown Fig. 3.4(b) if $\boldsymbol{u}^{xy}_{\mathrm{s}} = 0$. Thus, the reference voltage $\boldsymbol{u}^{xy}_{\mathrm{s,ref}}$ should be set to zero in this case (i.e. $\boldsymbol{u}^{xy}_{\mathrm{s,ref}} = \boldsymbol{u}^{XY}_{\mathrm{s,ref}} = 0$). On the

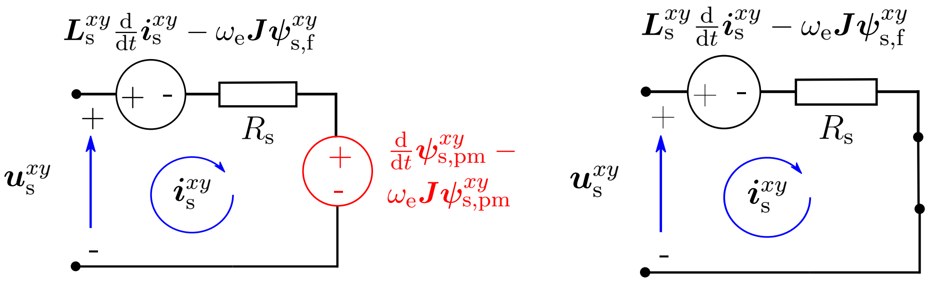

(a) (b)

Fig. 3.4. Equivalent circuits of the xy subspace showing that equivalent to (a) for the employed ADT-IPMSM highlighting in red the model elements related to the PM harmonics (details in Section 2.1.4.2) and (b) represents the equivalent xy circuit for induction and PM machines, as in [49, 72, 79].

other hand, the reference xy voltage $\boldsymbol{u}_{\mathrm{s,ref}}^{xy}$ must not be set to zero (i.e. $\boldsymbol{u}_{\mathrm{s,ref}}^{xy} \overset{!}{\neq} 0$ or $\boldsymbol{u}_{\mathrm{s,ref}}^{XY} \overset{!}{\neq} 0$) for the ADT-IPMSM in Fig. 3.4(a); owing to the presence of harmonic current component and the necessity to compensate for such harmonics. Thus, the proposed SVPWM does not nullify $\boldsymbol{u}_{\mathrm{s,ref}}^{XY}$ in (3.10) [48], unlike [72,79].

Timing sequence and digital realization

Upon computing the dwell times in (3.10), the distribution of the dwell times within a switching period and the selected voltage vectors is considered degrees of freedom [72, 79]. This thesis adopts the timing sequence of the 24-sector SVPWM in [79], where further explanations are presented assuming that the voltage reference $\boldsymbol{u}_{\mathrm{s,ref}}^{\alpha\beta}$ is in sector I $\left(\text{see } \boldsymbol{u}_{\mathrm{s,ref}}^{\alpha\beta} \text{ in sector I-24 in Fig. 3.3(a)}\right)$.
The computed dwell times t_{V_1}, t_{V_2}, t_{V_3}, and t_{V_4} are assigned to the following active vectors (5, 60), 37, 36, 52, where the dwell time t_{V_1} is divided among the vectors 5 and 60 [79]. The selected active vectors are highlighted (in ▭) in Fig. 3.3(a)-(b). The zero vector dwell time is assigned to the zero vector 7. The distribution of the vectors is shown in Fig. 3.5 with the following discussion:

- The selected voltage vectors are symmetrical per half switching period, denoted as T_{s}. Thus, it is sufficient to only mention the switching vectors per half the switching period and the corresponding time diagram would be identified. The switching vectors per sector are given in Table 3-III [79];

- The switching vectors are constant per sector. By decoding each vector number to its binary form it is possible to plot the switching instants ON/OFF per every sector similar to the switching instants in Fig. 3.5;

- Each switching period T_{sw} is divided into 12 portions with 11 instants termed t_{κ}, where $\kappa \in \{1, 2, ..., 11\}$ seen in Fig. 3.5;

- Upon computing the dwell times from (3.10), each dwell time in Fig. 3.5(b) is assigned to the corresponding switching vector in Fig. 3.5(a). Accordingly, the timing assigned to vector 7 $T_7 = t_{\mathrm{V}_0}$, vectors 5 and 60 $T_5 = T_{60} = \frac{t_{\mathrm{V}_1}}{2}$, vector 37 $T_{37} = t_{\mathrm{V}_2}$, vector 36 $T_{36} = t_{\mathrm{V}_3}$, and vector 52 $T_{52} = t_{\mathrm{V}_4}$;

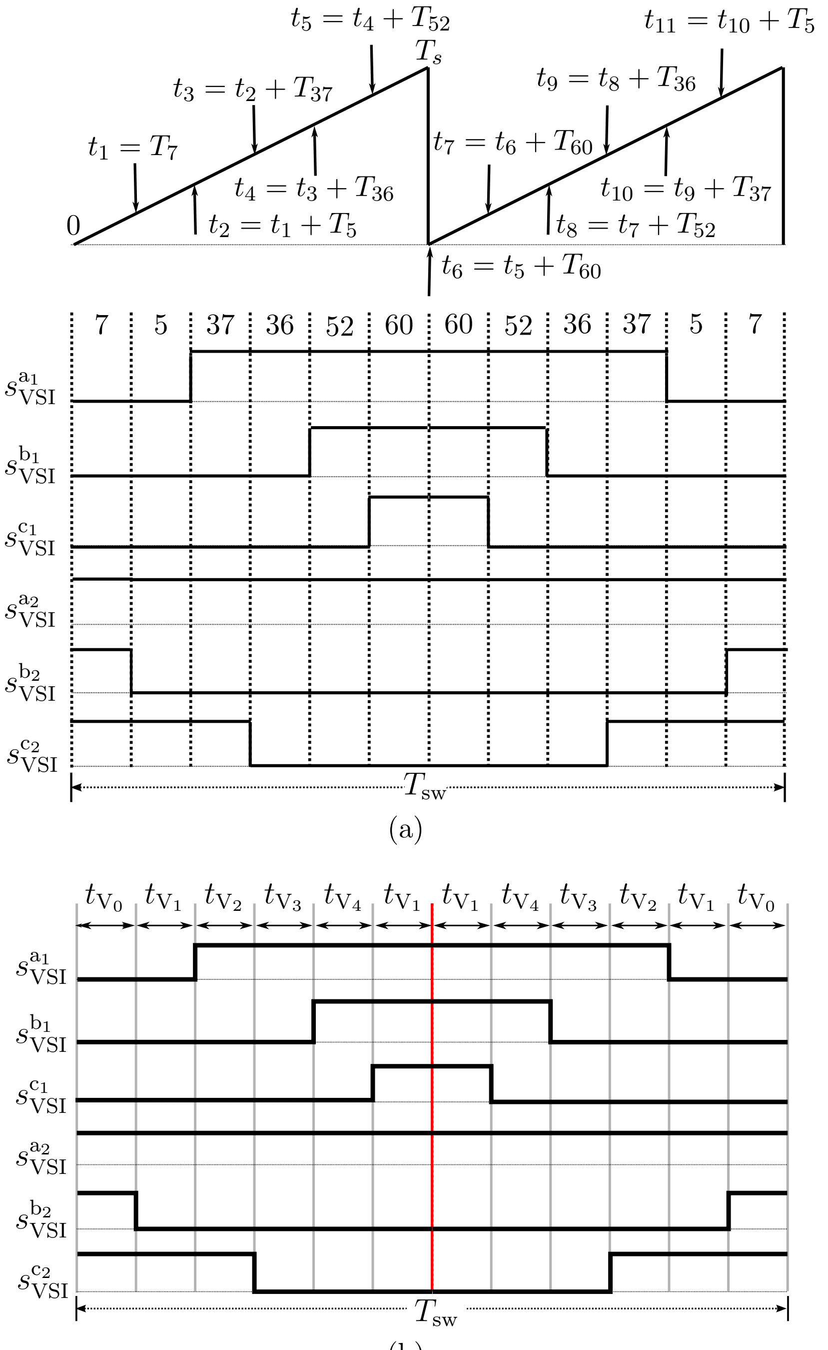

(a)

(b)

Fig. 3.5. Timings distribution in sector I of the employed SVPWM technique, showing (a) the switching instants t_κ, where $\kappa \in \{1, 2, ..., 11\}$ and the switching vectors according to [79], while (b) shows the computed dwell times assigned to the corresponding switching vector in (a).

- Upon computing the dwell times, assigning them to the active vectors $\big($see Fig. 3.5(b)$\big)$, and drawing the switching instants, it is possible to implement in real time system the ON/OFF instants for every element in the switching vector $\boldsymbol{s}_{\mathrm{VSI}}^{\mathrm{a_1 \to c_2}}$. For example, starting from the beginning of the switching period T_{sw}, the switching state $s_{\mathrm{VSI}}^{\mathrm{a_1}}$ in sector I is OFF (i.e. $s_{\mathrm{VSI}}^{\mathrm{a_1}} = 0$). When reaching the instant t_2, then $s_{\mathrm{VSI}}^{\mathrm{a_1}}$ is toggled to ON till reaching instant t_{10}, where its

Table 3-III. Switching table for the 24-sector SVPWM showing the switching vectors within half the switching period T_{sw} for every sector [79].

Sector number	Switching sequence	Sector number	Switching sequence
I	7-5-37-36-52-60	XIII	56-58-26-27-11-3
II	7-39-37-36-52-48	XIV	56-24-26-27-11-15
III	0-32-36-52-54-27	XV	63-31-27-11-9-8
IV	0-4-36-52-54-62	XVI	63-59-27-11-9-1
V	56-60-52-54-22-6	XVII	7-3-11-9-41-57
VI	56-48-52-54-22-23	XVIII	7-15-11-9-41-40
VII	63-55-54-22-18-16	XIX	0-8-9-41-45-47
VIII	63-62-54-22-18-2	XX	0-1-9-41-45-61
IX	7-6-22-18-26-58	XXI	56-57-41-45-37-5
X	7-23-22-18-26-24	XXII	56-40-41-45-37-39
XI	0-16-18-26-27-31	XXIII	63-47-45-37-36-32
XII	0-2-18-26-27-59	XXIV	63-61-45-37-36-4

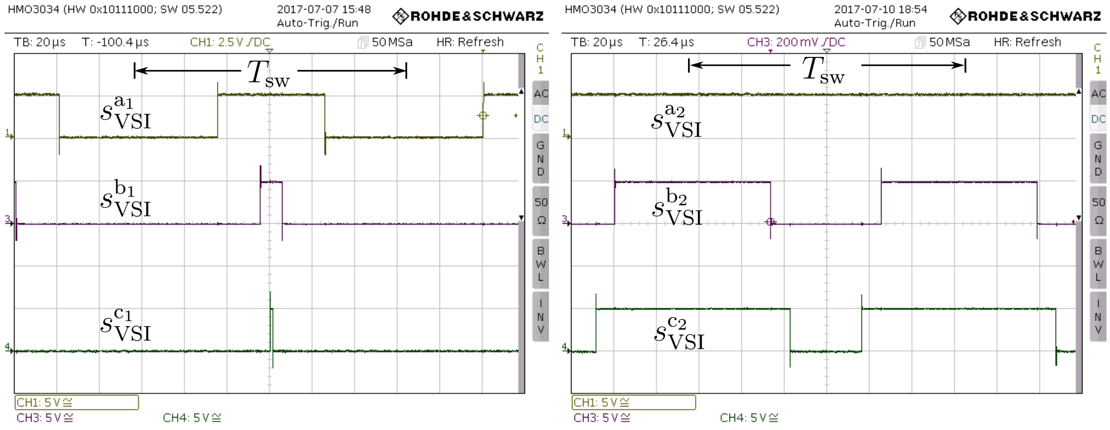

(a) (b)

Fig. 3.6. Experimental results similar to the given example in Fig. 3.5 showing the switching states (a) $s_{\mathrm{VSI}}^{\mathrm{a}_1}$, $s_{\mathrm{VSI}}^{\mathrm{b}_1}$, $s_{\mathrm{VSI}}^{\mathrm{c}_1}$, (b) $s_{\mathrm{VSI}}^{\mathrm{a}_2}$, $s_{\mathrm{VSI}}^{\mathrm{b}_2}$, and $s_{\mathrm{VSI}}^{\mathrm{c}_2}$ for a voltage reference $\boldsymbol{u}_{\mathrm{s,ref}}^{\alpha\beta}$ in sector I.

state is switched OFF.

Experimental validations

The experimental results showing the switching vector $\boldsymbol{s}_{\mathrm{VSI}}^{\mathrm{a}_1\rightarrow\mathrm{c}_2}$ for a voltage reference $\boldsymbol{u}_{\mathrm{s,ref}}^{\alpha\beta}$ in sector I are shown in Fig. 3.6. It is worth to mention that the proposed realization scheme based on the switching instants is compatible with other types of SVPWM. Fig. 3.7(a) shows another 24-sector SVPWM proposed in [72], where all switching states toggle their state within a switching period T_{sw}, in comparison with that in Fig. 3.5, where one of switching states does not toggle its state within a switching period $\big($see $s_{\mathrm{VSI}}^{\mathrm{a}_2}$ in Figs. 3.5(a)-(b)$\big)$. Also, Fig. 3.7(b) shows an example of the 12-sector SVPWM in [49], which is more complex than the 24-sector SVPWM; since the switching waveforms are not symmetrical around half the switching period T_{s}. Using the same realization scheme per every instant t_κ where

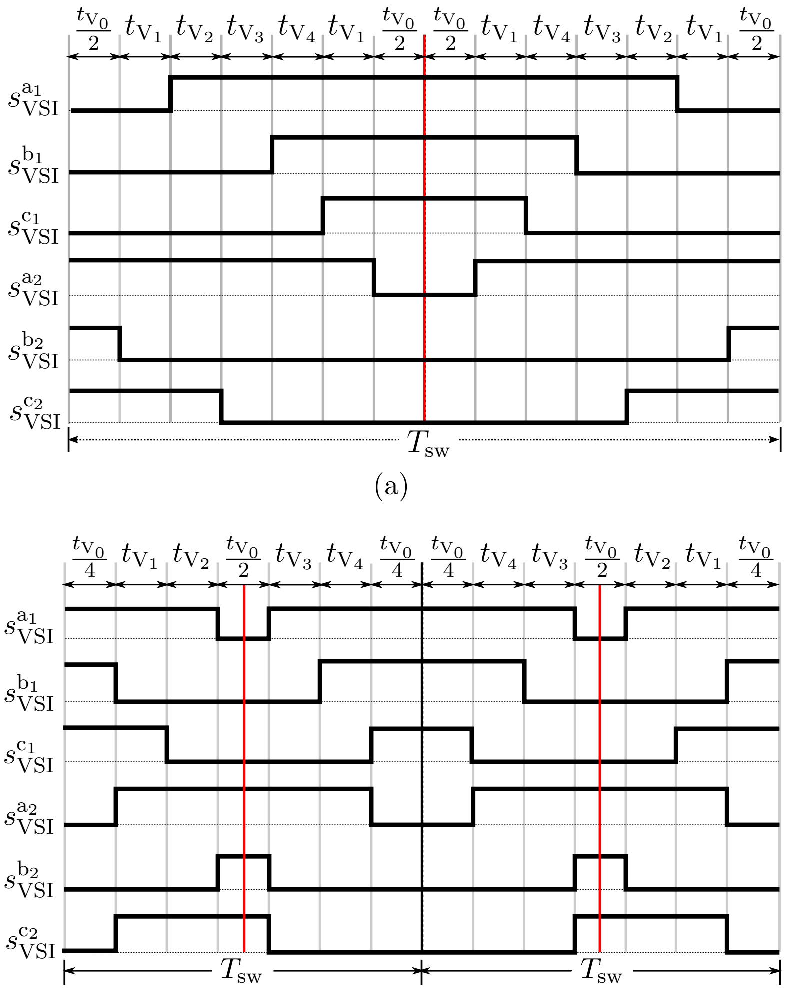

(a)

(b)

Fig. 3.7. Example of the switching patterns in sector I for (a) the 24-sector SVPWM in [72], and (c) 12-sector SVPWM in [49] for a given $\boldsymbol{u}_{\mathrm{s,ref}}^{\alpha\beta}$ along with their corresponding dwell times.

$\kappa \in \{1, 2, ..., 11\}$, the corresponding experimental results are shown in Figs. 3.8(a)-(b) for such 24-sector SVPWM, while Figs. 3.8(c)-(d) show the corresponding states for the 12-sector SVPWM. To conclude, the proposed SVPWM realization scheme is compatible with the SVPWM techniques available in literature.

Fig. 3.9 shows the experimental results on the stator currents upon employing the 24-sector SVPWM similar to that in Fig. 3.5. To be able to implement in real-time the proposed realization scheme, the dSPACE real-time controller was flashed and programmed with the digital waveform output (DWO) programming language available from dSPACE® [80], which is a low-level programming language and to high extent similar to the programming language Assembly.

In this test, the ADT-IPMSM is rotated at a constant speed of 500 rpm at rated torque, where $||\boldsymbol{i}_{\mathrm{s}}^{\alpha\beta}|| = \hat{i}_{\mathrm{s,rated}}$ (recall ADT-IPMSM parameters in Table 2-I). The presence of 5th and 7th harmonics in the XY subspace makes it insufficient to control the $\boldsymbol{i}_{\mathrm{s}}^{XY}$ by just setting $\boldsymbol{u}_{\mathrm{s,ref}}^{XY} = 0$ as in [72, 79]. This is evident in Fig. 3.9(a), which shows the presence of $\boldsymbol{i}_{\mathrm{s}}^{XY}$ and correspondingly highly distorted stator currents (see

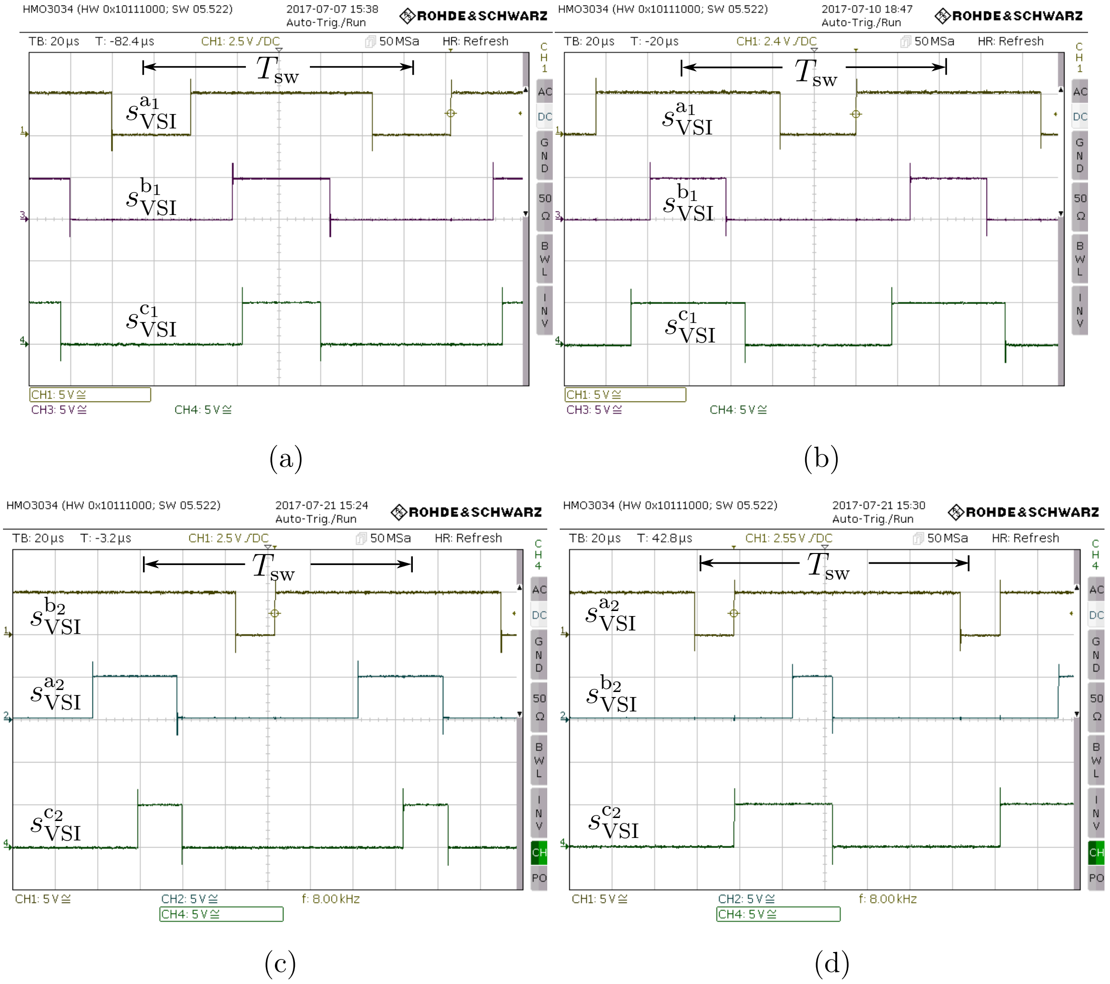

(a) (b)

(c) (d)

Fig. 3.8. Switching states to validate the proposed realization scheme for other SVPWM methods: (a), (b) the 24-sector SVPWM in [72], and (c), (d) for the 12-sector SVPWM in [49].

Fig. 3.9(b)). Analyzing the stator currents by means of FFT shows substantial 5th and 7th harmonic content, resulting in a total harmonic distortion of THD $= 16.32\%$. Upon considering the effect of compensating the XY current components via setting $\boldsymbol{u}_{\text{s,ref}}^{XY} \neq 0$, the XY current vector $\boldsymbol{i}_{\text{s}}^{XY}$ is nullified at steady state as seen in 3.9(b). Moreover, the stator currents waveforms are improved in Figs. 3.9(d), where the corresponding harmonic analysis in 3.9(e) indicates a significant improvement with a recorded THD $= 1.69\%$.

3.1.2 Carrier-based PWM

During healthy operation, the illustrated SVPWM technique in Section 3.1.1 ensures high quality stator currents $\boldsymbol{i}_{\text{s}}^{a_1 \to c_2}$ with low harmonic content in comparison with other SVPWM schemes available in literature [49,72,79]. In the post-fault operation, it is still possible to implement a modified SVPWM based on the active voltage vectors, which are related to the remaining healthy phases [81]. Given that there are 156 possible combinations of phases before operating as a single machine, this would require implementing and storing 156 modified SVPWM strategies, where the

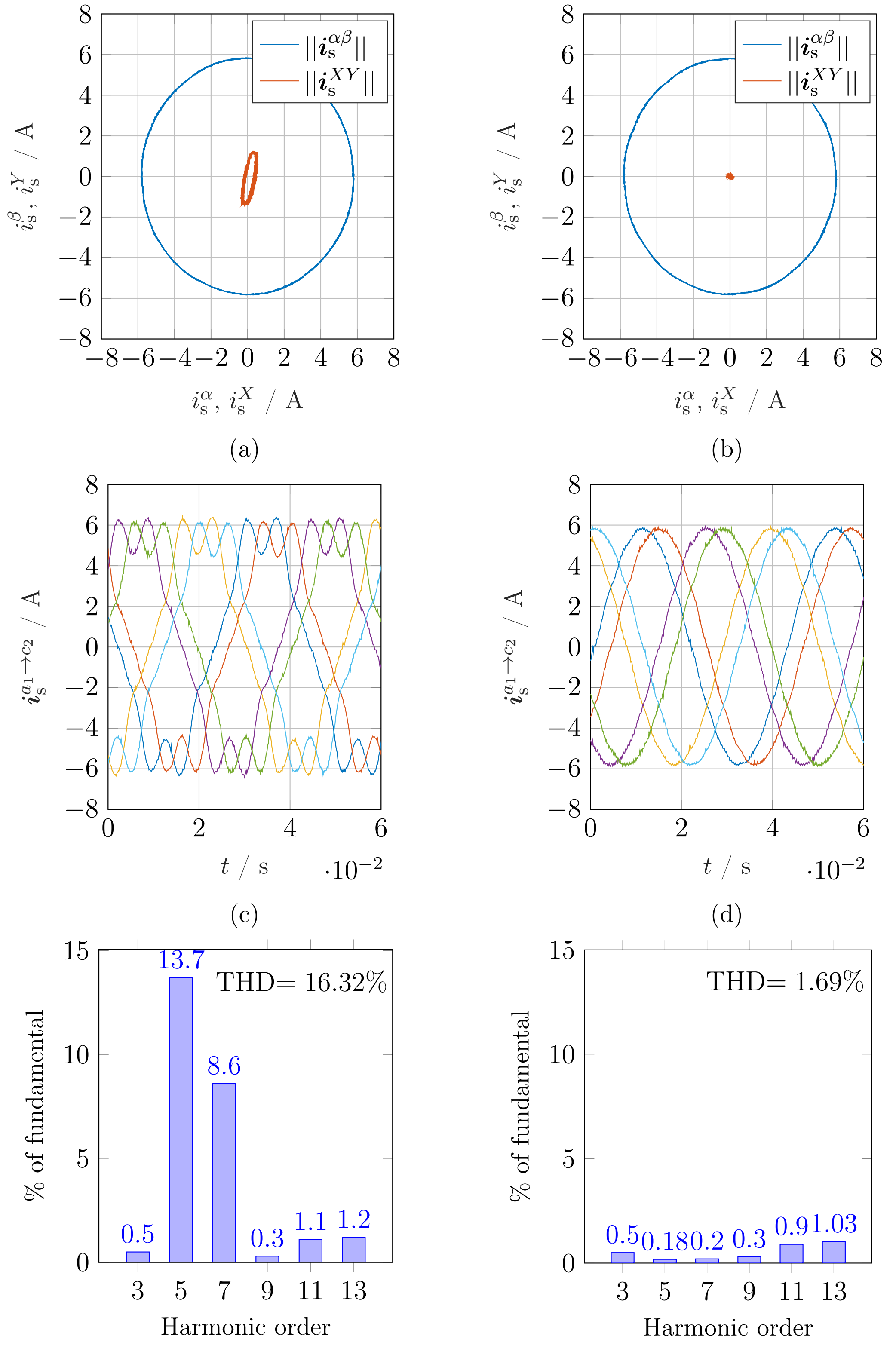

(a) (b) (c) (d) (e) (f)

Fig. 3.9. Effect of discarding and accounting for $\boldsymbol{u}_{\mathrm{s,ref}}^{XY}$ within the SVPWM dwell times in (3.10), showing the corresponding effect on {(a),(b)} the current loci in the $\alpha\beta$ and XY planes, {(c),(d)} the stator currents, and {(e),(f)} the corresponding FFT for each case.

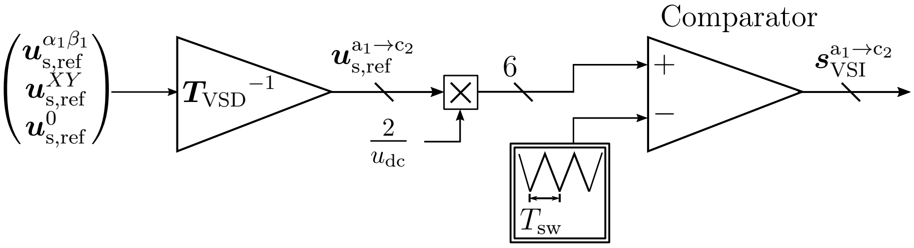

Fig. 3.10. Block diagram of the implemented sinusoidal PWM, which is employed in the post-fault operation subspace control system, where the references are computed as explained in section 4.3.

corresponding SVPWM would be triggered based on the available healthy phases. On the other hand, sinusoidal carrier-based PWM - as in three-phase drives - would be the simplest PWM technique to dispatch the required reference voltage, with a compromise between easy implementation and acceptable performance. Fig. 3.10 shows the block diagram for transferring the calculated reference voltages of the different subspaces to meaningful switching states $\boldsymbol{s}_{\mathrm{VSI}}^{\mathrm{a_1\to c_2}}$ sent to the inverter gate drivers.

3.2 Torque maps and minimum loss operation

3.2.1 Torque maps

For AWES, the flying path is tracked by the kite, while the drive is either speed controlled [23] or torque controlled [27,82], with the later being more common among industrial partners. Up till now, none of the available AWE concepts have proven viability, where the currently employed concepts use over-rated drives, such that both the reeling-in and out speeds would be less than the drive rated speed. In other words, over-speeding control strategies for drives (i.e. field-weakening (FW)) are not utilised so as to simplify the drive control structure. Such operating procedure (i.e. torque controlled drive of rated speed higher than the reeling-in speed) motivates the need for optimal controller design, that would ensure precise electromechanical torque production as demanded and minimize the stator electrical copper losses[2]. Recall from (2.10) that $m_{\mathrm{e}} = 3n_{\mathrm{p}}\boldsymbol{i}_{\mathrm{s}}^{dq\top}\boldsymbol{J}\boldsymbol{\psi}_{\mathrm{s}}^{dq}$. Taking the non-linearity of $\boldsymbol{\psi}_{\mathrm{s}}^{dq}$ into account within $||\boldsymbol{i}_{\mathrm{s}}^{dq}|| \leq \hat{i}_{\mathrm{s,rated}}$ generates the so called *torque map* [47]. These maps take the effect of saturation and machine non-linearity into account, giving a graphical representation between m_{e} and $\boldsymbol{i}_{\mathrm{s}}^{dq}$. Fig. 3.11 shows the torque map in black line —— in the motor quadrant in the interval $-\hat{i}_{\mathrm{s,rated}} \leq i_{\mathrm{s}}^{d} \leq 0$ and $0 \leq i_{\mathrm{s}}^{q} \leq \hat{i}_{\mathrm{s,rated}})$. For every torque parabola in Fig. 3.11, finding the minimum $||\boldsymbol{i}_{\mathrm{s}}^{dq}||$ per every m_{e} parabola and connecting those loci together leads to the so call maxmimum-torque-per-current loci (MTPC). Such MTPA loci are saved to the AWE drive controller as a look-up-table (LUT) to ensure minimum copper losses throughout the entire reeling-in and out ranges.

---

[2] The electrical losses of a machine are divided between the stator copper losses and iron losses, where the later should be considered if the machine angular speed would be in the proximity of 10000 RPM or higher [58].

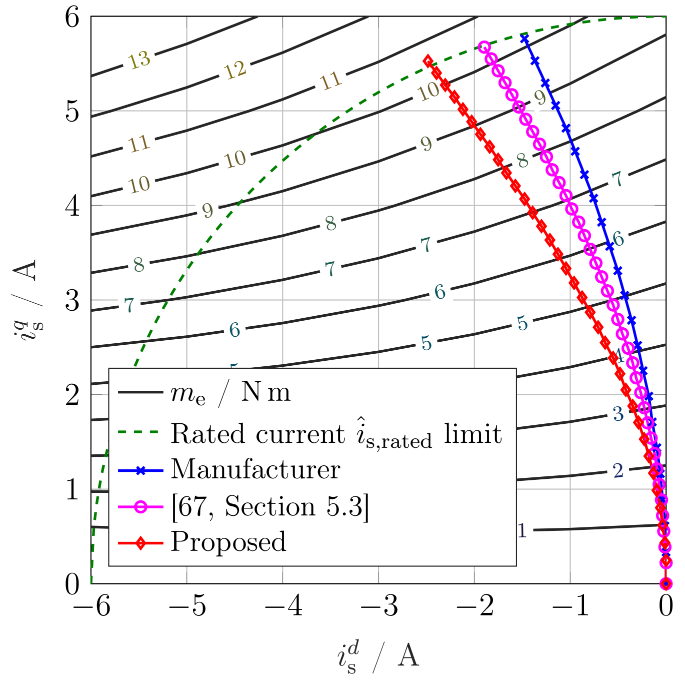

Fig. 3.11. MTPC current loci for the different torque computation methods and their intersection with the torque parabolas using the non-linear flux linkage $\boldsymbol{\psi}_\mathrm{s}^{dq}$.

Table 3-IV. Machine inductances provided by the manufacturer and recent literature [67].

Parameter	Value
Permanent magnet flux linkage constant $\psi_\mathrm{pm}{}^*$	0.178 Wb
Nominal d-axis inductance*	2 mH
Nominal q-axis inductance*	11.5 mH
Computed d-axis inductance $\bar{\bar{L}}_\mathrm{s}^{d**}$	6.7 mH
Computed q-axis inductance $\bar{\bar{L}}_\mathrm{s}^{q**}$	20 mH

[*] Half the manufacturer's value of the original three-phase machine due to halving the number of turns when carrying-out the rewinding to the dual three-phase machine.
[**] Computed as shown in [67, Section 5.3].

If the ADT-IPMSM is assumed to be linear, the torque equation can be expressed as

$$m_\mathrm{e,lin} = 3n_\mathrm{p}(\psi_\mathrm{pm} i_\mathrm{s}^q + (L_\mathrm{s,lin}^d - L_\mathrm{s,lin}^q) i_\mathrm{s}^d i_\mathrm{s}^q), \tag{3.11}$$

where the ψ_pm, $L_\mathrm{s,lin}^d$ and $L_\mathrm{s,lin}^q$ are substituted with the parameters provided by the manufacturer and recent literature [67] (see Table 3-IV). To emphasize the importance of using a non-linear model for $\boldsymbol{\psi}_\mathrm{s}^{dq}$ and correspondingly m_e, Fig. 3.12 shows a comparison between the torques with linear and non-linear assumptions invoked at $\boldsymbol{i}_\mathrm{s,ref}^{dq} = (-3.78\,\mathrm{A}, -3.78\,\mathrm{A})$. Comparing the experimentally measured torque for the test in Fig. 3.12 with the expected torque using the non-linear flux linkages $\boldsymbol{\psi}_\mathrm{s}^{dq}$ in Figs. 3.11(a)-(b) and the torques computed using the parameters in Table 3-IV highlights the superiority of the non-linear considerations in terms of coin-

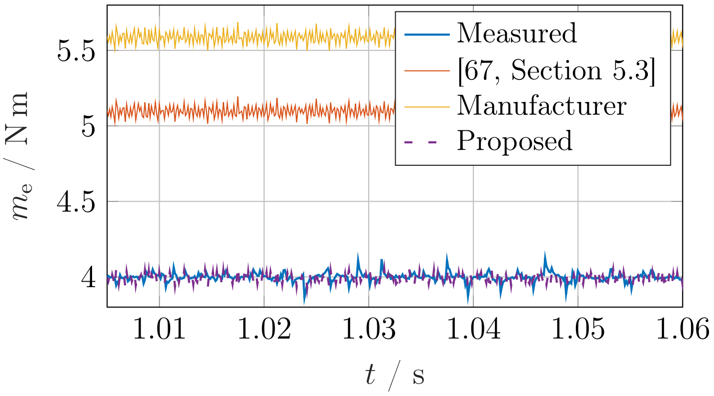

Fig. 3.12. Comparison at $\boldsymbol{i}_{\mathrm{s,ref}}^{dq} = (-3.78\,\mathrm{A}, -3.78\,\mathrm{A})$ between the electromechanical torques computed using the parameters acquired by different methods and the measured one. Note that the lines —— and - - - are overlapping.

ciding with the actual electromechanical torque. Using (3.11) the torque map is computed for the linear case, using the parameters given by the supplier or computed using [67, Section 5.3]. Plotting the difference between the measured torque and computed torques maps, the outcomes are shown in Figs. 3.13(a)-(c), indicating that the proposed method produces the minimal error, with respect to the measured torque, compared to those computed assuming a linear flux linkage $\boldsymbol{\psi}_{\mathrm{s}}^{dq}$ variation. The errors in Fig. 3.13(a)-(b) tend to increase and vary as the operating point is not in the vicinity of the origin point; since the effect of saturation and coupling between the dq coordinates starts to prevail. It should be noted that the error between the proposed method and the measured electromechanical torque in Fig. 3.13(c) is not perfectly zero; since the acquired flux linkage maps in Fig. 2.11(a)-(b) has undergone some off-line smoothing leading to numerical errors. Furthermore, practical compensation of the effect of torque losses during measurements acquisition is not perfect over the entire speed range. Nevertheless, the acquired results are acceptable.

3.2.2 Stator copper losses minimization

In terms of power losses with respect to linear systems, using the torque maps computed using (3.11) with the parameters given by manufacturer and [67, Section 5.3], the MTPC loci for torque maps of the linear case are depicted in Fig. 3.11) as blue —— and magneta —— lines, respectively. Comparing the MTPC loci reveals the presence of discrepancy between the different MTPC loci in Fig. 3.11. Such discrepancies in MTPC loci grow as $m_{\mathrm{e,ref}}$ increases (i.e. flux saturation prevails), which will eventually affect the generated stator copper losses. Assuming at *steady-state* that $\boldsymbol{i}_{\mathrm{s}}^{xy} = 0$ for the 2N connection or both $\boldsymbol{i}_{\mathrm{s}}^{xy} = \boldsymbol{i}_{\mathrm{s}}^{0} = 0$ for the 1N connection, and defining the stator copper losses as

$$P_{\mathrm{Cu}} := 3R_{\mathrm{s}}\,||\boldsymbol{i}_{\mathrm{s}}^{dq}||^2. \tag{3.12}$$

Fig. 3.14 shows the percentage of errors between the stator copper losses $\Delta P_{\mathrm{Cu}}\%$ produced by the MTPC loci, obtained by the manufacturer's and [67, Section 5.3] parameters, and the non-linear flux linkage maps. It is clear that the proposed

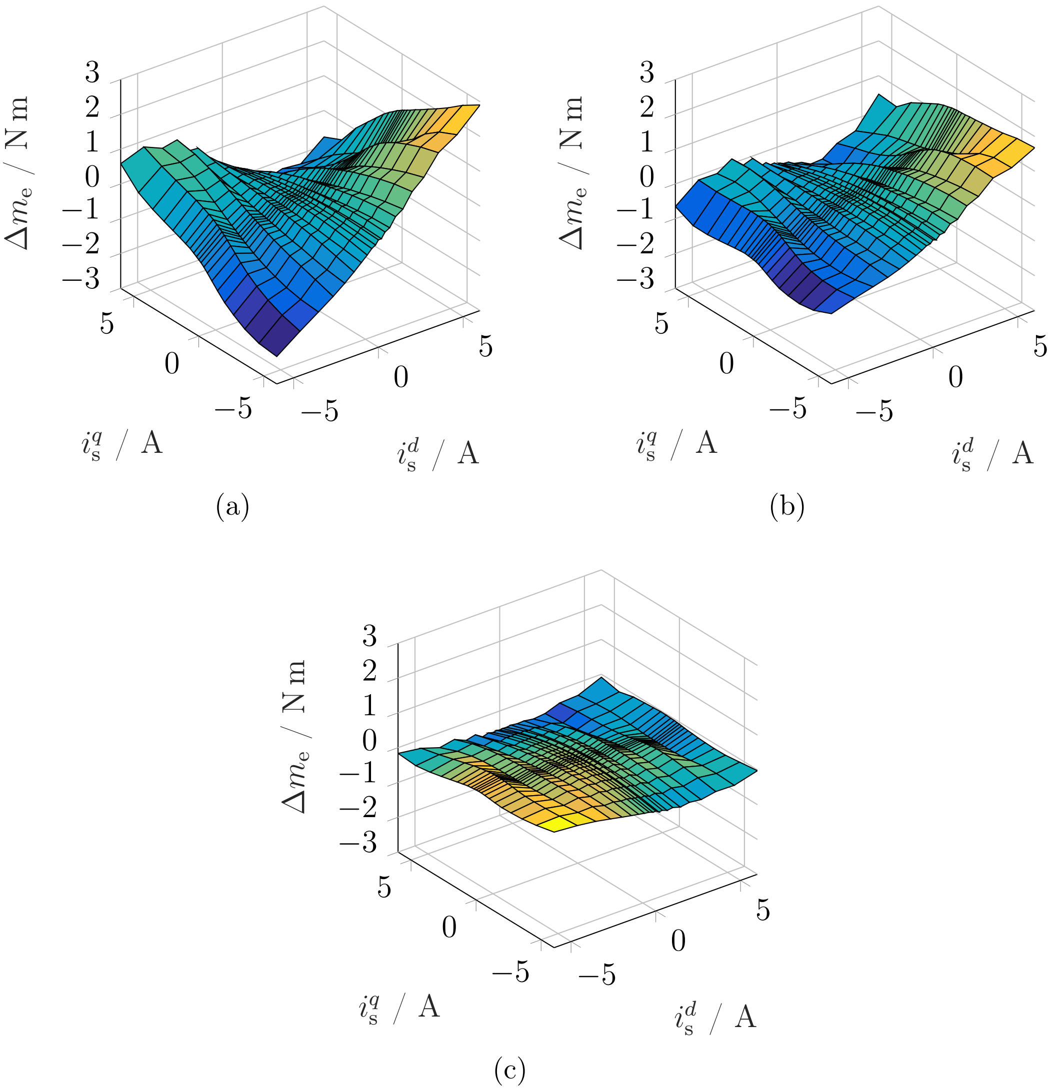

Fig. 3.13. Error between the measured electromechanical torque and the computed one using the parameters provided by (a) the manufacturer, (b) [67, Section 5.3], and (c) the non-linear flux linkage maps.

method has recorded the lowest level of stator losses in comparison with the other techniques of linear machine. Thus, the effectiveness of the proposed method for torque production and losses minimization is verified.

3.3 Stator current controller

3.3.1 Fundamental current controllers

The control structure for ADT-IPMSMs utilized in Fig. 2.3 is similar to that in [64,66,83] in terms of the invoked assumptions, that the PI controllers in the dq and xy subspaces deal with the fundamental component (see $\boldsymbol{u}_{\mathrm{PI}}^{dq}$ and $\boldsymbol{u}_{\mathrm{PI}}^{xy}$ in Fig. 2.3), while the R controllers deal solely with the harmonic current components (see $\boldsymbol{u}_{\mathrm{R}}^{dq}$ and $\boldsymbol{u}_{\mathrm{R}}^{xy}$ in Fig. 2.3). Based on the computed differential inductances $\boldsymbol{L}_{\mathrm{s}}^{dq}$ and $\boldsymbol{L}_{\mathrm{s}}^{xy}$

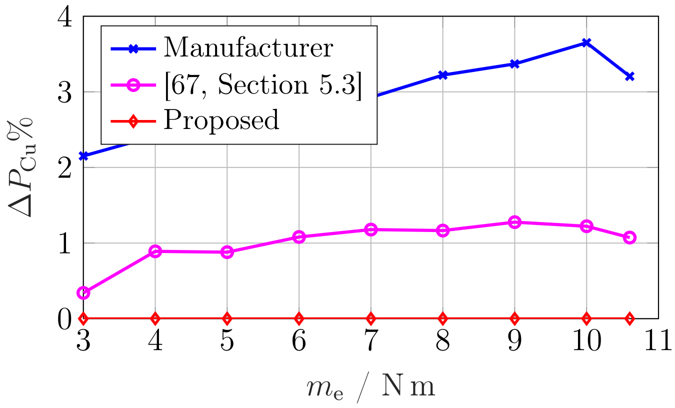

Fig. 3.14. Comparison of $\Delta P_{\mathrm{Cu}}\%$ computed with the parameters of the different methods with respect to the losses computed when adopting the non-linear flux linkage maps.

(see Fig. 2.6 and Fig. 2.8), it is possible to retune the PI and R controllers gains to adapt per operating point to the machine non-linear behaviour and thus ensure fast tracking. By defining the transfer function of a PI controller as

$$G_{\mathrm{PI}}(s) = V_{\mathrm{p}}(1 + \frac{1}{T_{\mathrm{i}}\, s}), \tag{3.13}$$

where the controller gain V_{p} (in Ω) and time constant T_{i} (in s) in the dq and xy subspaces are selected based on the magnitude-optimum criterion along with updating the PI controller according to $\boldsymbol{i}_{\mathrm{s}}^{dq}$ and $\boldsymbol{i}_{\mathrm{s}}^{xy}$, respectively, similar to [68, 76]. Accordingly, the PI controllers in the dq and xy subspaces is expressed as [51]

$$\left.\begin{aligned} \left(V_{\mathrm{p}}^{d},\ V_{\mathrm{p}}^{q},\ V_{\mathrm{p}}^{x},\ V_{\mathrm{p}}^{y}\right) &= \frac{1}{2T_{\mathrm{sw}}}\left(\hat{L}_{\mathrm{s}}^{d},\ \hat{L}_{\mathrm{s}}^{q},\ \hat{L}_{\mathrm{s}}^{x},\ \hat{L}_{\mathrm{s}}^{y}\right), \\ \left(T_{\mathrm{i}}^{d},\ T_{\mathrm{i}}^{q},\ T_{\mathrm{i}}^{x},\ T_{\mathrm{i}}^{y}\right) &= \frac{1}{R_{\mathrm{s}}}\left(\hat{L}_{\mathrm{s}}^{d},\ \hat{L}_{\mathrm{s}}^{q},\ \hat{L}_{\mathrm{s}}^{x},\ \hat{L}_{\mathrm{s}}^{y}\right), \end{aligned}\right\} \tag{3.14}$$

where

$$\left.\begin{aligned} \left(\hat{L}_{\mathrm{s}}^{d},\ \hat{L}_{\mathrm{s}}^{q}\right) &= \det\left(\boldsymbol{L}_{\mathrm{s}}^{dq}\right)\left(\frac{1}{L_{\mathrm{s}}^{q}},\ \frac{1}{L_{\mathrm{s}}^{d}}\right), \\ \left(\hat{L}_{\mathrm{s}}^{x},\ \hat{L}_{\mathrm{s}}^{y}\right) &= \det\left(\boldsymbol{L}_{\mathrm{s}}^{xy}\right)\left(\frac{1}{L_{\mathrm{s}}^{y}},\ \frac{1}{L_{\mathrm{s}}^{x}}\right). \end{aligned}\right\} \tag{3.15}$$

In [68], the disturbance feedforward compensation enhances the tracking speed of the PI controllers. The disturbance voltage $\boldsymbol{u}_{\mathrm{s,dist}}^{dq}$ encompasses the coupling terms between the dq frame coordinates, assuming the machine parameters are identified, which is the case here upon computing $\boldsymbol{\psi}_{\mathrm{s}}^{dq}$ and $\boldsymbol{L}_{\mathrm{s}}^{dq}(\boldsymbol{i}_{\mathrm{s}}^{dq})$. As proven in [68], $\boldsymbol{u}_{\mathrm{s,dist}}^{dq}$ is computed by

$$\boldsymbol{u}_{\mathrm{s,dist}}^{dq} = -L_{\mathrm{m}}^{dq}\begin{bmatrix} 0 & \dfrac{1}{\hat{L}_{\mathrm{s}}^{q}} \\ \dfrac{1}{\hat{L}_{\mathrm{s}}^{d}} & 0 \end{bmatrix}\left(\boldsymbol{u}_{\mathrm{s}}^{dq} - R_{\mathrm{s}}\,\boldsymbol{i}_{\mathrm{s}}^{dq} - \omega_{\mathrm{e}}\,\boldsymbol{J}\boldsymbol{\psi}_{\mathrm{s}}^{dq}\right) - \omega_{\mathrm{e}}\,\boldsymbol{J}\boldsymbol{\psi}_{\mathrm{s}}^{dq}. \tag{3.16}$$

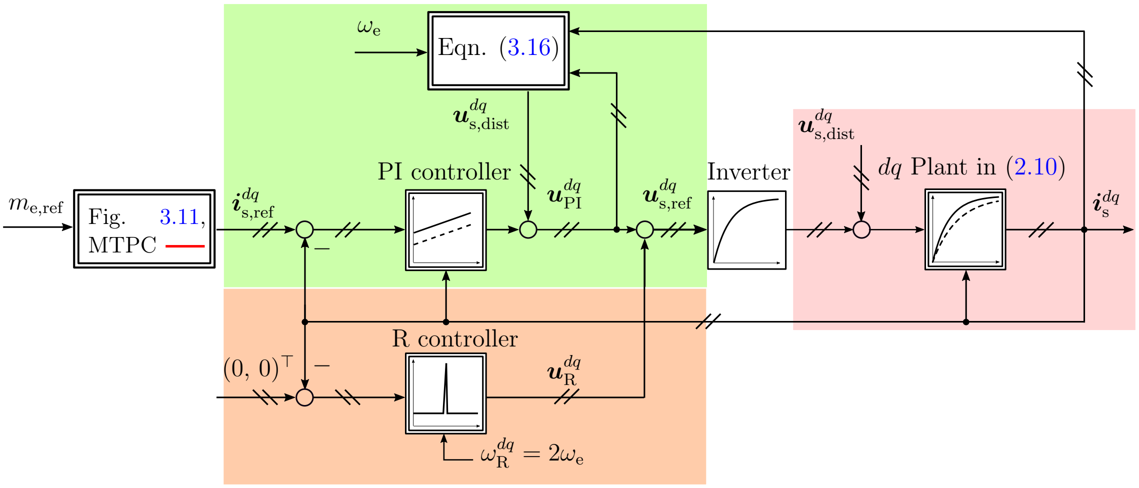

Fig. 3.15. Block diagram of the dq subspace control system, highlighting (in 🟩) the non-linear PI controller with the feedforward compensation, (in 🟧) the resonant controller with the designated resonant frequencies, and (in 🟥) the plant with variable parameters owing to the non-linear flux linkage maps in Figs. 2.5(a)-(b).

Similarly, the coupling between the xy subspaces can be decoupled using a similar approach as in (3.16) leading to

$$\boldsymbol{u}^{xy}_{\mathrm{s,dist}} = -L^{xy}_{m} \begin{bmatrix} 0 & \dfrac{1}{\hat{L}^{y}_{\mathrm{s}}} \\ \dfrac{1}{\hat{L}^{x}_{\mathrm{s}}} & 0 \end{bmatrix} \left(\boldsymbol{u}^{xy}_{\mathrm{s}} - R_{\mathrm{s}}\, \boldsymbol{i}^{xy}_{\mathrm{s}} - \omega_{\mathrm{e}}\, \boldsymbol{J} \boldsymbol{\psi}^{xy}_{\mathrm{s}}\right) + \omega_{\mathrm{e}}\, \boldsymbol{J} \boldsymbol{\psi}^{xy}_{\mathrm{s}}. \tag{3.17}$$

From (3.14)-(3.17), the non-linear dq and xy PI controllers are realized, where both $\boldsymbol{u}^{dq}_{\mathrm{s,dist}}$ and $\boldsymbol{u}^{xy}_{\mathrm{s,dist}}$ are taken into account as shown in the closed loop PI controller blocks in Figs. 3.15 and 3.16 for the dq and xy subspaces, respectively. Note that for the xy subspace in Fig. 3.16, an additional disturbance component $\frac{\mathrm{d}}{\mathrm{d}t}\boldsymbol{\psi}^{xy}_{\mathrm{s,pm}}$ was added; to show the contribution of the PM 6th harmonic to the xy subspace, which represents the 5th and 7th in the statioray XY subspace (see details in Section 2.1.4.2).

3.3.2 Harmonic current controllers

The presence of undesired harmonics per subspace contributes to significant torque ripples and acoustic noise as well as additional copper losses. This infers the necessity of employing R controllers to mitigate such effect. To ensure a zero steady-state error per subspace, the digital R controller must be carefully implemented [84]. The continuous R controller transfer function is

$$G_{\mathrm{R}}(s) = T_{\mathrm{R}} \frac{s}{s^2 + {\omega_{\mathrm{R}}}^2}, \tag{3.18}$$

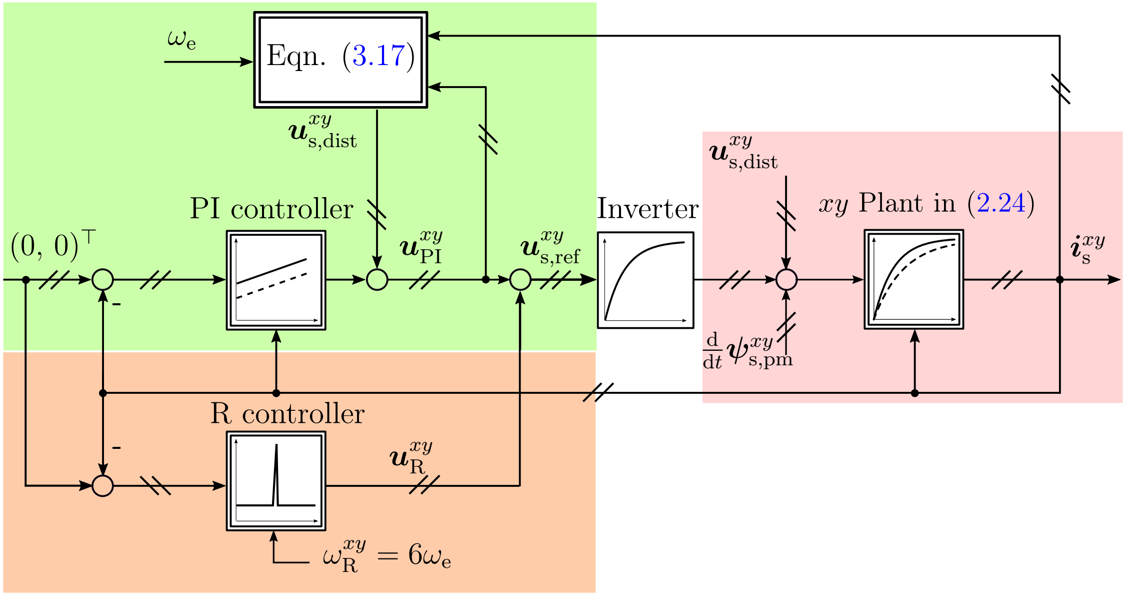

Fig. 3.16. Block diagram of the xy subspace control system, highlighting (in 🟩) the non-linear PI controller with the feedforward compensation, (in 🟧) the resonant controller with the designated resonant frequencies, and (in 🟥) the plant with variable parameters owing to the non-linear flux linkage maps in Figs. 2.7(a)-(b).

where T_{R} (in s) is the resonant controller time constant and ω_{R} (in rad/s) is the controller resonant angular frequency such that

$$\omega_{\mathrm{R}} = h\,\omega_{\mathrm{e}}, \text{ such that } h \in \mathbb{N}. \tag{3.19}$$

Unlike the employed R controller in [64], $G_{\mathrm{R}}(s)$ in (3.18) is discretized using the impulse invariant method, resulting in the transfer function [52, 84–86]

$$G_{\mathrm{R}}(z) = T_{\mathrm{R}}\,T_{\mathrm{sw}}\,\frac{\cos(2\omega_{\mathrm{R}}T_{\mathrm{sw}}) - z^{-1}\cos(\omega_{\mathrm{R}}T_{\mathrm{sw}})}{1 - 2z^{-1}\cos(\omega_{\mathrm{R}}T_{\mathrm{sw}}) + z^{-2}}, \tag{3.20}$$

to ensure a correct lock on the desired resonant frequency as well as stable operation through the entire speed range. The time constant of such R controllers T_{R} is carried out similar to the method shown in [52], which leads to

$$\begin{pmatrix} T^d_{\mathrm{R}} & T^q_{\mathrm{R}} & T^x_{\mathrm{R}} & T^y_{\mathrm{R}} \end{pmatrix} = \frac{100}{R_{\mathrm{s}}} \begin{pmatrix} \frac{\hat{L}^d_{\mathrm{s}}}{\omega^{dq}_{\mathrm{R}}} & \frac{\hat{L}^q_{\mathrm{s}}}{\omega^{dq}_{\mathrm{R}}} & \frac{\hat{L}^x_{\mathrm{s}}}{\omega^{xy}_{\mathrm{R}}} & \frac{\hat{L}^y_{\mathrm{s}}}{\omega^{xy}_{\mathrm{R}}} \end{pmatrix}, \tag{3.21}$$

where the time constants T^d_{R}, T^q_{R}, T^x_{R}, and T^y_{R} as well as the assigned resonant frequencies ω^{dq}_{R} and ω^{xy}_{R} are operating point-dependent and adapted online. The resonant frequencies ω^{dq}_{R} and ω^{xy}_{R} correspond to designated frequencies stated in Figs. 3.15 and 3.16, respectively, which are $\omega^{dq}_{\mathrm{R}} = 2\omega_{\mathrm{e}}$ for dq subspace and $\omega^{xy}_{\mathrm{R}} = 6\omega_{\mathrm{e}}$ for xy subspace. As for the *zero* subspace, it is activated only for the 1N connection. Recall from Section 2.1.3, that the *zero* subspace comprises the triplets harmonics 3γ, where $\gamma = \{1,\,3,\,5,\,...\}$. Thus, several proportional-resonant (PR) controllers, each with transfer

$$G_{\mathrm{PR}}(z) = V_{\mathrm{p}} + G_{\mathrm{R}}(z), \tag{3.22}$$

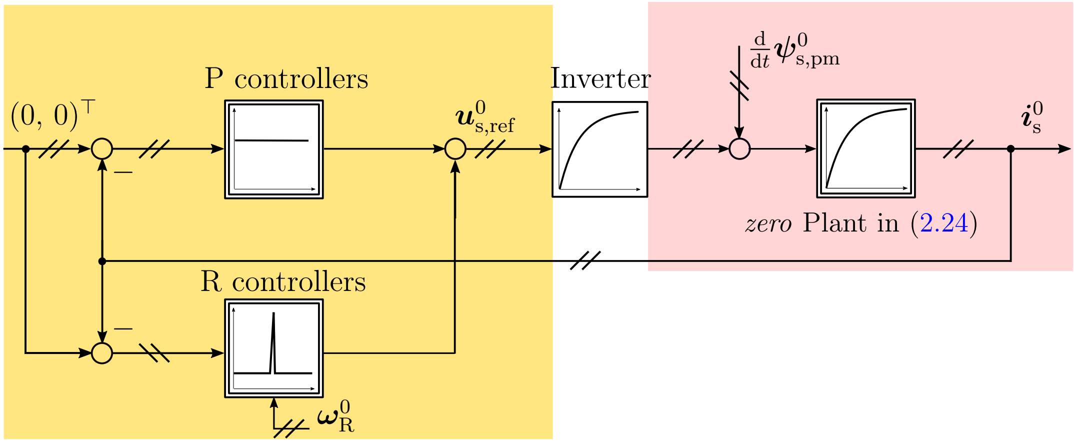

Fig. 3.17. Block diagram of the *zero* subspace control system, highlighting (in 🟨) the PR controllers with their designated resonant angular frequencies and (in 🟥) the assumed linear plant.

are required to compensate for such harmonics[3]. Practically, it was found that compensating up to the 9th lead to acceptable results. The resonant frequency vector for the *zero* subspace is defined as

$$\boldsymbol{\omega}^{0}_{\mathrm{R}} = \left(3\omega_{\mathrm{e}},\quad 9\omega_{\mathrm{e}}\right)^{\top}, \tag{3.23}$$

where each resonant frequency is assigned to the corresponding PR controller. Given that the variation of *zero* subspace flux was assumed linear in Section 2.1.4.3, thus, the PR controllers gains were set according to the magnitude optimum criteria[4] as

$$\left.\begin{array}{rcl} \left(V^{0^+}_{\mathrm{p}},\quad V^{0^-}_{\mathrm{p}}\right) & = & \dfrac{1}{2T_{\mathrm{sw}}}\left(\mathrm{mean}(L^{d_0}_{\mathrm{s}}),\quad \mathrm{mean}(L^{q_0}_{\mathrm{s}}),\right) \\ \left(T^{0^+}_{\mathrm{R}},\quad T^{0^-}_{\mathrm{R}}\right) & = & \dfrac{1}{R_{\mathrm{s}}}\left(\mathrm{mean}(L^{d_0}_{\mathrm{s}}),\quad \mathrm{mean}(L^{q_0}_{\mathrm{s}}),\right) \end{array}\right\} \tag{3.24}$$

where $\mathrm{mean}(L^{d_0}_{\mathrm{s}})$ and $\mathrm{mean}(L^{q_0}_{\mathrm{s}})$ are the approximated constant values for the differential inductances $L^{d_0}_{\mathrm{s}}$ and $L^{q_0}_{\mathrm{s}}$ in the *zero* subspace (see details in Section 2.1.4.3 and (2.22)). The block diagram of the *zero* subspace controller is shown in Fig. 3.17, where the disturbance term $\frac{\mathrm{d}}{\mathrm{d}t}\boldsymbol{\psi}^{0}_{\mathrm{s,pm}}$ represents the PM contribution of the 3rd and 9th harmonics in such subspace (see Section 2.1.4.3 for details).

3.3.3 Dynamic evaluation

The same setup used in the Appendix A was employed to test the control structure using the flux linkage maps. The tuning of the PI controllers was set as decribed in section 3.3. Since the transient behaviour of ADT-IPMSM is governed by $\boldsymbol{i}^{dq}_{\mathrm{s}}$,

---

[3] Only R controllers were used for the dq and xy subspace, unlike PR controller for the *zero* subspace, since the proportional gains of the dq and xy controllers are already present from PI controller (see Fig. 3.15 and Fig. 3.16).

[4] The PI controller in the synchronously rotating frame is equivalent to the PR controller in the stationary frame. Thus, the magnitude optimum criteria is applicable for both controllers. More details can be found in [87, 88].

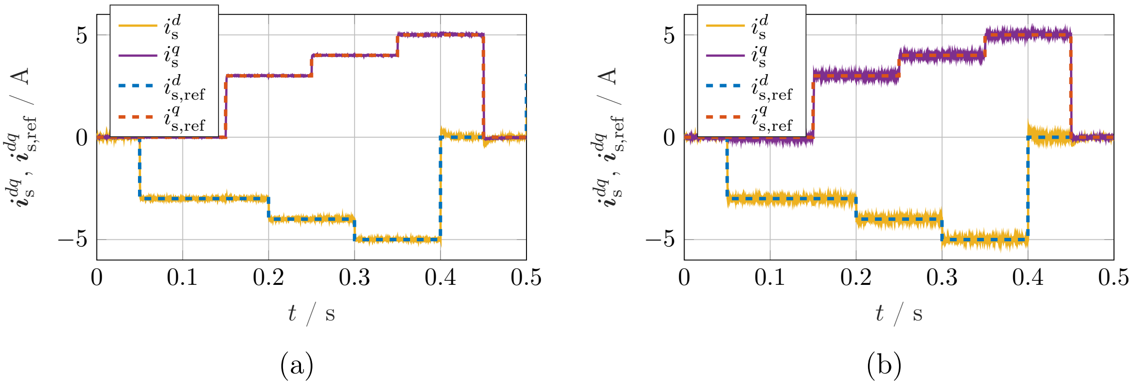

Fig. 3.18. (a) Simulation and (b) experimental transient response comparison for the 1N case w.r.t. $\boldsymbol{i}_\mathrm{s}^{dq}$ with harmonic compensation at 1200 rpm.

the dynamic performance is evaluated through step changes in $\boldsymbol{i}_\mathrm{s,ref}^{dq}$ for the 1N case with harmonic compensation. Figs. 3.18(a)-(b) plot the simulation and experimental results, respectively, which show the current dynamics and the tracking ability of the desired reference $\boldsymbol{i}_\mathrm{s,ref}^{dq}$, while illustrating minimum interaction between i_s^d and i_s^q, exhibiting the expected $dq-$decoupling as well as fast transient response [68].

Chapter 4

Fault detection and post-fault operation

The inherent fault-tolerant capability of ADT-IPMSM in comparison with standard three-phase drives is the main motivation for adopting such drives for AWE. In Section 1.3, it was explained, based on statistical data, that for the most common types of recorded faults (i.e. converter leg partial/complete failure, connections between VSI and machine, and windings), the electrical protection system operates and isolates the faulty phase. Such fault isolation leads to the so called open-phase fault (OPF). Literature has recently witnessed a proliferation of publications concerning fault detection, clearing, and post-fault operation.

The main contribution of this thesis with respect to fault tolerance is identifying the post-fault torque-speed characteristics, exploiting and quantifying the complete drive capability in the post-fault case, while maintaining minimum stator copper losses. The developed post-fault optimization relies on the acquired non-linear model in Section 2.1.4, in particular that of the dq subspace. Furthermore, an OPF detection scheme is employed, which was developed as part of the supervised master thesis [89]. When coupling the detection scheme with the proposed post-fault optimization, a reliable post-fault operation is realized, in a sense that the transition from the pre-fault (i.e. healthy) to the post-fault case would be expedited, while maintaining minimum stator copper losses. First, the OPF detection scheme is derived and validated in Section 4.1. Afterwards, the post-fault controller and the latest optimization strategies are discussed in detail in Section 4.2. Finally, the proposed optimization strategy is presented in Section 4.3 along with the experimental validation tests in Section 4.4.

4.1 Phase fault detection

Multi-phase (i.e. more than three) drives are inherently fault tolerant, where they can still operate even if post-fault optimizations were not implemented [89, 90]. Nevertheless, post-fault operations vary depending on the remaining healthy phases, based on which the proper post-fault optimization schemes are enabled. Thus, the link between the pre- and post-fault cases is mandatory; to distinguish between the healthy phases and the faulty ones. Moreover, detection times should be as short as possible (typically less than one fundamental period) [91]. In general, the fault detection method should in principle possess the following requirements [91]:

- Avoid additional hardware installations (e.g.: additional voltage sensors in [92, 93]);
- Short detection times without exceeding the rated values of the drives such as voltages/current [94];
- Avoid complex approaches with high implementation effort; and
- Independence from the machine parameters and/or control strategy [95].

The proposed fault-detection scheme aimed at extending the work developed in [91] in terms of [89]:

- The applicability of the detection algorithm for both 1N and 2N configuration, where only the 2N connection was considered in [91]; and
- Shortening the detection time by making it speed dependent without compromising the performance of the detection method.

4.1.1 Fault detection algorithm

4.1.1.1 Proposed detection technique

Depending on the neutral point configuration and the faulty phase(s), coupling between the different subspaces arises. Based on the stated requirements of any employed detection scheme, the detection algorithm aims at identifying such relations (i.e. couplings) between the different subspaces, defining fault indices along with assigning threshold values; for fault recognition and smooth transition from the pre- and post-fault cases. In the event of fault, the protection system operates and the current of the corresponding phase is *zero*. Recalling (2.8), it is possible to rewrite the relation between the $\boldsymbol{i}_{\mathrm{s}}^{a_1 \to c_2}$ and the subspace currents as

$$\begin{pmatrix} i_{\mathrm{s}}^{\mathrm{a}_1} \\ i_{\mathrm{s}}^{\mathrm{b}_1} \\ i_{\mathrm{s}}^{\mathrm{c}_1} \\ i_{\mathrm{s}}^{\mathrm{a}_2} \\ i_{\mathrm{s}}^{\mathrm{b}_2} \\ i_{\mathrm{s}}^{\mathrm{c}_2} \end{pmatrix} = \underbrace{\begin{bmatrix} 1 & 0 & 1 & 0 & 1 & 0 \\ -\frac{1}{2} & \frac{\sqrt{3}}{2} & -\frac{1}{2} & -\frac{\sqrt{3}}{2} & 1 & 0 \\ -\frac{1}{2} & -\frac{\sqrt{3}}{2} & -\frac{1}{2} & \frac{\sqrt{3}}{2} & 1 & 0 \\ \frac{\sqrt{3}}{2} & \frac{1}{2} & -\frac{\sqrt{3}}{2} & \frac{1}{2} & 0 & 1 \\ -\frac{\sqrt{3}}{2} & \frac{1}{2} & \frac{\sqrt{3}}{2} & \frac{1}{2} & 0 & 1 \\ 0 & -1 & 0 & -1 & 0 & 1 \end{bmatrix}}_{\overset{(2.8)}{=} \boldsymbol{T}_{\mathrm{VSD}}^{-1}} \begin{pmatrix} i_{\mathrm{s}}^{\alpha} \\ i_{\mathrm{s}}^{\beta} \\ i_{\mathrm{s}}^{X} \\ i_{\mathrm{s}}^{Y} \\ i_{\mathrm{s}}^{0+} \\ i_{\mathrm{s}}^{0-} \end{pmatrix}. \tag{4.1}$$

Assuming that a fault in phase a_1 was detected and cleared (i.e. $i_{\mathrm{s}}^{\mathrm{a}_1} = 0$), the first row in (4.1) can be rewritten as

$$1 = \frac{-(i_{\mathrm{s}}^{X} + i_{\mathrm{s}}^{0^+})}{i_{\mathrm{s}}^{\alpha}} =: \delta_{\mathrm{a}_1}, \tag{4.2}$$

where δ_{a_1} is defined as the fault index for phase a_1 and has the following properties and remarks:

- In the pre-fault case, both $i_\mathrm{s}^X = i_\mathrm{s}^{0^+} = 0$ as explained in Section 3.3.1. Accordingly, by substituting in (4.2), $\delta_{\mathrm{a}_1} = 0$ in the healthy case;
- Since (4.2) utilizes the instantaneous values of its variables, δ_{a_1} cannot attain a constant value through out an entire period; owing to instants as *zero-crossings* of i_s^α (i.e. division by 0). Thus, post-processing of δ_{a_1} in terms of a discrete moving average (MA) is necessary to avoid spikes in measurements and false fault alarms. The implementation of MA is in the upcoming section.
- The presumable values for δ_{a_1} in the healthy case assume a perfect balance between the stator currents, which cannot be practically guaranteed. Also, it is assumed that all other phases are healthy.
- For an AWE system, the electrical drive is either heavily/lightly loaded during reeling-out/in (see Section 1.2.1). In other words, a pure no-load case where $\boldsymbol{i}_\mathrm{s}^{\alpha\beta} = 0$ is not a valid case.

By following the same procedure in deriving δ_{a_1} in (4.2), the remaining indices can be derived as [89, 91]

$$\left.\begin{aligned}
\delta_{\mathrm{b}_1} &= \frac{i_\mathrm{s}^X - 2i_\mathrm{s}^{0^+}}{i_\mathrm{s}^\alpha - \sqrt{3}(i_\mathrm{s}^\beta - i_\mathrm{s}^Y)}\\
\delta_{\mathrm{c}_1} &= \frac{i_\mathrm{s}^X - 2i_\mathrm{s}^{0^+}}{i_\mathrm{s}^\alpha + \sqrt{3}(i_\mathrm{s}^\beta - i_\mathrm{s}^Y)}\\
\delta_{\mathrm{a}_2} &= \frac{-\sqrt{3}i_\mathrm{s}^X + 2i_\mathrm{s}^{0^-}}{\sqrt{3}i_\mathrm{s}^\alpha + i_\mathrm{s}^\beta + i_\mathrm{s}^Y}\\
\delta_{\mathrm{b}_2} &= \frac{-\sqrt{3}i_\mathrm{s}^X - 2i_\mathrm{s}^{0^-}}{\sqrt{3}i_\mathrm{s}^\alpha - i_\mathrm{s}^\beta - i_\mathrm{s}^Y}\\
\delta_{\mathrm{c}_2} &= \frac{-i_\mathrm{s}^Y + i_\mathrm{s}^{0^-}}{i_\mathrm{s}^\beta}
\end{aligned}\right\}, \tag{4.3}$$

where each index has the same properties as that of δ_{a_1}.

4.1.1.2 Fault indices post-processing

It was found practically that the instantaneous values of the fault indices will experience high oscillations (i.e. chattering) in the presence of measurement noise and/or when one or more phases are disconnected. Accordingly, before passing the fault indices to the discrete moving average, a hysteresis band for every index is employed, which is defined as [89, 91]

$$\bar{\delta}_\kappa = \begin{cases} \delta_\kappa & 1-\epsilon \le \delta_\kappa \le 1+\epsilon,\\ 0 & \text{Otherwise}, \end{cases} \tag{4.4}$$

where $\kappa \in \{\mathrm{a}_1, \mathrm{b}_1, ..., \mathrm{c}_2,\}$ and $\epsilon \in \{0, 1\}$ is a safety factor, which when decreased the algorithm becomes more immune to noise at the expense of poor performance;

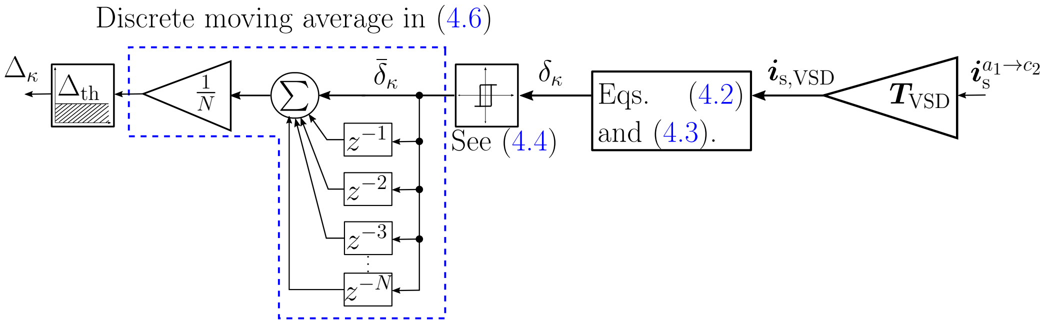

Fig. 4.1. Block diagram summarizing the proposed OPF detection algorithm.

Table 4-I. Parameters of the proposed fault detection algorithm in Section 4.1.

Parameter	Value
ϵ	0.1
σ	0.4
Δ_{th}	0.15

since the output of such hysteresis is passed later to the discrete MA. Typically ϵ is set to 10%.

Upon computing the fault indices for all phases, a discrete MA is employed. Unlike [91], the proposed MA window (i.e. the domain through which the average value is computed) is set proportional to the fundamental period to expedite the detection time at high rotational speeds. Moreover, a lower bound is set for the detection speed, to avoid sluggish performance at low speeds. By defining the discrete samples instants as $w \in \mathbb{N}_{\text{o}}$, where $\mathbb{N}_{\text{o}} := 0 \cup \mathbb{N}$, the proposed MA is mathematically represented by

$$\Delta_\kappa = \frac{1}{N} \sum_{w=0}^{N-1} \bar{\delta}_\kappa(w), \tag{4.5}$$

where

$$N = \sigma \frac{2\pi f_{\text{sw}}}{\omega_{\text{e,rated}}}, \tag{4.6}$$

is the number of samples passed within the computation of the MA. The variable σ in (4.6) is set as a tradeoff between filtering quality and performance. Finally, the output of the moving average is compared to a a preset threshold value Δ_{th}, which if exceeded, a corresponding a flag in the controller is raised implying the presence of the a cleared fault in the corresponding phase. The presence of such threshold is essential to be able to discard the variation of the fault indices of the healthy phases, which tend to increase in the post-fault operation [89, 91].

4.1.2 Validating the phase fault detection technique

Fig. 4.1 summerizes the employed fault detection technique in section 4.1.1. In terms of the stator current regulation, the same control structure of the *dq*, *xy*, and *zero* subspaces in Figs. 3.15, 3.16 and 3.17, respectively, is used. In this experiment,

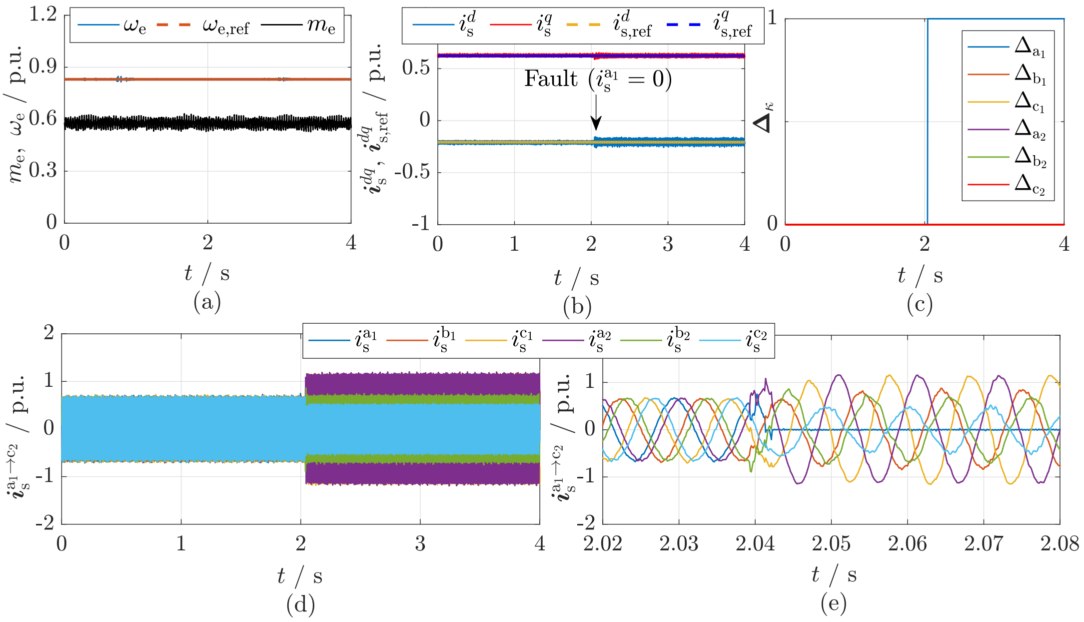

Fig. 4.2. Validation of the proposed fault detection algorithm for the 1N connection for an applied fault $i_s^{a_1} = 0$ showing (a) the mechanical quantities, (b) $\boldsymbol{i}_s^{dq}$ and $\boldsymbol{i}_{s,ref}^{dq}$, (c) the fault indices, (d) the corresponding stator currents with their zoomed versions in (e) at the instant of fault.

the parameters of the fault detection algorithm are set as shown in Table 4-I. In Fig. 4.2, the drive is allowed to operate at a 1N configuration at $m_e = 0.6$ p.u. and $\omega_e = 0.83$ p.u., before deliberately disconnecting phase a_1 by means of a circuit breaker at $t = 2.05$ s $\big($see fault highlight in Fig. 4.2(b)$\big)$. The detection algorithm was able to detect the faulty phase after 1.3×10^{-3} s, as seen in Fig. 4.2(c). Even though at $t = 2.05$ s minimum disturbance and electrical transients occurred (see Fig. 4.2(a)-(b)), Figs. 4.2(d)-(e) indicate that the stator currents $i_s^{c_1}$ and $i_s^{a_2}$ exceeded the rated current $\hat{i}_{s,rated}$ by 16% for $t > 2.05$ s.

Based on such discussion, this confirms that the ADT-IPMSM drive is inherently fault-tolerant even if post-fault optimization algorithms were not embraced. In case of failure in more than one phase, this simple detection algorithm functions as expected. To test the proposed algorithm for more than one phase failure, the drive was first set to operate at a lower torque $m_e = 0.3$ p.u. and accordingly lower $\boldsymbol{i}_{s,ref}^{dq}$ $\big($see Fig. 4.3(a)$\big)$; to avoid exceeding the rated current $\hat{i}_{s,rated}$ upon disconnection. Then, the circuit breaker of phase b_2 was disconnected at $t = 7$ s after the disconnection of phase a_1 at $t = 4$ s (see Fig. 4.3(b)-(d)). For either case, the detection algorithm was able to detect both faults as clearly indicated by the change of Δ_{a_1} and Δ_{b_2} in Fig. 4.3(e). Furthermore, the proposed detection technique covers the 2N operation as indicated in Fig. 4.4, where the drive was set to produce $m_e = 0.5567$ p.u. in the healthy case before disconnecting phase a_1 at $t = 3.575$ s, as seen in Fig. 4.4(d)-(e).

The applied detection technique is simple without extensive computational burden, promoting such technique to be applied for the ADT-IPMSM drive; facilitating the transition from the healthy case to the post-fault operation. On the other hand, exceeding the rated value $\hat{i}_{s,rated}$ will lead to thermal build-up in the stator and, eventually, failure. Surpassing the rated current $\hat{i}_{s,rated}$ depends on the the operating

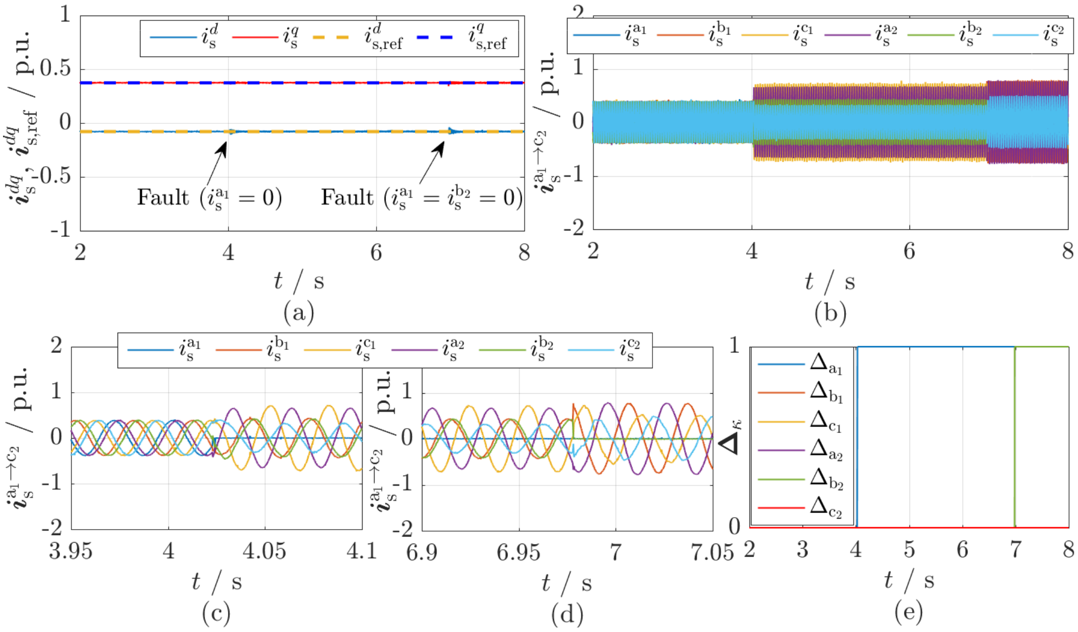

Fig. 4.3. Validation of the proposed fault detection algorithm for the 1N connection for the applied faults $i_s^{a_1}=0$ and $i_s^{b_2}=0$ showing (a) $\boldsymbol{i}_s^{dq}$ and $\boldsymbol{i}_{s,ref}^{dq}$, (b) the corresponding stator currents with their zoomed versions at the instant of the fault (c) $i_s^{a_1}=0$ and (d) $i_s^{b_2}=0$, and (e) the fault indices.

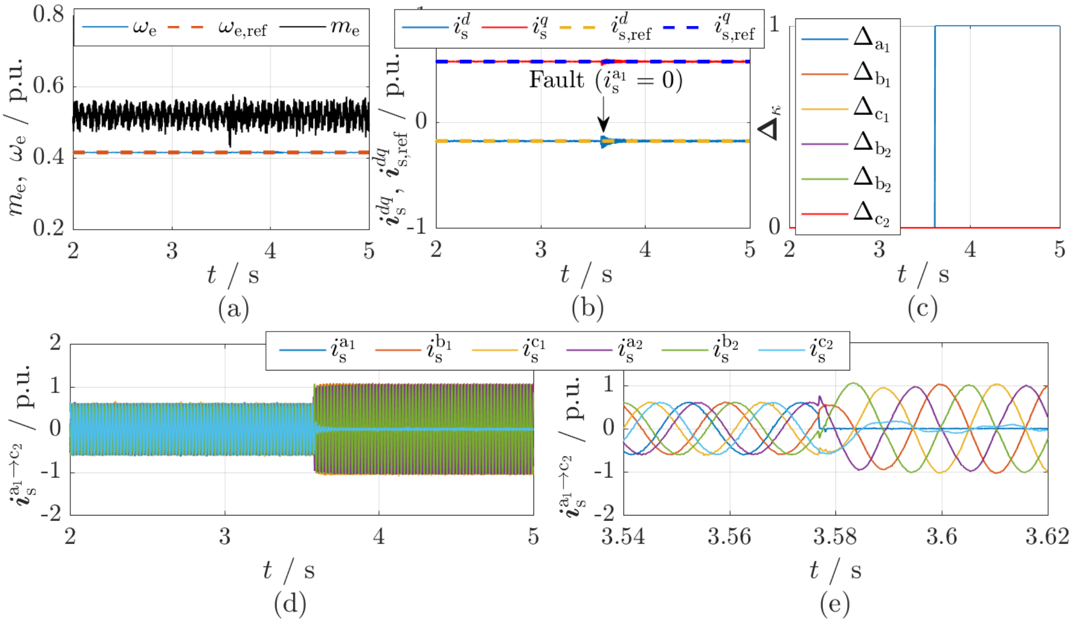

Fig. 4.4. Validation of the proposed fault detection algorithm for the 2N connection for an applied fault $i_s^{a_1}=0$ showing (a) the mechanical quantities, (b) $\boldsymbol{i}_s^{dq}$ and $\boldsymbol{i}_{s,ref}^{dq}$, (c) the fault indices, (d) the corresponding stator currents with their zoomed versions in (e) at the instant of fault and (f) after applying the post-fault optimization strategy.

conditions (i.e. m_e and ω_e), remaining healthy phases, and neutral points configuration, which are impossible to predict in advance. The aforementioned factors are also the requirements for designing a proper post-fault controller, as discussed in detail in the upcoming section.

4.2 State-of-the-art post-fault operation

4.2.1 Post-fault concept of the stator current controller

In the literature, several fault-tolerant control strategies can be found for multiphase machines. Most of them are based on traditional FOC, where the machine phase variables are transformed to their sequence component using the decomposition matrix transformation (e.g. $\boldsymbol{T}_{\mathrm{VSD}}$ for ADT machines). Based on the employed transformation matrix, the employed current controllers are classified into two main categories:

4.2.1.1 Controllers employing reduced order transformation

Similar to [96], in the event of fault occurrence, the number of independent control variables decreases. Accordingly, the transformation matrix $\boldsymbol{T}_{\mathrm{VSD}}$ and the system order will, therefore, be reduced. For example, let the faulty phase be c_2 (i.e. $i_{\mathrm{s}}^{\mathrm{c}_2} = 0$) for the 2N connection. Thus, $i_{\mathrm{s}}^{\mathrm{a}_2} = -i_{\mathrm{s}}^{\mathrm{b}_2}$ and $i_{\mathrm{s}}^{0+} = i_{\mathrm{s}}^{0-}$. The resulting subspace currents are computed by

$$\begin{pmatrix} i_{\mathrm{s}}^{\alpha} \\ i_{\mathrm{s}}^{\beta} \\ i_{\mathrm{s}}^{X} \\ i_{\mathrm{s}}^{Y} \\ i_{\mathrm{s}}^{0+} \\ i_{\mathrm{s}}^{0-} \end{pmatrix} \overset{(2.8)}{=} \frac{1}{3} \begin{bmatrix} 1 & -\frac{1}{2} & -\frac{1}{2} & \frac{\sqrt{3}}{2} & -\frac{\sqrt{3}}{2} & 0 \\ 0 & \frac{\sqrt{3}}{2} & -\frac{\sqrt{3}}{2} & \frac{1}{2} & \frac{1}{2} & -1 \\ 1 & -\frac{1}{2} & -\frac{1}{2} & -\frac{\sqrt{3}}{2} & \frac{\sqrt{3}}{2} & 0 \\ 0 & -\frac{\sqrt{3}}{2} & \frac{\sqrt{3}}{2} & \frac{1}{2} & \frac{1}{2} & -1 \\ 1 & 1 & 1 & 0 & 0 & 0 \\ 0 & 0 & 0 & 1 & 1 & 1 \end{bmatrix} \begin{pmatrix} i_{\mathrm{s}}^{\mathrm{a}_1} \\ i_{\mathrm{s}}^{\mathrm{b}_1} \\ i_{\mathrm{s}}^{\mathrm{c}_1} \\ i_{\mathrm{s}}^{\mathrm{a}_2} \\ i_{\mathrm{s}}^{\mathrm{b}_2} \\ 0 \end{pmatrix}, \tag{4.7}$$

which leads to $i_{\mathrm{s}}^{Y} = -i_{\mathrm{s}}^{\beta}$ and $i_{\mathrm{s}}^{0-} = 0$. This concludes the possibility of controlling the stator currents of the healthy phases by regulating only three components i_{s}^{α}, i_{s}^{β}, and i_{s}^{X} (i.e. three degrees of freedom) via three current controllers[1] in comparison with four controllers for the fundamental component in the healthy case (i.e. two pairs of PI controllers for the rotating dq and xy subspaces). Therefore, the reduced order VSD matrix can be found by substituting $i_{\mathrm{s}}^{0+} = i_{\mathrm{s}}^{0-} = 0$, $i_{\mathrm{s}}^{\mathrm{c}_1} = -(i_{\mathrm{s}}^{\mathrm{a}_1} + i_{\mathrm{s}}^{\mathrm{b}_1})$, $i_{\mathrm{s}}^{\mathrm{b}_2} = -i_{\mathrm{s}}^{\mathrm{a}_2}$ and $i_{\mathrm{s}}^{\mathrm{c}_2} = 0$ in (4.7), resulting in

$$\begin{pmatrix} i_{\mathrm{s}}^{\alpha} \\ i_{\mathrm{s}}^{\beta} \\ i_{\mathrm{s}}^{X} \end{pmatrix} = \frac{1}{3} \begin{bmatrix} 1 & 0 & \sqrt{3} \\ \frac{\sqrt{3}}{2} & \sqrt{3} & 0 \\ 1 & 0 & -\sqrt{3} \end{bmatrix} \begin{pmatrix} i_{\mathrm{s}}^{\mathrm{a}_1} \\ i_{\mathrm{s}}^{\mathrm{b}_1} \\ i_{\mathrm{s}}^{\mathrm{a}_2} \end{pmatrix}. \tag{4.8}$$

This technique has the advantage of employing minimum number of current regulators, which is typically equal to the system order. However, the main constraint of this technique is that it entails different controller structure for different combinations of the faulty phases, making such control approach tedious to implement.

---

[1] The stated current controllers in this context of discussion refers to the fundamental current controllers.

4.2.1.2 Controllers employing full-order transformation

In this case, the full-order transformation matrix $\boldsymbol{T}_{\text{VSD}}$ is used to decompose the phase currents $\boldsymbol{i}_{\text{s}}^{a_1 \to c_2}$ into their sequence components (Recall (2.8) $\left(\boldsymbol{f}_{\text{s}}^{\alpha\beta}, \ \boldsymbol{f}_{\text{s}}^{XY}, \ \boldsymbol{f}_{\text{s}}^{0}\right)^{\top} = \boldsymbol{T}_{\text{VSD}} \boldsymbol{f}_{\text{s}}^{a_1 \to c_2}$, where $\boldsymbol{f} \in \{\boldsymbol{u}, \boldsymbol{i}, \boldsymbol{\psi}\}$), where the disconnected phase(s) will have zero current value(s). The control structure is similar to that of the healthy case (see control structures of the *dq*, *xy* and *zero* subspaces in Figs. 3.15-3.17). Even though the stator current controllers correspond to redundant current regulators, the same controller structure can be preserved for all fault types [38, 39, 41–44, 97]. Accordingly, such controller is adopted in this thesis.
It was explained in [42, 44] that by introducing the full-order VSD matrix $\boldsymbol{T}_{\text{VSD}}$ in the post-fault operation, the following would hold:

I. The $\alpha\beta$ subspace is still solely responsible for the electromechanical energy conversion, irrespective of the remaining healthy phases and/or neutral point configuration;

II. The number of independent control variables must be equal to the order of the system, which is dependent on the neutral points connection and the faulty phases;

III. The inevitable coupling between the $\alpha\beta$ and the remaining subspaces in the post-fault case motivated the concept of forcing the control system to inject fundamental currents XY and *zero* subspaces, where $\boldsymbol{i}_{\text{s}}^{XY} \propto \boldsymbol{i}_{\text{s}}^{\alpha\beta}$ and $\boldsymbol{i}_{\text{s}}^{0} \propto \boldsymbol{i}_{\text{s}}^{\alpha\beta}$. The amount of injected fundamental currents in the XY and *zero* subspaces is dependent on the faulty phases and the neutral points configurations (i.e. 1N or 2N) [98].

Based on the arguments (I)-(III), the block diagram of the post-fault controller is shown in Fig. 4.5, where the post-fault controller is coupled with the fault detection technique presented in Section 4.1.1; to ensure a smooth transition from the healthy to the post-fault case. The block "Post-fault optimization" refers to the post-fault control strategy, which relates $\boldsymbol{i}_{\text{s}}^{XY}$ and $\boldsymbol{i}_{\text{s}}^{0}$ to $i_{\text{s}}^{\alpha}\beta$ (or $\boldsymbol{i}_{\text{s}}^{dq}$), as explained in the upcoming section. The fundamental PI and R controllers in the torque-producing subspace (i.e. $dq \to \alpha\beta$) in Fig. 4.5 are identical to those in the healthy case presented previously in Fig. 3.15. The following changes took place in the non torque-producing subspaces (i.e. XY and *zero* subspaces), in comparison with the controllers used in the healthy case (see Figs. 3.16 and 3.17):

i. Fundamental current components, dependent on $\boldsymbol{i}_{\text{s,ref}}^{\alpha\beta}$ at an angular frequency of ω_{e}, are injected in the XY subspace and are given by $\boldsymbol{i}_{\text{s,ref}}^{XY}$. The current $\boldsymbol{i}_{\text{s,ref}}^{XY}$ can be then controlled by means of PI controllers upon applying Park's transformation $\boldsymbol{T}_{\text{p}}(\phi_{\text{e}})^{-1}$. The anti-synchronous (i.e. rotating with $-\phi_{\text{e}}$) PI controllers in the xy frame along with the R controllers tuned at the resonant angular frequency $\omega_{\text{R}}^{xy} = 6\omega_{\text{e}}$ (details in Section 3.3.1) are identical to those in Fig. 3.16. The tuning of the synchronous PI controller (i.e. $\boldsymbol{i}_{\text{s}}^{XY}$ controller after applying $\boldsymbol{T}_{\text{p}}(\phi_{\text{e}})^{-1}$) is identical to that of the xy components, which is based on the tuning law in (3.14).

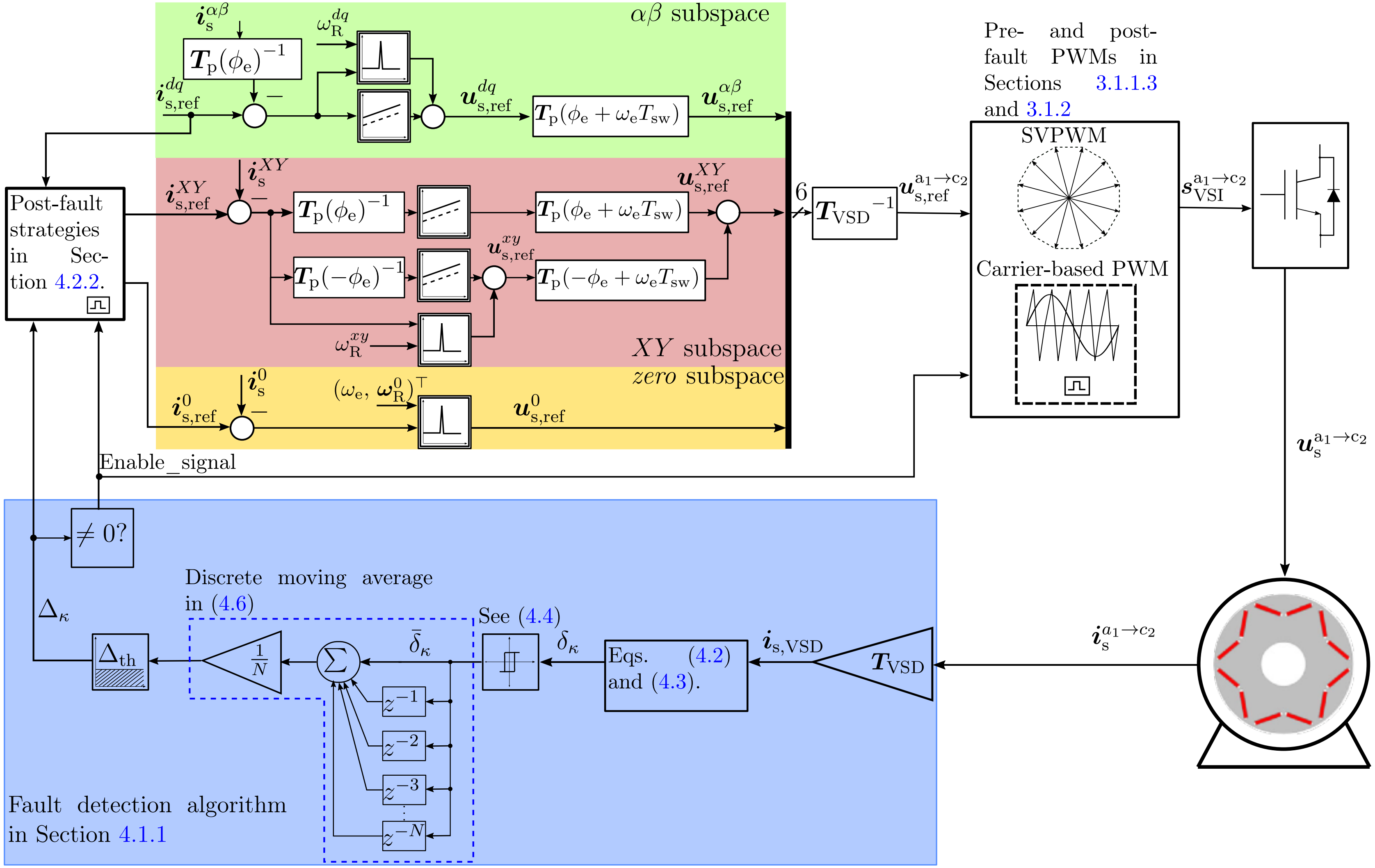

Fig. 4.5. Block diagram showing the pre- and post-fault current controllers along with the complete steps of the fault detection algorithm in Section 4.1.1. The threshold Δ_{th} check block enables the post-fault optimization block and the carrier-based PWM for the VSI (see Section 3.1.2 for details on VSI switching).

ii. The injected fundamental component in the *zero* subspace is controlled by a PR controller at an angular resonant frequency ω_e, which is tuned similar to the tuning law in (3.24). It is also possible to use PI controllers in the synchronously rotating frame (i.e. applying $\boldsymbol{T}_\mathrm{p}(\phi_\mathrm{e})^{-1}$) as in [42]. The compensation of the 3rd and 9th harmonics is carried-out similar to that in Fig. 3.17.

4.2.2 Post-fault optimization strategies

Assuming that the fault is detected and cleared, several post-fault control strategies have been proposed for one or more open-phase faults (OPFs) [39, 41]. In the post-fault operation, fundamental currents are forced into the non-fundamental subspaces; as an attempt to restore - at *steady state* - the same magneto-motive force in the air-gap as in the healthy case and generate the desired torque $m_\mathrm{e,ref}$, as first introduced in [98]. Enhancing the proposed post-fault optimzation in [98] took place through the last decade as recorded in [38, 42, 43], where the amplitudes and phase shifts of the forced fundamental currents are varied based on three main optimization strategies: minimum Joule losses (ML), maximum torque (MT), and a *hybrid* minimum losses maximum torque (MLMT) [42, 43].
The main difference between such optimization techniques lies in the defined optimization constraints, which affect how the amplitudes and phase shifts of the forced fundamental currents are scaled in the different subspace coordinates. Based on the discussion in Section 4.2.1.2, the general relation between the subspace currents can be expressed for the 1N configuration by

$$\begin{pmatrix} \bar{\boldsymbol{i}}_\mathrm{s}^{XY} \\ \bar{\boldsymbol{i}}_\mathrm{s}^{0} \end{pmatrix} = \underbrace{\begin{bmatrix} k_X^\alpha & k_X^\beta \\ k_Y^\alpha & k_Y^\beta \\ k_{0+}^\alpha & k_{0+}^\beta \\ -k_{0+}^\alpha & -k_{0+}^\beta \end{bmatrix}}_{=:\boldsymbol{T}_\mathrm{k} \,\in\, \mathbb{R}^{4\times 2}} \bar{\boldsymbol{i}}_\mathrm{s}^{\alpha\beta}, \tag{4.9}$$

where the accent "$\bar{\square}$" is the phasor description of a variable at *steady state*[2] and $\boldsymbol{T}_\mathrm{k}$ is the optimization matrix with k_X^α, k_X^β, k_Y^α, k_Y^β, k_{0+}^α, and k_{0+}^β as its elements. By defining p_Cu as the normalized stator copper losses with respect to the healthy case, the sets of phases as $\mathbb{S} \in \{\mathrm{a}_1, \ldots, \mathrm{c}_2\}$, faulty phases $\mathbb{S}_\mathrm{f}$ and the healthy phases $\mathbb{S}_\mathrm{h} := \mathbb{S} \setminus \mathbb{S}_\mathrm{f}$ (i.e. $\mathbb{S}_\mathrm{h} \cap \mathbb{S}_\mathrm{f} = \varnothing$); the generalized objective function is formulated as

$$\min_{\boldsymbol{T}_\mathrm{k}} \; p_\mathrm{Cu} = \frac{(\boldsymbol{i}_\mathrm{s}^{\gamma_\mathrm{h}})^\top \boldsymbol{i}_\mathrm{s}^{\gamma_\mathrm{h}}}{6(i_\mathrm{s,rated})^2}, \quad \forall \; \gamma_\mathrm{h} \in \mathbb{S}_\mathrm{h}, \tag{4.10}$$

subject to the following constraints:

$$\left.\begin{aligned} g_1 :\quad & i_\mathrm{s}^{\gamma_\mathrm{f}} = 0, \quad \forall \; \gamma_\mathrm{f} \in \mathbb{S}_\mathrm{f} \\ g_2 :\quad & \begin{cases} \displaystyle\sum_{\gamma_\mathrm{h}} i_\mathrm{s}^{\gamma_\mathrm{h}} = 0 & \text{1N case,} \\ \displaystyle\sum_{\gamma_1 \in \{a_1, b_1, c_1\}} i_\mathrm{s}^{\gamma_1} = 0 \text{ and } \sum_{\gamma_2 \in \{a_2, b_2, c_2\}} i_\mathrm{s}^{\gamma_2} = 0, & \text{2N case,} \end{cases} \\ g_3 :\quad & m_\mathrm{e} = m_\mathrm{e,ref}, \\ g_4 :\quad & \begin{cases} \hat{i}_\mathrm{s}^{\gamma_\mathrm{h}} = \hat{i}, \text{ where } \hat{i} \geq 0 & \text{MT case,} \\ ||\boldsymbol{i}_\mathrm{s}^{\gamma_\mathrm{h}}||_\infty \leq \hat{i}_\mathrm{s,rated}, & \text{MLMT case,} \end{cases} \end{aligned}\right\} \tag{4.11}$$

---

[2] Setting $\bar{i}_\mathrm{s}^{0^-} = \bar{i}_\mathrm{s}^{0^+} = 0$ corresponds to the 2N connection.

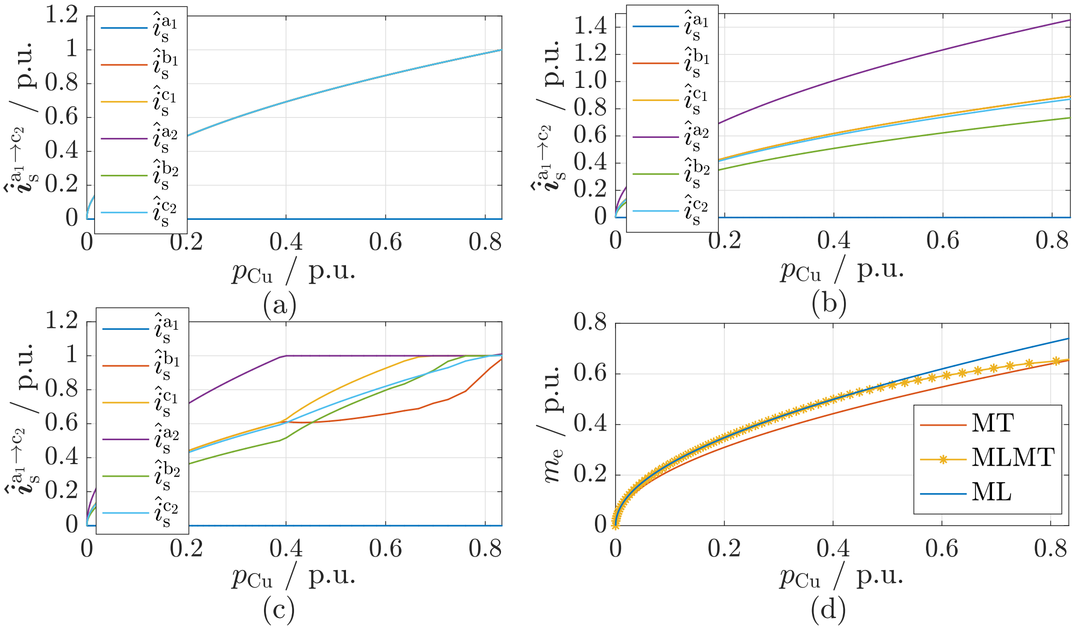

(a) (b) (c) (d)

Fig. 4.6. Post-fault optimization strategies of the 1N connection, showing the variation of the current amplitudes of the healthy phases against the generated copper losses with respect to (a) MT, (b) ML, and (c) MLMT, along with (d) the corresponding generated torque m_e per every strategy.

The ML optimization constraints minimize the total stator Joule copper losses for a given reference torque, without setting a per phase constraint (i.e. unequal amplitudes $\hat{\boldsymbol{i}}_s^{\mathbb{S}_h}$). MT constrains the losses per every phase $\mathbb{S}_h$ to be equal, as the currents $\boldsymbol{i}_s^{\mathbb{S}_h}$ are incremented equally up to the rated current value $\hat{i}_{s,rated}$ (i.e. equal loading for the healthy phases $\mathbb{S}_h$). MLMT outcome combines the merits of both MT and MT strategies, where the operation starts in the beginning similar to the ML operation and finally converges to the MT operation and all currents will reach $\hat{i}_{s,rated}$. This can be further explained with the following example.

Suppose that the post-fault operation takes place for $i_s^{a_1} = 0$, the relation between the subspace currents in (4.9), the objective function (4.10) and its constraints (4.11) are passed to the non-linear toolbox *fmincon* in Matlab, while incrementing the reference torque $m_{e,ref}$ and loading its corresponding MTPC loci (see Fig. 3.11, MTPC red loci ——). Upon executing *fmincon* for the ML, MT, MLMT strategies, the comparison between the optimzation strategies is depicted in Fig. 4.6.

By referring to Fig. 4.6 for the 1N connection, it can be seen in Fig. 4.6(a) that the MT keeps equal current magnitudes till reaching 1 p.u. (i.e. per-unit) in the functioning healthy phases, resulting in a maximum torque of ≈0.67 p.u. in Fig. 4.6(d). On the other hand, ML achieves lower losses than MT for $p_{Cu} \leq 0.4$ p.u. in Fig. 4.6(d). For $p_{Cu} > 0.4$ p.u., Fig. 4.6(b) shows that ML optimization would result in a thermal build up in the machine (i.e. $i_s^{a_2} > 1$ p.u.). The torque limit for ML is only 0.48 p.u. (see Fig. 4.6(d)). As a conclusion, the main drawback of the ML lies in the limited torque-production capability; where the amplitude of one or more of the healthy phases can exceed the rated current [99]. It was shown in [43] that the hybrid MLMT optimization is capable of combining the merits of ML and MT, such that minimum losses are ensured for every permissible torque reference. Such hybrid strategy manipulates the currents in the non-fundamental subspace (i.e. by varying

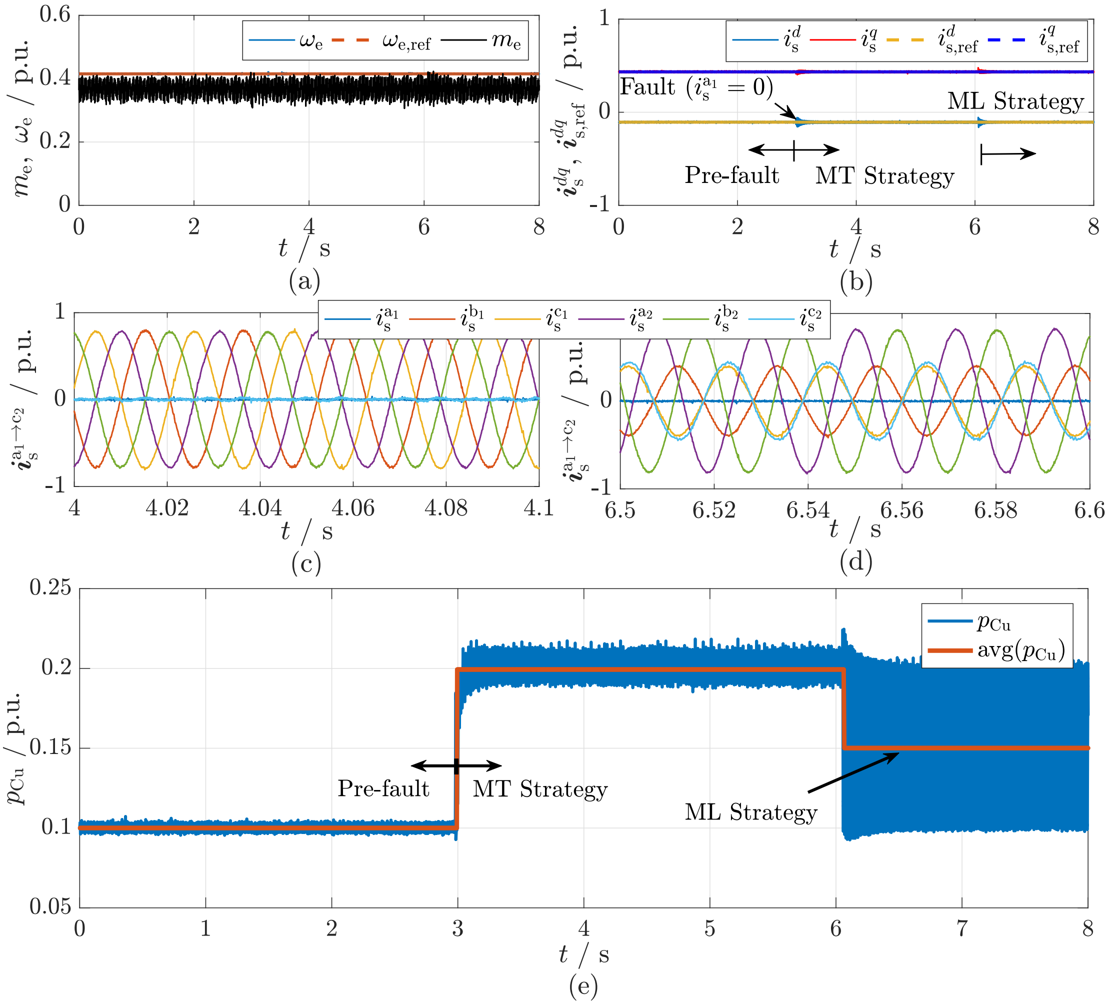

(a) (b) (c) (d) (e)

Fig. 4.7. Application of the ML and MT optimization strategies for the same $m_\mathrm{e,ref}$ during a 2N connection showing (a) the measured electromagnetic torque and speed, (b) $\boldsymbol{i}_\mathrm{s}^{dq}$ and $\boldsymbol{i}_\mathrm{s,ref}^{dq}$, the stator currents when applying the (c) MT and (d) ML strategies, and finally (e) the corresponding stator copper losses.

$\boldsymbol{T}_\mathrm{k}$) to keep the losses minimized for every given torque. For $p_\mathrm{Cu} \leq 0.4$ p.u. in Fig. 4.6(c)-(d), the MLMT coincides in results (i.e. amplitudes of stator currents and the generated torque) with the ML optimization. For higher torque reference, the subspace currents are manipulated to ensure that the currents in the healthy phases do not exceed 1 p.u.; until reaching the maximum permissible torque when all currents are equal in amplitude to 1 p.u. (i.e. coinciding with the maximum permissible loci of the MT strategy).

The aforementioned optimization strategies ML, MT, MLMT are also applicable for the 2N connection, where the concluded differences between the optimization strategies are valid for the 2N connection, as seen experimentally with the aid of Fig. 4.7. For a given operating point with ω_e and m_e in Fig. 4.7(a)-(b), a fault in phase a_1 was deliberately induced at $t = 3\,\mathrm{s}$. The fault detection algorithm (details in Section 4.1) identifies the faulty phase and applies directly the MT strategy, leading to equal phase currents in Fig. 4.7(c). At $t \approx 6\,\mathrm{s}$, the ML is triggered, producing the same $m_\mathrm{e,ref}$, while keeping the healthy currents unbalanced. Applying the MT optimization comes at the expense of higher total copper losses, when compared with ML [42], as indicated in the resulting stator copper losses p_{Cu} and its average value $\mathrm{avg}(p_{\mathrm{Cu}})$ shown in Fig. 4.7(e).

Finally, the maximally permissible torque reserve for a given fault was identified in [39], where it was proved that there are only 9 unique fault combinations, such that the remaining possible fault combinations would result in the same torque reserve as of those unique faults. The 9 unique faults with their corresponding torque reserve are shown in Fig. 4.8 for the 1N connection.

The available publications focused on optimizing the production of the desired torque, under the following assumptions:

- The neutral configuration 1N is the preferred configuration, owing to its higher torque production in the post-fault case [42, 43];
- The DC-link voltage reserve is not taken into account in the optimization algorithm. This implies that the rated stator voltage would not be surpassed and the machine can be driven at the same speeds as in the healthy case. This assumption is unachievable and critical for some applications, where the drive operates in the overspeed region (i.e. field-weakening (FW)) is inevitable as in E-vehicles [100] or if applied to AWE during reeling-in.

With the aim of covering the aforementioned gaps in literature, the upcoming sections in this chapter take into account the stator voltages as constraints within the MLMT optimization algorithm, which correspondingly relate to the achievable speeds of the drive, as seen in the recent study in [101] which focused only on three-phase induction machines. A comparison between the torque-speed characteristics of the 1N and 2N configurations is carried-out. It will be shown that the 2N connection is capable of extending the overspeed region compared to the 1N connection, which was favoured previously in literature in terms of torque production [39]. Furthermore, a hybrid neutral point connection is proposed to combine the merits of both 1N and 2N connections based on the torque-speed operating point. Although the proposed optimization is carried-out for one open-phase fault (OPF), the presented methodology can be extrapolated to cover the remaining unique OPFs shown in Figs. 4.8(a)-(i) [39].

4.3 Proposed post-fault torque-speed exploitation

4.3.1 Post-fault subspace and phase currents reformulation

The upcoming analysis lays its foundation on the post-fault MLMT optimization in (4.10) and (4.11), which was recently introduced in [43, 97]. The analysis will be derived for the 1N case, which is the general case. By substituting $i_{\mathrm{s}}^{0^+} = i_{\mathrm{s}}^{0^-} = 0$, then the obtained results would correspond to the 2N case.

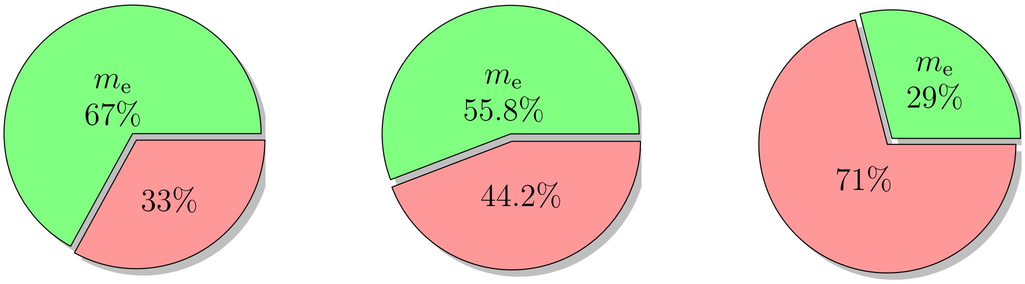

(a) 1 OPF: phase a_1 (b) 2 OPF: phase a_1b_1 (c) 2 OPF: phase a_1a_2

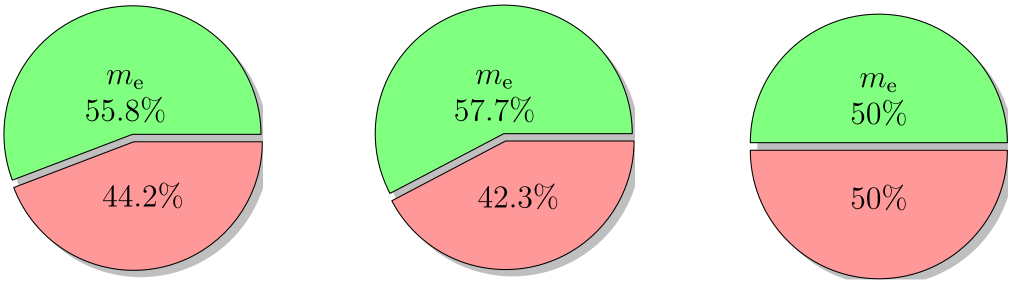

(d) 2 OPF: phase a_1b_2 (e) 2 OPF: phase a_1c_2 (f) 3 OPF: phase $a_1b_1c_1$

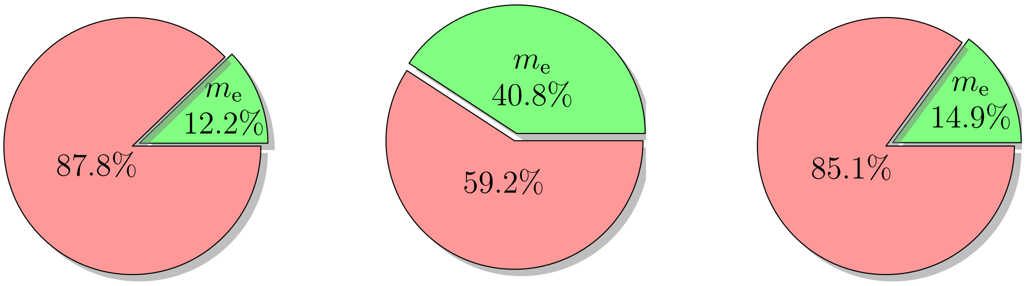

(g) 3 OPF: phase $a_1b_1a_2$ (h) 3 OPF: phase $a_1b_2c_2$ (i) 3 OPF: phase $a_1b_1b_2$

Fig. 4.8. The torque reserve (in 🟢) compared to the derating (in 🔴) corresponding to the unique faults of the 1N connection as described in [39].

Assuming the fault in phase a_1, then by substituting in (2.8)

$$\begin{pmatrix} i_\mathrm{s}^{\alpha} \\ i_\mathrm{s}^{\beta} \\ i_\mathrm{s}^{X} \\ i_\mathrm{s}^{Y} \\ i_\mathrm{s}^{0+} \\ i_\mathrm{s}^{0-} \end{pmatrix} \overset{(2.8)}{=} \frac{1}{3} \begin{bmatrix} 1 & -\frac{1}{2} & -\frac{1}{2} & \frac{\sqrt{3}}{2} & -\frac{\sqrt{3}}{2} & 0 \\ 0 & \frac{\sqrt{3}}{2} & -\frac{\sqrt{3}}{2} & \frac{1}{2} & \frac{1}{2} & -1 \\ 1 & -\frac{1}{2} & -\frac{1}{2} & -\frac{\sqrt{3}}{2} & \frac{\sqrt{3}}{2} & 0 \\ 0 & -\frac{\sqrt{3}}{2} & \frac{\sqrt{3}}{2} & \frac{1}{2} & \frac{1}{2} & -1 \\ 1 & 1 & 1 & 0 & 0 & 0 \\ 0 & 0 & 0 & 1 & 1 & 1 \end{bmatrix} \begin{pmatrix} 0 \\ i_\mathrm{s}^{\mathrm{b}_1} \\ i_\mathrm{s}^{\mathrm{c}_1} \\ i_\mathrm{s}^{\mathrm{a}_2} \\ i_\mathrm{s}^{\mathrm{b}_2} \\ i_\mathrm{s}^{\mathrm{c}_2} \end{pmatrix}, \tag{4.12}$$

one can deduce that by adding the first and third row in (4.12) that

$$i_\mathrm{s}^{0+} = -i_\mathrm{s}^{\alpha} - i_\mathrm{s}^{X}, \tag{4.13}$$

which is a constraint for that particular fault and holds for transient and steady state. Thus, by substituting (4.9) with respect to $\bar{\boldsymbol{i}}_\mathrm{s}^{X}$ in (4.13), one can rewrite

(4.13) at *steady state* as

$$\bar{i}_{\mathrm{s}}^{0+} \overset{(4.9)}{=} -i_{\mathrm{s}}^{\alpha} - (k_X^{\alpha}\,\bar{i}_{\mathrm{s}}^{\alpha} + k_X^{\beta}\,\bar{i}_{\mathrm{s}}^{\beta}) = -(1+k_X^{\alpha})\bar{i}_{\mathrm{s}}^{\alpha} - k_X^{\beta}\,\bar{i}_{\mathrm{s}}^{\beta}. \tag{4.14}$$

Comparing (4.14) with (4.9) with respect to $\bar{i}_{\mathrm{s}}^{0+}$ and given that $i_{\mathrm{s}}^{0^-} = -i_{\mathrm{s}}^{0^+}$, the relation between the subspace currents and $\bar{\boldsymbol{i}}_{\mathrm{s}}^{\alpha\beta}$ can be expressed as [43,97]

$$\begin{pmatrix} \bar{\boldsymbol{i}}_{\mathrm{s}}^{\alpha\beta} \\ \bar{\boldsymbol{i}}_{\mathrm{s}}^{XY} \\ \bar{\boldsymbol{i}}_{\mathrm{s}}^{0} \end{pmatrix} = \underbrace{\begin{bmatrix} 1 & 0 \\ 0 & 1 \\ k_X^{\alpha} & k_X^{\beta} \\ k_Y^{\alpha} & k_Y^{\beta} \\ -1-k_X^{\alpha} & -k_X^{\beta} \\ 1+k_X^{\alpha} & k_X^{\beta} \end{bmatrix}}_{=:\boldsymbol{T}_{\mathrm{k}}' \,\in\, \mathbb{R}^{6\times 2}} \bar{\boldsymbol{i}}_{\mathrm{s}}^{\alpha\beta}, \tag{4.15}$$

such that the phase currents $\bar{\boldsymbol{i}}_{\mathrm{s}}^{a_1\to c_2}$ can be expressed in terms of $\bar{\boldsymbol{i}}_{\mathrm{s}}^{\alpha\beta}$ as [42,43]

$$\bar{\boldsymbol{i}}_{\mathrm{s}}^{a_1\to c_2} \overset{(2.8),(4.15)}{=} \boldsymbol{T}_{\mathrm{VSD}}^{-1}\,\boldsymbol{T}_{\mathrm{k}}'\,\bar{\boldsymbol{i}}_{\mathrm{s}}^{\alpha\beta}. \tag{4.16}$$

Note that (4.15) shows that the optimization matrix $\boldsymbol{T}_{\mathrm{k}}'$ has four variables k_X^{α}, k_X^{β}, k_Y^{α}, and k_Y^{β}. This coincides with the fact that for a 1N configuration and $i_{\mathrm{s}}^{\mathrm{a}_1} = 0$, the system has only four degrees of freedom.

4.3.2 Post-fault voltages

The post-fault analysis studies, at *steady state*, the effect of injecting fundamental currents in the non-torque-producing subspaces. Thus, the study of the voltage evolution in the different subspaces deals only with the fundamental component. The R controllers contribution to the fundamental voltages in every subspace is considered negligible in comparison with the fundamental component [51]. Nevertheless, the harmonic controllers are implemented during the experimental validation, to compensate unwanted harmonics (see Fig. 4.5). Thus, for a given m_{e} and ω_{e}, the post-fault fundamental *steady state* model for the different subspaces can be deduced from (2.10) as

$$\left.\begin{aligned} \boldsymbol{u}_{\mathrm{s}}^{dq} &= R_{\mathrm{s}}\,\boldsymbol{i}_{\mathrm{s}}^{dq} + \omega_{\mathrm{e}}\,\boldsymbol{J}\boldsymbol{\psi}_{\mathrm{s}}^{dq}, \\ \bar{\boldsymbol{u}}_{\mathrm{s}}^{XY} &= R_{\mathrm{s}}\,\bar{\boldsymbol{i}}_{\mathrm{s}}^{XY} + \omega_{\mathrm{e}}\boldsymbol{J}\boldsymbol{L}_{\mathrm{s}}^{XY}\,\bar{\boldsymbol{i}}_{\mathrm{s}}^{XY}, \\ \bar{\boldsymbol{u}}_{\mathrm{s}}^{0} &= R_{\mathrm{s}}\,\bar{\boldsymbol{i}}_{\mathrm{s}}^{0} + \omega_{\mathrm{e}}\boldsymbol{J}\boldsymbol{L}_{\mathrm{s}}^{0}\,\bar{\boldsymbol{i}}_{\mathrm{s}}^{0}, \end{aligned}\right\} \tag{4.17}$$

where

$$\boldsymbol{L}_{\mathrm{s}}^{XY} = \begin{bmatrix} \mathrm{mean}(L_{\mathrm{s}}^{x}) & \mathrm{mean}(L_{\mathrm{m}}^{xy}) \\ \mathrm{mean}(L_{\mathrm{m}}^{yx}) & \mathrm{mean}(L_{\mathrm{s}}^{y}) \end{bmatrix} = \begin{bmatrix} \mathrm{mean}(L_{\mathrm{s}}^{x}) & 0 \\ 0 & \mathrm{mean}(L_{\mathrm{s}}^{y}) \end{bmatrix}. \tag{4.18}$$

The reason for employing $\boldsymbol{L}_{\mathrm{s}}^{XY}$ instead of the non-linear differential inductance matrix $\boldsymbol{L}_{\mathrm{s}}^{xy}$ is that the final results were almost identical; owing to the minor variation of the inductances L_{s}^{x}, L_{s}^{y}, and L_{m}^{yx} (i.e. less than ±10% in Fig. 2.8) through the

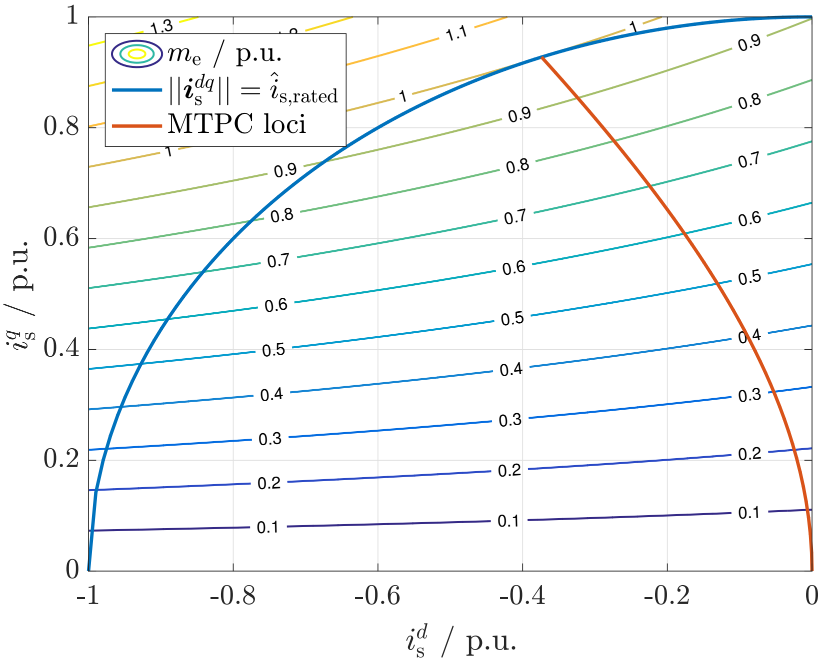

Fig. 4.9. Torque map of the employed ADT-IPMSM, showing the current loci $\boldsymbol{i}_\mathrm{s}^{dq}$ for every torque parabola m_e.

entire operating range. Thus, it would be simpler to employ the approximation in (4.18) to speed up the optimization execution process on Matlab.

It is desired to rewrite the currents $\bar{\boldsymbol{i}}_\mathrm{s}^{XY}$ and $\bar{\boldsymbol{i}}_\mathrm{s}^{0}$ in (4.15) in terms of $\boldsymbol{i}_\mathrm{s}^{dq}$; since the optimizer *fmincon* would be initiated in every iteration with a torque m_e corresponding to a certain dq current parabola. The non linear correlation between $\boldsymbol{i}_\mathrm{s}^{dq}$ and m_e is expressed graphically with the *torque* map, which was computed in Section 3.2.1, and is shown here in Fig. 4.9. After expressing $\bar{\boldsymbol{i}}_\mathrm{s}^{XY}$ and $\bar{\boldsymbol{i}}_\mathrm{s}^{0}$ in terms of $\boldsymbol{i}_\mathrm{s}^{dq}$, the voltage equations in (4.17) would be function of the dq current vetor $\boldsymbol{i}_\mathrm{s}^{dq}$ and the angular speed ω_e, for which the optimizer should compute the corresponding $\boldsymbol{T}_\mathrm{k}^{'}$; to satisfy both the required torque $m_\mathrm{e,ref}$ for every angular speed ω_e. The optimizer sweeps the $\boldsymbol{i}_\mathrm{s}^{dq}$ loci per every torque m_e, to find the minimum current magnitude $||\boldsymbol{i}_\mathrm{s}^{dq}||$ p.u. that would satisfy the desired torque $m_\mathrm{e,ref}$ and ω_e.

Using (4.15) and the phasor representation of the $\alpha\beta$ in terms of the dq variables

$$\bar{\boldsymbol{i}}_\mathrm{s}^{\alpha\beta} \overset{(2.9)}{=} ||\boldsymbol{i}_\mathrm{s}^{dq}|| \begin{pmatrix} \cos(\omega_\mathrm{e}t + \phi_{dq}) \\ \sin(\omega_\mathrm{e}t + \phi_{dq}) \end{pmatrix}, \text{ where } \tan(\phi_{dq}) = \frac{i_\mathrm{s}^{q}}{i_\mathrm{s}^{d}}, \tag{4.19}$$

one can rewrite (4.15) in polar coordinates through mathematical manipulations shown in Appendix B.1, which results in

$$\begin{pmatrix} \bar{\boldsymbol{i}}_{\mathrm{s}}^{\alpha\beta} \\ \bar{\boldsymbol{i}}_{\mathrm{s}}^{XY} \\ \bar{\boldsymbol{i}}_{\mathrm{s}}^{0} \end{pmatrix} \underset{\text{Appendix B.1}}{\overset{(4.15),(4.19)}{=}} ||\boldsymbol{i}_{\mathrm{s}}^{dq}|| \begin{pmatrix} \angle\phi_{dq} \\ \angle(\phi_{dq} - \frac{\pi}{2}) \\ \hat{k}_X^{\alpha\beta}\,\angle(\phi_{dq} - \phi_x) \\ \hat{k}_Y^{\alpha\beta}\,\angle(\phi_{dq} - \phi_y - \frac{\pi}{2}) \\ \hat{k}_{0+}^{\alpha\beta}\,\angle(\phi_{dq} - \phi_0) \\ \hat{k}_{0+}^{\alpha\beta}\,\angle(\phi_{dq} - \phi_0 - \pi) \end{pmatrix}, \tag{4.20}$$

where

$$\left.\begin{array}{lcl} \phi_x & := & \tan^{-1}(k_X^{\beta}/k_X^{\alpha}), \\ \phi_y & := & \tan^{-1}(k_Y^{\alpha}/k_Y^{\alpha}), \\ \phi_0 & := & \tan^{-1}\big(k_X^{\beta}/(1+k_X^{\alpha})\big), \\ \hat{k}_X^{\alpha\beta} & := & \sqrt{(k_X^{\alpha})^2 + (k_X^{\beta})^2}, \\ \hat{k}_Y^{\alpha\beta} & := & \sqrt{(k_Y^{\alpha})^2 + (k_Y^{\beta})^2}, \\ \hat{k}_{0+}^{\alpha\beta} & := & \sqrt{(1+k_X^{\alpha})^2 + (k_X^{\beta})^2}. \end{array}\right\} \tag{4.21}$$

Substituting (4.20) in (4.17), the subspace voltages can be expressed in terms of $\boldsymbol{i}_{\mathrm{s}}^{dq}$ as

$$\left.\begin{array}{lcl} \boldsymbol{u}_{\mathrm{s}}^{dq} & = & R_{\mathrm{s}}\,\boldsymbol{i}_{\mathrm{s}}^{dq} + \omega_{\mathrm{e}}\,\boldsymbol{J}\boldsymbol{\psi}_{\mathrm{s}}^{dq}, \\ \bar{\boldsymbol{u}}_{\mathrm{s}}^{XY} & = & ||\boldsymbol{i}_{\mathrm{s}}^{dq}||\Big(R_{\mathrm{s}}\begin{pmatrix} \hat{k}_X^{\alpha\beta}\,\angle\phi_{dq}-\phi_x \\ \hat{k}_Y^{\alpha\beta}\,\angle\phi_{dq}-\phi_y-\frac{\pi}{2} \end{pmatrix} + \omega_{\mathrm{e}}\boldsymbol{J}\boldsymbol{L}_{\mathrm{s}}^{XY}\begin{pmatrix} \hat{k}_X^{\alpha\beta}\,\angle\phi_{dq}-\phi_x \\ \hat{k}_Y^{\alpha\beta}\,\angle\phi_{dq}-\phi_y-\frac{\pi}{2} \end{pmatrix}\Big), \\ \bar{\boldsymbol{u}}_{\mathrm{s}}^{0} & = & ||\boldsymbol{i}_{\mathrm{s}}^{dq}||\Big(R_{\mathrm{s}}\begin{pmatrix} \hat{k}_{0+}^{\alpha\beta}\,\angle\phi_{dq}-\phi_0 \\ \hat{k}_{0+}^{\alpha\beta}\,\angle\phi_{dq}-\phi_0-\pi \end{pmatrix} + \omega_{\mathrm{e}}\boldsymbol{J}\boldsymbol{L}_{\mathrm{s}}^{0}\begin{pmatrix} \hat{k}_{0+}^{\alpha\beta}\,\angle\phi_{dq}-\phi_0 \\ \hat{k}_{0+}^{\alpha\beta}\,\angle\phi_{dq}-\phi_0-\pi \end{pmatrix}\Big). \end{array}\right\} \tag{4.22}$$

Finally, it is possible to compute the corresponding stator phase voltages by applying the inverse of the VSD matrix in (2.8) leading to

$$\bar{\boldsymbol{u}}_{\mathrm{s}}^{a_1\to c_2} = \boldsymbol{T}_{\mathrm{VSD}}^{-1}\,\bar{\boldsymbol{u}}_{\mathrm{s,VSD}}. \tag{4.23}$$

It is necessary to mention that the unbalance that took place with one or more OPFs may require the application of unbalanced voltages in order to sustain the desired magneto-motive force and, hence, the developed electromagnetic torque. Accordingly, it is essential to ensure that the line-to-line stator voltages of the healthy phases $\bar{\boldsymbol{u}}_{\mathrm{s,2N}}^{ltl}$ for the 2N case

$$\bar{\boldsymbol{u}}_{\mathrm{s,2N}}^{ltl} = \underbrace{\begin{bmatrix} 0 & 1 & -1 & 0 & 0 & 0 \\ 0 & 0 & 0 & 1 & -1 & 0 \\ 0 & 0 & 0 & 0 & 1 & -1 \\ 0 & 0 & 0 & -1 & 0 & 1 \end{bmatrix}}_{=:\boldsymbol{T}_{\mathrm{2N}}^{ltl}\,\in\,\mathbb{R}^{4\times 6}} \bar{\boldsymbol{u}}_{\mathrm{s}}^{a_1\to c_2}, \tag{4.24}$$

and $\bar{\boldsymbol{u}}_{\mathrm{s,1N}}^{ltl}$ for the 1N case

$$\bar{\boldsymbol{u}}_{\mathrm{s,1N}}^{ltl} = \underbrace{\begin{bmatrix} 0 & 1 & -1 & 0 & 0 & 0 \\ 0 & 1 & 0 & -1 & 0 & 0 \\ 0 & 1 & 0 & 0 & -1 & 0 \\ 0 & 1 & 0 & 0 & 0 & -1 \\ 0 & 0 & 1 & -1 & 0 & 0 \\ 0 & 0 & 1 & 0 & -1 & 0 \\ 0 & 0 & 1 & 0 & 0 & -1 \\ 0 & 0 & 0 & 1 & -1 & 0 \\ 0 & 0 & 0 & 0 & 1 & -1 \\ 0 & 0 & 0 & -1 & 0 & 1 \end{bmatrix}}_{=:\boldsymbol{T}_{\mathrm{1N}}^{ltl} \in \mathbb{R}^{10\times 6}} \bar{\boldsymbol{u}}_{\mathrm{s}}^{a_1 \to c_2}, \tag{4.25}$$

would not exceed the rated peak value $\hat{u}_{\mathrm{s,rated}}^{ltl}$, which determines the required u_{dc} through the relation [73]

$$u_{\mathrm{dc}} \geq \frac{2}{\sqrt{3}} \hat{u}_{\mathrm{s,rated}}^{ltl}. \tag{4.26}$$

Practically, the DC-link voltage u_{dc} is normally set higher $\frac{2}{\sqrt{3}}\hat{u}_{\mathrm{s,rated}}^{ltl}$; since that limit assumes linear operation of VSIs, which is not the case owing to the nonlinear characteristics of the inverter semiconductor switches and neglected dead-time effects [73].

In (4.24), the line-to-line voltages $\bar{\boldsymbol{u}}_{\mathrm{s,2N}}^{ltl}$ consider the voltages of the two three-phase sets separately; since the neutral points are isolated. As for (4.25), all possible voltage combinations, excluding the faulty phase(s) should be considered, owing to the unbalanced voltages in the post-fault operation. Taking such voltages $\bar{\boldsymbol{u}}_{\mathrm{s,1N}}^{ltl}$ and $\bar{\boldsymbol{u}}_{\mathrm{s,2N}}^{ltl}$ into account ensures also that the dual three-phase inverter will not be driven into the over-modulation region [55].

4.3.3 Post-fault optimization

The proposed post-fault optimization adopts the same constraints for the MLMT strategy in (4.11) with the same objective function in (4.10). Additionally, the terminal voltages for the 1N and 2N connections $\bar{\boldsymbol{u}}_{\mathrm{s,1N}}^{ltl}$ and $\bar{\boldsymbol{u}}_{\mathrm{s,2N}}^{ltl}$, respectively, are added additionally as constraints so as not to exceed the rated value $\hat{u}_{\mathrm{s,rated}}^{ltl}$ for a given torque $m_{\mathrm{e,ref}}$ and speed ω_{e}. Thus, the optimization function

$$\min_{\boldsymbol{T}_{\mathrm{k}}'} \; p_{\mathrm{Cu}} = \frac{(\boldsymbol{i}_{\mathrm{s}}^{\gamma_{\mathrm{h}}})^\top \boldsymbol{i}_{\mathrm{s}}^{\gamma_{\mathrm{h}}}}{6(i_{\mathrm{s,rated}})^2}, \quad \forall \;\; \gamma_{\mathrm{h}} \in \mathbb{S}_{\mathrm{h}}, \tag{4.27}$$

is subject to the following constraints:

$$
\left.
\begin{array}{ll}
g_1: & i_{\mathrm{s}}^{\gamma_{\mathrm{f}}}=0, \quad \forall\ \gamma_{\mathrm{f}} \in \mathbb{S}_{\mathrm{f}} \\
g_2: & \begin{cases} \sum\limits_{\gamma_{\mathrm{h}}} i_{\mathrm{s}}^{\gamma_{\mathrm{h}}}=0 & \text{1N case,}\\ \sum\limits_{\gamma_1\in\{a_1,b_1,c_1\}} i_{\mathrm{s}}^{\gamma_1}=0 \text{ and } \sum\limits_{\gamma_2\in\{a_2,b_2,c_2\}} i_{\mathrm{s}}^{\gamma_2}=0, & \text{2N case,}\end{cases}\\
g_3: & m_{\mathrm{e}}=m_{\mathrm{e,ref}},\\
g_4: & ||\boldsymbol{i}_{\mathrm{s}}^{\gamma_{\mathrm{h}}}||_\infty \leq \hat{i}_{\mathrm{s,rated}},\\
g_5: & \begin{cases} ||\bar{\boldsymbol{u}}_{\mathrm{s,1N}}^{ltl}||_\infty \leq \hat{u}_{\mathrm{s,rated}}^{ltl}, & \text{1N case,}\\ ||\bar{\boldsymbol{u}}_{\mathrm{s,2N}}^{ltl}||_\infty \leq \hat{u}_{\mathrm{s,rated}}^{ltl}, & \text{2N case,}\end{cases}
\end{array}
\right\}
\tag{4.28}
$$

Compared to MLMT strategy in (4.11) [43], the constraint g_5 has been introduced to take into account the effect of the limited voltage reserve, especially when the machine is driven into the field-weakening (FW) region. Considering g_5, unlike in [43,97], will achieve in the post-fault operation limited speeds per every permissible torque, termed $\Omega_{\mathrm{e}}^{\mathrm{MTPC}}$, which defines the loci of the maximum speeds corresponding to the MTPC criteria. The maximum FW speed trajectories for every torque is termed $\Omega_{\mathrm{e}}^{\mathrm{FW}}$, while the maximum achievable speed within $\Omega_{\mathrm{e}}^{\mathrm{FW}}$ is $\omega_{\mathrm{e,max}}^{\mathrm{FW}}$, which is the maximum FW speed at no-load.

The optimization begins by setting the reference torque $m_{\mathrm{e,ref}}=0$ and loading the corresponding $\boldsymbol{i}_{\mathrm{s}}^{dq}$ loci for such torque. The algorithm is initialized with $\boldsymbol{i}_{\mathrm{s}}^{dq}$ at the MTPC point. Starting from standstill, ω_{e} is varied while ensuring the constraints in (4.28) are satisfied and recording the parameters in $\boldsymbol{T}_{\mathrm{k}}^{'}$. Moreover, the remaining $\boldsymbol{i}_{\mathrm{s}}^{dq}$ points are swept and the corresponding parameters in $\boldsymbol{T}_{\mathrm{k}}^{'}$ are stored. Afterwards, the reference torque is increased while repeating the similar process, as previously explained, till reaching the point that the initializing MTPC point does not satisfy g_4. The proposed optimization is summarized in the flowchart shown in Fig. 4.10(a) with the aid of Fig. 4.10(b). In Fig. 4.10(a), the decision block for $g_1 \rightarrow g_3$ is to ensure that the constraints g_1 and g_2 of the physical system are not violated, as well as the produced torque matches $m_{\mathrm{e,ref}}$ (i.e. g_3), when searching for a feasible $\boldsymbol{T}_{\mathrm{k}}^{'}$. By running the optimization function *fmincon* in Matlab, it was concluded that failure to find a feasible $\boldsymbol{T}_{\mathrm{k}}^{'}$ per every iteration would result from violating g_4 and/or g_5. The post-processing of the optimization involves plotting Figs. 4.11-4.15 for 1N and 2N, extraction of the $\Omega_{\mathrm{e}}^{\mathrm{MTPC}}$ and $\Omega_{\mathrm{e}}^{\mathrm{FW}}$ loci, and the maximal speed limit $\omega_{\mathrm{e,max}}^{\mathrm{FW}}$. The outcomes of such optimization are detailed in the next section.

4.3.4 Torque-speed characteristics

Upon completing the described optimization in Section 4.3.3, the relation between the permissible torques, speeds, currents and the corresponding parameters in $\boldsymbol{T}_{\mathrm{k}}^{'}$ can be graphically represented in Figs. 4.11-4.15, respectively. Figs. 4.11(a)-(b) highlight in 🟦 the post-fault FW permissible region of the 1N and 2N connections, respectively. The current loci indicated by "*" represent the feasible loci for the MLMT strategy [43]. The derating is clear with respect to the pre-fault (i.e. healthy) case.

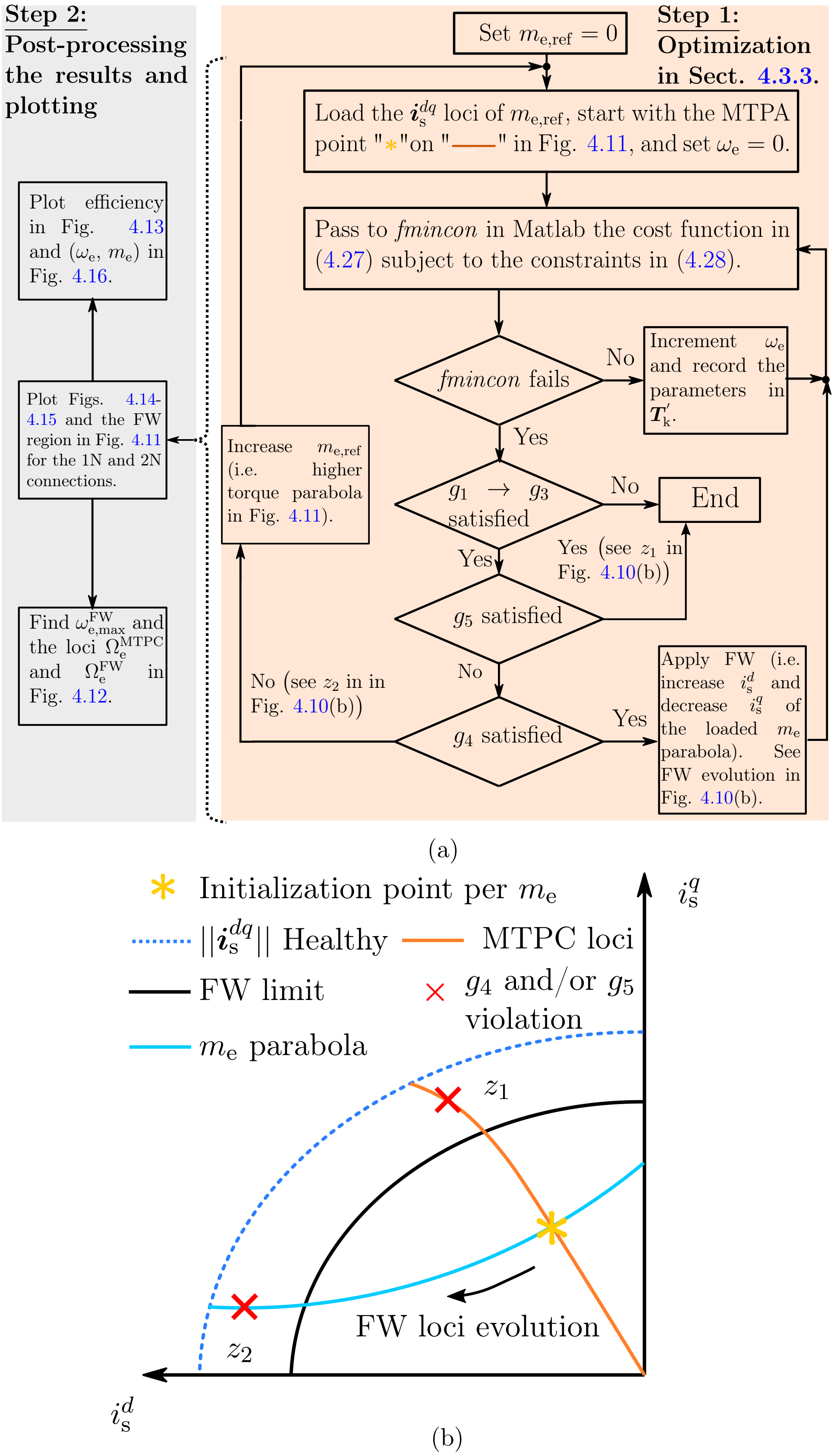

Fig. 4.10. (a) Post-fault flowchart of the proposed optimization applied for the 1N and 2N configurations along with (b) an exemplary representation showing the evolution of $\boldsymbol{i}_s^{dq}$ points for a loaded m_e parabola. Points similar to z_1 (i.e. on the MTPC loci and beyond the FW limit) violate g_5 in (4.28), while points similar to z_2 (i.e. on the FW loci and beyond the FW limit) violate g_4 and g_5.

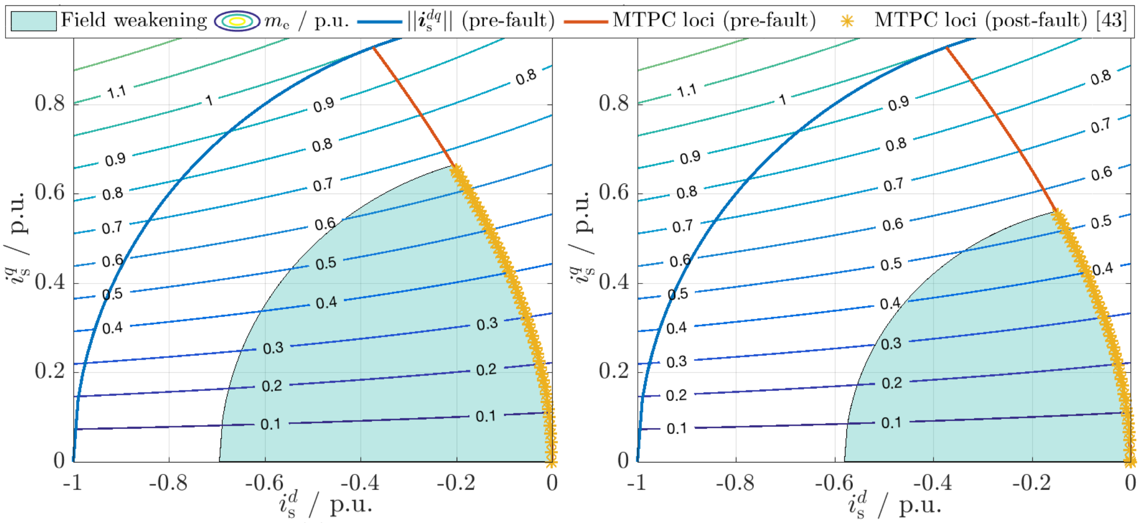

(a)

(b)

Fig. 4.11. Post-fault $\boldsymbol{i}_s^{dq}$ loci comparison between the presented post-fault algorithm in [43] and proposed optimization in Section 4.3.3, which covers additionally the FW region of (a) 1N and (b) 2N neutral configurations.

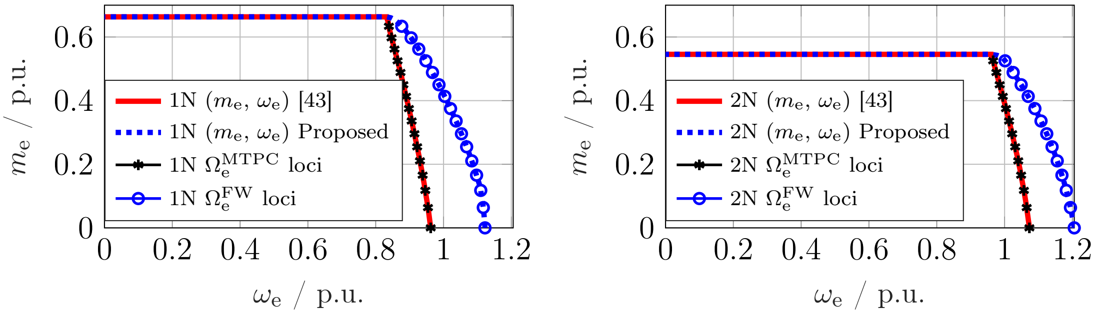

(a)

(b)

Fig. 4.12. Post-fault comparison of the permissible $(m_e,\ \omega_e)$ characteristics between the presented algorithm in [43] and proposed optimization in Section 4.3.3 with respect to the (a) 1N and (b) 2N neutral configurations, showing the enhancement in terms of extending the permissible speed ranges.

The fact that the 1N connection covers a larger operating area within the dq current loci in Fig. 4.11(a), in comparison with the 2N connection in Fig. 4.11(b), adheres to the drawn conclusions in [39, 42, 43], that the torque reserve for the 2N connection would be lower than that of the 1N connection. Defining $m_{e,\max}$ as the maximum torque for a given neutral point configuration, the torque per ampere capability of the 1N is superior with a recorded $m_{e,\max}$, which is 22% higher than that of the 2N connection.

On the other hand, the achievable maximum speeds (i.e. Ω_e^{MTPC} and Ω_e^{FW}) in Fig. 4.12(a) are inferior to the 2N case as illustrated in Fig. 4.12(b). This is due to the fact that the available voltage reserve is distributed among the dq and XY subspaces in the 2N connection, compared to the 1N case, which additionally regulates the *zero* subspace. This property is crucial, when the demanded speeds and/or the constant power range (i.e. in the FW mode) are as critical as the applied electromagnetic torque, as for EV [100] and AWE during reeling-in [23, 27, 82]. Compared to the

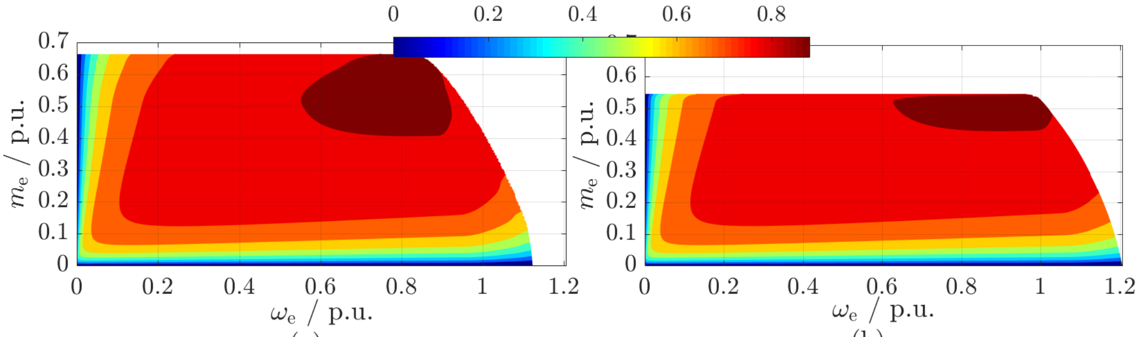

(a) (b)

Fig. 4.13. Post-fault efficiency maps of (a) 1N and (b) 2N connections within the (m_e, ω_e) range of the proposed optimization in Section 4.3.3.

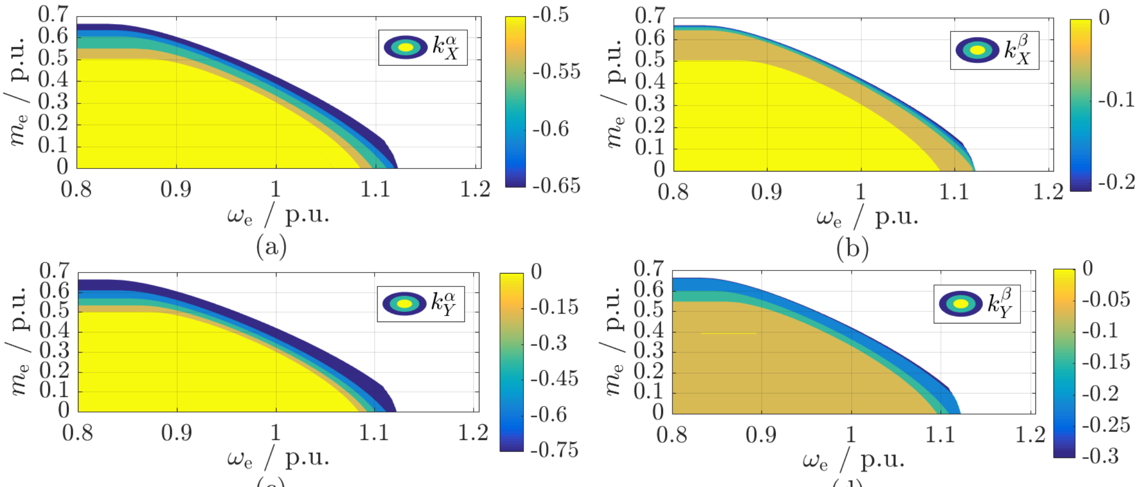

(a) (b) (c) (d)

Fig. 4.14. Post-fault parameters in $\boldsymbol{T}_k'$ within the FW region for the 1N connection (see FW region in Fig. 4.11(a)) computed using the proposed optimization in Section 4.3.3: (a) k_X^α, (b) k_X^β, (c) k_Y^α, and (d) k_Y^β.

1N optimization in [43], the proposed optimization in (4.27) and (4.28) extends the speed range for the 1N and 2N connections by 16.64% and 25.23%, respectively, when comparing $\omega_{\mathrm{e,max}}^{\mathrm{FW}}$ to the speed corresponding to the operating point of $m_{\mathrm{e,max}}$, which is the maximum operating point obtained in [39, 42, 43]. It is worth to mention that the maximum achievable speed in the healthy case for the employed ADT-IPMSM is 1.43 p.u.; owing to the distributed winding configuration and high characteristic current (i.e. d-axis current required to diminish the PM flux), is approximately 11 times the current $\hat{i}_{\mathrm{s,rated}}$ in Table 2-I.

Since the speed is taken into account in the presented study, it is of interest to illustrate the post-fault efficiency maps for both connections. Figs. 4.13(a)-(b) show the variation of the experimentally-identified efficiency throughout the permissible operating range for both the 1N and 2N connections, respectively. The electrical losses used in calculating the efficiency were limited to the stator copper losses. Core losses were neglected since they become significant only at high operational speeds, which is not the case here [58]. It was found out that the difference in efficiency be-

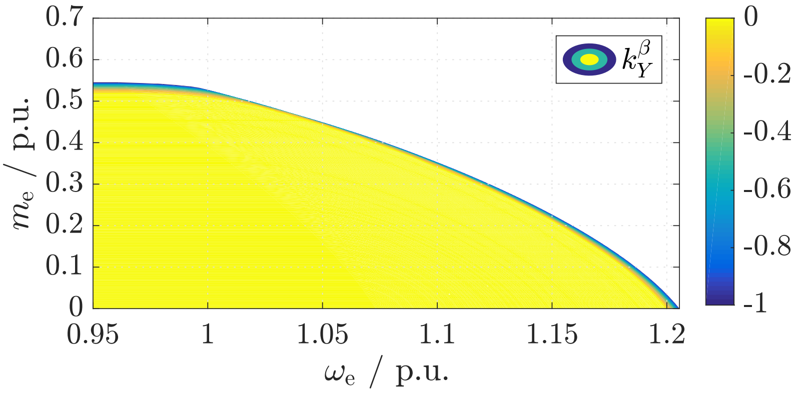

Fig. 4.15. Post-fault k_Y^β within the FW region for the 2N connection (see FW region in Fig. 4.11(b)) computed using the optimization in Section 4.3.3.

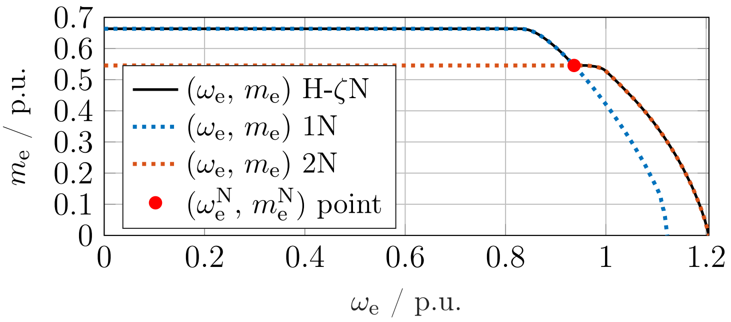

Fig. 4.16. Post-fault $(m_e,\ \omega_e)$ characteristics 1N, 2N, and H-ξN connections.

tween both connections is minor within the common $(m_e,\ \omega_e)$ loci. Nevertheless, it was concluded that the 1N connection achieves higher efficiency at low-speed/high-torque regions in comparison with the 2N connection which achieves relatively higher efficiencies at high speeds. Owing to the additional degree of freedom of the 1N connection for a given torque, the optimization selects lower values for the parameters of $\boldsymbol{T}_k^{'}$ compared to the 2N connection case. Thus, at low-speed/high-torque operation, the magnitude of the $\boldsymbol{i}_s^{XY}$ and $\boldsymbol{i}_s^0$ currents of the 1N connection are lower than that of $\boldsymbol{i}_s^{XY}$ of the 2N connection.

The corresponding parameters in $\boldsymbol{T}_k^{'}$ for both neutral point connections in the FW mode are indicated in Figs. 4.14-4.15, which represent the necessary variations throughout points to satisfy the constraints in (4.28). For the 2N case, since $i_s^{0+} = i_s^{0-} = 0$, then substituting in (4.14) results in $k_X^\alpha = -1$, $k_X^\beta = 0$. The optimization output in terms of k_Y^β is shown in Fig. 4.15, while $k_Y^\alpha = 0$ was considered by the optimizer the optimum value throughout the entire operating range. From a real-time implementation point of view, the 2N connection could be favourable owing to the lower memory requirements; as only k_Y^β needs to be saved as a look-up-table (LUT) compared to the 1N connection (i.e. k_X^α, k_X^β, and k_Y^α should be additionally stored as well).

It is possible to combine the merits of both neutral point connections by installing a neutral point switch altering between 1N or 2N connections (see Fig. 2.3), leading to a hybrid neutral point connection termed H-ξN, where $\xi \in \{1, 2\}$. Accordingly,

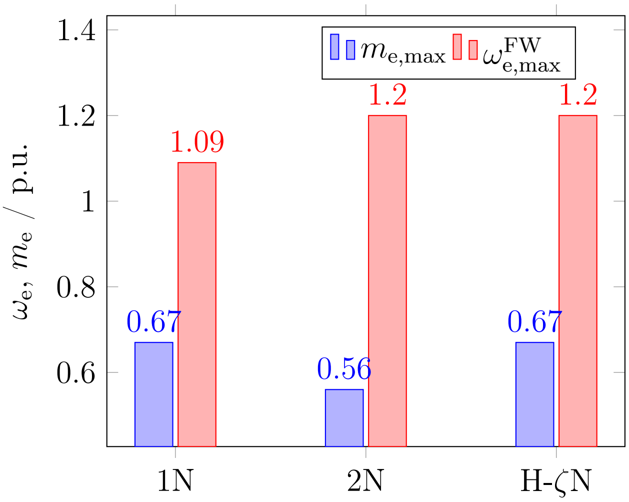

Fig. 4.17. Post-fault comparison between the exploited torque-speed limits of the proposed H-ζN connection and those achieved by the 1N and 2N connections upon applying the optimization in Section 4.3.3.

torque-speed characteristics are shown in Fig. 4.16, where both the maximum torque and speed of the 1N and 2N connections are realized. The highlighted intersection point "●" ($\omega_{\mathrm{e}}^{\mathrm{N}}$, $m_{\mathrm{e}}^{\mathrm{N}}$) in Fig. 4.16 represents the boundary point separating the H-1N and H-2N connections, where the ADT-IPMSM operates in the 1N mode only if $\omega_{\mathrm{e}} < \omega_{\mathrm{e}}^{\mathrm{N}}$ OR $m_{\mathrm{e}} > m_{\mathrm{e}}^{\mathrm{N}}$. Otherwise, the 2N connection is selected. Accordingly, the parameters of $\boldsymbol{T}_{\mathrm{k}}^{'}$ are selected as shown in Figs. 4.14 and 4.15 depending on the selected neutral point. Further illustrations are shown in the experimental results in Section 4.4. Finally, the maximum limits in terms of torque-speed for 1N, 2N, and H-ξN are illustrated as a bar plot shown in Fig. 4.17. It is clear that the proposed H-ζN connection combines both merits of 1N and 2N configurations, maximizing the drive's torque and speed capability in the post-fault operation.

4.4 Experimental results

The proposed post-fault optimization, employs the same control structure in Fig. 4.5; to validate experimentally the proposed post-fault optimization for $i_{\mathrm{s}}^{\mathrm{a}_1} = 0$. The line-to-line voltages $\bar{\boldsymbol{u}}_{\mathrm{s,1N}}^{ltl}$ and $\bar{\boldsymbol{u}}_{\mathrm{s,2N}}^{ltl}$ for the 1N and 2N connections, respectively, were computed based on the reference voltages $\boldsymbol{u}_{\mathrm{s,ref}}^{\mathrm{a}_1 \rightarrow \mathrm{c}_2}$ in Fig. 4.5.

4.4.1 Validating the post-fault strategy for the 1N connection

The presented optimization is tested first for the 1N connection shown in Fig. 4.18, where the torque is set to 0.6 p.u., such that the speed reference is varied in Fig. 4.18(a) in steps, corresponding to points lying on $\Omega_{\mathrm{e}}^{\mathrm{MTPC}}$ and $\Omega_{\mathrm{e}}^{\mathrm{FW}}$ loci. Afterwards, the speed is set to the maximum permissible speed $\omega_{\mathrm{e,max}}^{\mathrm{FW}}$ for the 1N connection, which in return nullifies the generated torque. This is evident by the i_{s}^{q} current in Fig. 4.18(b). If the operating point was set to the maximum permissible torque of ≈ 0.67 p.u., then operating speed points on the loci $\Omega_{\mathrm{e}}^{\mathrm{MTPC}}$ and $\Omega_{\mathrm{e}}^{\mathrm{FW}}$ would be identical. Owing to the employed control structure in Fig. 4.5, the stator

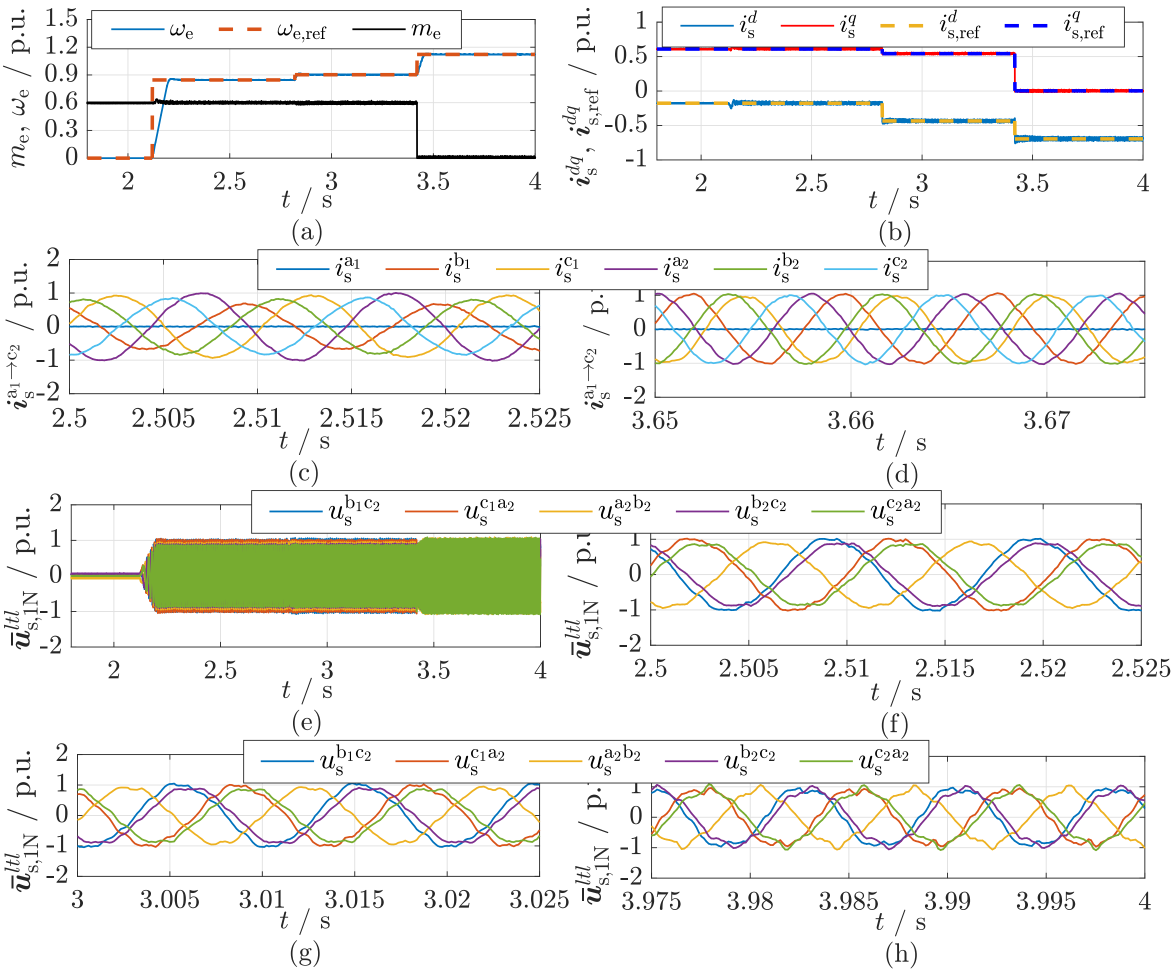

Fig. 4.18. Post-fault operation results of the proposed optimization for the 1N connection: (a) speed and torque, (b) dq currents, (c)-(d) stator currents at Ω_e^{MTPC} and maximum Ω_e^{FW}, the corresponding significant line-to-line voltages in (e) along with the zoomed versions in (f)-(h).

currents track the fundamental component while compensating the unwanted harmonics, as seen in the Figs. 4.18(c)-(d). On the other hand, the most significant line-to-line voltages of $\bar{\boldsymbol{u}}_{s,1N}^{ltl}$ (i.e. voltages approaching 1 p.u.) in (4.25), are observed in Fig. 4.18(e), with their zoomed plots in Figs. 4.18(f)-(h). For different time intervals, depending on the m_e and ω_e variations, the parameters of $\boldsymbol{T}_k^{'}$ manipulate the subspace currents to keep the voltages within 1 p.u. (i.e. satisfying g_5 for the 1N case) as well as satisfying g_4, validating the proposed post-fault optimization for the 1N connection. It should be noted that the line-to-line voltage distortions increase with speed (see Figs. 4.18(g)-(h)). This is due to the increased control action of the harmonic controllers, which distorts the reference voltages $\boldsymbol{u}_{s,ref}^{a_1 \to c_2}$ (see Fig. 4.5) to force sinusoidal currents $\boldsymbol{i}_s^{a_1 \to c_2}$ through the stator terminals [51].

4.4.2 Validating the post-fault strategy for the 2N connection

For the 2N neutral configuration, a lower torque reference 0.4 p.u. has been set; since a torque reference of 0.6 p.u. would violate g_4 (see the point z_1 "×" in Fig. 4.10(b)). To achieve the maximum possible speed $\omega_{e,max}^{\mathrm{FW}}$ for the 2N case, the maximum current

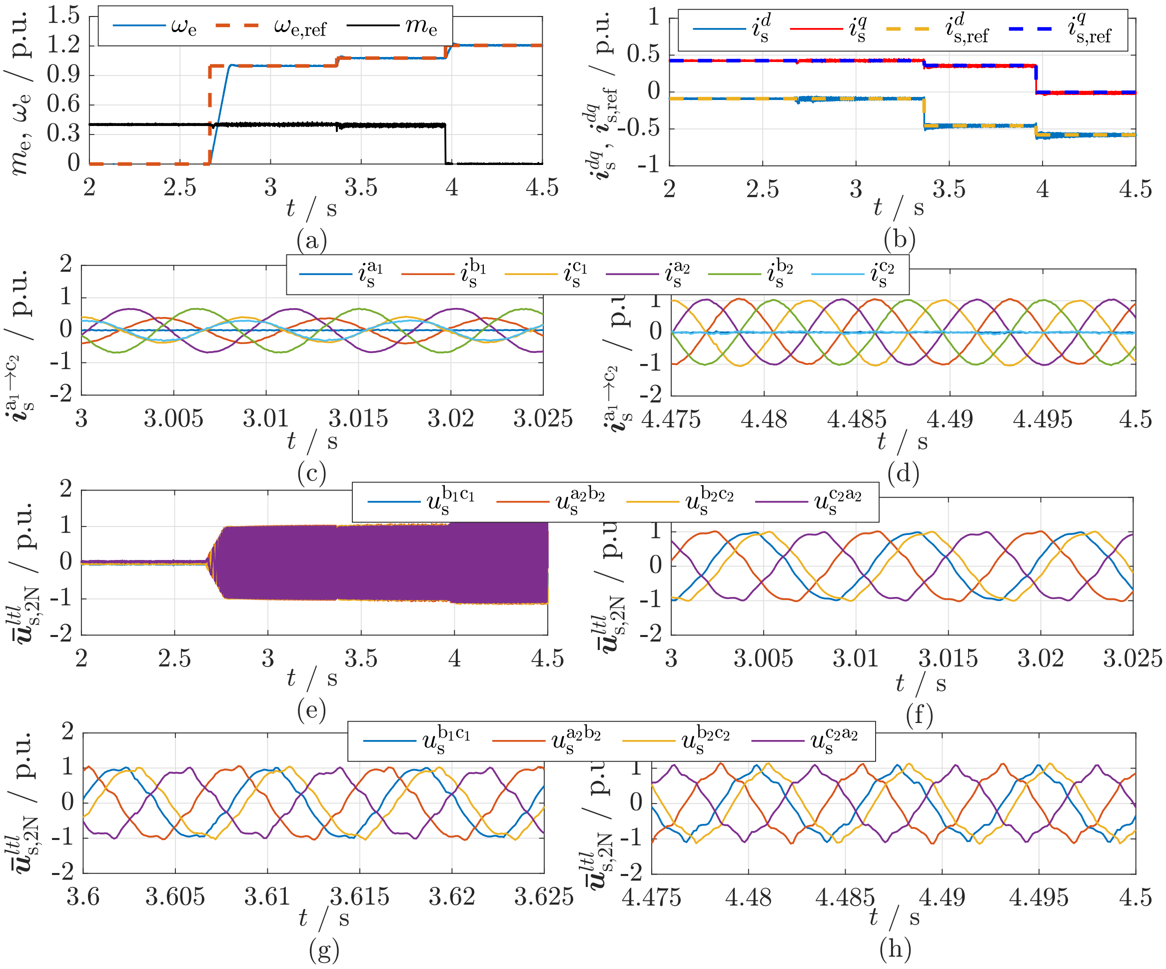
(a) (b) (c) (d) (e) (f) (g) (h)

Fig. 4.19. Post-fault operation results of the proposed optimization for the 2N connection: (a) speed and torque, (b) dq currents, (c)-(d) stator currents at Ω_e^{MTPC} and maximum Ω_e^{FW}, the corresponding line-to-line voltages in (e) along with the zoomed versions in (f)-(h).

vector was set in the d current direction, as seen in Fig. 4.19(b). The stator line-to-line voltages in that case are shown in Fig. 4.19(e), with their zoomed versions in Figs. 4.19(f)-(h). When the machine is brought to its maximum speed limit, the voltages distortions increase, as seen in Fig. 4.19(h), to inject sinusoidal stator currents shown in Fig. 4.19(d). Owing to the harmonic controllers, the line-to-line voltage vector $\bar{\boldsymbol{u}}_{s,2N}^{ltl}$ at $\omega_{e,\max}^{\mathrm{FW}}$ in Fig. 4.19(h) tends to exceed the 1 p.u. range, yet in a limited range (i.e. 1.04 p.u.), which is mitigated by raising the PWM voltage limit through the DC-link voltage u_{dc} by only 4%. It is worth to mention that even if a high percentage of over-voltage is allowed (at least for low voltage motors), a significant imminent danger is not overseen; since the winding insulation is usually designed to withstand much higher voltages than the rated one. However, over-voltage operations tend to increase the leakage current to ground point through the bearings, which in turn decrease their average lifetime (i.e. operating hours) [102].

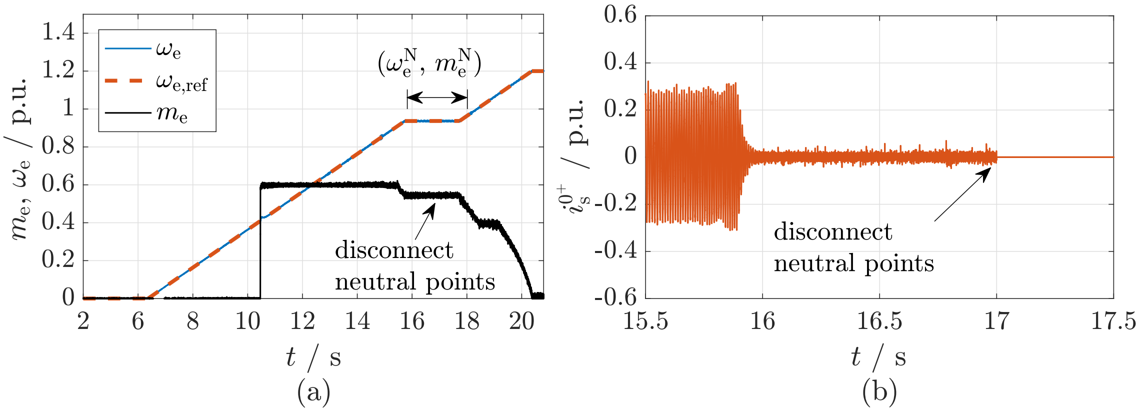

Fig. 4.20. Post-fault H-ζN operation showing (a) the torque-speed profile highlighting the (ω_e^N, m_e^N) points and the instant of disconnecting the neutral points, which is evident in (b) showing i_s^{0+} before and after disconnection according to the explained sequence in Section 4.4.3.

4.4.3 Validating the hybrid neutral point connection

Next, the merits of both 1N and 2N connections in Sections 4.4.1 and 4.4.2, respectively, are realized by the proposed H-ζN connection, which is tested experimentally in Figs. 4.20(a)-(b). The speed ramps up from standstill to the $\omega_{e,max}^{FW}$ of the 2N case (i.e. $\omega_{e,max}^{FW} = 1.2$ p.u.), while the applied torque combines those operating points of 1N and 2N tests (i.e. 0.6 p.u. and 0.4 p.u.), as seen in Fig. 4.20(a). The neutral point breaker should be switched ON/OFF depending on the location of the operating point in Fig. 4.16 with respect to (ω_e^N, m_e^N) point, as explained in Section 4.3.4 and in Fig. 4.16. When the neutral point connection is set to H-2N, then the *zero* frame controller is deactivated and vice-versa for the H-1N case. Practically, to avoid switching in the presence of neutral currents when changing from H-1N to H-2N connection, the controller first switches to the parameters in $\boldsymbol{T}_k'$ of the 2N connection; sets $\boldsymbol{i}_{s,ref}^0 = 0$; then the neutral switch state is toggled; and finally the *zero* sequence controller is deactivated (see Fig. 4.20(b)). Indeed, improved practical neutral points toggling schemes could be studied, such as faster toggling scheme and/or introducing hysteresis band to avoid chattering, if the operating point is located near (ω_e^N, m_e^N). However, such toggling strategies will be considered in future work. The objective is to illustrate the philosophy of neutral point switching and its effect on both torque and speed. Since the neutral point controls the flow of only $\boldsymbol{i}_s^0$, it is expected that toggling the neutral point status would not affect the electromechanical torque, as shown in Fig. 4.20(a).

Chapter 5

Conclusions and outlook

5.1 Conclusions

In addition to the intuitively obvious dependence of energy consumption on population, there exists a well-established correlation between energy consumption and the economic well-being of a nation. Owing to the limited fossil fuel resources, stimulated by global warming, climate change and water drought, the strive for efficient, reliable and unlimited energy alternatives provoked modifications not only on a scientific level, but also on national and international policies. The last decade witnessed the meetings of world-leaders; to lay down stringent policies in terms of energy production and consumption, which accordingly pushed the boundaries of renewable energy penetration in modern life. Airborne wind energy systems demonstrated *theoretically* strong potential as a highly efficient cost-effective replacement for conventional wind turbines, promoting them to be one of the most reliable renewable energy sources in the future energy market. However, several highly correlated design, operational and engineering aspects hinder the commercialization of such technology and a suitable compromise has not been proved yet. One of those challenges, from an electrical point of view, is the selection of a highly efficient and fault-tolerant electrical drive, especially for those AWE concepts based on reel-in/out for power generation. The on-going trend of employing the same topology of three-phase electrical drives as those for conventional wind turbines (CWT)s is *non-optimal* due to the following:

- When safety measures are embraced for the most common faults as those of CWTs, the faulty part is disconnected leading to a single phase machine, which is non-self-starting and incapable of reversing rotation direction;
- Significant vibratory behavior due to the associated huge torque ripples of single-phase machines;
- Derating up to $\approx 33\%$ of the pre-fault condition to avoid substantial overheating;
- Difficulty of invoking encoderless technique to determine the initial stand-still position of the machine; owing to the ongoing trend of selected machines of

either surface-mounted permanent magnet (SPMSM) machines or induction machines. Thus, either additional back-up encoders are installed or face the possibility of complete system shutdown, since the encoder is considered a single source of failure.

Moreover, some companies tend to install an entire back-up drive just for the sake of fault tolerance enhancement, which is neither a cost-effective solution nor optimal when limited installation space would be a requirement. Furthermore, precise modelling and control of the electrical drive were not considered a priority within the ongoing design procedures at the industrial partners, even though optimized electrical generation meant maximizing the life time and minimizing failures. Within the AWESCO project, industrial partners imposed drastic simplifications and assumptions in terms of the electrical drive capabilities, which could not represent real-life scenarios.
Motivated by such limitations, this thesis tackled - by selecting an appropriate machine topology - the aforementioned AWE challenges from several aspects:

- Efficiency enhancement by adopting an interior PMSM (IPMSM) instead of SPMSM and appropriate optimal feed-forward control;
- IPMSM facilitates the adoption of encoderless control, thus, removing one of the two single sources of failures;
- Enhancing immensely the fault-tolerance capability due to the proposed rewinding of a standard three-phase IPMSM into an asymmetrical dual-three phase IPMSM (ADT-IPMSM); and
- Improved operation during healthy condition with low torque ripples (i.e. lower acoustic noise);

From an electrical drive perspective, the contribution of this thesis is related to the ADT-IPMSM drive in terms of pre- and post-fault modelling and control in the following aspects:

- Chapter 2 provided the mathematical non-linear modelling of ADT-IPMSM and the followed procedure to precisely reproduce through simulations the experimental results obtained from the available test-bench. Thus, the ADT-IPMSM can be easily augmented within the complete model of an AWE plant;
- Chapter 3 designs a fast tracking efficient stator current controller based on the developed mathematical model in Chapter 2. Moreover, since the electrical drives of AWES are often torque controlled, a proposed feedforward torque controller was proposed based on the non-linear models in Chapter 2. The proposed feedforward torque controller ensures minimum stator copper losses as well as precise torque production according to the desired reference torque. On the other hand, the control of the dual-three phase inverter in terms of dispatching the reference voltage through a modified space-vector modulation was derived. The proposed technique is simple and can be implemented on modest real-time platforms;

- Chapter 4 discusses the fault detection and post-fault operation of the adopted drive, where the proposed optimization strategy exploits the full torque-speed characteristics of the dual three-phase IPMSM drive, which was not covered by literature. Furthermore, the proposed post-fault optimization expands the torque and speed limits of the drive compared to the available body of literature concerning fault tolerance of such drives;

A 2.5 kW ADT-IPMSM validated the aforementioned contributions.

5.2 Outlook and future work

Even though the main challenges in terms of modelling and control of an ADT-IPMSM drive were tackled in this thesis, there is still room for improvement and enhancement, which should be taken into account in future work:

- Design a stator current controller not per subspace assuming ideal decoupling, but rather a controller that would dispatch directly its reference voltage taking into account the possible correlation between the different subspaces;

- Consider other winding topologies for dual three-phase machines, such as symmetrical windings, since asymmetrical winding configurations could not be always guaranteed to be realized from a standard three-phase machine. The symmetrical windings, on the other hand, could be realized on any three-phase machine;

- Employing dual three-phase inverters with higher number of levels when targeting AWE systems in the high kW and MW ranges, due to improved output voltage waveforms and increased power ratings. In particular, multi-level VSI topologies are capable of reaching high output voltage amplitudes by using standard power switches with low voltage ratings [103,104]. It is worth to mention that modular multilevel converters (MMC) topologies are viable solutions for enhancing both the performance, reliability as well as the reduction the switching losses [105]. Finally, a comparison with the proposed ADT-IPMSM topology in this thesis must be drawn to justify the added complexity with its merits and demerits;

- Scrutinize techniques and observers that tend to track the evolution of the non-linearity effects of the ADT-IPMSM machine and update the corresponding flux linkage and differential inductance dependent-schemes accordingly. This will eventually ensure a robust controller throughout the lifetime of the drive;

- Investigating further encoderless and sampling techniques as in [106], as an alternative to the high frequency injection method, thus lower acoustic noise and lower torque ripples would occur;

- Augmenting DC-link voltage estimators to enhance the reliability of the drive and lower its susceptibility to complete shutdown [107];

- Adopting energy storage systems like batteries or flywheel systems along with their appropriate introduction at the DC-link side [108–110]. Such adoption aims at enhancing the fault-tolerance capability of the drive and reducing the risk of complete shutdown, since a DC-link fault is classified as a single source of failure; and

- Enhance the speed and/or techinique of the neutral point disconnection scheme, compared to that used in the post-fault technique in Section 4.4.3, as well as develop a hysteresis band to prevent chattering near the toggling point between the 1N and 2N controllers.

Appendix A

ADT-IPMSM Test-bench

In order to validate practically the theoretical findings and derivations presented in this thesis, a 2.5 kW hardware-in-the loop (HiL) test bench was assembled in the laboratory. The detailed components of the HiL system is described in details in the following sections.

A.1 Prime mover

A standard three-phase induction machine (IM) has been coupled to the ADT-IPMSM under study as shown in Fig. A.1-1; to act as a prime mover, mimicking the kite or aircraft of a typical pumping AWE system. The IM parameters are shown in Table A.1-I. The IM is controlled via standard direct field-oriented control as in [60,62], while the ADT-IPMSM is torque controlled as explained in Section 3.2.1.

Table A.1-I. Parameters of the induction machine, used as a prime mover in the HiL setup.

Parameter	Value
Stator resistance	$2.3\,\Omega$
Rotor resistance	$1.55\,\Omega$
Pole-pair	1
Rated stator peak current	8.1 A
Rated stator peak voltage	327 V
Rated flux (amplitude)	1.2 Wb
Rated speed	298.4 rad/s
Rated torque	10.05 N m
Rated power factor	0.93
Magnitizing inductance	340 mH
Stator leakage inductance	16.5 mH
Rotor leakage inductance	16.5 mH

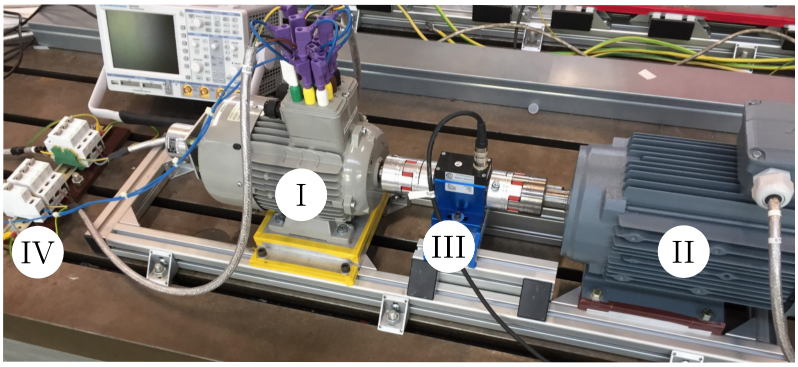

Fig. A.1-1. Test bench: (I) ADT-IPMSM, (II) induction machine (i.e. prime mover), (III) torque sensor, and (IV) stator and neutral points circuit breakers.

A.2 Asymmetrical dual three-phase IPMSM

For machines with distributed windings, if the number of phases is divisible by three, then the multi-phase machine can be realized out of a conventional three-phase machine through rewinding of the stator [55], which is the case in this thesis. Although the thesis is concerned with ADT-IPMSM drives, the following rewinding procedure is independent from the type of the employed AC machine. In other words, it can be employed as well for rewinding of induction machines or other types of PM-based drives as SPMSM or reluctance synchronous machines. It is crucial to identify in advance the machine ratings and few of its machine design parameters to be capable of drawing the new dual three-phase winding layout. Moreover, it is important to keep in mind that the machine attains the same power rating irrespective of the number of phases. This means that upon rewinding, either the rated six-phase line-to-neutral voltage $u_{\mathrm{s,6ph}}$ or the rated line current $i_{\mathrm{s,6ph}}$ must be half their respective three-phase variables $u_{\mathrm{s,3ph}}$ or $i_{\mathrm{s,3ph}}$ to attain the same output power, i.e.

$$p_{\mathrm{s,3ph}} = 3u_{\mathrm{s,3ph}}\, i_{\mathrm{s,3ph}} = 6u_{\mathrm{s,6ph}}\, i_{\mathrm{s,6ph}} = p_{\mathrm{s,6ph}}. \tag{A.2.1}$$

Halving either $u_{\mathrm{s,6ph}}$ or $i_{\mathrm{s,6ph}}$ is a degree of freedom and should be practically selected depending on the drive conditions in terms of supply current capability, the available DC-link reserve, and the VSI switches specifications. Halving $u_{\mathrm{s,6ph}}$ will not only halve the number of turns per coil; to keep the same magnetomotive force (MMF) as in the three-phase case, but will also halve the demanded DC-link voltage required to achieve the rated speed. While halving $i_{\mathrm{s,6ph}}$ does not alter the number of turns per coil but rather reduce the current rating of the VSI switches.
A dual three-phase machine is composed of two three-phase sets, namely $a_1b_1c_1$ and $a_2b_2c_2$, while a three-phase machine comprises abc. Since this section aims at exploiting the stator windings, it is assumed that the inner coils, which when connected in series form the windings $a_1b_1c_1$ of the ADT-IPMSM and abc of the three-phase IPMSM, are abc (see Fig. A.2-2). The inner windings forming $a_2b_2c_2$ are uvw. Before proceeding with the rewinding procedure, it is essential to define some common terms used in machine design:

- *ingoing and outgoing conductors* differentiate between the coil sides belonging

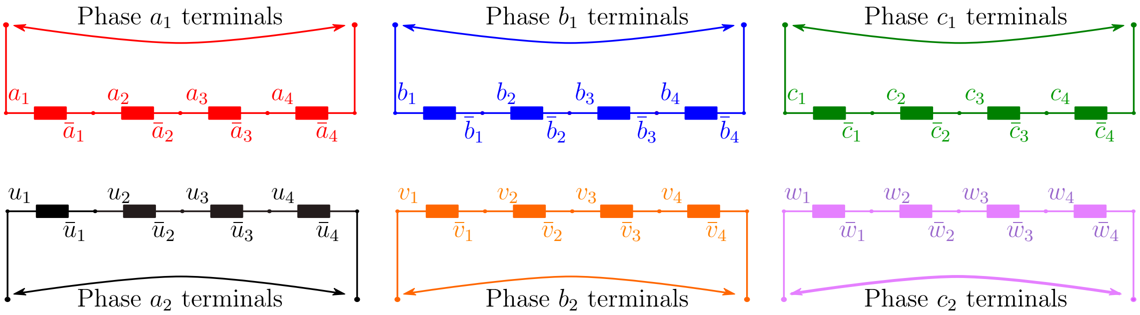

Fig. A.2-2. An exemplary winding diagram showing the inner coils abc and uvw of the stator phases $a_1b_1c_1$ and $a_2b_2c_2$, respectively. Each phase in this example consists of four inner coils as $\gamma_q\bar{\gamma}_q$ where $\gamma \in \{a,\ b,\ c,\ u,\ v,\ w\}$ and $q \in \{1,\ 2,\ 3,\ 4\}$. γ_q and $\bar{\gamma}_q$ denote the two terminals of the inner coil q.

to the same coil, where one side is assumed to be carrying the positive current flows into it (see $\otimes$ in Fig. A.2-3), while the other coil side carries the current in the opposite direction indicated by $\odot$ in Fig. A.2-3;

- *Distributed and concentrated windings* refer to the windings layout within the stator slots. If the windings per phase are distributed among the stator circumference (i.e. each pole has one or more coil side of every phase) then distributed windings are employed. If the entire coil sides of a phase are concentrated and distributed only among two slots, then concentrated winding layout is adopted. Distributed windings tend to enhance the flux content and the fundamental component is the dominant component, while the harmonic content for concentrated windings is considerably high. The former is relatively easier to control and realize from standard three-phase drives, while the latter requires custom made stator designs and is challenging from a control perspective. On the other hand, concentrated windings are advantageous in terms of fault tolerance, owing to the weak coupling between the machine phases [111];

- *Single layer and double layer windings* describe whether the stator windings are distributed in a single layer (i.e. each slot has one coil side as in Fig. A.2-3(a)) or two layers (i.e. each slot carries two coil sides as in Fig. A.2-3(b)). Double layer windings enhance the flux content in the air-gap and correspondingly the magnetomotive force at the expense of strengthening the magnetic coupling between the phases in comparison to the single winding layout. This aforementioned coupling is considered a disadvantage from fault-tolerance point of view, where the such magnetic coupling will affect negatively the machine transients [111];

- *Pole span* describes the number of slots under each north (N) and south (S) pole, designated by s_{pole}, and can be obtained by dividing the number of slots n_{slot} by $2n_{\text{p}}$ (i.e. $s_{\text{pole}} = n_{\text{slot}}/2n_{\text{p}}$). Each pole in Fig. A.2-3 spans 6 slots;

- *Coil span* describes the number of slots between the coil sides of a coil and is given by s_{coil}, as highlighted (in ▭) in Figs. A.2-3(a)-(b);

- *Full pitch and chorded windings* indicate whether the coil span is the same as the pole span (i.e. full pitch) or less (i.e. chorded). The factor $r = s_{\text{coil}}/s_{\text{pole}}$

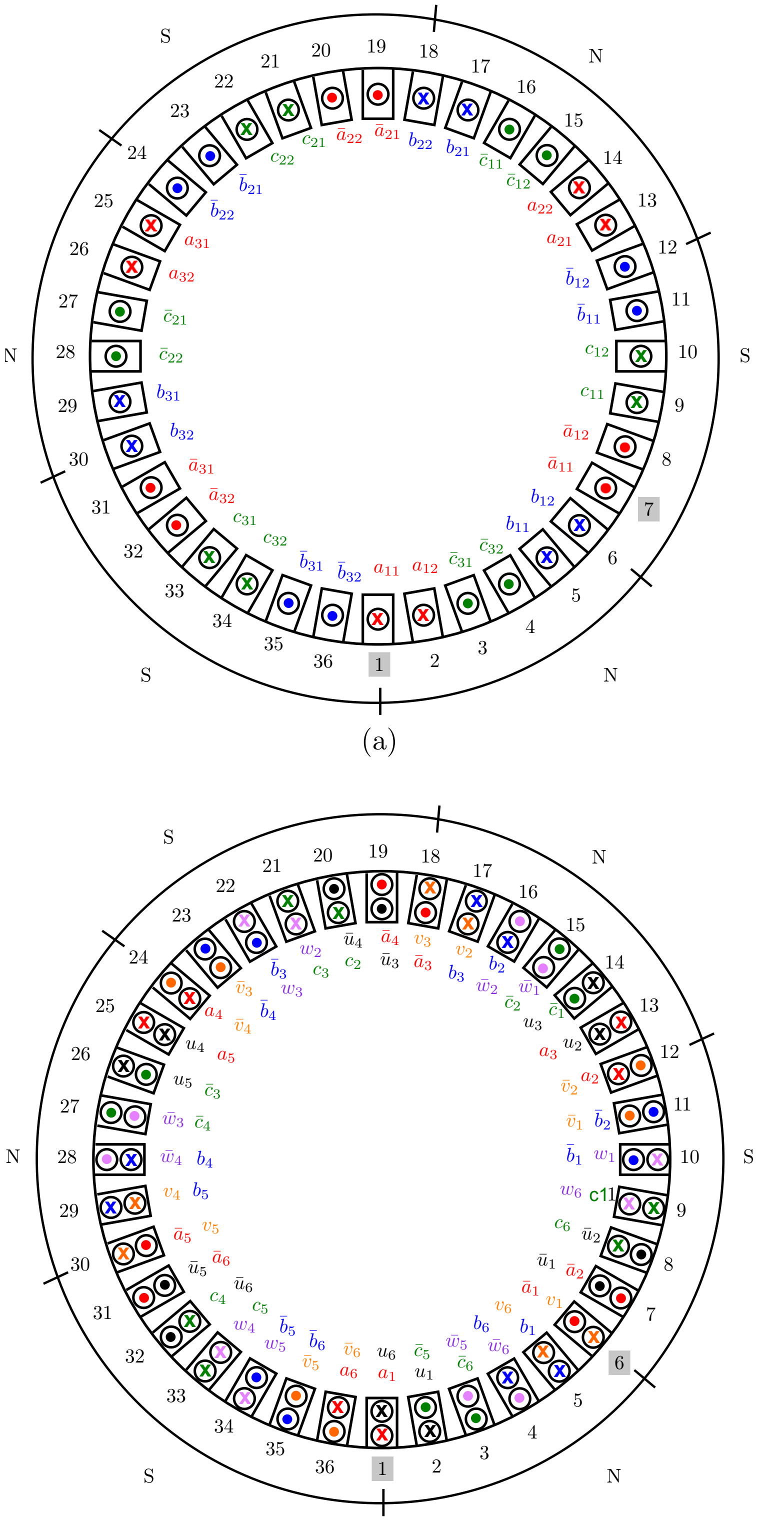

(a)

(b)

Fig. A.2-3. (a) Single-layer three-phase and (b) double-layer asymmetrical dual-three phase windings applied to the 6-pole Merkes IPMSM. The double-layer windings are pitched by $5/6$ (i.e. coil span is 5 slots), while the single-layer windings are full pitched (i.e. coil span is 6 slots) as highlighted (in ▭) for their inner coils $a_1\bar{a}_1$, $a_{11}\bar{a}_{11}$, respectively.

Table A.2-II. Electrical, mechanical and stator winding parameters comparison between the three-phase IPMSM machine, as purchased from the manufacturer, and upon rewinding to an asymmetrical dual three-phase machine.

	Parameter	Value (3ph)	Value (6ph)
Electrical and mechanical parameters	Stator resistance R_s	$2.2\,\Omega$	$1.1\,\Omega$
	Pole-pair n_p	3	3
	Inertia Θ *	$0.01\ \mathrm{kg\,m^2}$	$0.01\ \mathrm{kg\,m^2}$
	Viscous friction coefficient ν *	$0.8 \times 10^{-3}\ \mathrm{N\,m\,s}$	$0.8 \times 10^{-3}\ \mathrm{N\,m\,s}$
	Coulomb friction torque m_c *	$0.2725\ \mathrm{N\,m}$	$0.2725\ \mathrm{N\,m}$
	Rated stator peak current $\hat{i}_{s,rated}$	$4.1\sqrt{2}\ \mathrm{A}$	$4.1\sqrt{2}\ \mathrm{A}$
	Rated stator peak voltage $\hat{u}^{ltl}_{s,rated}$	$340\sqrt{2}\ \mathrm{V}$	$170\sqrt{2}\ \mathrm{V}$
	Rated torque $m_{e,rated}$	$10.6\ \mathrm{N\,m}$	$10.6\ \mathrm{N\,m}$
	Rated mechanical speed	2300 rpm	2300 rpm
Winding parameters**	Slots	36	36
	Number of slots s_{pole}	36	36
	Pole span s_{pole}	6	6
	Coil sides per slot	1	2
	Slot per pole per phase	2	1
	Number of turns per coil	30	15
	Number of turns per slot	30	30
	Conductor cross-sectional area	$0.71\,\mathrm{mm^2}$	$0.71\,\mathrm{mm^2}$
	Coil span s_{coil}	6	5
	Chording r	1	5/6

* Parameters obtained as in [65].

** Parameters obtained upon disassembling the machine at the workshop.

is a direct indicator if the chording has been applied. It is worth to mention that chording can only be applied to double layer windings (see Fig. A.2-3(b) and Fig. A.2-4).

Based on those definitions and the previous discussion, while iterating finite element simulations, Table A.2-II shows the employed winding layout parameters and the modifications to the machine parameters in comparison to the manufacturer three-phase version of the machine. Halving the rated voltage was selected when rewinding the machine. The winding layouts are shown in Figs. A.2-3(a)-(b). For the inner windings in Fig. A.2-3(a), the first subscript indicates the coil group number, while the second subscript is the coil number (i.e. each coil group has one or more number of coils bundled together). Note that coil group refers to the coils which are assembled externally and then mounted within the stator slots. Afterwards, the coil groups are connected in series to form the phase terminals *abc*. This is not the case in Fig. A.2-3(b), where each coil group is formed of only two coil sides (e.g. ⊗⊙ of $a_1\bar{a}_1$), to facilate the rewinding procedure. This will lead to 6 coil groups connected afterwards in series to form the stator terminals $a_1b_1c_1$ and $a_2b_2c_2$.

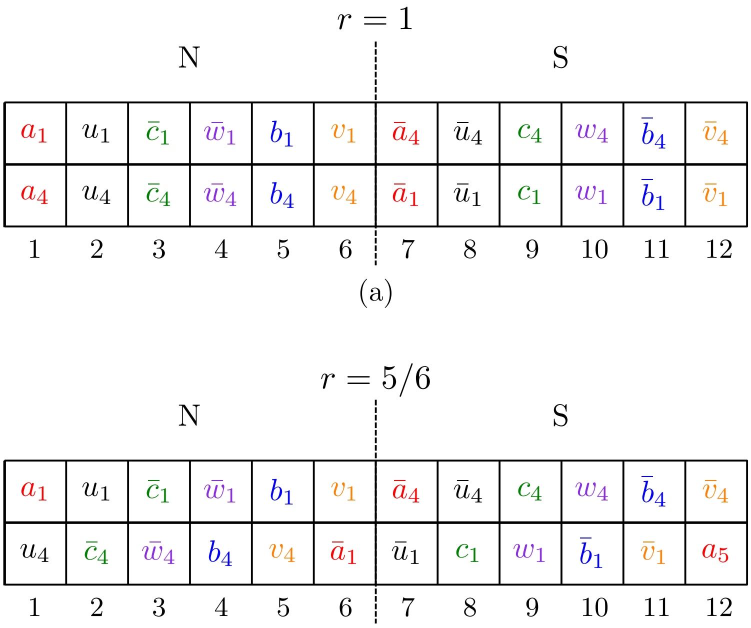

$r = 1$

N S

a_1	u_1	$\bar{c}_1$	$\bar{w}_1$	b_1	v_1	$\bar{a}_4$	$\bar{u}_4$	c_4	w_4	$\bar{b}_4$	$\bar{v}_4$
a_4	u_4	$\bar{c}_4$	$\bar{w}_4$	b_4	v_4	$\bar{a}_1$	$\bar{u}_1$	c_1	w_1	$\bar{b}_1$	$\bar{v}_1$
1	2	3	4	5	6	7	8	9	10	11	12

(a)

$r = 5/6$

N S

a_1	u_1	$\bar{c}_1$	$\bar{w}_1$	b_1	v_1	$\bar{a}_4$	$\bar{u}_4$	c_4	w_4	$\bar{b}_4$	$\bar{v}_4$
u_4	$\bar{c}_4$	$\bar{w}_4$	b_4	v_4	$\bar{a}_1$	$\bar{u}_1$	c_1	w_1	$\bar{b}_1$	$\bar{v}_1$	a_5
1	2	3	4	5	6	7	8	9	10	11	12

(b)

Fig. A.2-4. Cross-section of the 6-pole asymmetrical IPMSM by Merkes in the laboratory, illustrating the effect of (a) full-pitch $r = 1$ and (b) chorded windings $r = 5/6$ on the position of coil sides of a double-layer winding configuration.

A.3 Voltage-source inverters

The 2.5 kW ADT-IPMSM is powered by two off-the-shelf 15 kW three-phase VSIs by SEW® (see Fig. A.3-5) sharing a common DC-link voltage of 580 V, which is supplied by a three-phase diode rectifier energized by the utility grid. During breaking instants of the drive, the kinetic energy stored in the machine is extracted and fed back to the DC-link, where a DC/DC chopper dissipates the energy in a resistor bank. Thus, avoiding overcharging of the DC-link capacitors. The three-phase IM in section A.1 is controlled by a three-phase VSI 22 kW from the same company. The aforementioned VSIs are equipped with current measurements, which are isolated towards the power side due to the galvanic isolated current transducers. The switching action of the inverter is governed by a built-in field programmable gate array (FPGA) which translates the switching commands sent by the dSPACE DS5101 PWM card into meaningful switching action applied to the gate signal of the insulated-gate bipolar junction transistors (IGBTs). The switching frequency limit is 16 kHz.

A.4 dSPACE real-time system

The control algorithm is implemented on a dSPACE platform (see Fig. A.4-6) by means of the Matlab/Simulink interface. The dSPACE is powered by a powerful DS1007 2 GHz dual-core processor, combining the merits of high computing power as well as fast closed-loop rates. The PWM switching signals (i.e. elements of the

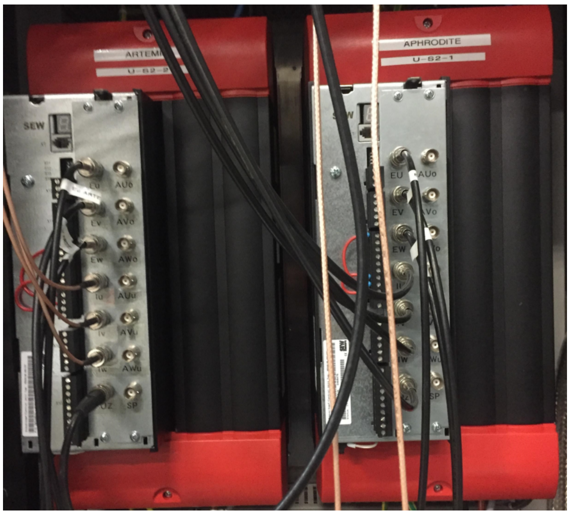

Fig. A.3-5. Dual three-phase 22kW VSIs by SEW® connected to the stator terminals of the ADT-IPMSM.

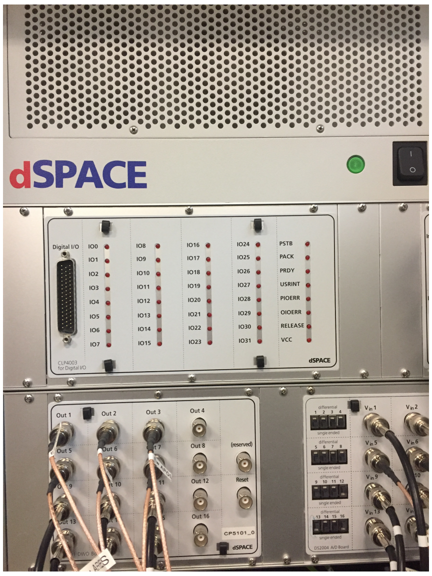

Fig. A.4-6. dSPACE real-time interface with its extension cards.

switching vector $\boldsymbol{s}_{\mathrm{VSI}}^{\mathrm{a_1 \to c_2}}$) are sent to the VSIs via the DS5101 PWM card, which is manually flashed and programmed to ensure precise timings and sampling instants. The A/D DS2004 board is triggered by the DS5101 board to carry-out the measurements in the middle of the switching period. The encoder outputs are connected to the incremental encoder interface board DS3001, for decoding the measured signals into rotor angular position and speed. The stator currents of both IM and ADT-IPMSM are measured via the on-board current sensors within the employed VSIs and measured signals or sent to the DS2004 A/D board for post-processing.

Fig. A.6-7. Incremental 2048 lines encoder by Heidenhein mounted on the ADT-IPMSM and IM.

A.5 Torque sensor

To validate the non-linear machine model and compare the expected and generated electromagnetic torque, the test-bench adopts a DR2212-R Lorenz® ± 30 N m torque sensor connected between the ADT-IPMSM and IM, as seen in Fig. A.1-1. The measurement is taken only from one side of the torque sensor, which is coupled to the ADT-IPMSM. The torque sensor is powered by an external off-the-shelf ± 5 V DC supply, while its output is linearly proportional to the measured torque and ranges between 0-10 V.

A.6 Encoders

The test-bench in Fig. A.1-1 is equipped with two incremental encoders, each with 2048 lines, mounted on every machine. Fig. A.6-7 depicts the adopted encoders. The encoder outputs are fed to the respective dSPACE encoder interface as explained in Section A.4. The encoder is powered with the external off-the-shelf ± 5 V DC supply.

A.7 Series circuit breaker

Six circuit breakers rated at 16 A are placed in series between the dual three-phase inverter and the ADT-IPMSM, while a neutral point circuit breaker is placed in between the neutral points of the three-phase sets $a_1b_1c_1$ and $a_2b_2c_2$ of the ADT-IPMSM, to facilitate the manipulation of the achievable speed range in accordance with the machine limits, as explained in the post-fault operation chapter 4.

Appendix B

Mathematical derivations

This appendix chapter shows long derivations, which were omitted from the thesis and placed in the appendix for the sake of easier understanding and enhance the grasping of the main topics under study.

B.1 Fault-tolerance derivations

During the post-fault operation, the electromechanical energy conversion is still governed by the fundamental component in the fundamental subspace (i.e. $\alpha\beta$ or dq subspaces). Assuming that the reference torque is within the limits in the post-fault operation, the *steady-state* $\alpha\beta$ reference currents $\bar{\boldsymbol{i}}^{\alpha\beta}_{\mathrm{s,ref}}$ can be expressed in terms of $\boldsymbol{i}^{dq}_{\mathrm{s,ref}}$ as

$$\bar{\boldsymbol{i}}^{\alpha\beta}_{\mathrm{s,ref}} \quad = \quad ||\boldsymbol{i}^{dq}_{\mathrm{s,ref}}|| \begin{pmatrix} \cos(\omega_{\mathrm{e}}t + \phi_{dq}) \\ \sin(\omega_{\mathrm{e}}t + \phi_{dq}) \end{pmatrix}, \text{ where } \tan(\phi_{dq}) = \frac{i^{q}_{\mathrm{s,ref}}}{i^{d}_{\mathrm{s,ref}}}. \tag{B.1.1}$$

It was discussed in [43, 97] that it is possible to ensure a steady torque generation by inducing *fundamental* currents in the stationary non-fundamental subspaces (i.e. XY and $0^{+}0^{-}$ subspaces) depending on the neutral point configuration and the applied post-fault strategy (maximum torque (MT), minimum losses (ML), and *hybrid* minimum losses maximum torque (MLMT)). Given that for 1N case, $i^{0+}_{\mathrm{s}} = -i^{0-}_{\mathrm{s}}$ as a physical circuit constraint, the relation between the subspace currents and the $\alpha\beta$ currents at steady state is mathematically modelled as

$$\begin{pmatrix} \bar{i}^{X}_{\mathrm{s,ref}} \\ \bar{i}^{Y}_{\mathrm{s,ref}} \\ \bar{i}^{0+}_{\mathrm{s,ref}} \\ \bar{i}^{0-}_{\mathrm{s,ref}} \end{pmatrix} = \begin{bmatrix} k^{\alpha}_{X} & k^{\beta}_{X} \\ k^{\alpha}_{Y} & k^{\beta}_{Y} \\ k^{\alpha}_{0+} & k^{\beta}_{0+} \\ -k^{\alpha}_{0+} & -k^{\beta}_{0+} \end{bmatrix} \bar{\boldsymbol{i}}^{\alpha\beta}_{\mathrm{s,ref}}, \tag{B.1.2}$$

which can be re-written as

$$\begin{pmatrix} \bar{i}^{X}_{\mathrm{s,ref}} \\ \bar{i}^{Y}_{\mathrm{s,ref}} \\ \bar{i}^{0+}_{\mathrm{s,ref}} \\ \bar{i}^{0-}_{\mathrm{s,ref}} \end{pmatrix} \overset{(\mathrm{B.1.1})}{=} ||\boldsymbol{i}^{dq}_{\mathrm{s,ref}}|| \begin{pmatrix} \hat{k}^{\alpha\beta}_{X}\big(\frac{k^{\alpha}_{X}}{\hat{k}^{\alpha\beta}_{X}}\cos(\omega_{\mathrm{e}}t+\phi_{dq}) + \frac{k^{\beta}_{X}}{\hat{k}^{\alpha\beta}_{X}}\sin(\omega_{\mathrm{e}}t+\phi_{dq})\big) \\ \hat{k}^{\alpha\beta}_{Y}\big(\frac{k^{\alpha}_{Y}}{\hat{k}^{\alpha\beta}_{Y}}\cos(\omega_{\mathrm{e}}t+\phi_{dq}) + \frac{k^{\beta}_{Y}}{\hat{k}^{\alpha\beta}_{Y}}\sin(\omega_{\mathrm{e}}t+\phi_{dq})\big) \\ \hat{k}^{\alpha\beta}_{0+}\big(\frac{k^{\alpha}_{0+}}{\hat{k}^{\alpha\beta}_{0+}}\cos(\omega_{\mathrm{e}}t+\phi_{dq}) + \frac{k^{\beta}_{0+}}{\hat{k}^{\alpha\beta}_{0+}}\sin(\omega_{\mathrm{e}}t+\phi_{dq})\big) \\ -\hat{k}^{\alpha\beta}_{0+}\big(\frac{k^{\alpha}_{0+}}{\hat{k}^{\alpha\beta}_{0+}}\cos(\omega_{\mathrm{e}}t+\phi_{dq}) + \frac{k^{\beta}_{0+}}{\hat{k}^{\alpha\beta}_{0+}}\sin(\omega_{\mathrm{e}}t+\phi_{dq})\big) \end{pmatrix}, \qquad (\mathrm{B.1.3})$$

where $\hat{k}^{\alpha\beta}_{X} = \sqrt{(k^{\alpha}_{X})^2 + (k^{\beta}_{X})^2}$, $\hat{k}^{\alpha\beta}_{Y} = \sqrt{(k^{\alpha}_{Y})^2 + (k^{\beta}_{Y})^2}$, and $\hat{k}^{\alpha\beta}_{0+} = \sqrt{(k^{\alpha}_{0+})^2 + (k^{\beta}_{0+})^2}$. By defining $\tan(\phi_x) = \dfrac{k^{\beta}_{X}}{k^{\alpha}_{X}}$; $\tan(\phi_y) = \dfrac{k^{\alpha}_{Y}}{k^{\beta}_{Y}}$; $\tan(\phi_0) = \dfrac{k^{\beta}_{0+}}{k^{\alpha}_{0+}}$, then (B.1.3) can be rewritten as

$$\begin{pmatrix} \bar{i}^{X}_{\mathrm{s,ref}} \\ \bar{i}^{Y}_{\mathrm{s,ref}} \\ \bar{i}^{0+}_{\mathrm{s,ref}} \\ \bar{i}^{0-}_{\mathrm{s,ref}} \end{pmatrix} = ||\boldsymbol{i}^{dq}_{\mathrm{s,ref}}|| \begin{pmatrix} \hat{k}^{\alpha\beta}_{X}\big(\cos(\omega_{\mathrm{e}}t+\phi_{dq})\cos(\phi_x) + \sin(\omega_{\mathrm{e}}t+\phi_{dq})\sin(\phi_x)\big) \\ \hat{k}^{\alpha\beta}_{Y}\big(\sin(\phi_y)\cos(\omega_{\mathrm{e}}t+\phi_{dq}) + \cos(\phi_y)\sin(\omega_{\mathrm{e}}t+\phi_{dq})\big) \\ \hat{k}^{\alpha\beta}_{0+}\big(\cos(\omega_{\mathrm{e}}t+\phi_{dq})\cos(\phi_0) + \frac{k^{\beta}_{0+}}{\hat{k}^{\alpha\beta}_{0+}}\sin(\omega_{\mathrm{e}}t+\phi_{dq})\sin(\phi_0)\big) \\ -\hat{k}^{\alpha\beta}_{0+}\big(\cos(\omega_{\mathrm{e}}t+\phi_{dq})\cos(\phi_0) + \frac{k^{\beta}_{0+}}{\hat{k}^{\alpha\beta}_{0+}}\sin(\omega_{\mathrm{e}}t+\phi_{dq})\sin(\phi_0)\big) \end{pmatrix}, \qquad (\mathrm{B.1.4})$$

Using the trigonometric identities,

$$\left.\begin{aligned} \cos(\gamma+\Gamma) &= \cos(\gamma)\cos(\Gamma) - \sin(\gamma)\sin(\Gamma), \\ \sin(\gamma+\Gamma) &= \sin(\gamma)\cos(\Gamma) + \cos(\gamma)\sin(\Gamma), \end{aligned}\right\} \qquad (\mathrm{B.1.5})$$

it is possible to simplify (B.1.4) into

$$\begin{pmatrix} \bar{i}^{X}_{\mathrm{s,ref}} \\ \bar{i}^{Y}_{\mathrm{s,ref}} \\ \bar{i}^{0+}_{\mathrm{s,ref}} \\ \bar{i}^{0-}_{\mathrm{s,ref}} \end{pmatrix} \overset{(\mathrm{B.1.3}),(\mathrm{B.1.5})}{=} ||\boldsymbol{i}^{dq}_{\mathrm{s,ref}}|| \begin{pmatrix} \hat{k}^{\alpha\beta}_{X}\ \cos(\omega_{\mathrm{e}}t+\phi_{dq}-\phi_x) \\ \hat{k}^{\alpha\beta}_{Y}\ \sin(\omega_{\mathrm{e}}t+\phi_{dq}+\phi_y) \\ \hat{k}^{\alpha\beta}_{0+}\ \cos(\omega_{\mathrm{e}}t+\phi_{dq}-\phi_0) \\ -\hat{k}^{\alpha\beta}_{0+}\ \cos(\omega_{\mathrm{e}}t+\phi_{dq}-\phi_0) \end{pmatrix}. \qquad (\mathrm{B.1.6})$$

Since the post-fault analysis is carried-out in *steady-state*, the phasor representation of (B.1.6) is

$$\begin{pmatrix} \bar{i}^{X}_{\mathrm{s,ref}} \\ \bar{i}^{Y}_{\mathrm{s,ref}} \\ \bar{i}^{0+}_{\mathrm{s,ref}} \\ \bar{i}^{0-}_{\mathrm{s,ref}} \end{pmatrix} = ||\boldsymbol{i}^{dq}_{\mathrm{s,ref}}|| \begin{pmatrix} \hat{k}^{\alpha\beta}_{X} \angle(\phi_{dq} - \phi_{x}) \\ \hat{k}^{\alpha\beta}_{Y} \angle(\phi_{dq} + \phi_{y} - \pi/2) \\ \hat{k}^{\alpha\beta}_{0+} \angle(\phi_{dq} - \phi_{0}) \\ \hat{k}^{\alpha\beta}_{0+} \angle(\phi_{dq} - \phi_{0} - \pi) \end{pmatrix}. \tag{B.1.7}$$

Bibliography

[1] X. Yang, Y. Song, G. Wang, and W. Wang, "A comprehensive review on the development of sustainable energy strategy and implementation in china," *IEEE Transactions on Sustainable Energy*, vol. 1, pp. 57–65, Jul. 2010.

[2] E. A. Martinez-Cesena and J. Mutale, "Wind power projects planning considering real options for the wind resource assessment," *IEEE Transactions on Sustainable Energy*, vol. 3, pp. 158–166, Jan. 2012.

[3] C. Palanichamy, N. S. Babu, R. K. Chelvan, and C. Nadarajan, "Restructuring the indian power sector with energy conservation as the motive for economic and environmental benefits," *IEEE Transactions on Energy Conversion*, vol. 14, pp. 1589–1596, Dec. 1999.

[4] T. J. Hammons, Z. Bicki, V. A. Djangirov, S. Goethe, L. Kapolyi, S. Kiciman, M. Klawe, Y. Kucherov, V. Y. Kurochkin, Z. Reguly, J. Schwarz, A. Tombor, and N. I. Voropai, "Eastern and western european policy on electricity infrastructure, interconnections and electricity exchanges," *IEEE Transactions on Energy Conversion*, vol. 15, pp. 328–341, Sept. 2000.

[5] X. Yang, Y. Song, G. Wang, and W. Wang, "A comprehensive review on the development of sustainable energy strategy and implementation in China," *IEEE Transactions on Sustainable Energy*, vol. 1, pp. 57–65, Jul. 2010.

[6] North American Electric Reliability Council (NERC), "Preparing the electric power systems of North America for transition to the year 2000," *IEEE Power Engineering Review*, vol. 19, pp. 9–11, Jan. 1999.

[7] R. Kunzig (National Geographic), "Germany Could Be a Model for How We will Get Power in the Future." `https://www.nationalgeographic.com/magazine/2015/11/germany_renewable_energy_revolution`, 2015. Accessed: 04-11-2018.

[8] United Nations, "The Paris Agreement." `https://unfccc.int/process_and_meetings/the_paris_agreement/the_paris_agreement`, 2015. Accessed: 28-08-2018.

[9] The National Aeronautics and Space Administration (NASA), "Why a half degree temperature rise is a big deal?." `https://climate.nasa.gov/news/2458/why_a_half_degree_temperature_rise_is_a_big_deal/`, 2018. Accessed: 22-08-2018.

[10] The World Bank Database, "Access to electricity." `https://data.worldbank.org/indicator/eg.elc.accs.zs?end=2016&start=1990`, 2016. Accessed: 09-09-2018.

[11] D. Watson, C. Hastie, and M. Rodgers, "Comparing different regulation offerings from a battery in a wind R&D park," *IEEE Transactions on Power Systems*, vol. 33, pp. 2331–2338, May 2018.

[12] P. Chen and T. Thiringer, "Analysis of energy curtailment and capacity overinstallation to maximize wind turbine profit considering electricity price-wind correlation," *IEEE Transactions on Sustainable Energy*, vol. 8, pp. 1406–1414, Oct. 2017.

[13] M. Marinelli, P. Maule, A. N. Hahmann, O. Gehrke, P. B. Nørgrd, and N. A. Cutululis, "Wind and photovoltaic large-scale regional models for hourly production evaluation," *IEEE Transactions on Sustainable Energy*, vol. 6, pp. 916–923, Jul. 2015.

[14] United States Department of Transportation, "Transportation Statistics Annual Report." `https://www.bts.dot.gov/sites/bts.dot.gov/files/docs/TSAR2016.pdf`, 2016. Accessed: 10-09-2018.

[15] European Enviromental Agency (EEA), "Greenhouse gas emissions from transport." `https://www.eea.europa.eu`, 2017. Accessed: 10-09-2018.

[16] J. Dargay, D. Gately, and M. Sommer, "Vehicle ownership and income growth, worldwide: 1960-2030," *The Energy Journal*, vol. 28, no. 4, pp. 143–170, 2007.

[17] Deutschlandsnetzagentur, "Strommarktdaten." `https://www.smard.de/home`. Accessed: 10-09-2018.

[18] Renewable Energy Policy Network for the 21st Centruy (REN21), "10 Years of Renewable Energy Progress." `http://www.ren21.net`. Accessed: 05-09-2018.

[19] B. B. Global wind energy council, "Global wind statistics 2017," Februarry 2018.

[20] D. Milborrow, "Recent development in wind turbine design," *E&T Energy-Power Hub*, 2017.

[21] C. Dirscherl, C. Hackl, and K. Schechner, "Modellierung und Regelung von modernen Windkraftanlagen: Eine Einführung," in *Elektrische Antriebe – Regelung von Antriebssystemen* (D. Schröder, ed.), ch. 24, pp. 1540–1614, Springer-Verlag, 2015.

[22] "Offshore wind in europe: Key trends and statistics," *Wind Europe*, 2017.

[23] Enerkite GmbH, "Weltkarte der Wirtschaftlichkeit für 100-kW-Anlagen." `https://www.enerkite.de`. Accessed: 30-10-2018.

[24] R. Schmehl, *Airborne Wind Energy: Advances in Technology Development and Research*. Green Energy and Technologies, Berlin Heidelberg: Springer-Singapore, 2018.

[25] L. ML., "Crosswind kite power (for large-scale wind power production)," *J.energy*, vol. 4, no. 3, pp. 106–111, 1980.

[26] A. Cherubini, A. Papini, R. Vertechy, and M. Fontana, "Airborne wind energy systems: A review of the technologies," *Renewable and Sustainable Energy Reviews*, vol. 51, pp. 1461–1476, 2015.

[27] Ampyx Power BV, "The Energy of Tomorrow." `https://www.ampyxpower.com`. Accessed: 29-10-2018.

[28] Makani, "Our Journey." `https://x.company/makani`. Accessed: 30-10-2018.

[29] Altaeros Energies, "Cost-effective tethered airbone platforms." `http://www.altaeros.com/index.html`. Accessed: 28-10-2018.

[30] "IEEE recommended practice and requirements for harmonic control in electric power systems," *IEEE Std 519-2014 (Revision of IEEE Std 519-1992)*, pp. 1–29, Jun. 2014.

[31] "IEEE recommended practice for monitoring electric power quality," *IEEE Std 1159-2009 (Revision of IEEE Std 1159-1995)*, pp. c1–81, Jun. 2009.

[32] C. L. Archer and K. Caldeira, "Global assessment of high-altitude wind power," *Energies*, vol. 2, no. 2, pp. 307–319, 2009.

[33] E. Lunney, M. Ban, N. Duic, and A. Foley, "A state-of-the-art review and feasibility analysis of high altitude wind power in northern ireland," *Renewable and Sustainable Energy Reviews*, vol. 68, pp. 899–911, 2017.

[34] EU-AWESCO Project, "Airborne Wind Energy System Control and Optimization (AWESCO)." `http://awesco.eu/partners.html`. Accessed: 27-10-2018.

[35] T. A. Huynh and M. Hsieh, "Comparative study of pm-assisted synrm and ipmsm on constant power speed range for ev applications," *IEEE Transactions on Magnetics*, vol. 53, pp. 1–6, Nov. 2017.

[36] B. Hahn, M. Durstewitz, and K. Rohrig, "Reliability of wind turbines, experiences of 15 years with 1500 WTs," in *Wind Energy* (J. Peinke, P. Schaumann, and S. Barth, eds.), Proceedings of the Euromech Colloquium, pp. 329–332, Berlin: Springer-Verlag, 2007.

[37] M. Katanic, "Encoderless control of dual three-phase IPMSM drives for awe applications," Master's thesis, Munich School of Engineering, Dec. 2017.

[38] I. Gonzalez-Prieto, M. J. Duran, H. S. Che, E. Levi, M. Bermúdez, and F. Barrero, "Fault-tolerant operation of six-phase energy conversion systems with parallel machine-side converters," *IEEE Transactions on Power Electronics*, vol. 31, pp. 3068–3079, Apr. 2016.

[39] W. N. W. A. Munim, M. Duran, H. S. Che, M. Bermudez, I. Gonzalez-Prieto, and N. A. Rahim, "A unified analysis of the fault tolerance capability in six-phase induction motor drive," *IEEE Transactions on Power Electronics*, vol. 32, no. 10, pp. 7824–7836, 2016.

[40] G. R. Catuogno, G. O. Garcia, and R. Leidhold, "Fault tolerant control in six-phase PMSM under four open-circuits fault conditions," in *42nd Annual Conference of the IEEE Industrial Electronics Society (IECON'16)*, pp. 5754–5759, Oct. 2016.

[41] W. Wang, J. Zhang, M. Cheng, and S. Li, "Fault-tolerant control of dual three-phase permanent-magnet synchronous machine drives under open-phase faults," *IEEE Trans. on Power Electron.*, vol. 32, pp. 2052–2063, Mar. 2017.

[42] H. S. Che, M. J. Duran, E. Levi, M. Jones, W. P. Hew, and N. A. Rahim, "Postfault operation of an asymmetrical six-phase induction machine with single and two isolated neutral points," *IEEE Transactions on Power Electronics*, vol. 29, pp. 5406–5416, Oct. 2014.

[43] F. Baneira, J. Doval-Gandoy, A. G. Yepes, . López, and D. Pérez-Estévez, "Control strategy for multiphase drives with minimum losses in the full torque operation range under single open-phase fault," *IEEE Transactions on Power Electronics*, vol. 32, pp. 6275–6285, Aug. 2017.

[44] H. Eldeeb, A. S. Abdel-Khalik, and C. Hackl, "Post-fault full torque-speed exploitation of dual three-phase IPMSM drives," *IEEE Transactions on Industrial Electronics*, vol. 66, pp. 6746–6756, Sept. 2019.

[45] C. Stephan J, *Electric Machinery Fundamentals.* Die Grundlehren der mathematischen Wissenschaften, New York: McGraw-Hill, 4th ed., 2005.

[46] H. Eldeeb, C. M. Hackl, L. Horlbeck, and J. Kullick, "A unified theory for optimal feedforward torque control of anisotropic synchronous machines," *International Journal of Control*, pp. 1–30, 2017.

[47] H. Eldeeb, M. Abdelrahem, C. Hackl, and A. S. Abdel-Khalik, "Enhanced electromechanical modeling of asymmetrical dual three-phase ipmsm drives," in *IEEE 27th International Symposium on Industrial Electronics (ISIE'18)*, pp. 126–132, Jun. 2018.

[48] H. Eldeeb, C. Hackl, M. Abdelrahem, and A. S. Abdel-Khalik, "A unified SVPWM realization for minimizing circulating currents of dual three phase machines," in *2017 IEEE 12th International Conference on Power Electronics and Drive Systems (PEDS)*, pp. 925–931, Dec. 2017.

[49] D. Hadiouche, L. Baghli, and A. Rezzoug, “Space-vector pwm techniques for dual three-phase ac machine: analysis, performance evaluation, and dsp implementation,” *IEEE Transactions on Industrial Applications*, vol. 42, pp. 1112–1122, Jul. 2006.

[50] D. Glose, *Modulation Strategies for Symmetrical Six-Phase Drives.* Dissertation, Technische Universität München, München, 2016.

[51] H. M. Eldeeb, A. S. Abdel-Khalik, and C. M. Hackl, “Dynamic modeling of dual three-phase ipmsm drives with different neutral configurations,” *IEEE Transactions on Industrial Electronics*, vol. 66, pp. 141–151, Jan. 2019.

[52] A. G. Yepes, J. Doval-Gandoy, F. Baneira, D. Perez-Estevez, and O. Lopez, “Current harmonic compensation for n -phase machines with asymmetrical winding arrangement and different neutral configurations,” *IEEE Transactions on Industrial Applications*, vol. 53, pp. 5426–5439, Nov. 2017.

[53] A. G. Yepes, J. Malvar, A. Vidal, O. López, and J. Doval-Gandoy, “Current harmonics compensation based on multiresonant control in synchronous frames for symmetrical$n$-phase machines,” *IEEE Transactions on Industrial Electronics*, vol. 62, pp. 2708–2720, May 2015.

[54] E. A. Klingshirn, “High phase order induction motors - part i. description and theoretical considerations,” *IEEE Power Engineering Review*, vol. PER-3, pp. 27–27, Jan. 1983.

[55] E. Levi, D. Dujic, M. Jones, and G. Grandi, “Analytical determination of dc-bus utilization limits in multiphase vsi supplied ac drives,” *IEEE Transactions on Energy Conversion*, vol. 23, pp. 433–443, Jun. 2008.

[56] S. Kallio, M. Andriollo, A. Tortella, and J. Karttunen, “Decoupled d-q model of double-star interior-permanent-magnet synchronous machines,” *IEEE Transactions on Industrial Electronics*, vol. 60, pp. 2486–2494, Jun. 2013.

[57] M. L. Woldesemayat, H. Lee, S. Won, and K. Nam, “Modeling and verification of a six-phase interior permanent magnet synchronous motor,” *IEEE Transactions on Power Electronics*, vol. 33, pp. 8661–8671, Oct. 2018.

[58] J. Kim, I. Jeong, K. Nam, J. Yang, and T. Hwang, “Sensorless control of PMSM in a high-speed region considering iron loss,” *IEEE Transactions on Industrial Electronics*, vol. 62, pp. 6151–6159, Oct. 2015.

[59] M. H. Vafaie, B. M. Dehkordi, P. Moallem, and A. Kiyoumarsi, “Minimizing torque and flux ripples and improving dynamic response of pmsm using a voltage vector with optimal parameters,” *IEEE Transactions on Industrial Electronics*, vol. 63, pp. 3876–3888, Jun. 2016.

[60] C. M. Hackl, *Non-identifier based adaptive control in mechatronics: Theory and Application.* No. 466 in Lecture Notes in Control and Information Sciences, Berlin: Springer International Publishing, 2017.

[61] R. Cai, R. Zheng, M. Liu, and M. Li, “Robust control of pmsm using geometric model reduction and µ-synthesis,” *IEEE Transactions on Industrial Electronics*, vol. 65, pp. 498–509, Jan. 2018.

[62] D. Schröder, *Elektrische Antriebe - Regelung von Antriebssystemen.* Berlin Heidelberg: Springer-Verlag, 4 ed., 2015.

[63] Y. Zhao and T. A. Lipo, “Space vector pwm control of dual three-phase induction machine using vector space decomposition,” *IEEE Transactions on Industrial Applications*, vol. 31, pp. 1100–1109, Sept. 1995.

[64] Y. Hu, Z. Q. Zhu, and K. Liu, “Current control for dual three-phase permanent magnet synchronous motors accounting for current unbalance and harmonics,” *IEEE Journal of Emerging and Selected Topics in Power Electron.*, vol. 2, pp. 272–284, Jun. 2014.

[65] K. Yahia, D. Matos, J. O. Estima, and A. J. M. Cardoso, “Modeling synchronous reluctance motors including saturation, iron losses and mechanical losses,” in *2014 International Symposium on Power Electronics, Electrical Drives, Automation and Motion*, pp. 601–606, Jun. 2014.

[66] H. S. Che, E. Levi, M. Jones, W. P. Hew, and N. A. Rahim, “Current control methods for an asymmetrical six-phase induction motor drive,” *IEEE Transactions on Power Electronics*, vol. 29, pp. 407–417, Jan. 2014.

[67] S. Kallio, J. Karttunen, P. Peltoniemi, P. Silventoinen, and O. Pyrhonen, “Determination of the inductance parameters for the decoupled d-q model of double-star permanent magnet synchronous machines,” *IET Electric Power Applications*, vol. 8, pp. 39–49, Feb. 2014.

[68] C. M. Hackl, M. J. Kamper, J. Kullick, and J. Mitchell, “Current control of reluctance synchronous machines with online adjustment of the controller parameters,” in *in Proceedings of the 2016 IEEE International Symposium on Ind. Electron. (ISIE 2016)*, (Santa Clara, CA, USA), pp. 156–160, 2016.

[69] J. Liu, C. Gong, Z. Han, and H. Yu, “IPMSM model predictive control in flux-weakening operation using an improved algorithm,” *IEEE Transactions on Industrial Electronics*, vol. 65, pp. 9378–9387, Dec. 2018.

[70] Q. Chen, W. Zhao, G. Liu, and Z. Lin, “Extension of virtual-signal-injection-based MTPA control for five-phase IPMSM into fault-tolerant operation,” *IEEE Transactions on Industrial Electronics*, vol. 66, pp. 944–955, Feb. 2019.

[71] H. S. Che, A. S. Abdel-Khalik, O. Dordevic, and E. Levi, “Parameter estimation of asymmetrical six-phase induction machines using modified standard tests,” *IEEE Transactions on Industrial Electronics*, vol. 64, no. 8, pp. 6075–6085, 2017.

[72] K. Marouani, L. Baghli, D. Hadiouche, A. Kheloui, and A. Rezzoug, “A new pwm strategy based on a 24-sector vector space decomposition for a six-phase vsi-fed dual stator induction motor,” *IEEE Trans. on Ind. Electron.*, vol. 55, pp. 1910–1920, May 2008.

[73] D. G. Holmes and T. A. Lipo, *Pulse width modulation for power converters : principles and practice*. 445 Hoes Lane Piscataway, NJ 08854: Wiley-IEEE Press, v1.0 ed., 2003.

[74] D. G. Holmes and T. A. Lipo, *Modulation of Three-Phase Voltage Source Inverters*. IEEE, 2003.

[75] D. Dujic, E. Levi, and M. Jones, “DC bus utilisation in multiphase vsi supplied drives with a composite stator phase number,” in *IEEE International Conference on Industrial Technology*, pp. 1495–1500, Mar. 2010.

[76] J. Kullick, “Simulation and control of a small-scale wind turbine system with reluctance synchronous generator,” Master’s thesis, MSE Research Group “Control of renewable energy systems”, Technische Universität München, 2015.

[77] T. Lipo, “A d-q model for six phase induction machines,” in *Proceedings of the International Conference Electric Machines (ICEM)*, pp. 860–867, 1980.

[78] S. A. Singh, G. Carli, N. A. Azeez, and S. S. Williamson, “Modeling, design, control, and implementation of a modified Z-source integrated PV/Grid/EV DC charger/inverter,” *IEEE Transactions on Industrial Electronics*, vol. 65, pp. 5213–5220, Jun. 2018.

[79] C. Wang, K. Wang, and X. You, “Research on synchronized svpwm strategies under low switching frequency for six-phase vsi-fed asymmetrical dual stator induction machine,” *IEEE Transactions on Industrial Electronics*, vol. 63, pp. 6767–6776, Nov. 2016.

[80] dSPACE, “DS5101 Digital Waveform Output Board.” `https://www.dspace.com/en/inc/home/products/hw/phs_hardware/i_o_boards/digital_waveform_output.cfm`, 2005. Accessed: 09-11-2018.

[81] J. Zheng, S. Huang, F. Rong, and M. Lye, “Six-phase space vector PWM under stator one-phase open-circuit fault condition,” *Energies*, vol. 11, p. 1796, Jul. 2018.

[82] “Kitepower.” `https://kitepower.nl`. Accessed: 2018-10-30.

[83] S. Hu, Z. Liang, W. Zhang, and X. He, “Research on the integration of hybrid energy storage system and dual three-phase pmsm drive in ev,” *IEEE Trans. on Ind. Electron.*, 2017 (early-access).

[84] A. G. Yepes, F. D. Freijedo, J. Doval-Gandoy, . López, J. Malvar, and P. Fernandez-Comesaña, “Effects of discretization methods on the performance of resonant controllers,” *IEEE Transactions on Power Electronics*, vol. 25, pp. 1692–1712, Jul. 2010.

[85] H. Eldeeb, A. Massoud, A. S. Abdel-Khalik, and S. Ahmed, “A sensorless kalman filter-based active damping technique for grid-tied vsi with lcl filter,” *International Journal of Electrical Power & Energy Systems*, vol. 93, pp. 146 – 155, Dec. 2017.

[86] A. G. Yepes, F. D. Freijedo, J. Doval-Gandoy, . López, J. Malvar, and P. Fernandez-Comesaña, “Effects of discretization methods on the performance of resonant controllers,” *IEEE Transactions on Power Electronics*, vol. 25, pp. 1692–1712, Jul. 2010.

[87] C. Hackl, “On the equivalence of proportional-integral and proportional-resonant controllers with anti-windup,” *arXiv*, pp. 1–9, 2016.

[88] D. N. Zmood, D. G. Holmes, and G. H. Bode, “Frequency-domain analysis of three-phase linear current regulators,” *IEEE Transactions on Industry Applications*, vol. 37, pp. 601–610, Mar. 2001.

[89] F. Hamadto, “Natural frame modelling and open-phase fault detection of dual three-phase drives,” Master’s thesis, Munich School of Engineering, Oct. 2018.

[90] E. Levi, “Multiphase electric machines for variable-speed applications,” *IEEE Trans. on Ind. Electron.*, vol. 55, pp. 1893–1909, May 2008.

[91] M. J. Duran, I. Gonzalez-Prieto, N. Rios-Garcia, and F. Barrero, “A simple, fast, and robust open-phase fault detection technique for six-phase induction motor drives,” *IEEE Trans. on Power Electron.*, vol. 33, pp. 547–557, Jan. 2018.

[92] J. Hang, J. Zhang, M. Cheng, and S. Ding, “Detection and discrimination of open-phase fault in permanent magnet synchronous motor drive system,” *IEEE Transactions on Power Electronics*, vol. 31, pp. 4697–4709, Jul. 2016.

[93] B. Sen and J. Wang, “Stator interturn fault detection in permanent-magnet machines using pwm ripple current measurement,” *IEEE Transactions on Industrial Electronics*, vol. 63, pp. 3148–3157, May 2016.

[94] M. Salehifar, R. S. Arashloo, M. Moreno-Eguilaz, V. Sala, and L. Romeral, “Observer-based open transistor fault diagnosis and fault-tolerant control of five-phase permanent magnet motor drive for application in electric vehicles,” *IET Power Electronics*, vol. 8, no. 1, pp. 76–87, 2015.

[95] L. Zarri, M. Mengoni, Y. Gritli, A. Tani, F. Filippetti, G. Serra, and D. Casadei, “Detection and localization of stator resistance dissymmetry based on multiple reference frame controllers in multiphase induction motor drives,” *IEEE Transactions on Industrial Electronics*, vol. 60, pp. 3506–3518, Aug. 2013.

[96] H.-M. Ryu, J.-W. Kim, and S.-K. Sul, “Synchronous-frame current control of multiphase synchronous motor under asymmetric fault condition due to open phases,” *IEEE Transactions on Industry Applications*, vol. 42, pp. 1062–1070, Jul. 2006.

[97] A. G. Yepes, J. Doval-Gandoy, F. Baneira, and H. Toliyat, “Control strategy for dual three-phase machines with two open phases providing minimum loss in the full torque operation range,” *IEEE Transactions on Power Electronics*, 2018 (doi:10.1109/TPEL.2018.2830507).

[98] J.-R. Fu and T. A. Lipo, “Disturbance-free operation of a multiphase current-regulated motor drive with an opened phase,” *IEEE Transactions on Industry Applications*, vol. 30, pp. 1267–1274, Sept. 1994.

[99] J. Lemmens, P. Vanassche, and J. Driesen, “Optimal control of traction motor drives under electrothermal constraints,” *IEEE Journal of Emerging and Selected Topics in Power Electronics*, vol. 2, pp. 249–263, Jun. 2014.

[100] E. Trancho, E. Ibarra, A. Arias, I. Kortabarria, J. Jurgens, L. Marengo, A. Fricassè, and J. V. Gragger, “PM-assisted synchronous reluctance machine flux weakening control for ev and hev applications,” *IEEE Transactions on Industrial Electronics*, vol. 65, pp. 2986–2995, Apr. 2018.

[101] M. Tousizadeh, H. S. Che, N. A. Rahim, J. Selvaraj, and B. T. Ooi, “Performance comparison of fault-tolerant three-phase induction motor drives considering current and voltage limits,” *IEEE Transactions on Industrial Electronics*, 2018 (doi:10.1109/TIE.2018.2850006).

[102] J. M. Erdman, R. J. Kerkman, D. W. Schlegel, and G. L. Skibinski, “Effect of pwm inverters on ac motor bearing currents and shaft voltages,” *IEEE Transactions on Industrial Applications*, vol. 32, pp. 250–259, Mar. 1996.

[103] G. Grandi, J. Loncarski, and O. Dordevic, “Analysis and comparison of peak-to-peak current ripple in two-level and multilevel PWM inverters,” *IEEE Transactions on Industrial Electronics*, vol. 62, pp. 2721–2730, May 2015.

[104] A. Ruderman, “About voltage total harmonic distortion for single- and three-phase multilevel inverters,” *IEEE Transactions on Industrial Electronics*, vol. 62, pp. 1548–1551, Mar. 2015.

[105] M. Espinoza, R. Cardenas, J. C. Clare, D. Soto, M. Diaz, E. Espina, and C. M. Hackl, “An integrated converter and machine control system for mmc-based high power drives,” *IEEE Transactions on Industrial Electronics*, pp. 1–1, 2018.

[106] G. Wang, J. Kuang, N. Zhao, G. Zhang, and D. Xu, “Rotor position estimation of pmsm in low-speed region and standstill using zero-voltage vector injection,” *IEEE Transactions on Power Electronics*, vol. 33, pp. 7948–7958, Sept. 2018.

[107] T. A. Najafabadi, F. R. Salmasi, and P. Jabehdar-Maralani, “Detection and isolation of speed-, dc-link voltage-, and current-sensor faults based on an adaptive observer in induction-motor drives,” *IEEE Transactions on Industrial Electronics*, vol. 58, pp. 1662–1672, May 2011.

[108] E. Ribeiro, A. J. M. Cardoso, and C. Boccaletti, “Fault-tolerant strategy for a photovoltaic dc–dc converter,” *IEEE Transactions on Power Electronics*, vol. 28, pp. 3008–3018, Jun. 2013.

[109] C. Jin and P. Wang, “Enhancement of low voltage ride-through capability for wind turbine driven DFIG with active crowbar and battery energy storage system,” in *IEEE PES General Meeting*, pp. 1–8, Jul. 2010.

[110] P. Arboleya, C. Gonzalez-Moran, M. Coto, M. C. Falvo, L. Martirano, D. Sbordone, I. Bertini, and B. D. Pietra, “Efficient energy management in smart micro-grids: Zero grid impact buildings,” *IEEE Transactions on Smart Grid*, vol. 6, pp. 1055–1063, Mar. 2015.

[111] A. M. EL-Refaie, “Fractional-slot concentrated-windings synchronous permanent magnet machines: Opportunities and challenges,” *IEEE Transactions on Industrial Electronics*, vol. 57, pp. 107–121, Jan. 2010.